universität wien

DISSERTATION

Titel der Dissertation

"Alkali Interdiffusion in Alkali Feldspars"

Verfasserin

Anne-Kathrin Schäffer MSc

angestrebter akademischer Grad

Doktorin der Naturwissenschaften (Dr. rer. nat.)

Wien, 2014

Studienkennzahl lt. Studienblatt:	A 791 426
Dissertationsgebiet lt. Studienblatt:	Erdwissenschaften
Betreuer:	Univ.-Prof. Dr. Rainer Abart
	Prof. Dr. Wilhelm Heinrich

Contents

Physical Constants

Gas Constant	R	=	$8.314\ 4621\ \frac{J}{molK}$
Boltzmann Constant	k_b	=	$1.380\ 6488\ x10^{-23}\mathrm{J}K^{-1}$

Symbols

Symbol	Name	Unit
D	Interdiffusion Coefficient	$\frac{m^2}{s}$
D^*	Tracer-Diffusion Coefficient	$\frac{m^2}{s}$
E_A	Activation Energy	$\frac{kJ}{mol}$
T	Absolute Temperature	K
D_0	Pre-exponential Factor	$\frac{m^2}{s}$

Chapter 1

Introduction

Feldspars form a solid solution series between the end-members anorthite ($CaAl_2Si_2O_8$), albite ($NaAlSi_3O_8$) and orthoclase ($KAlSi_3O_8$), the alkali feldspars being constituted by the latter two. Their abundance in the Earth's crust and occurrence in a wide variety of environments makes it vital to have a sound knowledge of the large variety of intracrystalline microstructures they exhibit, and the processes and parameters controlling their formation. In particular the chemical composition, zoning patterns, and exsolution lamellae may bear important petrogenetic information (Spear, 1993). Many of these processes are controlled by diffusion, which influences the compositional and structural characteristics of feldspar.

In single crystals volume diffusion is the only mechanism for cations to move from one location to the other, and thus controls the rates of many solid state transformations, e.g. the homogenisation of primary growth zoning, loss of radiogenic nuclides or exsolution. A profound knowledge of diffusion rates allows us to infer thermal histories from frozen-in diffusion profiles and to assess whether a sample is applicable for age dating and geothermometry or has been reset by being exposed to temperatures that enable cation exchange with surrounding rocks.

Chemical alteration of alkali feldspar in the solid state requires interdiffusion of $Na^+$and K^+ and potential substituting of minor components on the cation sublattice. Major efforts to understand diffusion in alkali feldspars have been made especially during the 1970s and 80s. Important studies were conducted by Bailey (1971), Lin and Yund (1972), Foland (1974), Kasper (1975), Giletti et al. (1974), Petrović (1972), and Cherniak (2010) with focus mainly on tracer-diffusion of cations and Christoffersen et al. (1983), Brady and Yund (1983), Hokason and Yund (1986), and Snow and Kidman (1991) with emphasis on interdiffusion. Good summaries of the existing diffusion coefficients were given by Freer (1981) and Brady (1995), though some newer studies are not included in these

data digests. Looking at the existing data it quickly becomes obvious that the diffusion coefficients attained so far cover a wide range of values and that many questions regarding the mechanisms controlling diffusion are still unanswered. Furthermore, although anisotropy is to be expected for diffusion in crystals, it is only treated in very few of the existing studies.

The accuracy of any data is limited by the analytical techniques available at the time. Many tracer-diffusion experiments were conducted as bulk-exchange experiments, or the sectioning technique with a limited depth resolution and accuracy was used. In some cases it can be suspected that the values might be influenced by artefacts caused by fast diffusion pathways, e.g. micro-cracks or inhomogeneities of the starting materials and run products that were not documented.

Tracer- and interdiffusion in ionic crystals can be linked by the Nernst-Planck- or Manning equation (Manning, 1968). However, due to the aforementioned wide range in existing tracer-diffusion data, the calculation of the interdiffusion coefficients is uncertain. Thus it is desirable to determine the interdiffusion coefficient directly. For alkali feldspars with intermediate compositions of $0.1 \leq X_{Or} \leq 0.8$, with $X_{Or} = \frac{K}{K+Na}$ representing the mole fraction of potassium in the feldspar, this was done by Christoffersen et al. (1983) in diffusion couple experiments using albite and adularia. They found a strong anisotropy of interdiffusion with values being lower by a factor of ten for interdiffusion parallel to the *b*-axis relative to interdiffusion in the *a*-*c*-plane. They also found a strong composition dependence of interdiffusion with a minimum at X_{Or} 0.4 and a pronounced rise towards higher X_{Or}. This trends fits the values predicted with the Nernst-Planck equation using tracer-diffusion data by Kasper (1975) and Foland (1974), however, their values for a given composition were lower by one to two orders of magnitude, depending on crystallographic direction. This discrepancy raises the question whether the problem only lies in the tracer-diffusion data used, or if there may also be a need for adjustments to the model. Also, the composition range $0.8 \leq X_{Or} \leq 1$, into which most natural Or-rich feldspars fall, was not considered.

Additionally, due to the composition dependence and anisotropy of the lattice parameters any compositional shift leads to coherency strain. Studies by Petrović (1972), Neusser et al. (2012) and Scheidl et al. (2013) observed the occurrence of cracks when the feldspar composition is shifted by more than 10 mole-%. In the experimental setup by Christoffersen et al. (1983) the overall shift is more than 50 mole-% which would have to lead to creep or micro-cracking to accommodate the strain, however, no mention is made to this effect.

In this study one half of the diffusion couple was replaced by salt melt to minimize mechanical effects influencing diffusion. The other half is a crystallographically oriented

plate of single crystal feldspar. Feldspars with exchanged surface layers in the composition range $0.65 \leq X_{Or} \leq 1$ were produced using two varieties of sanidine with different initial compositions. The exchanged area is separated from the internal regions of the grain by a composition front, which can be interpreted as a diffusion front because Na-K interdiffusion is a necessity for cation exchange in single crystals. Depending on crystallographic orientation, run duration, and extent of the chemical shift a variety of different phenomena could be observed and evaluated.

For shifts towards more sodium-rich compositions, lattice contraction produces a very regular, sub-parallel system of cracks due to the coherency strain caused by the chemical shift. Their strict geometry allows for an analysis of the fracture mechanics to estimate the fracture toughness. In the case of composition shifts towards more potassium-rich compositions the systematics and geometry of the cracks are much more complex and cannot be as readily evaluated. Fractures in these experiments are often roughly parallel to the diffusion fronts and curve where the diffusion fronts propagating in different crystallographic directions link up. To gain insight into the coherency strain created by shifts towards more potassium-rich compositions, EBSD and the cross correlation method were employed to determine the full stress tensor across the diffusion fronts.

The diffusion fronts show different geometries depending on crystallographic direction and extent of the chemical shift. For shifts towards more sodium-rich compositions and small shifts towards more potassium-rich compositions, diffusion profiles develop that indicate a constant interdiffusion coefficient. However, for larger shifts to $X_{Or} > 0.95$ they take a shape that is characterised by two plateaus and an inflection point of the diffusion front itself, which indicates a composition dependence. The interdiffusion coefficient is extracted from a large number of measured profiles using Boltzmann's transformation. The results are compared to the data published by Christoffersen et al. (1983) as well as interdiffusion coefficients calculated according to a theoretical interdiffusion model for ionic crystals.

Chapter 2

Alkali Feldspars

Most feldspars pertain to a ternary solid solution series between the three end-members anorthite ($CaAl_2Si_2O_8$), albite ($NaAlSi_3O_8$) and orthoclase ($KAlSi_3O_8$) (figure 2.1). The alkali feldspars comprise the solid solution series between albite and orthoclase.

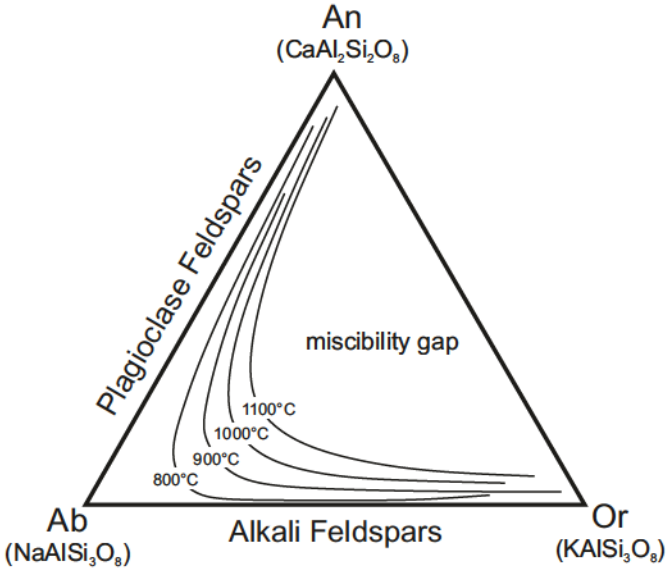

FIGURE 2.1: Ternary diagram An-Ab-Or; at high temperatures a solid solution between the alkali feldspars can exist, with decreasing temperature the miscibility gap in the ternary system broadens; modified after Spear (1993)

Alkali feldspars form a solid solution at high temperatures, but possess a miscibility gap which widens with decreasing temperature (figure 2.2). This leads to separation of feldspars with intermediate compositions into a K-rich and Na-rich phase at lower temperatures. This exsolution can occur on a variety of scales, forming submicroscopic cryptoperthites, microperthites visible with a microscope, or macroperthites visible to the naked eye (Deer et al., 2001).

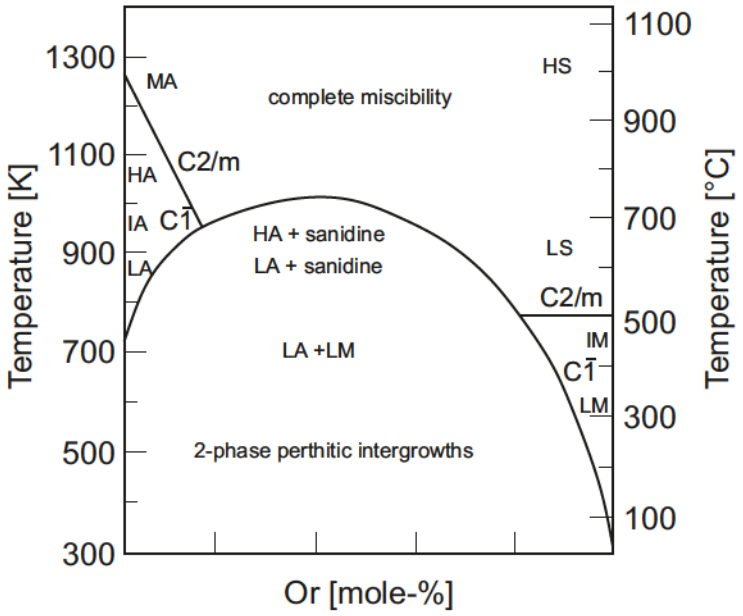

FIGURE 2.2: T-X diagram of alkali feldspars: at high temperatures the alkali feldspars are completely miscible, with decreasing temperatures the miscibility gap widens. For Na-rich feldspars the space group changes from monoclinic C2/m to triclinic C$\bar{1}$; phases: MA - monalbite, HA - high albite, IA - intermediate albite, LA - low albite, HS - high sanidine, LS - low sanidine, IM - intermediate microcline, LM - low microcline; modified after Deer et al. (2001)

Feldspars are framework silicates and have perfect cleavages on the (001) and (010) planes. The main building blocks of the feldspar framework are two types of four-membered rings of corner-shared AlO_4^{3-}- and SiO_4^{4-}-tetrahedra. One type of these rings is oriented roughly normal to the a-axis, the other roughly normal to the b-axis of the crystal (figure 2.3).

The rings parallel to the a-axis are built up by two pairs of non-equivalent tetrahedra, T_1 and T_2. The tetrahedral sites can either be occupied by Si^{4+} or Al^{3+}. The proportion of these sites occupied by Al gives the degree of order and is designated with a lower case t. For monoclinic feldspars the degree of order is calculated as:

$$\frac{t1 - t2}{t1 + t2} \tag{2.1}$$

One of the tetrahedra pairs is pointing up while the other points down. The downward pointing vertices are connected to the upward pointing vertices of the next ring along the a-axis. Thus every ring is connected to equivalent rings above and below, which leads to the formation of the second type of ring parallel to the b-axis (Taylor, 1933). These continuous chains of tetrahedron rings form crankshaft-like structures parallel to the a-axis (figures 2.4 and 2.5).

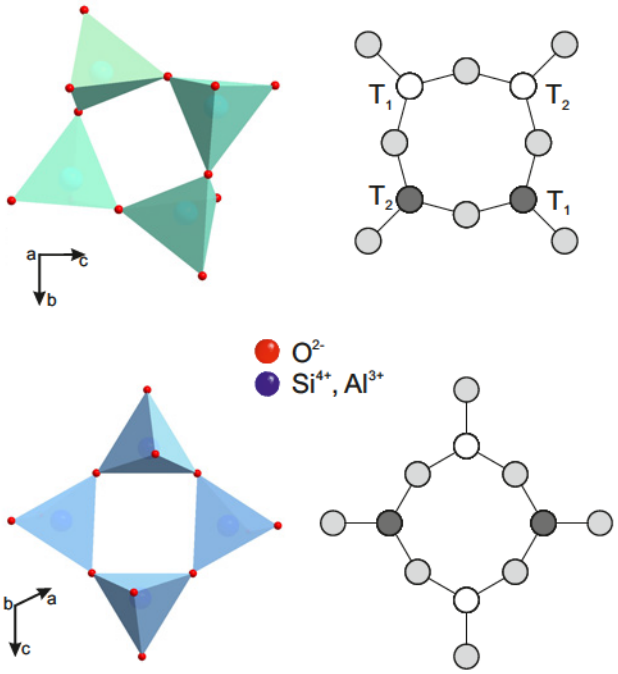

FIGURE 2.3: Four-membered rings of corner-shared AlO_4- and SiO_4-tetrahedra: one type of ring is oriented normal to the a-axis (top) while the other is normal to the b-axis (bottom); actual depiction of the crystal structure (left) created with Diamond using data for low sanidine by Phillips and Ribbe (1973) and schematic representation (right) with white circles indicating upwards-pointing, and dark grey circles downwards-pointing tetrahedra

The crankshaft chains are further corner-shared parallel to the b- and c-axes. Two different larger building units, made up of crankshaft chains interconnected through shared oxygen atoms, can be distinguished.

In monoclinic feldspars the crankshaft chains connect in a mirror relation parallel to (010) and two-fold rotation axes normal to b at $\frac{1}{4}b$ and $\frac{3}{4}b$ (Parsons, 1994), forming sheet-like units of interconnected crankshaft chains parallel to $(20\bar{1})$ (figure 2.6). The rings within these sheets are connected by shared oxygen atoms, denoted O_A. The sheets in turn are stacked along the a-axis, the oxygen atoms joining them being denoted O_B (figure 2.6).

Crankshaft chains are linked through adjacent O_B atoms in the b-direction, creating another sheet-like unit of connected crankshaft-like chains. These sheets are stacked parallel to c^* and connected by O_A atoms in this direction. The O_A atoms are located on the two-fold axes normal to b while the O_A atoms are located on the mirror planes parallel to (010) (figure 2.7).

On the basis of these sheet-like units of crankshaft chains connected by shared oxygen atoms parallel to b and c^*, it is possible to explain the perfect (010) and (001) cleavage planes.

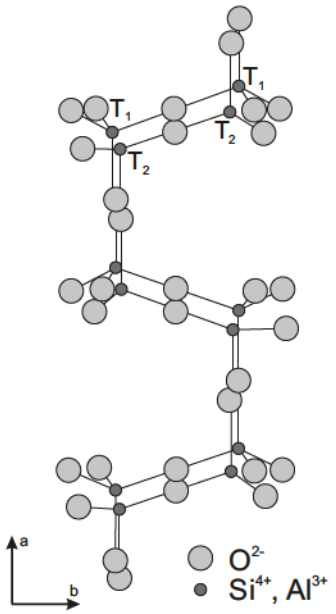

FIGURE 2.4: Crankshaft-like chains extending parallel to the a-direction are formed by alternating corner-shared tetrahedra rings; modified after Taylor (1933)

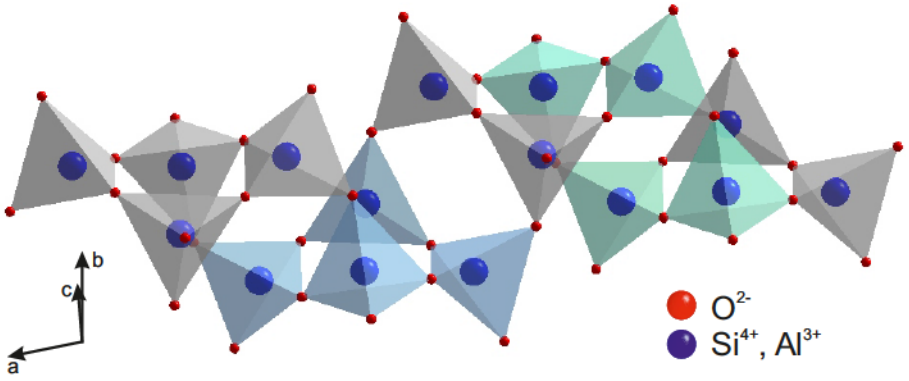

FIGURE 2.5: Every four-member ring oriented parallel to a is connected to adjacent equivalent rings forming nearly co-planar rings normal to b; created with Diamond using data for low sanidine by Phillips and Ribbe (1973)

Large irregular cavities form between the interconnected chains (figure 2.8). These cavities in the tetrahedral framework are occupied by the Na^+ and K^+ cations with minor substitution by Rb^+, Ba^{2+} and Ca^{2+} (Ribbe, 1983). Feldspars with significant Ba-content, termed Celsian ($BaAl_2Si_2O_8$), are very uncommon in nature, however, they can constitute a component in potassium-rich feldspars.

In some crystallographic directions the large cavities form channel-like structures that can ease movement of the large cations through the crystal. The largest of these channels exist parallel to [101] (figure 2.9), while the smallest are found in the direction 90° from [101] rotated around the b-axis, which is approximately $[10\bar{2}]$ (figure 2.10). Along the b-axis, which is one of the main directions examined in this study, the channels are of intermediate size (figure 2.11).

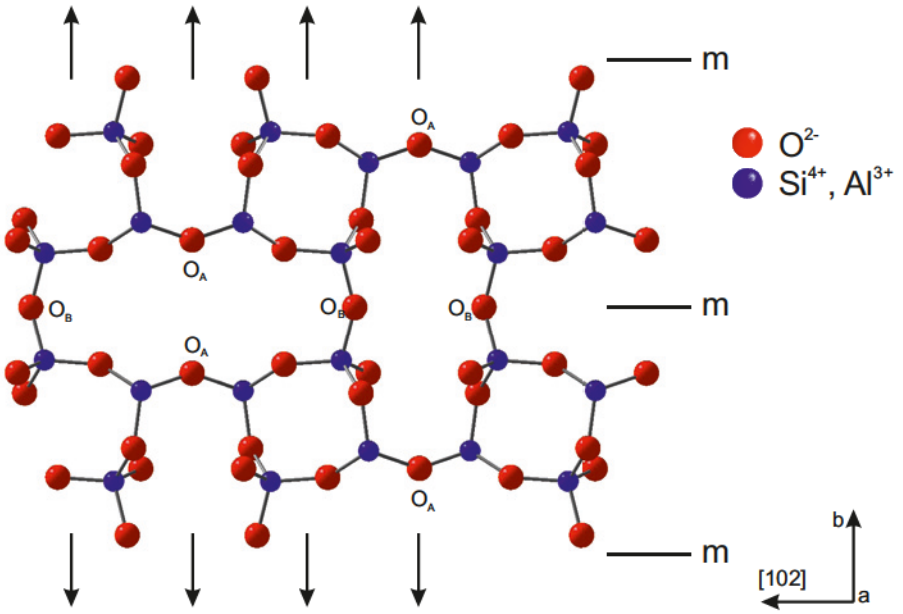

FIGURE 2.6: Crankshaft-like chains related by symmetry elements (m - mirror plane, arrows - two-fold rotation axes) form sheets parallel to the a-axis, projection on $(20\bar{1})$ seen along a; created with Diamond using data for low sanidine by Phillips and Ribbe (1973)

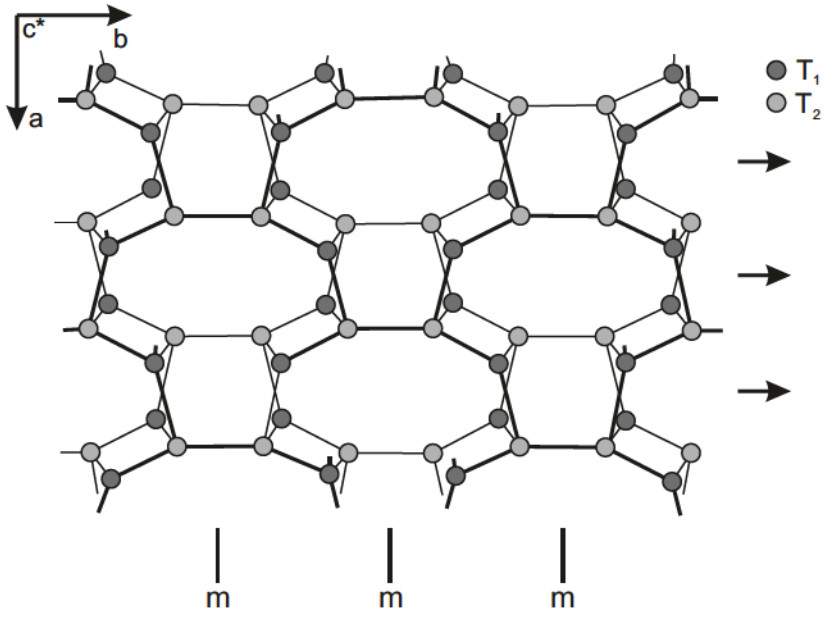

FIGURE 2.7: Crankshaft-like chains related by symmetry elements (m - mirror plane, arrows - two-fold rotation axes) form sheets parallel to the c^*-axis; modified after Ribbe (1983)

Incorporation of differently sized cations is mainly accommodated by the stretch of the crankshaft-like chains parallel to the a-axis (Petrović, 1972; Angel et al., 2012). This leads to a pronounced anisotropy of the composition dependence of the lattice parameters (figure 2.12), which is about five times higher in the a-direction than in the b- and c-directions (Kroll et al., 1986; Angel et al., 2012). Thus any compositional heterogeneity

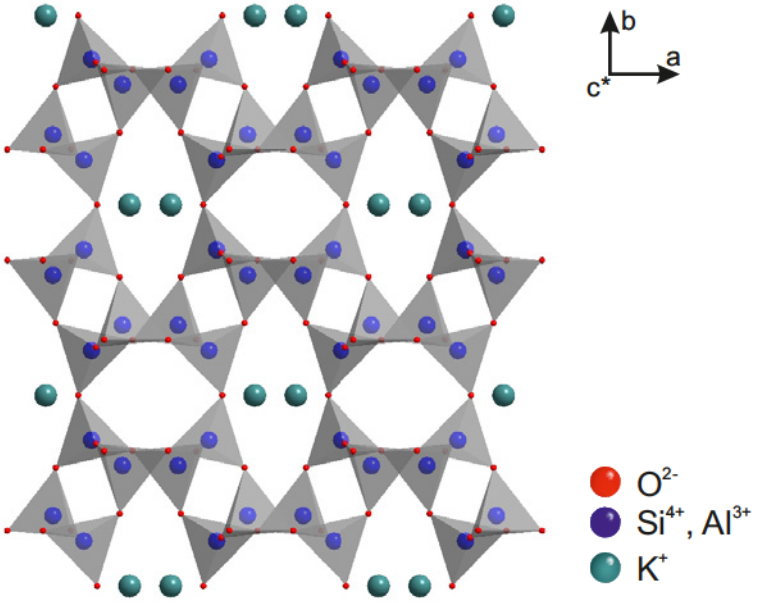

FIGURE 2.8: The big cations are located in large irregular cavities in the feldspar structure formed by the interconnected crankshaft-like chains; created with Diamond using data for low sanidine by Phillips and Ribbe (1973)

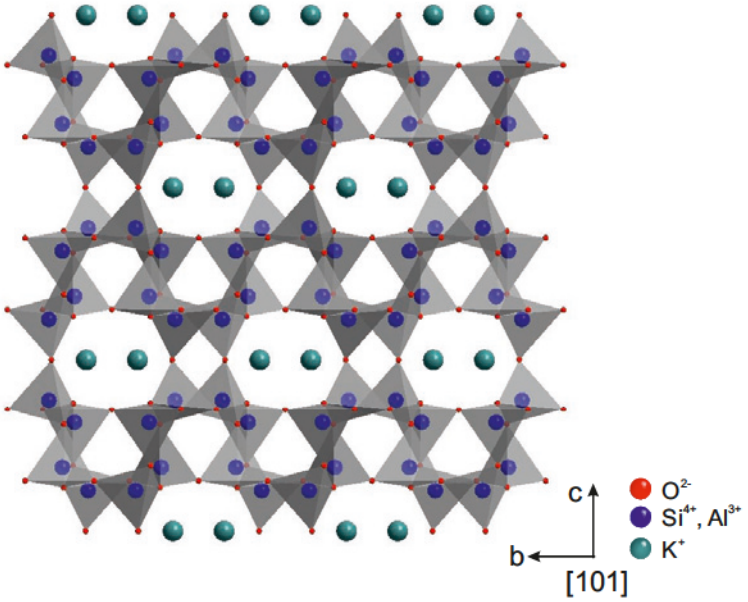

FIGURE 2.9: Large channels facilitate the movement of the cations through the feldspar structure, the largest channels are found along [101]; created with Diamond using data for low sanidine by Phillips and Ribbe (1973)

in alkali feldspar causes coherency stress.

The structural state and degree of Al/Si-ordering on the tetrahedral sites of feldspar are dependent on the temperature of crystallization and the thermal history it was subjected to (Deer et al., 2001). The simplest feldspar structure is that of sanidine ($KAlSi_3O_8$) with a monoclinic symmetry of C2/m, which was first described by Taylor (1933). To

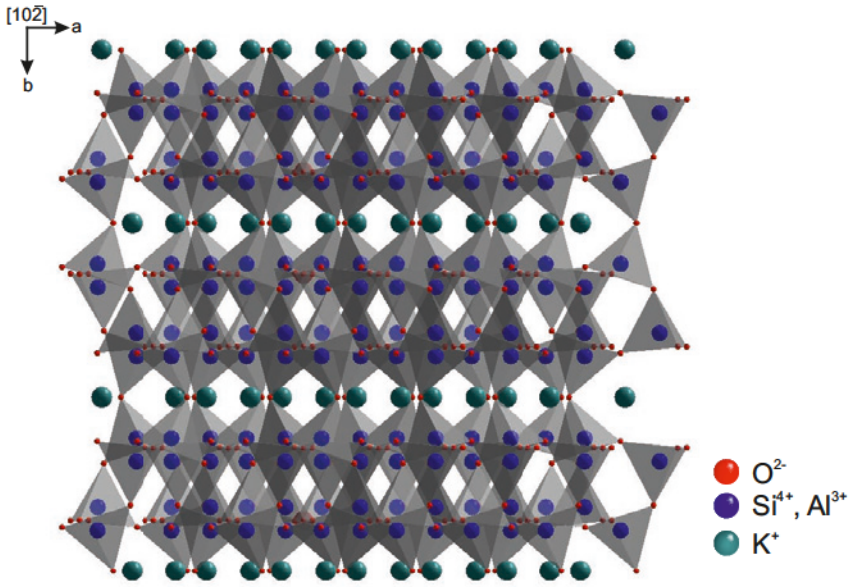

FIGURE 2.10: Along [10$\bar{2}$] the channels are smallest, making the structure almost impassable for cations in this direction; created with Diamond using data for low sanidine by Phillips and Ribbe (1973)

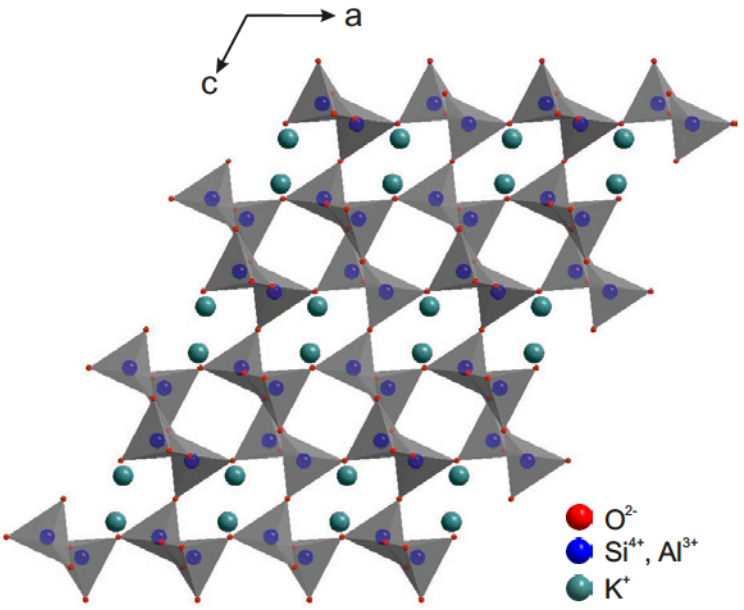

FIGURE 2.11: Channels along the *b*-axis of the feldspar structure are of intermediate size; created with Diamond using data for low sanidine by Phillips and Ribbe (1973)

fully describe a feldspar, the symmetry and Al/Si- order have to be known as well as the chemical composition.

For K-rich feldspars low sanidine (fully disordered, monoclinic), orthoclase (pseudo monoclinic), intermediate and low microcline (fully ordered, triclinic) are distinguished. Sodium-rich feldspars are differentiated between monalbite (fully disordered, monoclinic), analbite (partially ordered) as well as high (disordered, triclinic), intermediate

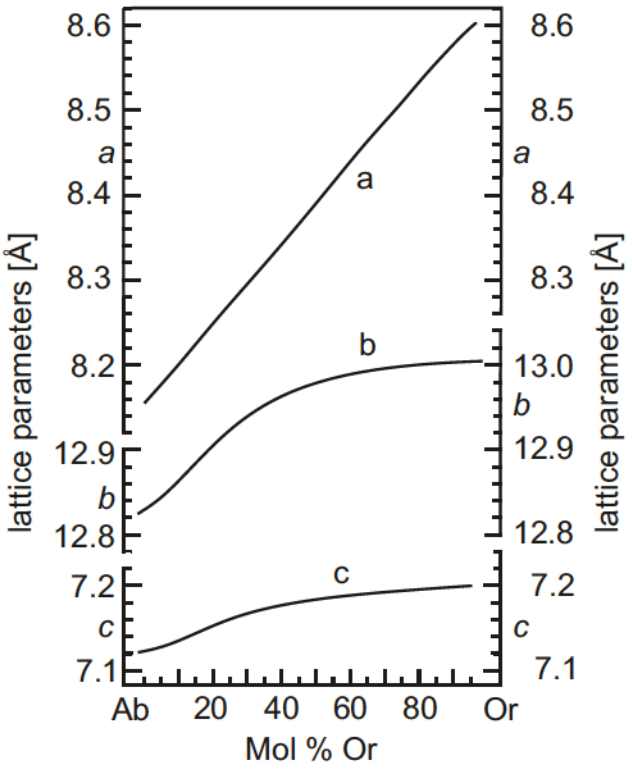

FIGURE 2.12: Composition dependence of the lattice parameters in alkali feldspar; modified after Kroll et al. (1986)

(intermediate disorder, triclinic) and low albite (fully ordered, triclinic) (Deer et al., 2001). Another factor affecting the symmetry aside from the positions of Al and Si in the tetrahedra is the size of the incorporated cations. The K^+-cation is considerably larger than the Na^+ cation, their ionic radii being 1.59 Å and 1.25 Å, respectively (Okrusch and Matthes, 2009). While the larger K^+ has sufficient size to keep up a monoclinic tetrahedral framework, the network collapses around the smaller Na^+. However, at higher temperatures the effective radius of the Na^+ cation is increased by the increased oscillation frequency so that the lattice becomes monoclinic. This is what leads to the symmetry change indicated in the phase diagram in figure 2.2. The different ionic radii also account for the miscibility gap. The capacity for incorporating the larger K^+ into the smaller lattice of sodium-rich alkali feldspar decreases with decreasing temperature and vice versa.

In contrast to Al and Si in the tetrahedra, the cations are coordinated to more oxygen atoms (K^+ nine-fold, Na^+ six- to seven-fold) and thus the bond strengths are weaker. This allows the cations to be mobile during diffusion processes while the Al-Si-framework remains unchanged.

Chapter 3

Diffusion

Diffusion is a process based on random thermally activated molecular motions transporting matter from one part of a system to another. In gases and liquids it is faster by several orders of magnitude than in solids, where atoms can leave their positions in the lattice due to thermal excitation and move through the lattice by way of crystal defects. The driving force for diffusion are macroscopic concentration gradients or, more commonly, chemical potential gradients. Very good coverage of the topic can be found in Manning (1968), Crank (1975), Mehrer (2007) and Zhang (2010), which were also the main sources used for the following short overview.

3.1 Diffusion Mechanisms

Diffusion in crystalline solids occurs by atomic jumps through the lattice. The rate of diffusion depends on the size and charge of the diffusing species, as well as the sites available in the crystal lattice. To move from one site to the next a moving atom needs to break bonds with neighbours, and distorts the lattice in passing. Thus structure, symmetry and bond strengths are defining factors (Zhang, 2010).

Defects of the lattice play an important role in diffusion. In an ideal crystal with no defects each movement of an atom would cause a significant increase in energy and thus be unfavourable. Point defects, especially vacancies, facilitate the movement as they create positions the atoms can occupy. Special types of point defects introducing vacancies to maintain charge neutrality are Frenkel defects that consist of an interstitial and a vacancy, and Schottky defects that consist of a pair of vacancies where a positively charged and negatively charged ion of the lattice is missing respectively. Although extended defects such as line defects, domain boundaries, and grain boundaries generally

are not as important as point defects in mediating diffusion, they can nevertheless create fast pathways for diffusion as they represent less strictly ordered domains in the crystal, which often have a dilated lattice.

The movement of single atoms in the absence of driving forces is more or less random and has no preferred direction. Macroscopic diffusion is achieved by a large number of atomic jumps executed by the diffusing particles. Lattice sites represent local energy minima in which the atoms are located. They vibrate with a certain frequency which is usually not high enough to overcome the energy barrier needed to leave their site and jump to a neighbouring vacancy or interstitial site. Rarely, random fluctuations will allow the frequency of the vibration to become large enough and result in the atom moving from its old position to a new site. After the jump it returns to oscillating in its new site before a new fluctuation allows it to leave again. As the direction of each jump is random, the number of jumps gives no information about the absolute distance the atom has moved from its original position, so its mean square displacement $\langle R^2 \rangle$ is considered:

$$\langle R^2 \rangle = X^2 + Y^2 + Z^2 \tag{3.1}$$

with X, Y and Z being the components of the movement along the main axes of the coordinate system. Several diffusion mechanisms can be discerned on the atomic scale. The most important ones to be considered in the scope of this study will be described in the following.

Direct Interstitial Mechanism

The direct interstitial mechanism is mostly relevant for small atoms that can move from one interstitial position to the next without causing too severe distortions of the host lattice. They move from an equilibrium position on an interstitial site to an adjacent one (figure 3.1). In the process the neighbouring atoms of the host lattice have to be slightly displaced to make room for the moving atom. However, this distortion is not permanent. The diffusing atom never occupies a regular lattice site which makes this diffusion mechanism independent of lattice defects, and fast compared to other mechanisms.

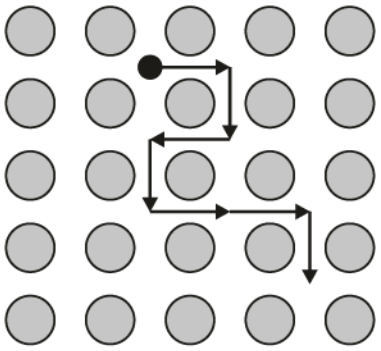

FIGURE 3.1: Direct interstitial mechanism of atomic movement in a crystal lattice; modified after Mehrer (2007)

Indirect Interstitial Mechanism

The indirect interstitial mechanism, or interstitialcy mechanism, mainly concerns atoms that have roughly the same size as atoms of the matrix. It consists of a coupled movement of two atoms; one atom located on an interstitial site moves to a regular lattice site while the atom occupying this position moves into the interstitial lattice (figure 3.2). In contrast to the direct interstitial mechanism a specific atom will not move over large distances through the lattice though the overall diffusivity achieved by these two mechanisms is comparable.

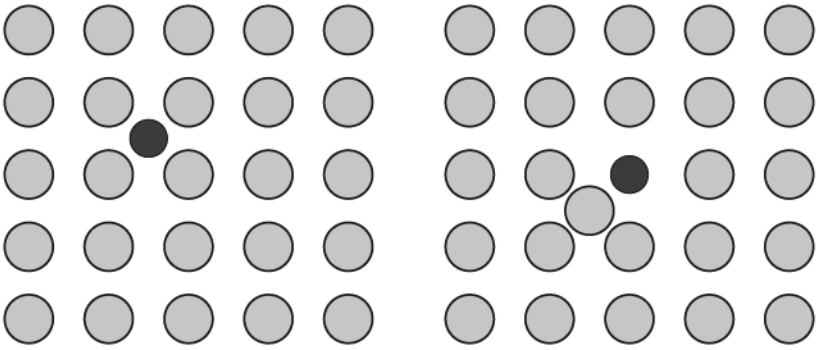

FIGURE 3.2: Indirect interstitial mechanism of atomic movement in a crystal lattice; modified after Mehrer (2007)

Vacancy Mechanism

As the name suggests the vacancy mechanism is dependent on the concentration of vacancies in the lattice, which are the most important form of thermally induced atomic point defect in ionic crystals (Mehrer, 2007). The concentration of vacancies c_v in a crystal is

$$c_v = exp(-\frac{G_v^f}{k_b T}) \tag{3.2}$$

with G_v^f being the Gibbs free energy of vacancy formation. An atom moving by this mechanism jumps into a neighbouring vacancy; after the exchange the atom and vacancy will move in opposite directions (figure 3.3).

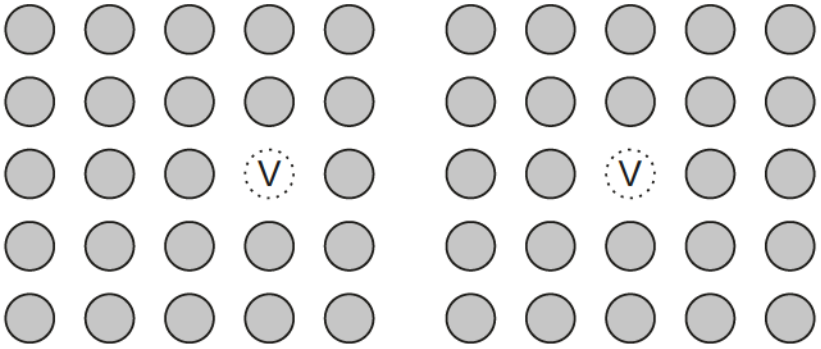

FIGURE 3.3: Vacancy mechanism of atomic movement in a crystal lattice; modified after Mehrer (2007)

3.2 Fick's Laws of Diffusion

Diffusion was first quantitatively described in 1855 by Fick (Fick, 1855), who adapted the mathematical equation for heat conduction, derived about thirty years earlier by Fourier, assuming that in isotropic substances the rate of transfer of a diffusing substance through a unit area is proportional to the concentration gradient normal to the section. Thus for a flux in one dimension in an isotropic medium Fick's first law can be written as:

$$J_x = -D\frac{\partial c}{\partial x} \tag{3.3}$$

where J_x is the flux of particles through the unit area, c the concentration of the diffusing particles and x the distance measured normal to the section. D is a proportionality constant with the unit $[\frac{m^2}{s}]$, called the diffusion coefficient. The negative sign ensures that diffusion takes place in the opposite direction of the concentration gradient when D is positive.

To describe diffusion in three dimensions the vector notation is employed:

$$\vec{J}(\vec{x},t) = -D\nabla\vec{c}(\vec{x},t) \tag{3.4}$$

with $\nabla\vec{c}(\vec{x},t) = \frac{\partial c_x}{\partial x} + \frac{\partial c_y}{\partial y} + \frac{\partial c_z}{\partial z}$.

Equations 3.3 and 3.4 are the general forms of Fick's first law. To take aspects such as composition dependence of the diffusion coefficient or diffusion anisotropy into account D has to be expressed accordingly, e.g. as a second rank tensor in the case of diffusion in anisotropic media (see section 3.4).

If there are no sinks or sources for the diffusing substance it can be assumed that the number of diffusing particles stays constant so that:

$$\frac{\partial c(\vec{x},t)}{\partial t} = -\nabla \cdot \vec{J}(\vec{x},t) \tag{3.5}$$

which is known as the continuity equation.

Combining the continuity equation (eq. 3.5) and Fick's first law (eq. 3.4) gives Fick's second law, which is also called the diffusion equation. The solution of this equation gives the relation of concentration to space and time:

$$\frac{\partial c(\vec{x},t)}{\partial t} = -\nabla \cdot (-D\nabla \vec{c}(\vec{x},t)). \tag{3.6}$$

Equation 3.6 is a second-order partial differential equation in time and space. To solve this kind of equation, initial and boundary conditions have to be defined; the solution allows a prediction on how an initial concentration distribution changes as diffusion progresses.

3.3 Types of Diffusion

On a first level, grain boundary and volume diffusion can be distinguished. Volume diffusion takes place in the interior of a phase while, as the name suggests, boundary diffusion occurs along interphase interfaces. Due to the high concentration of defects and more open crystal structure usually associated with boundaries, grain boundary diffusion is often much faster than volume diffusion. This is especially relevant at low temperatures as the concentration of point defects, necessary for several of the volume diffusion mechanisms, decreases with decreasing temperature. Further, the compatibility of the diffusing species is a limiting factor and has to be taken into account.

In the case of volume diffusion various diffusion coefficients can be defined, as the exact form of the diffusion coefficient varies depending on the driving forces present, as well as on the nature of the diffusing species. The term driving force is here defined as any process influencing the jumps of individual atoms and includes thermodynamic driving

forces like chemical potential gradients. The presence of a driving force adds a drift velocity $\langle\nu\rangle$ to the movement of every atom and contributes a term $c\langle\nu\rangle$ to the atom flux (Manning, 1968). Thus the diffusion equation becomes:

$$J_x = -D\frac{\partial c}{\partial x} + c\langle\nu\rangle \tag{3.7}$$

The nomenclature of the various kinds of diffusion and types of diffusion coefficients often differs from author to author. The definitions used in the following are mainly based on the definitions given by Manning (1968) and Zhang (2010) and may not be identical with definitions found in other sources.

The most basic diffusion coefficient that can be defined is the *self-diffusion coefficient*. It describes diffusion of atoms of the exact same species in the absence of a concentration gradient, i.e. of a gradient in chemical potentials. In this case the self-diffusion coefficient D_i^* of the species i is related to the diffusion coefficient D_i by

$$D_i^* = D_i(\partial ln(c_i)/\partial ln(a_i)) \tag{3.8}$$

with a being the activity of species i in the solution and c being its concentration. As true self-diffusion cannot be observed due to the identical atoms not being distinguishable from each other, experiments conducted to quantify self-diffusion coefficients often introduce an isotopic tracer and determine the so-called *tracer-diffusion coefficient*, which can be assumed identical in most cases, as long as the isotope effect is not too pronounced (Everett, 1972).

In the presence of a concentration gradient, diffusion is termed *chemical diffusion*, which includes *interdiffusion*, *multispecies diffusion*, *multicomponent diffusion* and *effective binary diffusion*. As interdiffusion is the main focus of this study the other types of diffusion will only be discussed very shortly.

Multispecies diffusion describes diffusion of a component that can be present in multiple species found in the system (Mehrer, 2007). Multicomponent diffusion involves the diffusive movement of three or more components in the system. As this case is hard to treat, it is often simplified by assuming effective binary diffusion, where diffusion of a component is treated as only being driven by its own concentration gradient. All other components are either treated as a single combined component, or their effect on the diffusion of the chosen component is ignored (Mehrer, 2007).

Interdiffusion describes the coupled movement of a given pair of species that move in opposite directions driven by opposing concentration gradients, their rate of movement

depending on the diffusion rates of both species (Manning, 1968). A special case of interdiffusion is *binary diffusion* which strictly refers to interdiffusion in a binary system (Zhang, 2010).

The interdiffusion coefficient is dependent on the self-diffusion coefficients of the separate diffusing species. If the system approaches the pure composition of one of its end-members, the self-diffusion of the diffusing species with the lower concentration is rate limiting.

There are two models for this relation. For neutral atomic interdiffusion, as often found in metals, the Darken equation (Darken, 1948) is used, while for ionic interdiffusion between isovalent ions, which is the focus in this work, the Nernst-Planck relation is relevant. To understand these models, the concept of the *intrinsic diffusion coefficient* D^I needs to be considered first. It describes fluxes in a system in reference to a co-moving reference frame affixed to a point in the lattice, as otherwise unequal diffusion coefficients of different species in a system would lead to relative movement of the lattice plains.

If the driving force of diffusion is proportional to a concentration gradient $\frac{\partial c}{\partial x}$, equation 3.7 can be written as

$$J_i = D_i^I(\frac{\partial c_i}{\partial x}) \tag{3.9}$$

with

$$D_i^I = D_i^* - \frac{c_i\langle\nu\rangle}{(\partial c_i/\partial x)}. \tag{3.10}$$

D_i^I is the intrinsic diffusion coefficient of the species i, and the subscript i on the other quantities indicates that only the contribution of this species is considered. Driving forces proportional to a concentration gradient arise from diffusion potentials in ionic crystals or non-ideal thermodynamic mixing (Manning, 1968). To simplify the considerations, an ideal solution can be assumed so that non-ideal relations between concentration and chemical potential can be ruled out.

In the case of neutral atomic interdiffusion, as found in metals where an abundance of highly mobile electrons can be assumed to balance any fluctuations in electric charge, the Darken equation is valid to describe the interdiffusion coefficient.

$$D = (X_B D_A^* + X_a D_B^*) \tag{3.11}$$

where X_A and X_B are the mole concentrations of the diffusing species A and B and D_A^* and D_B^* their self-diffusion coefficients.

If an ionic crystal is considered, charge neutrality cannot be as easily maintained; here the net flux of electric charge must equal zero. The following assumes an ionic crystal where anions remain fixed in position and all diffusion occurs by a vacancy mechanism on the cation sublattice. The fluxes of the two separate diffusing species can be expressed in terms of the intrinsic diffusion coefficients:

$$J_A = D_A^I(\frac{\partial c_A}{\partial x}) \tag{3.12}$$

and

$$J_B = D_B^I(\frac{\partial c_B}{\partial x}) \tag{3.13}$$

In the absence of driving forces the intrinsic diffusion coefficients are equal to the self-diffusion coefficients, $D_A^I = D_A^*$ and $D_B^I = D_B^*$. As binary diffusion is considered, the flux of one species has to equal the flux of the other with opposite sign, as they occur in opposing directions:

$$J_A = -J_B \tag{3.14}$$

and accordingly

$$\frac{\partial c_A}{\partial x} = -\frac{\partial c_B}{\partial x}. \tag{3.15}$$

If the self-diffusion coefficients of the species are not equal, a net flux of cations would be expected as

$$J_A + J_B = (D_B^* - D_A^*)(\frac{\partial c_A}{\partial x}) \neq 0. \tag{3.16}$$

However, as charge neutrality has to be maintained, and thus the net flux of electric charge hast to equal zero, the net flux of cations has to equal zero as well, if both species have the same charge q:

$$J_A + J_B = 0. \tag{3.17}$$

This is achieved by an electric field E_d, which is just large enough to make the cation flux equal zero and functions as a driving force qE_d. Analogous to equation 3.7 we get

$$J_A = -D_A^*(\frac{\partial c_A}{\partial x}) + qE_d D_A^* c_a/kT \tag{3.18}$$

and

$$J_B = +D_B^*(\frac{\partial c_A}{\partial x}) + qE_d D_B^* c_B/kT. \tag{3.19}$$

Assuming equation 3.17 and solving for E_d shows that the driving force is proportional to the concentration gradient. For the atom flux the same assumption leads to

$$J_A = -J_B = \frac{D_A^* D_B^*}{X_A D_A^* + X_B D_B^*} \frac{\partial c_A}{\partial x}. \tag{3.20}$$

where X_A and X_B are the mole fractions of the respective species. The intrinsic diffusion coefficient is the coefficient of $-\frac{\partial c_A}{\partial x}$, thus

$$D_A^I = \frac{D_A^* D_B^*}{X_A D_A^* + X_B D_B^*}. \tag{3.21}$$

If non-ideal solutions are to be taken into account a thermodynamic term has to be added. Also, as long as the velocity of lattice planes within the crystal is assumed zero, the intrinsic and interdiffusion coefficient are equal and we get:

$$D = \frac{D_A^* D_B^*}{X_A D_A^* + X_B D_B^*} \cdot [1 + \frac{\partial \ln \gamma_B}{\partial \ln X_B}] \tag{3.22}$$

which is referred to as the Nernst-Planck- or, less frequently, the Manning equation.

3.4 Diffusion in Anisotropic Materials

In anisotropic materials, such as monoclinic feldspars, diffusion is generally direction-dependent. In this case the diffusion coefficient is not a scalar but has to be expressed as a second rank tensor:

$$D = \begin{pmatrix} D_{11} & D_{12} & D_{13} \\ D_{21} & D_{22} & D_{23} \\ D_{31} & D_{32} & D_{33}. \end{pmatrix} \tag{3.23}$$

It follows from Onsager's reciprocity relations (Onsager, 1931) that the tensor is symmetrical. It can further be simplified by considering the symmetry of the material diffusion is taking place in. For monoclinic feldspars it becomes

$$D = \begin{pmatrix} D_{11} & 0 & D_{13} \\ 0 & D_{22} & 0 \\ D_{31} & 0 & D_{33}. \end{pmatrix} \tag{3.24}$$

if the y-axis is chosen along the b-direction and the two other axes as two mutually perpendicular directions in the a-c-plane of the feldspar. Thus measurements in four different crystallographic directions are necessary to determine the full diffusivity tensor.

Three orthogonal directions x_1, x_2, x_3 can be defined along which the flux is only dependent on the concentration gradient; these are the principle axes of diffusivity tensor.

$$j_{x_i} = -D_i \frac{\partial c}{\partial x_i} \tag{3.25}$$

with i standing for one of the three main directions and D_i being the diffusion coefficient along this axis. Diffusion along an arbitrary direction κ can be expressed as:

$$j_\kappa = -D_\kappa \frac{\partial c}{\partial \kappa} \tag{3.26}$$

with D_κ being $D_\kappa = D_1 cos^2\theta_1 + D_2 cos^2\theta_2 + D_3 cos^2\theta_3$ and θ_1, θ_2 and θ_3 being the angles between the arbitrary direction and the three main axes.

3.5 Solution of the Diffusion Equation for a Diffusion Couple

Solutions to the Diffusion equation can be divided in cases with steady-state diffusion, and non-steady-state, i.e. transient, diffusion. In the case of steady-state diffusion concentration stays constant with time

$$\frac{\partial c}{\partial t} = 0. \tag{3.27}$$

For transient diffusion concentration changes with time; the nature of the change depends on the initial distribution of the diffusing species and the geometry of the system. A typical example of transient diffusion with an extended initial distribution is a diffusion couple. Two semi-infinite bodies with different concentrations of the diffusing species are brought into contact at flat, polished surfaces. This geometry is often used in experimental set-ups to determine diffusion coefficients, as it approximates problems found in nature quite well. The initial distribution of the diffusing species at the time $t = 0$ is $c = c_0$ for $x < 0$ and $c = 0$ for $x > 0$ where c_0 is the initial concentration of the diffusing species in one of the bodies and $x = 0$ is the position of the interface between them.

If the diffusion coefficient is constant

$$c(x,t) = \frac{c_0}{2}\text{erfc}(\frac{x}{2\sqrt{Dt}}) \tag{3.28}$$

is a solution of equation 3.6, which takes the initial and boundary conditions mentioned earlier into account. In this case the diffusion profile can be fitted with an error function. The complementary error function erfc(x) is defined as:

$$\text{erfc}(x) = 1 - \text{erf}(x) = \frac{2}{\sqrt{\pi}}\int_x^\infty e^{-t^2}dt. \tag{3.29}$$

If it is assumed that the concentration at the interface stays constant, e.g. if one of the halves is replaced by a melt with constant concentration which functions as an inexhaustible source of the diffusing species, c_0 is replaced by c_s and equation 3.28 becomes

$$c(x,t) = c_s\text{erfc}(\frac{x}{2\sqrt{Dt}}) \tag{3.30}$$

where c_s is the fixed concentration assumed at the interface. It must be noted that solutions 3.28 and 3.30 are only valid if D = const. If D is composition dependent, Boltzmann's transformation can be applied to diffusion in infinite or semi-infinite media, and allows the transformation of a partial differential equation to an analytically solvable ordinary differential equation by introducing Boltzmann's variable. A detailed description of this method is given in the following section.

3.6 Boltzmann-Matano Method

Boltzmann's Transformation

The one-dimensional Fick's law with a diffusion coefficient D depending on the concentration c is:

$$\frac{\partial c}{\partial t} = \frac{\partial}{\partial x}\left[D\left(c\right)\frac{\partial c}{\partial x}\right], \tag{3.31}$$

where t is time and x distance. In this equation, the concentration is a function of t and x and thus c actually stands for $c\left(t,x\right)$.

In this partial differential equation (3.31), both the time variable t and space variables x are independent, making this equation difficult to solve analytically. In order to simplify the expression Boltzmann's transformation is applied, which transforms the partial differential equation into an ordinary differential equation.

The variable η is introduced which comprises both x and t:

$$\eta = \frac{x}{2\sqrt{t}}. \tag{3.32}$$

The partial derivatives of η are

$$\frac{\partial \eta}{\partial t} = -\frac{\eta}{2t}, \tag{3.33}$$

and

$$\frac{\partial \eta}{\partial x} = \frac{1}{2\sqrt{t}}. \tag{3.34}$$

This variable can then be introduced into equation 3.31 by expressing the partial derivatives with respect to t and x as a function of η by using the chain rule.

Hence, all the partial derivatives in equation 3.31 can be expressed as functions of η only:

$$\frac{\partial c}{\partial t} = -\frac{\eta}{2t}\frac{\partial c}{\partial \eta}, \tag{3.35}$$

$$\frac{\partial c}{\partial x} = \frac{1}{2\sqrt{t}}\frac{\partial c}{\partial \eta} \tag{3.36}$$

and

$$\frac{\partial}{\partial x}\left[D\left(c\right)\frac{\partial c}{\partial x}\right] = \frac{1}{4t}\frac{\partial}{\partial \eta}\left[D\left(c\right)\frac{\partial c}{\partial \eta}\right]. \tag{3.37}$$

Introducing these equations into equation 3.31 yields

$$-\frac{\eta}{2t}\frac{\partial c}{\partial \eta} = \frac{1}{4t}\frac{\partial}{\partial \eta}\left[D\left(c\right)\frac{\partial c}{\partial \eta}\right], \tag{3.38}$$

which can be simplified as

$$-2\eta\frac{dc}{d\eta} = \frac{d}{d\eta}\left[D\left(c\right)\frac{dc}{d\eta}\right]. \tag{3.39}$$

Here the only independent variable is η and the partial differential equation has been transformed to an ordinary differential equation.

Integration of the Diffusion Equation for $D = D(c)$

Typically Matano's method is applied in cases where two infinite media with different initial concentrations are brought into contact. The plane of contact is called Matano's interface. In the case of the study at hand one of these infinite media is replaced by the melt surrounding the crystal and we only take diffusion into the crystal itself into account while the melt can be considered a perfect source and sink for the diffusing substances due to the 40-times molar cation excess applied in the experiments. The feldspar can be considered as a one-dimensional semi-infinite medium, as the overall size of the crystal is large compared to the length of the diffusion profiles. The position of the boundary between crystal and melt is $x = 0$. Three conditions have to be considered. The initial condition is

$$c\,(t = 0, x > 0) = c_{initial}, \tag{3.40}$$

where $c_{initial}$ is the constant initial concentration of the feldspar. The boundary conditions of the experiments are

$$c\,(t \geq 0, x = 0) = c_m, \tag{3.41}$$

where c_m is the concentration of the diffusing substance in the feldspar in equilibrium with the melt, and

$$c\,(t \geq 0, x = +\infty) = c_{initial} \tag{3.42}$$

which expresses that in infinite distance from the melt-crystal boundary, the initial composition of the feldspar is retained.

In order to be applicable to equation 3.39 these boundary conditions have to be expressed in terms of Boltzmann's variable η.

Using the definition of η, the initial condition (3.40) becomes

$$c\,(\eta \to +\infty) = c_m, \tag{3.43}$$

and the boundary conditions (3.41 and 3.42) become

$$c\,(\eta = 0) = c_m \tag{3.44}$$

and

$$c\,(\eta = +\infty) = c_m. \tag{3.45}$$

It is immediately apparent that 3.43 and 3.45 are identical. Thus applying Boltzmann's transformation leads to merging of the initial and one of the boundary conditions so that only two boundary conditions have to be taken into account.

Equation 3.39 is integrated from $\eta = +\infty$ to a generic $\eta^\star$ and simplified:

$$-2\int_{\eta=+\infty}^{\eta=\eta^\star} \eta dc = \left[D(c)\frac{dc}{d\eta}\right]_{\eta=+\infty}^{\eta=\eta^\star}. \tag{3.46}$$

From this it can be derived that c should be used as the integration variable and the new lower bound of the integration is given by equations 3.43 and 3.44: $c = c_{initial}$, for $\eta = +\infty$. The upper boundary is changed from $\eta = \eta^\star$ to $c = c^\star$. The resulting integral is further simplified by applying the boundary conditions, which indicates that the profile is flat at either end and thus $D(c)\,dc/d\eta = 0$ for $c = c_f$:

$$-2\int_{c=c_{initial}}^{c=c^\star} \eta dc \;=\; D(c^\star)\left.\frac{dc}{d\eta}\right|_{c=c^\star}. \tag{3.47}$$

The time and space variables are then reintroduced using the definition for η. As the interdiffusion coefficient is to be determined from experiments with known run durations we can consider t as a constant which can be drawn out of the integrals. This yields the following equation, which allows the calculation of the interdiffusion coefficient at a specific composition:

$$D(c^\star) = -\frac{1}{2t}\left.\frac{dx}{dc}\right|_{c^\star}\int_{c_{initial}}^{c^\star} x dc. \tag{3.48}$$

All parts of this equation can be directly determined from the measured diffusion profiles. However, as in this equation the distance is dependent on the concentration, the axes of the measured data have to be switched. Then the first part of the equation equals the slope of the measured profile at the composition of interest and the second part the area under the curve in the composition interval between the initial composition of the feldspar and the composition considered in the calculation.

3.7 Temperature and Pressure Dependence of Diffusion

Diffusion depends strongly on temperature. For low temperatures it is very slow while it becomes exponentially faster with increasing temperature. The pressure dependence in

contrast is only minor within the pressure ranges accessible in laboratory experiments.

Temperature dependence of diffusivities is described by the Arrhenius relation

$$D = D_0 \exp(-\frac{E_A}{RT}) \tag{3.49}$$

with D_0 being the pre-exponential factor, E_A the activation energy and T the temperature in Kelvin. It follows from equation 3.49 that the logarithm of the diffusivity plotted against 1/T is a straight line with negative slope. The slope is proportional the activation energy and the axis intercept with the y-axis is proportional to D_0. The strong temperature dependence can be explained by different factors. On the one hand the number of vacancies rises with increasing temperature. On the other hand the frequency of the oscillation of the single atoms rises, making it more likely for them to overcome the energy barrier for jumps between lattice positions. The rate ν for a successful jump is given by

$$\nu = \nu_0 \exp(-\frac{G_m}{k_B T}). \tag{3.50}$$

The frequency ν_0 is the so-called *attempt frequency* which is the vibration around the equilibrium position towards the direction in which the jump will occur. G_m is the Gibbs free energy of migration and can be described as the difference in energy between the two stable positions and the higher energy needed to displace the neighbouring atoms during the jump between them.

The pressure dependence of diffusion is due to the Gibbs free energy of activation varying with pressure according to

$$\Delta G = \Delta H - T\Delta S = \Delta E - T\Delta S + p\Delta V. \tag{3.51}$$

where ΔE is the change in internal energy which is identical with the activation energy and p the hydrostatic pressure. ΔV is the activation volume of diffusion:

$$\Delta V = (\frac{\partial \Delta G}{\partial p})_T. \tag{3.52}$$

At high pressures the term $p\Delta V$ can be significant. At ambient pressure it is mostly negligible for diffusion in solids.

Chapter 4

State of Research

A number of studies have been conducted in the past investigating diffusion in feldspars. In the following a short overview over existing results is given, with focus on those studies which have investigated diffusion of sodium and potassium in alkali feldspars.

4.1 Tracer-Diffusion

Self-diffusion is defined as the diffusion of one species of atoms when the chemical gradient equals zero. As it is impossible to discern between two identical atoms of one species, tracer-diffusion coefficients have to be determined instead, using tracer isotopes. For both sodium and potassium different radioactive isotopes can be used as tracers. However, experimental procedures can be difficult in some cases due to their half-life, especially for potassium. To avoid this, stable isotopes could be used, but the fact that these already have an initial concentration in the sample material might impair the quality of the analysis. For sodium the isotopes ^{22}Na ($t^{1/2} \sim 2.6\ a$) (Bailey, 1971; Lin and Yund, 1972; Foland, 1974; Kasper, 1975) and ^{24}Na ($t^{1/2} \sim 14.6\ h$) (Sippel, 1963; Bailey, 1971) have been used. For potassium fewer studies have been conducted using ^{40}K ($t^{1/2} \sim 1.25\ x\ 10^9\ a$) (Lin and Yund, 1972) and ^{41}K (stable) (Foland, 1974).

Several methods can be employed to determine the tracer-diffusion coefficient. Earlier studies used the sectioning method (Sippel, 1963; Bailey, 1971), electrical conductivity (Maury, 1968) or bulk exchange methods (Bailey, 1971; Lin and Yund, 1972; Foland, 1974; Giletti et al., 1974; Kasper, 1975) to determine them directly or calculated them from interdiffusion coefficients (Petrović, 1972). Some of these are more accurate than others; they are, however, all limited by the quality of the starting material available. In order to determine just the influence of tracer-diffusion it is required that the change in chemistry is minimal during the experimental procedure (Giletti et al., 1974).

4.1.1 Sectioning Method

The basic principle of the sectioning method is to create a thin surface layer containing the radioactive tracer element on the surface of the sample which is then annealed at the desired temperature. Afterwards the surface is ground off in consecutive steps of a controlled thickness, and either the activity in the ground off material (Sippel, 1963) or the remaining solid (Bailey, 1971) is measured. Both authors used ^{24}Na as isotope tracer.

Sippel (1963) used albite, microcline and orthoclase as starting materials. The tracer isotope used was ^{24}Na ($t^{1/2} \sim 14.6\ h$), which was produced in place by deuteron bombardment of the surface of the disc-shaped sample until a roughly 20 μm thick layer had been created. The irradiated sample was then annealed at temperatures between 850 and 940°C. Afterwards the surface layer was ground off in steps, and the activity of the ground off material measured with a Geiger counter.

While the sectioning method can be considered the most accurate way of determining tracer-diffusion coefficients in feldspar there have been several problems leading to inaccuracies in the results of this study. Firstly, the exact thickness of the irradiated layer could only be estimated; no correction has been applied for this. Secondly, the starting material itself was not ideal for this kind of study as it contained grain boundaries and inclusions, and exhibited cracking, twinning and exsolution which constitute additional pathways for diffusion.

Bailey (1971) deposited ^{22}Na as tracer isotope by clamping a filter paper that had been doped with $^{22}NaCl$ against polished cleavage fractures of the sample material for an hour. After annealing at temperatures between 300 and 595°C the surface layer was ground off and the activity remaining in the solid was measured.

4.1.2 Bulk Exchange

For bulk exchange methods, crushed feldspar is used as starting material and exchanged with hydrothermal solutions containing the tracer isotope. Afterwards solution and feldspar are separated, and the uptake of the tracer isotope determined by counting the activity of the sample material. The tracer-diffusion coefficients are calculated from this data assuming either a spherical or cylindrical model for the shape of the separate grains in the bulk material.

Lin and Yund (1972) determined tracer-diffusion coefficients for both sodium and potassium using ^{22}Na and ^{40}K as tracers. Their starting material was pure microcline

perthite, which was crushed, sieved and exchanged with molten KCl several times in order to homogenise the perthite and create a pure orthoclase. An exchange with NaCl was done to prepare a low-albite.

The ^{40}K was only 1.9% enriched which led to a low counting rate, and thus a raised uncertainty in the calculated diffusion coefficients. The activity of ^{22}Na was much higher, leading to the counting error being negligible compared to the error induced by the assumed geometry of the grains and their variation in size.

200 mg of the starting material were put in 200 mg of a 2 molar ^{40}KCl solution and sealed in gold tubes before being heated in a cold-seal pressure vessel. After annealing at temperatures between 600 and 800°C the sample was quenched and the salt and feldspar separated. The uptake of ^{40}K was determined by counting the activity of the feldspar and the diffusion coefficients calculated based on the results. For sodium an analogous procedure was executed using the low-albite and a $^{22}NaCl$ solution, which were annealed at 200 to 600°C.

Foland (1974) and Kasper (1975) used almost identical methods to determine the self-diffusion coefficients at different ends of the composition spectrum, thus providing a consistent set of data that allows the interpolation of the self-diffusion coefficients for the whole composition range. To this end Kasper used albite ($An_{98.6}Or_1An_{0.4}$) after Foland had conducted experiments with orthoclase ($Or_{94}Ab_6$).

The sample material was carefully chosen and characterized. The equilibrium partitioning was determined and 1- or 2-molar chloride solutions containing the tracer isotopes (^{41}K and ^{22}Na) prepared such that the composition of the crystal stayed constant during exchange. A carefully weighed amount of the sample material was placed in a capsule and sealed together with the hydrothermal solution, the fluid to solid ratio ranging from 0.2 to 2.0 by weight. The capsules were heated to temperatures between 500 and 800° for run durations ranging from a few hours to several weeks. Afterwards both the fluid and feldspar were retrieved and the uptake of tracer isotopes measured. Most measurements were done by flame photometry using Li internal standards for both Na and K. Additionally some K-concentrations were determined mass spectrometrically. ^{22}Na activity was measured by γ-ray scintillation counting.

Foland (1974) calculated the diffusion coefficient using both a cylindrical and spherical model and postulated that the choice of model had a negligible influence. Kasper (1975) favoured the spherical model; using a more complex model giving a better fit to the actual shape for some chosen examples, he determined that the spherical model leads to an overestimation of the values of the self-diffusion coefficients by about 25%.

Petrović (1972) suggested that under hydrothermal conditions the dominating exchange mechanism is dissolution-precipitation rather than volume diffusion when the Na/K ratio of the fluid is too far from equilibrium.

4.1.3 Other Studies

Giletti and Shanahan (1997) measured K diffusion in an Amelia albite with X_{Ab} 0.985 using ^{41}K. They applied a drop of aqueous solution containing the $> 85\%$ enriched tracer isotope on the crystal surface. Different crystal orientations were used, though most experiments were conducted on (010) faces of the feldspar. The amount of tracer that remained on the surface after evaporation of the solution was chosen so that it could be assumed as an infinite source. The crystal was then welded into a gold or platinum capsule and heated to temperatures between 600 and 1000°C for run durations between 10 minutes and 6 weeks. Most experiments were conducted at 1 atm. However, one experiment was done at 100 MPa to investigate the effect of pressure on diffusion. Two experiments were performed to explore the effect of water pressure.

After exchange the samples were washed with deionized water in an ultrasonic bath to remove the tracer and dried at 110°C, before being mounted in epoxy for analysis with an ion microprobe (SIMS). They took specific measures to minimize an apparent enhancement of the diffusion coefficient due to migration of K during sputtering, which is a problematic aspect of this technique. The error function was used to reduce the data assuming a concentration-independent diffusion rate.

They found pressure and water fugacity to have no significant effect. No further mention is made of a directional dependence of K-diffusion although different crystallographic orientations were used for the experiments. Comparison of their results with data obtained by Kasper (1975) showed that the older values were higher by about an order of magnitude. This was interpreted as an indication that the bulk exchange method employed by Kasper probably overestimated the self-diffusion coefficient severely due to assuming a spherical geometry for the feldspar grains.

Based on their results and consideration of the ionic radii of the diffusing species, they suggest that sodium diffuses by an interstitial and potassium by a vacancy mechanism.

Wilangowski (2013) conducted experiments on Na-tracer-diffusion in sanidine in the temperature range from 370 to 900°C using the sectioning technique and sputtering method. Gem-quality feldspar from Volkesfeld (Eifel, Germany, X_{Or} 0.85) was prepared as discs of 6 to 8 mm diameter and 2 to 3 mm thickness. The polished surfaces of the discs corresponded to the (010) or (001) planes of feldspar. ^{22}Na was used as radiotracer

isotope. It was deposited by placing a drop of $^{22}NaCl$ solution on the surface and subsequently evaporating the water, leaving a thin film of the tracer isotope.

The prepared sample was then annealed in a lamp oven for 5 minutes to 3 hours. Depending on temperature, and thus the length of the diffusion profiles, the sample was then ground ($T \geq 600°C$) or sputtered using an ion beam ($T < 600°C$) to remove layers of $\geq 1\ \mu m$ or 2 nm, respectively. The material of each layer was collected and its activity measured by γ-ray scintillation counting. The diffusion coefficient was determined from the activity of the layers. The activity was plotted against penetration depth and the curve fitted using a Gaussian- or Error-function.

In contrast to all older studies dealing with tracer-diffusion Wilangowski (2013) determined the tracer-diffusion coefficient of Na in specific crystallographic directions. He found a clear anisotropy with Na-tracer-diffusion being faster normal to (001) than normal to (010) at $T < 800°C$. For low temperatures he observed significant changes in the diffusion behaviour which he interprets as a change in dominant diffusion mechanism.

4.2 Interdiffusion

Interdiffusion describes the diffusion of a given pair of species that move in opposite directions driven by opposite concentration gradients. The interdiffusion coefficient is thus dependent on the tracer-diffusion coefficients of the separate diffusing species as described by the Nernst-Planck relation. For K-Na-interdiffusion it can be written as

$$D(X_{Or}) = \frac{D^*_K(X_{Or})D^*_{Na}(X_{Or})}{X_{Or}D^*_K(X_{Or}) + (1 - X_{Or})D^*_{Na}(X_{Or})} \cdot [1 + \frac{\partial \ln \gamma_{Or}}{\partial \ln X_{Or}}] \tag{4.1}$$

with D^*_{Na} and D^*_K being the self-diffusion coefficients of Na and K, D the interdiffusion coefficient, and X_{Or} the mole fraction of potassium, representing the composition of the feldspar.

To determine the interdiffusion coefficient different approaches have been followed. Petrović (1972) exchanged feldspar with molten NaCl/KCl salt and determined the interdiffusion coefficient based on electron microprobe measurements across the diffusion fronts propagating into the starting material. Christoffersen et al. (1983) conducted diffusion couple experiments where they brought a K-rich and Na-rich feldspar into contact and measured diffusion profiles across the front. Brady and Yund (1983) and Hokason and Yund (1986) used perthites as naturally occurring diffusion couples and determined interdiffusion rates from homogenisation rates between the exsolution lamellae.

4.2.1 Diffusion Couple Experiments

Christoffersen (1982) used cylinders drilled from amelia albite and kristallina adularia as starting material. The end of the cylinders were ground, polished and brought into contact. Experiments were conducted at 5 and 15 kbar to check the influence of pressure on interdiffusion. As no effect beyond a better contact between the two crystals could be found, the majority of the following experiments were conducted at 15 kbar. Variations in water-content also showed no effect which is in good accordance with results from other studies (Brady and Yund (1983); Kasper (1975); Foland (1974)). The diffusion couples were sealed in Pt capsules and annealed at 900 and 1000°C in a modified Grigg's apparatus for 5 to 6 days. Afterwards longitudinal sections through the couples were prepared and concentration profiles measured across the contact.

Interdiffusion coefficients were calculated from the concentration profiles using the Boltzmann-Matano method, applying the equation published by Wagner (1969). This equation gives D as a function of composition in dependence of the initial composition of the halves of the diffusion couples, the concentration difference between the couple, the molar volume, time and the distance from the interface.

Snow and Kidman (1991) investigated the effects of fluorine on interdiffusion rates using the same starting materials as Christoffersen et al. (1983). The drilled crystal cylinders were brought into contact and bound together in a gold tube or by platinum wire before being sealed in a noble metal tube together with a fluorine buffer. Experiments were done at 600 to 800°C for 2 to 24 days. They found that, compared to the interdiffusion data by Christoffersen et al. (1983), interdiffusion rates were already significantly increased at relatively low fluorine fugacities.

Petrović (1972) used single crystals of low albite (Ab_{100} and $Ab_{96}Or_2An_2$) and adularia ($Or_{86}Ab_{14}$) as starting materials. He chose crystals that were at least partially bounded by crystal faces. These were sealed in silica glass capsules together with anhydrous NaCl-KCl melts of constant composition and exchanged at constant temperature. Based on fractionation curves of potassium between melt and feldspar, the melt composition was chosen so that the resulting shifts in composition were very small. After annealing the capsules were broken, and the feldspars retrieved by dissolving the salt. They were oriented by eye for mounting, which led to errors in orientation of up to 15°. Diffusion profiles were measured perpendicular to the crystal faces with an electron microprobe, and X-ray intensity plotted versus distance. A mean intensity curve for one particular direction was fitted visually to all points of the profiles measured perpendicular to the same kind of interface. The interdiffusion and self-diffusion coefficients were calculated from these profiles on the basis of equations and concentration profiles given by Crank

(1956) on the assumption that the coefficients are independent of composition, as the composition shifts generated in the experiments were very small.

He found that Na-diffusion is much faster than K-diffusion while both have roughly the same activation energy. From the comparatively low activation energies he concluded that the diffusion of large cations in alkali feldspars cannot involve the breaking of Al-Si-bonds. Further he proposed a combination of vacancy and direct interstitial mechanisms, which is intrinsically controlled.

Different types of fracturing were observed depending on the direction of the composition shift, its extent, and temperature. From this he concluded that the framework of alkali feldspars cannot sufficiently adapt to the gradient in the mean size of the alkali ions during exchange under anhydrous conditions, which leads to crack formation. Calculations gave an estimated coherency stress of about 10 kbar.

4.2.2 Homogenisation Experiments

Brady and Yund (1983) used the rate of homogenisation of lamellae in cryptoperthites to calculate interdiffusion rates in alkali feldspars. This method gives an average interdiffusion coefficient over the composition range given by the more sodium-rich and more potassium-rich areas of the crystal. Interdiffusion can only be estimated in the direction normal to the lamellae. They used a synthetic perthite prepared from natural adularia (homogenised composition $Ab_{57}Or_{43}$) and a natural perthite from Big Bend, Texas (homogenised composition $Ab_{60.8}Or_{39.2}An_{0.0}$) as starting materials. The synthetic perthite had very coherent interfaces between host and lamellae while they were less perfect in the natural sample due to the presence of dislocations. The coherency of the lamellae is an important characteristic of the starting material, as better coherence minimises the effects generated by the presence of an interface. Thus the natural samples are expected to have yielded less reliable results.

Before the experiments a hk0 X-ray precession photo of each crystal was taken. Then they were placed in Pt containers open to the atmosphere and annealed at 600 $\pm$ 5°C. The crystals were removed repeatedly and precession photos were taken to document the progression of homogenisation. The average interdiffusion coefficient was calculated using the diffusion equation for the finite, one-dimensional geometry of a lamellar intergrowth by Crank (1975), the critical values being the time needed for homogenisation, and the lamellar spacing.

The authors point out that the K-Na-interdiffusion coefficient cannot be constant for the conditions of their experiments according to literature data, and calculate the theoretical

interdiffusion coefficient using the Nernst-Planck relation, and the tracer-diffusion data by Foland (1974) and Kasper (1975). They found the average of the calculated data to be in good agreement with their results.

Hokason and Yund (1986) conducted the same experiments using a number of natural feldspars, focussing on the influence of the degree of ordering on homogenisation. They found that ordered samples did not homogenise, even when tempered at 1000°C, while disordered crystals already fully homogenised at 600°C. The generally good agreement between the values gained from the variety of samples was a result they had not expected. On the basis of this they questioned alkali diffusion in feldspars involving a vacancy mechanism because the probability of all samples having the same vacancy concentration is rather low. They argued that the high concentration of impurities in the samples might have led to a maximum of the number of unpaired vacancies which might explain this apparent lack of influence of the vacancy concentration.

All data for tracer-diffusion of sodium and potassium gained from the studies summarized above, as well as the interdiffusion coefficients by Christoffersen et al. (1983), have been plotted in figure 4.1 and a compilation of the data can be found in appendix B, table B.1.

It is immediately obvious that self-diffusion of sodium is generally faster than that of potassium in a given feldspar. There is reasonably good agreement between most studies, though more so for potassium than for sodium. Only the data by Lin and Yund (1972) deviate quite noticeably. As their starting material was produced by exchange of microcline grains with molten NaCl, which should lead to the formation of cracks (see chapter 7.2 for a more detailed discussion of this effect), their values are probably overestimated. The data has been deemed unreliable by several other studies (Petrović, 1973; Yund, 1984) and will not be taken into account for further considerations here. For both the diffusion of potassium as well as sodium the data of Kasper (1975) and Foland (1974) agree reasonably well which, given their nearly identical experimental procedures and conditions, was to be expected. The slight differences may be due to the effect of composition on the diffusion coefficients as they used starting materials of near-end member compositions from opposing ends of the composition spectrum (Yund, 1984).

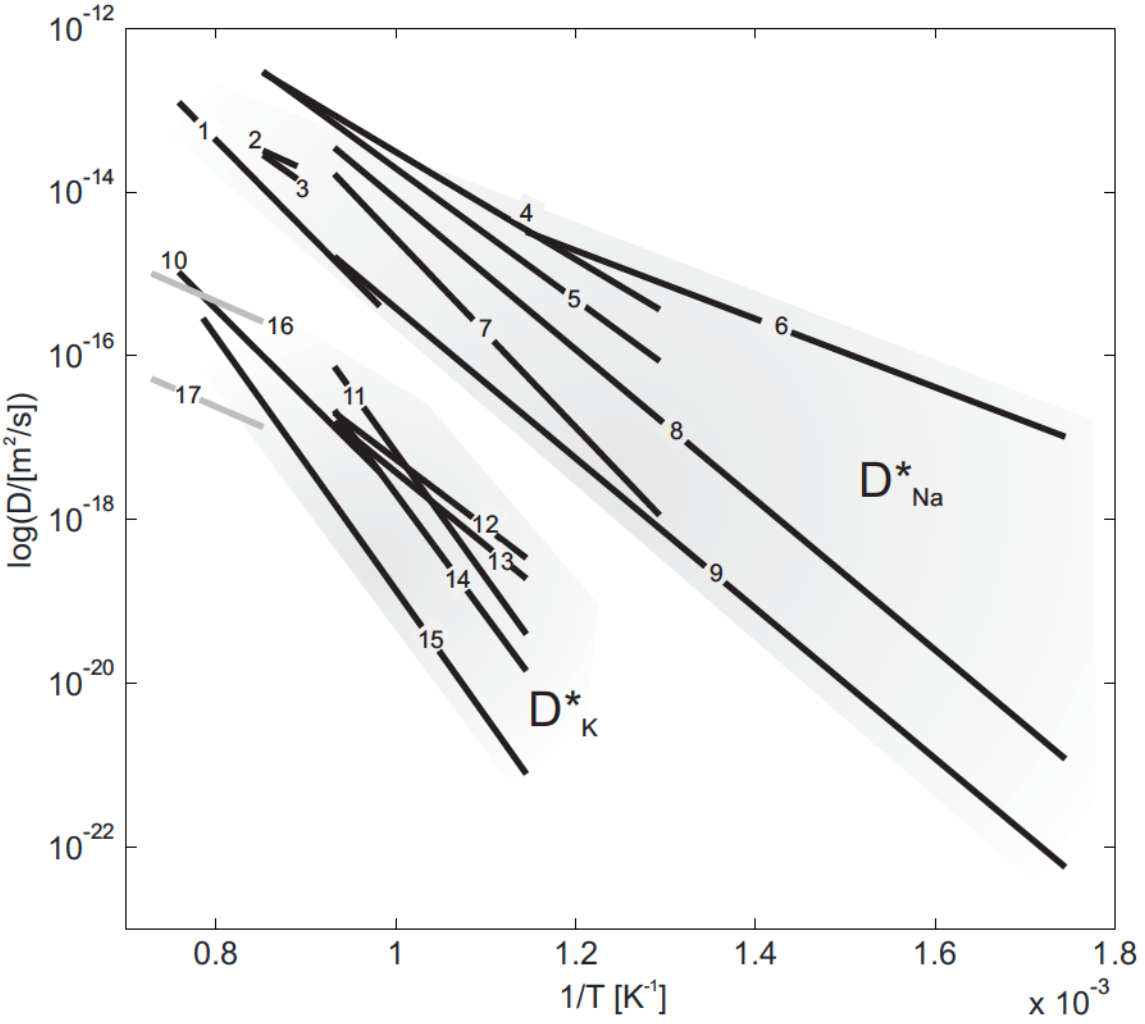

FIGURE 4.1: Arrhenius plot of Na- and K-tracer-diffusion and interdiffusion data for alkali feldspar: all data were determined for near end-member compositions; it is apparent that sodium diffusion is much faster than potassium diffusion for a given feldspar. There is a reasonably good agreement between the data of different studies for the same cation; 1 - D^*_{Na} - (PetrovicPhD); 2 - D^*_{Na} - Maury (1968); 3 - D^*_{Na} - Sippel (1963); 4 - $D^*_{Na} \perp (001)$ - Wilangowski (2013); 5 - $D^*_{Na} \perp (010)$ - Wilangowski (2013); 6 - D^*_{Na} - Lin and Yund (1972); 7 - D^*_{Na} - Foland (1974); 8 - D^*_{Na} - Bailey (1971); 9 - D^*_{Na} - Kasper (1975); 10 - D^*_K - Petrović (1972); 11 - D^*_K - Lin and Yund (1972); 12 - D^*_K - Giletti et al. (1974); 13 - D^*_K - Kasper (1975); 14 - D^*_K - Foland (1974); 15 - D^*_K - Giletti and Shanahan (1997); 16 - $D_{Na/K} \perp (001)$ - Christoffersen et al. (1983); 17 - $D_{Na/K} \perp (010)$ - Christoffersen et al. (1983) .

Chapter 5

Experiments

5.1 Starting Materials

Two sanidines from different localities in the Eifel (Germany) were used as starting material. Pieces of gem-quality material were analysed using scanning electron microscopy and electron microprobe measurements to ensure that the material is chemically homogeneous and devoid of cracks, twins, exsolutions, second phase precipitates, or other structural or chemical heterogeneities. Representative results of mineral chemical analyses of both materials can be found in table 5.1.

TABLE 5.1: Electron microprobe measurements of both starting materials; V5,V14,V16 and V22 are samples of Volkesfeld sanidine. The values for ERN3, ERS1 and ERS37, which represent sanidine from the Rockeskyller Kopf, were measured at the Ruhruniversität Bochum by Demtröder (2011)

	V5	V14	V16	V22	ERN3	ERS1	ERS37
SiO2	63.68	64.30	63.93	64.72	64.86	64.95	64.75
Al2O3	18.62	18.56	18.82	18.71	18.66	18.9	18.9
TiO2	0.00	0.00	0.04	0.00	0.03	0.03	0.04
FeO	0.18	0.14	0.18	0.10	0.15	0.16	0.21
MgO	0.00	0.00	0.00	0.00	0.01	0.01	0.02
CaO	0.01	0.01	0.01	0.02	0.01	0.01	0.02
Na2O	1.65	1.64	1.72	1.70	2.83	3.03	2.95
K2O	14.01	14.32	13.97	13.85	12.26	12.13	12.1
BaO	0.83	0.60	0.86	0.55	1.23	1.25	1.46
SrO	0.18	0.05	0.14	0.07	0.2	0.22	0.04
Rb2O	0.03	0.05	0.05	0.05	n/a	n/a	n/a
Σ	99.181	99.686	99.722	99.775	100.23	100.7	100.49

Eifel feldspars are widely known for their chemical homogeneity and have been well characterised in various studies (Riley and Bailey, 2003; Parsons and Lee, 2005; Weitz, 1972; Neusser et al., 2012; Demtröder, 2011). As a consequence these feldspars are very well documented and well suited for the experiments of the study at hand. The bulk of the experiments was done using sanidine from Volkesfeld as starting material.

The initial composition of the Volkesfeld sanidine can be described as $Or_{85}Ab_{14}Cs_1$, with minor Ba contents of up to 1 wt %, (0.02 apfu) and Fe contents of up to 0.2 wt. % (0.01 apfu). The chemical composition of the Rockeskyll sanidine is $Or_{72}Ab_{26}Cs_2$ (Demtröder, 2011) with minor Ba contents of up to 1.5 wt %, (0.02 apfu) and Fe contents of up to 0.2 wt. % (0.01 apfu), making the Ba-content slightly higher than in the Volkesfeld sanidine.

Both materials have a monoclinic symmetry and crystallize in the space group C2/m. Aluminium and silicon on the tetrahedral site are highly disordered with $\Sigma t_1 = 61$ (Volkesfeld) (Neusser et al., 2012) and $\Sigma t_1 = 58$ - 62 (Rockeskyll) (Demtröder, 2011). The chosen crystals are optically clear and free from inclusions and cracks apart from the (010) and (001) cleavages. The Volkesfeld material is either colourless or smoky brown. Although there is no difference in chemical composition or Al-Si-order between these two variants, all samples were prepared from the smoky brown variant to ensure the starting material being as uniform as possible. The feldspars from Rockeskyll are colourless.

Feldspars from the Eifel are known to show anomalous annealing behaviour. At temperatures exceeding 750°C the optical angle $2V_x$ changes rapidly and irreversibly (Bertelmann et al., 1985); the most significant changes can be observed at temperatures around 950°C (Schreuer et al., 2013). To investigate if this anomalous behaviour has an influence on interdiffusion, the temperatures of the experiments were chosen accordingly. Further, samples tempered at 1050°C for 4 days before exchange were prepared to compare the original samples and those that had already undergone the documented changes of optical properties.

5.2 Experimental Setup

The basic principle of the experimental setup was sealing feldspar in quartz glass tubes (inner diameter 7 mm, outer diameter 9 mm) under vacuum together with a salt melt containing K^+ and Na^+ cations in varying ratios to produce controlled composition shifts in the feldspar. The amount of salt was calculated so that a 40:1 molar proportion of the alkali cations contained in the salt relative to those contained in the feldspar

TABLE 5.2: Overview over the experimental conditions for all main experiments; all listed experiments were conducted using both samples with polished surfaces corresponding to the (010), and (001) planes of the feldspar

	T [°C]	X_K^{salt}	X_{Or}^{eq}	run duration [d]
Volkesfeld	800	0.48	0.80	32
		1.00	1.00	32
	850	0.30	0.70	1, 2, 4, 8, 16, 32, 64
		0.35	0.92	8
		0.60	0.97	1, 2, 4, 8, 16, 32, 64
		0.85	0.73	1, 2, 4, 8, 16, 32, 64
		1.00	1.00	1, 2, 4, 8, 16, 32, 64
	920	1.00	1.00	1, 2, 4, 8, 16
	950	1.00	1.00	1, 2
	1000	1.00	1.00	1
Rockeskyll	800	0.37	0.65	32
		0.55	0.80	32
	850	0.22	0.45	4, 8, 16
		0.50	0.85	4, 8, 16
		1.00	1.00	8
	920	0.50	0.82	2
	950	0.50	0.81	1
	1000	0.50	0.81	1

was obtained to ensure constant concentration boundaries during cation exchange. The tubes were then heated to temperatures between 800 and 1000°C in a muffle furnace at atmospheric pressure for 1 to 64 days. The temperature was monitored with a type N thermocouple and accurate within ± 2°; temperature variations were ± 1°. A listing of the experimental conditions can be found in table 5.2, a more detailed overview over all conducted experiments can be found in table B.3 in appendix B.

Two different types of experiments can be distinguished based on the geometry of the starting material. For the first type crushed feldspar was exchanged with salt melt comprised of a mixture of either NaCl-KCl or NaBr-KBr, depending on the temperature of the experiment. The ratio of the salts was varied systematically to determine a) the fractionation curve of K^+ between salt melt and feldspar, b) which composition shifts were best suited for subsequent experiments with geometrically well-defined samples, and c) the critical composition shift needed to initiate fracturing (see chapter 7.2).

For the second type of experiments plates of well-defined geometry were exchanged with salt melts of compositions chosen based on the first set of experiments. The resulting samples were used to determine the interdiffusion coefficient as a function of composition, and to analyse the fracture mechanics of cracks resulting from shifts of the initial

composition towards more sodium-rich compositions in regard to the fracture toughness of the material (chapter 7.2)

5.2.1 Crushed Material

Chlorides

The feldspar was crushed and sieved to a grain size of 200 to 400 μm. 0.1 g of the crushed material was sealed under vacuum in a quartz glass tube, together with a mixture of NaCl and KCl salts. The composition of the salt mixture was chosen based on the fractionation curve of K^+ between the resulting salt melt and the feldspar crystals at 850°C determined by Neusser et al. (2012). Six compositions were chosen, half of which shifted the initial composition towards more sodium-rich compositions (X_{KCl}0.2, 0.25 and 0.3) while the other three caused a shift towards more potassium-rich compositions (X_{KCl} 0.6, 0.85 and 1.0). The quartz glass tubes were heated to 850°C for 7 and 22 days, and then quenched instantly by immersing them into cold water. The tubes were opened and the feldspar grains retrieved by dissolving the salt with deionised water.

Strewn slides were prepared and the composition of the exchanged and unexchanged parts of the crystal grains determined with the electron microprobe (2 grains per experiment, 20 points per grain). The results of these measurements were plotted in figure 5.1 and fit the results by Neusser et al. (2012).

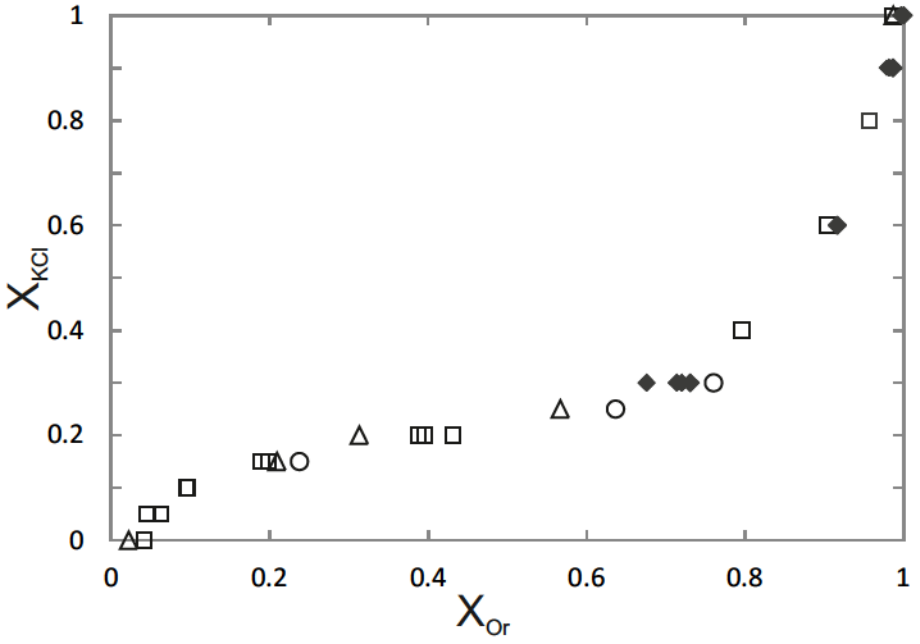

FIGURE 5.1: Fractionation of potassium between a KCl melt and feldspar determined at 850°C; open symbols represent data determined by Neusser et al. (2012), closed symbols represent results of this study

Four of the concentrations, three shifting the feldspar composition towards more potassium-rich composition (X_{KCl} 0.6, 0.85 and 1.0) and one shifting towards a more sodium-rich composition (X_{KCl} 0.3), were chosen for further experiments with well-defined starting geometry.

For experiments aimed at determining the critical shift needed to initiate fracturing for shifts towards more sodium-rich compositions the Volkesfeld sanidine was crushed and sieved to a grain size of 100 to 200 μm. 0.05 g feldspar was exchanged with salt melts of compositions varying systematically between X_{KCl} 0.35 to 0.31 to attain successively increasing composition shifts of the feldspar. The composition of the exchanged grains was determined with the electron microprobe and BSE imaging was employed to estimate at which composition the first cracks can be observed.

Bromides

The feldspar was crushed and sieved to a grain size of 100 to 200 μm. About 0.05 g of the crushed material was used for each experiment. The salt concentrations were chosen in 0.1 steps between 0 and 1 X_{KBr} to determine a fractionation curve for bromides at 800°C and 850°C in the whole composition range between X_{Or} 0 and 1.

Again strewn slides were prepared and the composition of the exchanged domains determined for twenty points on two grains per sample. Towards low X_{Or} values, the data points scatter significantly because the feldspar develops cracks for large composition shifts due to the composition dependence of the lattice parameters (see chapter 7.2). The spacing of these cracks becomes narrower the larger the composition shift is so that measurements with the EMP using a defocused beam are often impaired. The fractionation curve shows the same trend as that for chlorides with a sharp increase at very low and very high values for X_{Or} and only slight changes for intermediate compositions. The fractionation curves show that potassium is more likely to be found in the crystal at higher temperatures in the intermediate range, while little to no difference can be seen for the ranges with steep inclinations. The results of all measurements were plotted in figure 5.2.

5.2.2 Geometrically well-defined samples

The feldspar was prepared as polished plates of 3x3 mm size and 1 mm thickness. The plates were pre-polished by hand on a diamond polishing disc, the final polishing was done on a silk polishing cloth with 1 μm diamond powder. The polished surfaces corresponded to either the (001) or (010) planes of the feldspar for the bulk of the

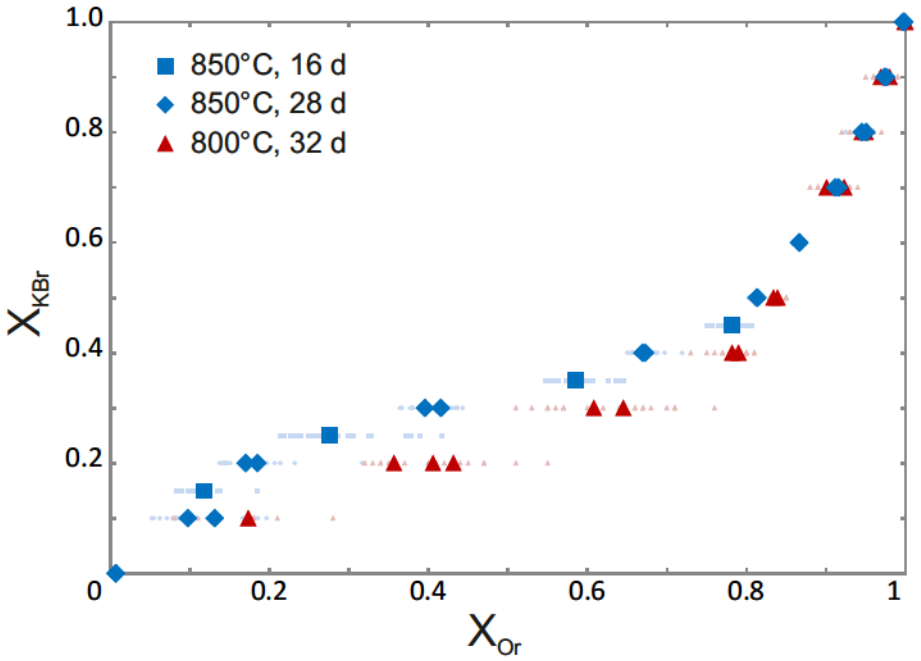

FIGURE 5.2: Fractionation of potassium between a KBr melt and feldspar determined at 800°C and 850°C; faded symbols represent the full range of experimental results while bold symbols are mean values

experiments. For the first plates only the polished (001) surface was pre-determined and thus the position of the c^*-axis known, while other axes could be rotated around it randomly. Later all (001) and (010) plates were pre-oriented on the basis of their optical extinction under polarised light.

Experiments with selected salt concentrations were conducted for different times between 1 and 64 days and at temperatures between 850°C and 1000°C using NaCl and KCl salt. For experiments at 800°C NaBr (T_M747°C) and KBr (T_M734°C) salts were used because they have lower melting points than the chlorides and thus still guarantee reliable cation transport. A complete overview over the experiments can be found in table B.3 in appendix B. The crystal plates retained their surface polish after cation exchange and no indication of surface reaction or recrystallisation was found. The exchanged plates were cut in two mutually perpendicular directions and thick slides were prepared that allowed chemical measurements in three crystallographic directions (figure 5.3).

Some additional plates with directions corresponding $(\sqrt{2}/2, \sqrt{2}/2, 0)$, $(\sqrt{2}/2, 0, \sqrt{2}/2)$ and $(0, \sqrt{2}/2, \sqrt{2}/2)$ were prepared and exchanged at 850°C for 8 days with pure KCl to provide data in 3 additional, independent directions within the *a*-*b*-, *a*-*c*-, and *b*-*c*-planes of the crystal.

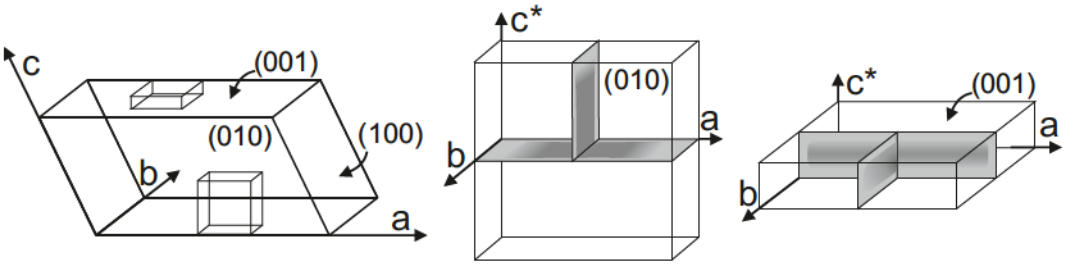

FIGURE 5.3: Sample geometry of the prepared platelets; the majority of plates were prepared so that the polished surfaces corresponded to either the (001) or (010) plane of the feldspar. After the experiment the plates were cut in two mutually perpendicular directions to allow documentation and measurements of diffusion profiles in different crystallographic directions.

Chapter 6

Methods

6.1 Analytical Methods

6.1.1 Scanning Electron Microscopy (SEM)

The scanning electron microscope uses electrons that are accelerated by a high voltage and focused on the specimen with the help of electromagnetic lenses. The electron beam interacts with the sample and thus creates several signals in the form of characteristic X-rays, secondary electrons and back-scattered electrons that can be interpreted to determine the surface topography and composition among other properties. These signals are displayed as greyscale pictures with the colour referring to differences in energy. For the electrons to interact with the sample without interference it has to be polished to minimize influences of surface topography. For imaging, samples were carbon coated using a double carbon-thread at a distance of about 8 cm from the sample surface under vacuum conditions better than 10^{-5} mbar chamber pressure to establish electrical conductivity.

6.1.2 Back-Scattered Electron Microscopy (BSE)

The analysis of back-scattered electrons (BSE) is based on the elastic scattering of electrons due to interaction with nuclei of atoms in the sample material. A certain fraction of the electrons is diffracted within the crystal (Schmidt and Olesen, 1989). These BSE are highly energetic and have an orientation that is correlated with the atomic number, thus allowing for chemical differentiation. The larger the atomic number, the higher is the probability for a deflection with high angles thus creating a stronger signal and leading to lighter coloured areas in the BSE image (Reed, 2005). An FEI Inspect

S scanning electron microscope with a tungsten filament electron source was used for BSE imaging. It was operated at beam acceleration voltages of 10 to 15 kV and a beam current of 8 nA. BSE imaging was done at high contrast settings so that variations in X_{Or} of a few percent could readily be discerned from changes in the grey shade on BSE images.

6.1.3 Electron Back-scatter Diffraction (EBSD)

Electron back-scatter diffraction is a technique allowing the analysis of effects caused by electrons experiencing Bragg reflection at atomic planes in crystalline materials. The sample was tilted to 70° in order to reach a beam incidence angle of 20° with respect to the sample surface. A fraction of the back-scattered electrons bears diffraction information, forming diffraction patterns, so-called Kikuchi patterns, on a fluorescent phosphor screen that converts electrons to visible photons which in turn are then recorded by a camera (Reed, 2005). These patterns consist of a number of bands that differ in their position, width and contrast to the background. Their position and width, which is inversely proportional to the distance between the lattice planes (Schmidt and Olesen, 1989), can be detected automatically by suitable software, and used for phase identification and to gain information on the orientation of the crystal (Reed, 2005). Orientation maps can be created by recording the Kikuchi patterns of points in a grid spaced over an area of interest ((Reed, 2005)).

In order to get the best possible signal for this technique it is essential to ensure a very smooth sample surface. To minimize surface roughness the sample was polished chemically with a colloidal silica suspension (Köstrosol, pH 9.2 to 10) on a rotary polisher after the initial mechanical polishing. For electron back-scatter diffraction analysis a thinner carbon coating than for imaging was applied, using only a single carbon thread at the same conditions to establish electrical conductivity.

EBSD data was acquired using a FEI Quanta 3D FEG microscope equipped with a field-emission electron source and an EDAX Digiview IV EBSD camera. The edges of the feldspar crystals were aligned parallel to the x- and y-directions of the scan reference system by stage rotation. The electron-beam was set to 15 kV accelerating voltage and 4 nA beam current in analytic mode using an SEM aperture of 1 mm. The working distance was between 8 and 14 mm. A 2x2 or 4x4 binning of the EBSD camera-resolution was applied. Hough settings were adjusted for each grain according to pattern quality of the grain. Common settings were 1° theta step size and a minimum peak distance of 10 to 12 ° for indexing 6 to 17 Hough peaks. A medium (9x9) or large (13x13) convolution mask was applied to the Hough space in order to eliminate artificial peaks and enhance

weak bands. Only the interior portion of the EBSD pattern was used for indexing, determined by the ρ-fraction of 60% to 85%.

The EBSD data was mapped by the beam moving in a raster scan pattern using a hexagonal grid at a step size of 15 μm in an area between 40 x 40 μm and 100 x 100 μm. The wide step width was chosen to ensure that the quality of subsequent patterns was not influenced during acquisition because feldspar has a low stability under the electron beam. The average measuring time was set to 0.3 points per second. The electron back-scatter diffraction patterns were acquired and processed using the software packages OIM Data Collection and Analysis. 10 to 100 data points were collected for each crystal. In case of inconsistent automatic indexing, results for single points and indexing statistics were checked in order to identify the correct orientation of the crystal.

6.1.4 EBSD Cross Correlation Technique

The cross correlation technique allows the determination of the full elastic strain tensor from electron back-scatter diffraction patterns employing the commercial software Cross court 3 by BLG Productions.

A series of square regions of interest (ROI) is placed on the recorded electron back-scatter diffraction patterns (EBSP). A reference pattern is chosen at a region which serves as a starting point for lattice strain determination and is ideally a part of the crystal that is known to be strain-free or which has an otherwise known state of strain. It is important that all acquisition parameters are kept constant during measurement of the reference and other patterns and that the relative positions of the reference area and the measurement area are well known. Shifts of the EBSPs' features in each ROI of a pattern are then compared to their equivalent in the reference pattern. Variations in these shifts across the pattern give insight into the nature of the strain within the diffracting volume (Wilkinson et al., 2009).

The sensitivity of the cross correlation method strongly depends on pattern quality. For very good patterns shifts as small as a few hundredths of pixels can be determined (Wilkinson and Britton, 2012); such a high quality can unfortunately not be achieved for feldspars due to the necessity for a carbon coating of the surface, the low symmetry and density of the crystal as well as its low stability under the electron beam. Furthermore, as the patterns were taken by integration over an approximately 50 μm^2 large area they contain an inherent horizontal blurring of about 0.5 pixels (pixel size is 80 μm). Nevertheless, the pattern quality obtained in our measurements was sufficient to reach a sensitivity of about 0.5 pixels (Wilkinson et al., 2006). The strain sensitivity for high resolution Kikuchi patterns is 1.3 x 10^{-4} (Wilkinson et al., 2006).

Fast fourier filters were employed on the ROIs in order to reduce high frequency intensity noise and low frequency intensity background influences. With this the translational shifts in the tested pattern ROI's can be tracked more accurately by the cross correlation in the fourier domain (Wilkinson et al., 2009). The low frequency cut off was set to 2 px^{-1} with a cut off width of 0 while the high frequency cut off was set to 15 px^{-1}, also with a cut off width of 0.

Electron back-scatter diffraction measurements were performed at the Max-Planck Institute for Iron Research in Düsseldorf using a Zeiss XB 1540 cross beam instrument with thermal field emission gun operated at 15 kV and about 5 nA beam current. Conductivity of the sample was established by a carbon sputter coating of 2 to 3 nm thickness applied with a Gatan PECS precision etching and coating instrument. The sample was mounted at 70°C sample tilt and the measurements were done at a working distance of 13 mm.

Profiles were measured normal to the polished (010) and (001) surfaces of the crystal; the sample was oriented so that the trace of the respective surface was parallel to the tilt axis. To minimize beam damage on the beam sensitive feldspar, patterns were collected by scanning the beam over a rectangular area of 1 x 50 μm with its long axis perpendicular to the trace of the chemical gradient. This window was moved in 1 μm steps for profiles normal to (010) and in 2 μm steps for profiles normal to (001).

The OIM Data Collection software 5.3 was used for data acquisition. A TSL Hikari EBSD detector with a 640 x 640 pixel resolution was used for pattern recording. A 1x1 binning of the EBSD-camera resolution was applied and the image corrected by subtracting a measured background, histogram normalisation and applying a dynamic background subtraction. The background pattern was taken on a carbon-coated glass sample mounted on the same sample holder.

Hough settings of 0.25 2θ step size, a binned pattern size of 240 and a large convolution mask (13x13) were used to identify 20 peaks with a minimum peak distance of 16. Only the inner part of the pattern was considered with the ρ-fraction of the Hough space being set to 84 %. For each pattern the camera exposition time was 200 ms and 40 patterns were averaged, resulting in a total exposure time of about 8 seconds.

The analysis of pattern distortion was performed on the basis of 253 square regions of interest (ROI) each with 64 x 64 pixel size placed on the recorded electron back-scatter diffraction patterns in a regular grid within the circular area of the pattern with an overlap area of 7.5 px^2 between neighbouring regions of interest.

As long as the rim is thin compared to the bulk of the sample the unexchanged core is mechanically much stronger than the thin misfitting surface layer. The internal region

of the crystal is therefore mechanically much stronger than the thin chemically altered surface layer. Accordingly, the pattern obtained at the inner end of the profile in the core of the crystal was chosen as reference pattern representing the original, unstrained lattice. Shifts of the EBSPs' features in the ROI of each pattern obtained along the measured profile further outwards and across the sharp composition front were then compared to their equivalent in the reference pattern. Variations in these shifts across the pattern give insight into the nature of the strain within the diffracting volume (Wilkinson et al., 2009).

6.1.5 Electron Microprobe (EMP)

The electron microprobe is a non-destructive method that allows the qualitative and quantitative determination of the chemical composition of a solid material. It provides a high lateral resolution down to about 1 μm. The principle of the EMP is based on the interaction of electrons in a highly focused beam with the sample. The beam causes the emission of characteristic X-rays, scattered electrons, backscattered electrons and cathodoluminescence that can be picked up with suitable spectrometers and detectors. For measurements carried out to test the homogeneity and initial composition of the starting material a CAMECA SX-100 at the Center for Earth Sciences, University of Vienna was used. A high voltage of 15 kV and a beam current of 15 to 20 nA were applied. The standards, spectrometers and underground positions used for calibration can be found in table 6.1. The beam had to be defocused to 3 μm in diameter to minimize the loss of Na and K by migration.

TABLE 6.1: EMP calibration

Element	Spectrometer Crystal	Standard	Counting time peak [s]	Counting time background [s]
Na	TAP	Albite	8	4
K	PET	Orthoclase	8	4
Fe	LIF	Almandine	20	10
Ba	PET	$BaSO_4$	25	15
Mg	TAP	Olivine	20	10
Al	TAP	Almandine	8	4
Si	TAP	Quartz	15	7.5

6.1.6 Field Emission Gun Scanning Electron Microscope (FEG-SEM)

The advantage of the use of a field-emission electron source is having a relatively narrow beam at high energy and thus a comparatively small exaltation volume which in turn allows for high spatial resolution. The field-emission cathode avoids typical problems of other emitters such as evaporation of the cathode material or thermal drift due to the necessity for heating the cathode. Instead the emission is achieved by placing a tungsten wire fashioned into a very sharp point into an electrical field where the high electrical potential gradient lowers the energy barrier, allowing the electrons to escape (Erdman et al., 2009).

Mineral chemical analysis of the cation exchanged samples was carried out at the Helmholtzzentrum Potsdam - German Research Centre for Geosciences using a JEOL Hyperprobe JXA-8500F with a thermal field-emission cathode. Profiles between 15 and 150 μm length with 0.5 μm or 1 μm step-width were measured, depending on the width and sharpness of the diffusion fronts. The profiles were measured normal to the traces of the surfaces of the exchanged samples which were cut in two mutually perpendicular directions (figure 5.3) and mounted in epoxy resin before polishing. The FEG-SEM was operated at 8 kV and 10 nA. The beam was defocussed to 10 μm for calibration and fully focussed during measurements. Peak counting times were set to 10 seconds and background counting time to 5 seconds to minimize loss of Na and K by migration during measurement. With these settings a lateral resolution of better than 500 nm could be achieved for mineral chemical analyses.

The comparatively small exaltation volume also makes the measurements sensitive to imperfections and contaminations of the surface which leads to some scattering of the data. Despite the scatter the analysed profiles clearly all show the same trends and reflect the shape of well-defined diffusion profiles. The error is within 3.5 to 4% for potassium, 7 to 8% for sodium. As we mainly look at the $\frac{K}{K+Na}$ ratio though, and measurements for both elements are equally influenced by any inaccuracies of the measurements, the overall error is only about 0.45%.

6.2 Treatment of Data

Given the 40-fold molar excess of the alkali cations contained in the salt-melt as compared to the alkali cations contained in the feldspar, the composition of the melt remains practically constant during cation exchange. Thus constant concentration boundary conditions can be assumed. When extracting the sodium-potassium interdiffusion coefficient from the concentration-distance data, the non-linear nature of the interdiffusion

process must be accounted for. A technique for integrating the diffusion equation with a composition dependent diffusion coefficient was developed by Boltzmann (1894) (see chapter 3.6). It has been adapted for application to the specific initial and boundary conditions corresponding to the experimental setting of the cation exchange experiments in Petrishcheva et al. (2014). Only diffusion in the directions perpendicular to the (001) and the (010) surfaces of the crystal plates was considered. Profiles were all measured at sufficiently large distances from the edges of the crystal plates and from cracks so that complexities of the chemical patterns by overlapping diffusion profiles were avoided. The possibility of unobserved cracks can of course not be ruled out completely. In the case of the samples that were shifted towards more sodium-rich compositions, however, the cracks exhibit the described, very strict geometry and regular spacing. This, in combination with the relatively small activation volume, allows the assumption that the probability of an unobserved crack being present beneath the sample surface is reasonably low. The diffusion process underlying the observed composition profiles can then be treated as strictly one-dimensional.

Time does not have an influence on the interdiffusion coefficient; longer run duration only allows the diffusion front to propagate further into the crystal while the interdiffusion processes and rates stay the same. All experiments for one temperature, salt composition, and direction could thus be reduced to one dataset comprising the data for all run times. The similarity variable was introduced which includes both the spatial and temporal aspects of the concentration profile. This was achieved by rescaling the space variable x for each experiment according to:

$$\eta_s = \frac{x}{2\sqrt{t_0}} \tag{6.1}$$

defined for $t > 0$ and with t_0 being the run time of the experiment.

$\eta = x/(2\sqrt{t})$ was calculated for each mole fraction profile, which was then recast in the form $c(\eta)$ and fitted using Wolfram Mathematica. The fitting method was adjusted depending on the type of diffusion front (see chapter 7.3).

The basic equation for obtaining the composition dependent sodium-potassium interdiffusion coefficient then reads:

$$D(c) = -2\frac{d\eta}{dc}\int_{c_2}^{c} \eta(c)dc, \tag{6.2}$$

where c is a shorthand notation for X_{Or}, c_2 is the initial bulk mole fraction in the feldspar crystal. The inverse function $\eta(c)$ was inserted into equation 6.2 to obtain the composition dependent interdiffusion coefficient $D_{NaK}(c)$. The validity of the analysis

was tested by back-modelling of the diffusion using the extracted sodium-potassium interdiffusion coefficient, which generally gave perfect agreement between calculated and experimentally observed mole fraction profiles.

Chapter 7

Results

7.1 Influence of the Direction of the Chemical Shift

The ratio of the potassium and sodium salts used in the experiments was varied to achieve composition shifts of different extent towards either more sodium- or potassium-rich compositions. Depending on the direction of the composition shift different geometries of diffusion profiles can be observed.

For a shift towards more K-rich compositions the diffusion profile exhibits two plateaus corresponding to an exchanged rim in equilibrium with the melt and a completely unexchanged core, respectively. Between these plateaus an exchange front with an inflection point develops that progresses into the crystal with time. The width of this diffusion front varies greatly with the extent of chemical shift and crystallographic direction. For a more detailed description see section 7.3.

A shift towards more Na-rich composition leads to the development of a very regular crack system. The exchange front developing in this case lacks the inflection point observed for shifts towards more K-rich compositions. For more information regarding this see section 7.2.

7.2 Fracturing

Due to the pronounced composition dependence of the lattice parameters in feldspar, which is about five times higher in the a-direction than in the b- and c-directions (Kroll et al., 1986; Angel et al., 2012) (see figure 2.12), any heterogeneity in composition is associated with the occurrence of coherency strain. If during cation exchange the composition is changed too severely, the associated lattice extension or contraction leads to

the formation of cracks. Depending on the direction of the composition shift the geometry of developing crack patterns is fundamentally different. For shifts towards more sodium-rich compositions the lattice contraction produces a very regular, sub-parallel system of tensile (mode I) cracks. Their strict geometry allows calculating the stress intensity factor from the systematic relation between crack spacing and coherency strain. Cracks for shifts towards more potassium-rich compositions have a much more complex geometry and cannot be as readily analysed.

7.2.1 Shifts towards Na

Characteristics of the Cracks

BSE imaging shows two types of cracks. The first type is a system of cracks running sub-parallel to each other in a (h0l) plane of the feldspar, which is a general crystallographic plane and not related to the cleavage planes of feldspar. These cracks are surrounded by an alterated, bell-shaped halo of more sodium-rich feldspar (figure 7.1). Usually these halos are bounded sharply in the direction parallel and much more softly normal to the cracks. The barium distribution remains unchanged over the diffusion fronts and around the cracks.

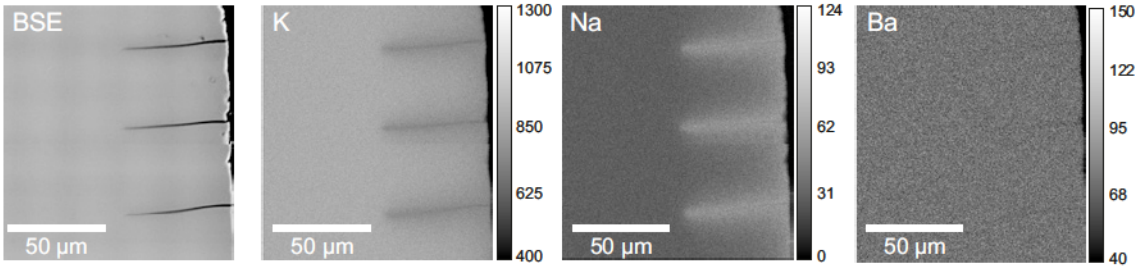

FIGURE 7.1: Element map across cracks in a Volkesfeld sanidine plate with polished (010) surfaces, exchanged for 16 days at 850°C and shifted to X_{Or}^{eq} 0.6; numbers on the greyscale legend indicate to counts per second

The orientation of the cracks differs slightly between the two starting materials used for the experiments. For sanidine from Volkesfeld (initial X_{Or} 0.85) the angle between cracks and negative a-axis is 83°± 2°, determined from 48 measurements in 3 samples. In sanidine from Rockeskyller Kopf (initial X_{Or}0.72) the angle was measured as 73°± 3°, determined from 33 measurements in 2 samples.

At the beginning of cation exchange only a very thin surface layer has been exchanged. If the extend of the chemical shift exceeds the critical shift for crack formation, short cracks emanate perpendicular to the surface of the grain within this layer. With increasing run duration the diffusion propagates into the crystal, and the cracks lengthen (figure 7.2) and are deflected into the common (h0l) plane (figure 7.3).

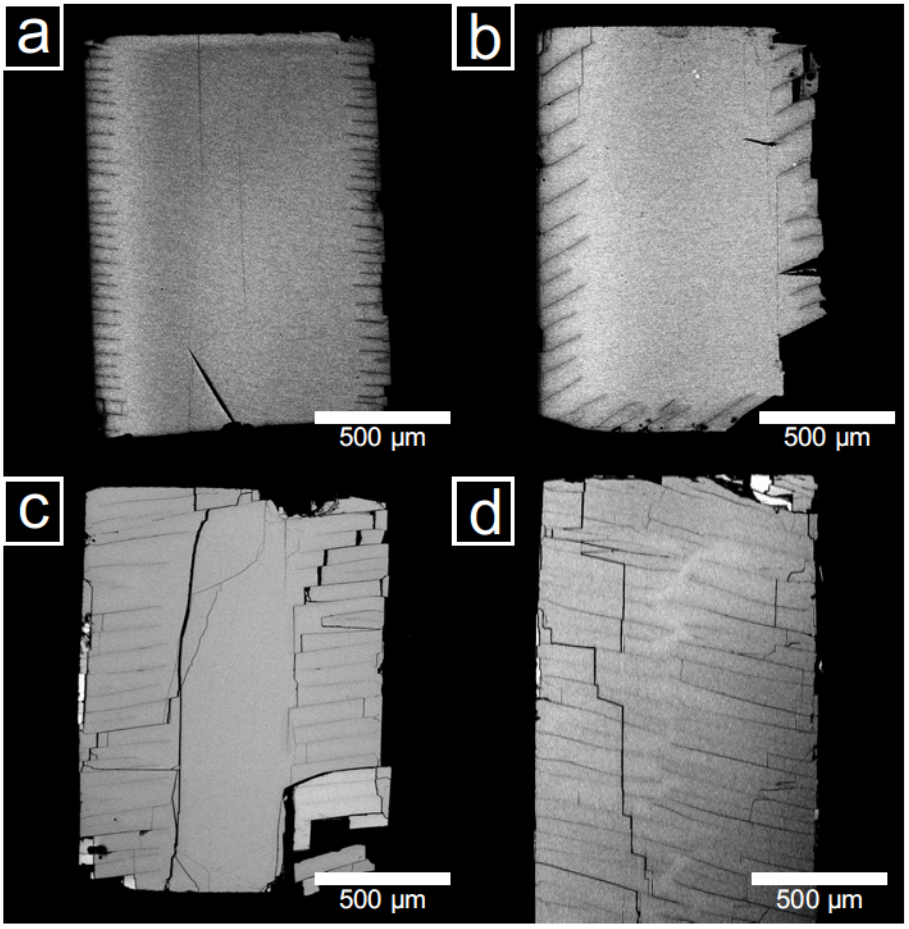

FIGURE 7.2: The cracks propagate into the crystal with time, for a given composition the crack spacing remains constant while the cracks propagate into the crystal; Volkesfeld sanidine plates with polished (001) surfaces exchanged with salt melt with X_{KCl} 0.3 at 850°C corresponding to a shift to X_{Or}^{eq} 0.65 after a) 8 days, b) 16 days, c) 32 days and d) 64 days

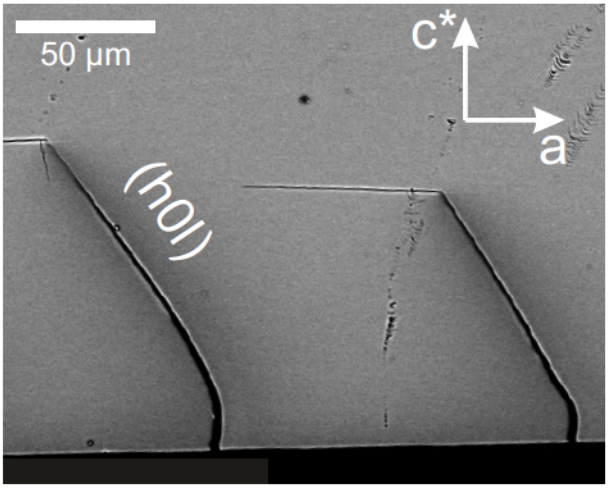

FIGURE 7.3: The cracks open perpendicular to the crystal surface before being deflected into the general crystallographic direction (h0l). Cracks of the second type running parallel to the sample edges do not show alteration haloes and can thus probably be interpreted as artefacts of quenching and preparation

The cracks function as enhanced diffusion pathways for cation exchange. Thus diffusion also occurs perpendicular to the surface of the cracks, forming the aforementioned alteration halos (figure 7.1). This additional diffusion leads to a much faster complete exchange of the crystal compared to unfractured crystals. After a time no new cracks develop and a very regular crack spacing has established (figures 7.4 and 7.5). Plotting the crack spacing as a function of composition shift shows that crack spacing systematically decreases with increasing composition shift for both sanidines, and for cracks emanating from both the (010) and (001) faces (figure 7.6).

The relation between crack spacing and composition shift appears to be non-linear, the relative decrease of crack-spacing becoming smaller for larger shifts. Generally the crack spacing for cracks emanating from polished (010) surfaces seems to be slightly narrower than for those emanating from polished (001) faces for a given chemical shift in both starting materials (figure 7.6). The crack spacing increases with decreasing shift as the coherency stress between the altered and unaltered areas of the crystal decreases when the compositional differences are smaller.

The cracks of the second type run parallel to the cleavage planes of the feldspar and are perfectly straight. In contrast to the cracks of the first type they are not surrounded by a more sodium-rich exchange halo and are most likely artefacts of quenching and/or preparation.

Experiments with higher temperatures and longer run durations were almost exclusively conducted for one composition shift using a salt melt with X_{KCl} 0.3. The composition shift in the feldspar corresponding to this melt composition depends on the temperature the experiment was conducted at because the fractionation of the cations between crystal and melt is temperature dependent. In these samples complex crack patterns with several hierarchical levels of cracks can be observed. The first hierarchical level propagates furthest into the crystal and has a very wide spacing in the order of 120 to 150 μm. The second set of cracks is slightly shorter and spaced about 15 to 20 μm apart. These cracks are straight for a certain length and then bent away from the cracks of the first hierarchical level forming a steeple-like shape with its apex being in the middle between two of the longer cracks. The last hierarchical level consists of very short cracks with a spacing of 6 to 10 μm. Not every sample shows all hierarchical levels of cracks (figure 7.7). All spacing measurements are listed in table B.4 in appendix B.

Two different sets of experiments were carried out to analyse the regular crack patterns. Some of the work was carried out by Katharina Scheidl as part of her master thesis in the scope of this project and was published in Scheidl et al. (2013), which has been attached to this work in appendix C.

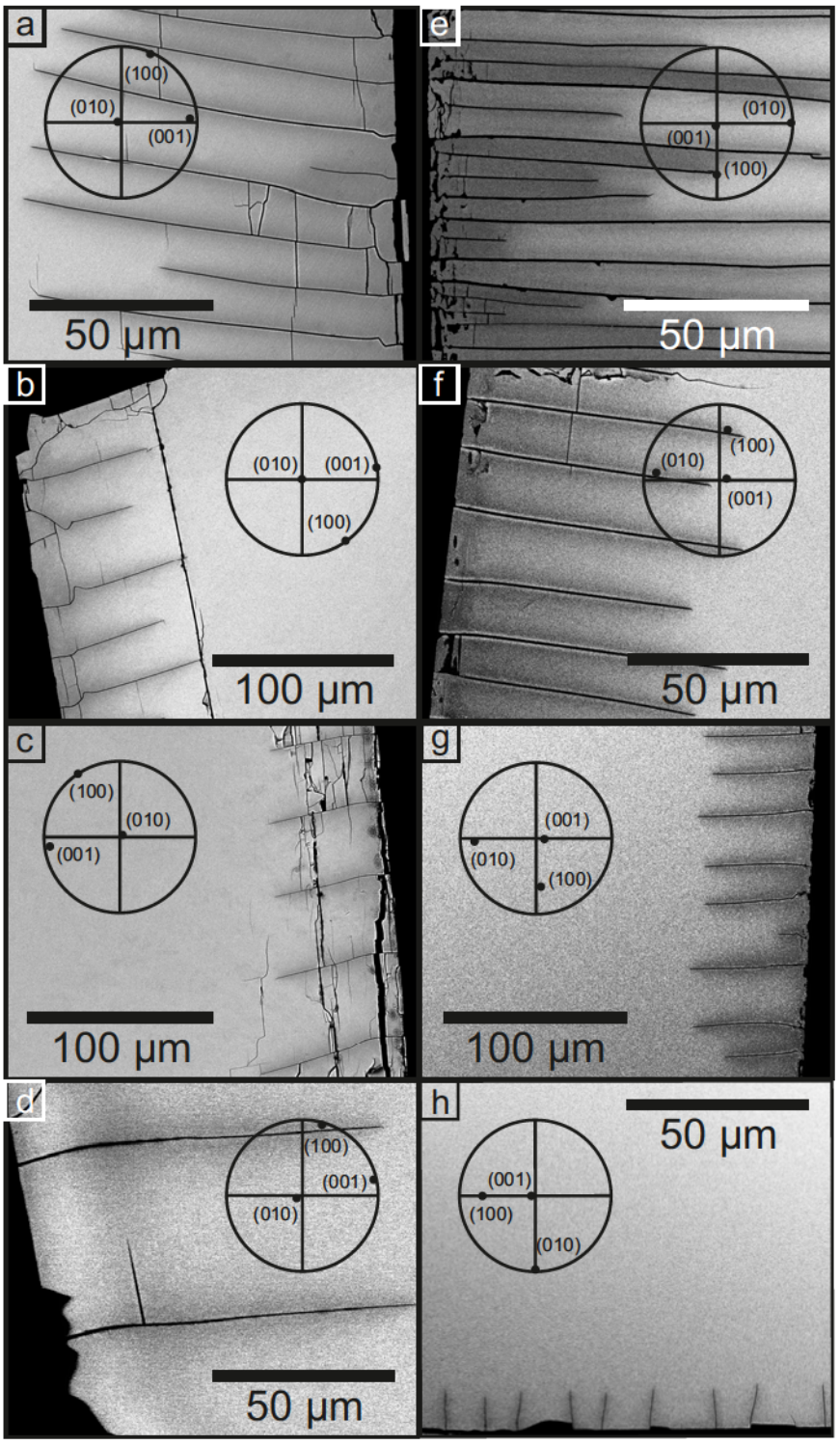

FIGURE 7.4: BSE image showing the relation between crack spacing and chemical shift in Volkesfeld sanidine, the material was exchanged for 7 to 8 days with salt melts of systematically varied composition to gain an equilibrium composition after exchange of a)/e) X_{Or}^{eq} 0.27, b)/f) X_{Or}^{eq} 0.5, c)/g) X_{Or}^{eq} 0.6, d)/h) X_{Or}^{eq} 0.64 with images a to d showing plates with polished surfaces parallel to (001) and e to f showing plates with polished surfaces parallel to (010); the stereoplots show a projection of the normals of the crystal planes in the upper hemisphere

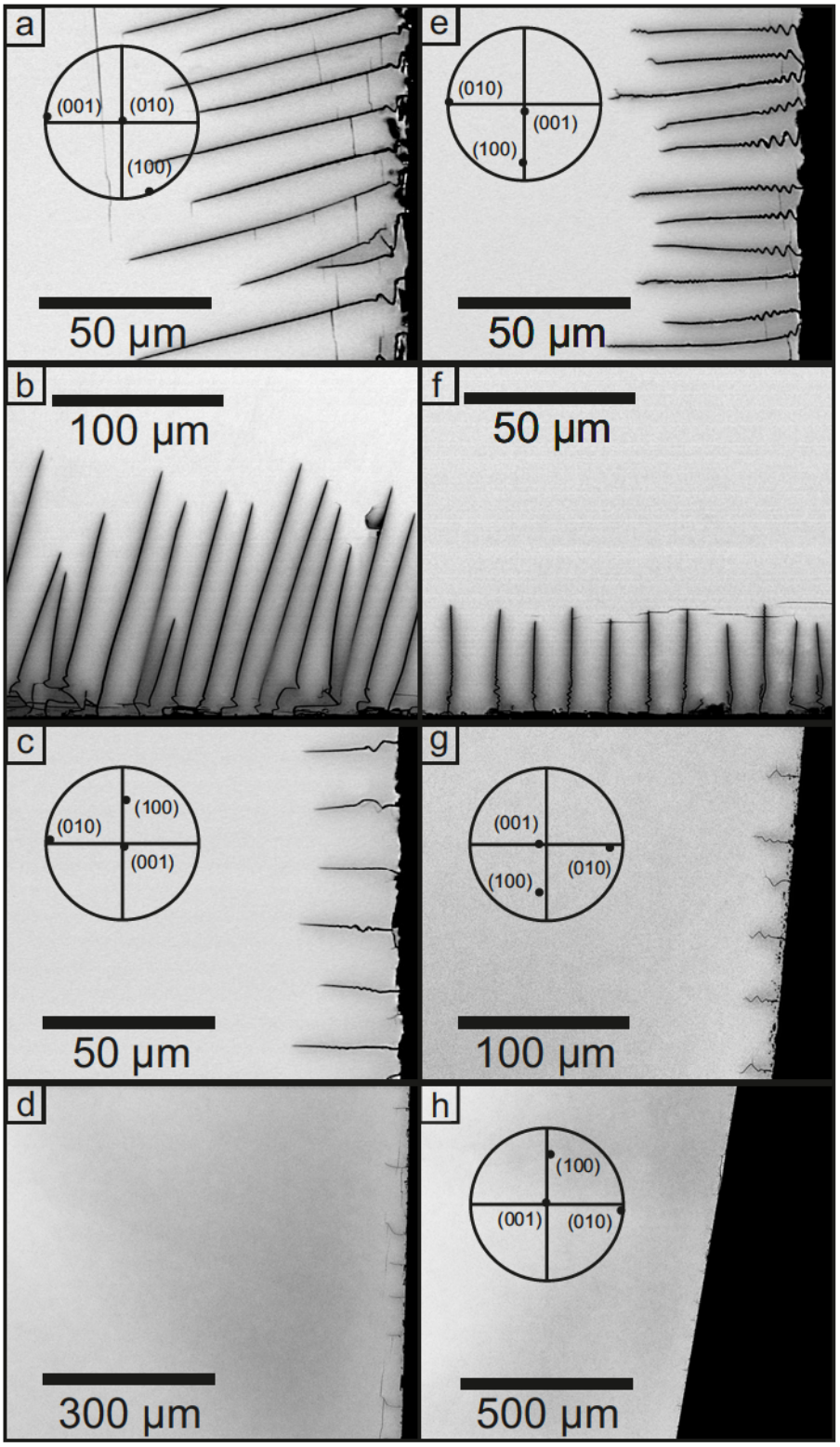

FIGURE 7.5: BSE image showing the relation between crack spacing and chemical shift in Rockeskyll sanidine, the material was exchanged for 7 to 8 days with salt melts of systematically varied composition to gain an equilibrium composition after exchange of a)/e) X_{Or}^{eq} 0.27, b)/f) X_{Or}^{eq} 0.5, c)/g) X_{Or}^{eq} 0.6, d)/h) X_{Or}^{eq} 0.64 with images a to d showing plates with polished surfaces parallel to (001) and e to f showing plates with polished surfaces parallel to (010); the stereoplots show a projection of the normals of the crystal planes in the upper hemisphere

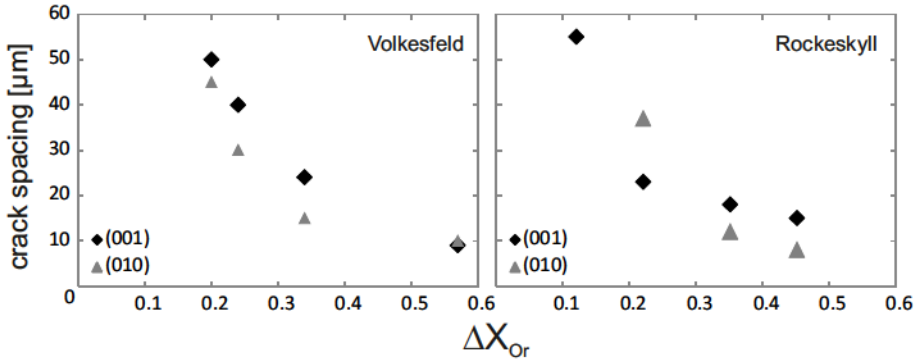

FIGURE 7.6: Crack-spacing as a function of the chemical shift $\Delta X_{Or} = X_{Or}^{initial} - X_{Or}^{eq}$ for sanidine from Volkesfeld and Rockeskyll

Critical shift to initiate fracturing

The first set of experiments using crushed feldspar samples was performed to determine the critical composition shift needed to initiate fracturing. To this end X_{KCl} of the salt melt was varied systematically between 0.35 to 0.31 to attain successively increasing composition shifts of the feldspar. BSE imaging of the exchanged samples showed that the minimum shift needed to induce fracturing is 9 mole-%. However, at these small shifts the formation of the cracks is still largely controlled by imperfections of the surface. The regularity characteristic for the crack patterns begins to develop at shifts of about 13 mole-%.

Correlation between chemical shift and crack spacing

The second set of experiments was carried out using plates of well-defined geometry to avoid imperfections of the surface topography of the grains influencing the cracks, and to allow for an easier analysis of the fracture mechanics. For these series of experiments the composition shift was varied between 15 and 55 mole-% to investigate correlation between chemical shift and crack spacing which had been implied by earlier observations by Neusser et al. (2012). The experiments were conducted at 850°C for a run duration of 7 to 8 days. Plates of both starting materials were exchanged, cut, and mounted so that the polished surface of the crystal was either (001) or (010). The orientation was determined using EBSD. As the cracks run parallel to an (h0l) plane they are perpendicular to polished (010) surfaces. In samples with polished (010) faces the crystals are oriented so that the *c*-axis is nearly perpendicular to the sample surface. As the cracks enclose an angle between 8° to 18° with the *c*-axis, the cracks are also nearly perpendicular to the sample surface, and the observed crack spacing very closely corresponds to the actual spacing. Thus for samples with polished (010) faces the actual crack spacing

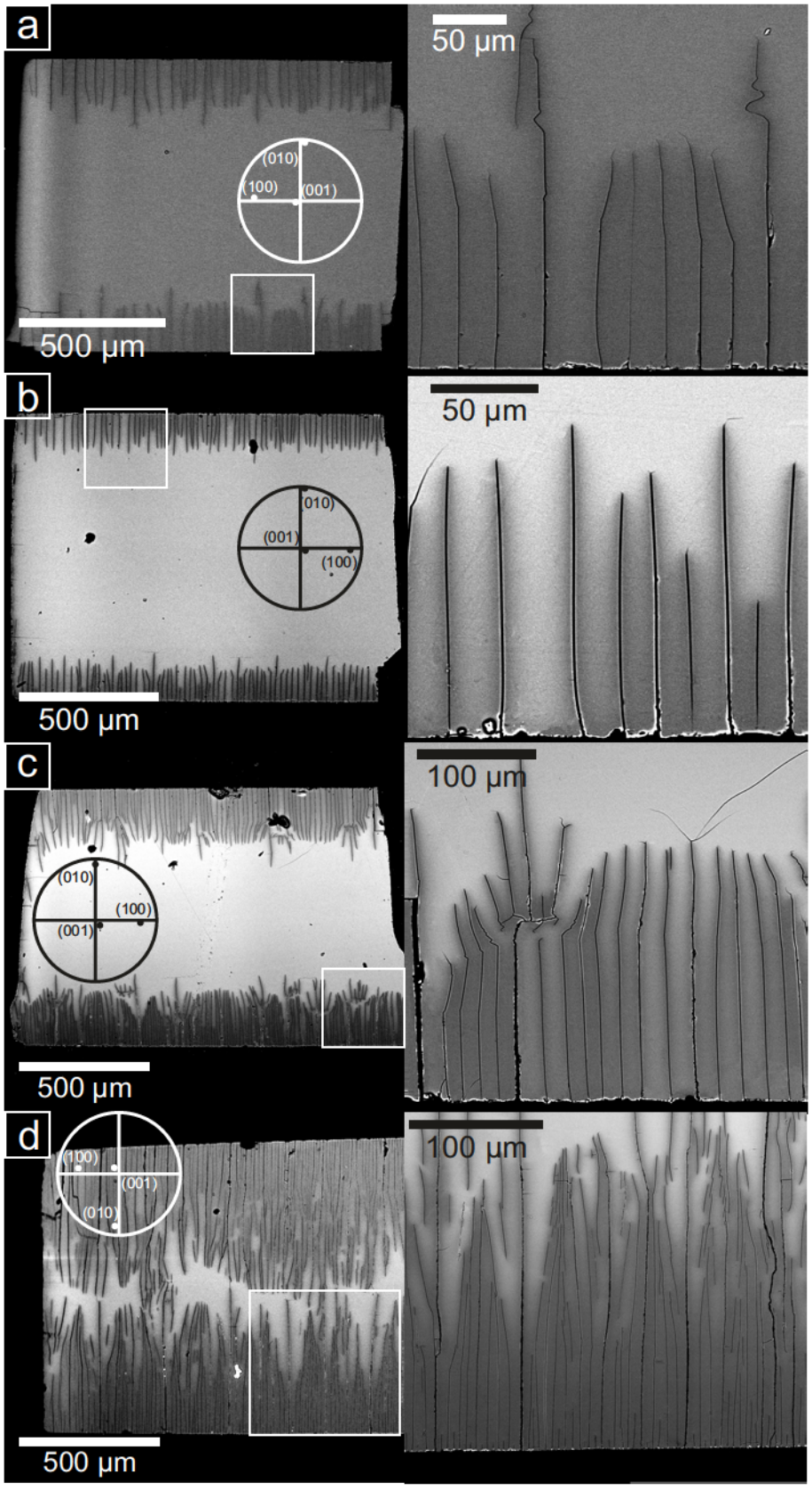

FIGURE 7.7: For longer run durations and higher temperatures more complex geometries of the cracks develop and several hierarchical levels of cracks can be observed; all samples used plates with polished (010) surfaces shifted to $X_{Or}eq$ 0.6 at the following run durations and temperatures: a) 32 days, 850°C, b) 2 days, 920°C, c) 2 days, 950°C d) 2 days, 1000°C; the right hand images are close ups of the areas marked in the corresponding left hand image; the stereoplots show a projection of the normals of the crystal planes in the upper hemisphere

is calculated according to

$$d = \sin\varepsilon d' \tag{7.1}$$

with d being the actual spacing, d' the apparent spacing and ε the angle between the normal of the cracks and the (001) plane. d' and ε can be determined from BSE images of the samples.

In samples with polished (001) faces the traces of the cracks are generally not perpendicular to the trace of the polished (001) plane, and observed crack spacing differs from actual spacing. The observed spacing is in the following referred to as the apparent crack spacing and to the observable angle between the traces of the cracks and the (001) face as the apparent angle of intersection. The angle the cracks enclose with the sample surfaces and thus the relation between the apparent and actual spacing, as well as the apparent angle of intersection, depend on crystal orientation. Given that the true angle of intersection between the cracks and the (001) surface is known, the actual crack spacing can be determined from the apparent spacing and apparent angle of intersection according to

$$d = \frac{\sin\varphi}{\sin\varphi'} \cdot \frac{\tan\varphi'}{\tan\varphi} \tag{7.2}$$

where, again, d is the actual a crack spacing, φ is the true and φ' the apparent angle of intersection. The true angle of intersection was determined as 83° for sanidine from Volkesfeld and 73° for sanidine from Rockeskyller Kopf. A sketch of the orientation of the cracks within the feldspar can be found in figure 7.8.

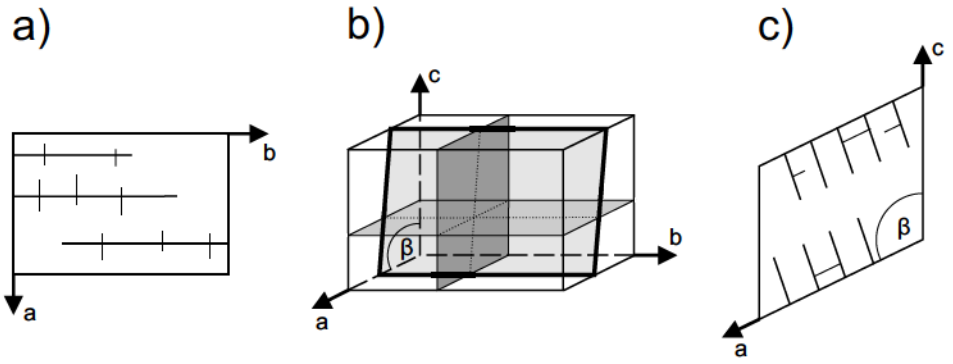

FIGURE 7.8: Schematic sketch of a plate showing the first and second level of cracks, a) view onto (001) along c^*, b) oblique view showing the orientation of the first level cracks (light grey plane) and second level cracks (dark grey planes), c) view on (010) along b (image courtesy of Katharina Scheidl)

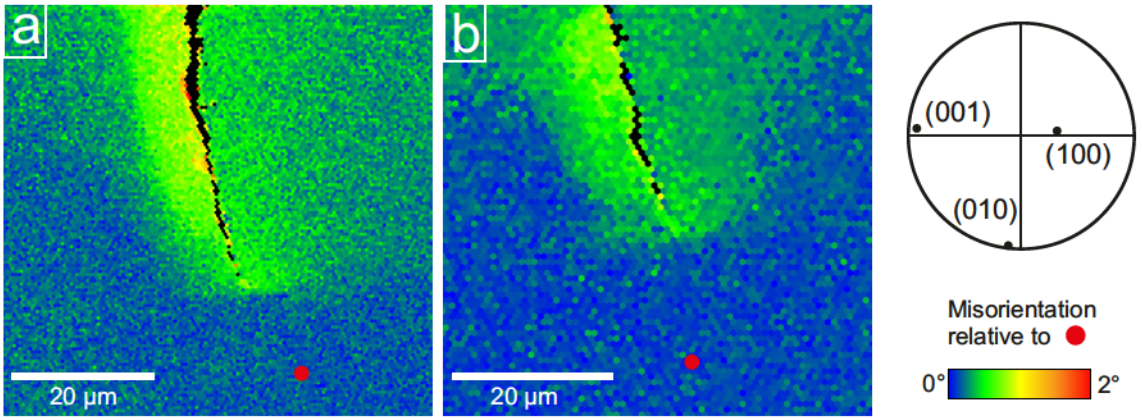

FIGURE 7.9: EBSD maps across crack tips in a Volkesfeld sanidine with polished (010) surfaces exchanged for 16 days at 850°C to $X^{e}_{Or}q$ 0.6, EBSD mapping with a) 0.4 μm step width, b) 0.8 μm step width, the stereoplot shows a projection of the normals of the crystal planes in the upper hemisphere

Two EBSD maps were recorded over crack tips in a plate of Volkesfeld sanidine with polished (010) surfaces exchanged for 2 days at 920° and shifted to X_{Or} 0.6. Both maps show an area of minor misorientation of the lattice of 0.5° to 1° on one side of the crack which is bounded quite sharply and becomes narrower towards the crack tip. A wider area of slighter misorientation is found on the other side of the crack and around the aforementioned sharply bounded area (figure 7.9). The shape of the whole misoriented area is reminiscent of the bell-shaped alteration halo documented in the element maps (figure 7.1).

7.2.2 Shifts towards K

For composition shifts towards more potassium-rich compositions the systematics and geometry of developing cracks are much more complex. Cracks were only observed in experiments with shifts by more than about 12 mole-% with run duration and temperature also being determining factors. For a complete listing for which experimental conditions cracks were observed see table 7.1. The observed cracks run roughly parallel to the diffusion fronts and curve close to the edges of the sample where the cracks which are parallel to two different surfaces of the sample link up (figure 7.10).

The shape of the cracks is further influenced by crystallographic direction. Most of the cracks run parallel to the a-axis of the feldspar while they are usually much shorter parallel to b- and c^*.

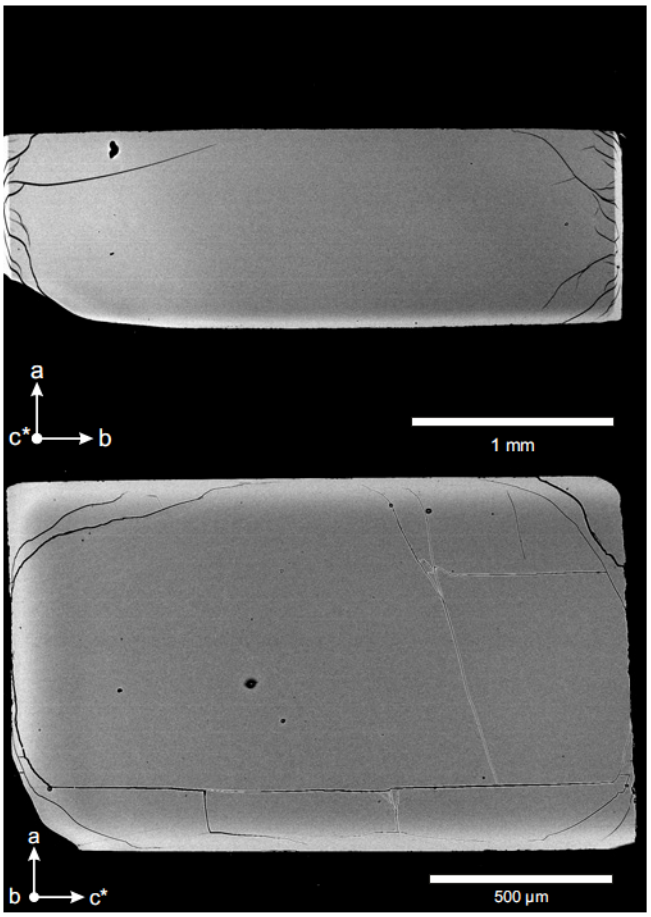

FIGURE 7.10: Shift towards more potassium-rich compositions leads to the formation of complex crack geometries. The shape of the cracks is influenced by crystallographic direction due to the anisotropy of the composition dependence of the lattice parameters of feldspar

7.3 Diffusion Fronts

Cation exchange leads to the formation of an exchanged rim all around the outer edges of the crystal, documenting that diffusion starts at the edges of the crystal and propagates inward. The exchanged rim is separated from the core of the crystal by a composition front. As cation exchange in the single crystal necessitates Na-K interdiffusion the composition fronts may be interpreted as diffusion fronts. In BSE images this exchanged rim appears darker for shifts towards more Na-rich compositions and lighter grey for shifts towards more K-rich compositions. In the latter case the diffusion fronts exhibit a pronounced anisotropy in sharpness and propagation width. Chemical profiles were measured from the edge of the crystal, across the diffusion front and into the unexchanged core area using a FEG-SEM.

TABLE 7.1: Occurrence of cracks in samples shifted towards more potassium-rich compositions listed by experimental conditions; x: cracks have been observed, -: no cracks have been observed

polished surfaces of sample plate		001			010		
composition salt melt		X_{KCl}			X_{KCl}		
temperature [°C]	duration [d]	1.00	0.85	0.60	1.00	0.85	0.60
800	32	x			x		
850	1	-	-	-	-	-	
	4	-	-	-	x		
	8	x	x	-	x	-	-
	16	x	-	-	x	-	-
	32	x	-	-	x	-	-
	64	x	-	-	x		
920	3	-			x		
	8	x			x		
	32	x	-	-	x		
					x		
950	2	x			x		
1000	2	x			x		

7.3.1 Shifts towards Na

Shifts towards more Na-rich compositions that are small enough not to cause the formation of cracks ($\Delta X_{Or} < 9$ mole-%) lead to the formation of a darker exchange rim of uniform thickness all around the crystal. The diffusion profiles measured across these fronts show a continuous increase of the sodium content from the core to the outer edge (figure 7.11). This shape of the diffusion profile is conform with what would be expected from diffusion with a constant interdiffusion coefficient in the case of constant concentration boundary conditions, which are given by the molar excess of the melt relative to the exchanged crystal. The profiles can therefore be fitted with an error function. Diffusion profiles measured in different crystallographic directions show no difference in shape, sharpness or propagation width.

7.3.2 Shifts towards K

When feldspar is reacted with potassium rich salt melt the formation of a K-rich surface layer can be observed, which is separated from the dark grey internal regions of the grain by more or less sharp composition fronts. Cation exchange in the single crystal

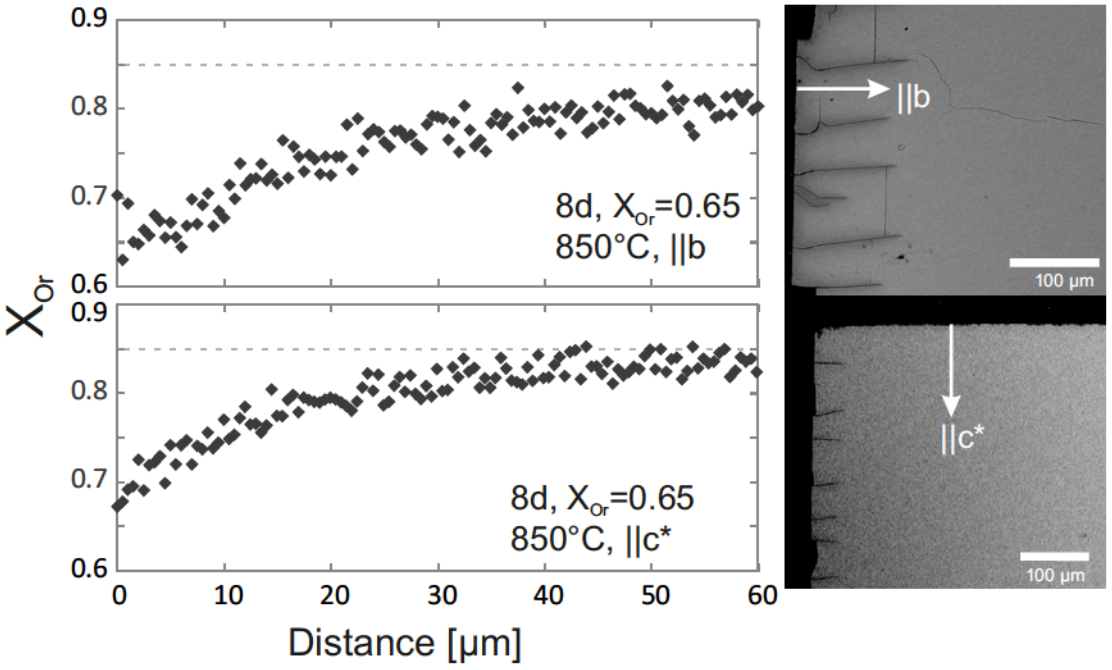

FIGURE 7.11: Chemical profiles measured across diffusion fronts in a crystal exchanged for 8 days at 850°C and shifted to a composition of X_{Or} 0.65

necessitates Na-K interdiffusion, and the composition fronts may be interpreted as diffusion fronts. The shape of the diffusion fronts, and in particular their sharpness, exhibits clear direction dependence. Wide, shallow diffusion fronts are observed in the *a*-*c*-plane of the feldspar while narrow, sharp fronts develop in the direction normal to (010).

Apart from crystallographic direction, the sharpness and shape of the diffusion front also depends on the extent of the chemical shift, i.e. the composition difference between the exchanged rim and unexchanged core. For composition shifts to X_{Or} 0.90 the exchange front is very indistinct in the BSE image, and the chemical profile shows a continuous increase of potassium-content from the core to the rim. It is thus very similar to the fronts observed for shifts towards more Na-rich compositions, and can also be fitted with an error function under the assumption that interdiffusion rates are constant in this composition range. For a shift to a composition of X_{Or} 0.95 the diffusion profile begins to show two plateaus corresponding to the exchanged rim and unexchanged core, respectively, and the diffusion front between the two plateaus exhibits an inflection point. In the BSE image a clear distinction between rim and core areas can be observed. If the composition is shifted to values of $X_{Or} > 0.95$, the diffusion front fully exhibits the characteristic shape that already began to develop for smaller shifts, with two sharply defined plateaus separated by the diffusion front with an inflection point (figure 7.12). This characteristic shape is very different from the error function which would be expected to describe the diffusion front in a crystal during experiments with constant concentration boundary

conditions if the interdiffusion coefficient was constant. This indicates that the interdiffusion coefficient in alkali feldspar is composition dependent, especially for high X_{Or}. The lack of an inflection point for profiles with smaller shifts and for shifts towards more Na-rich compositions, where the profiles can be fitted with an error function, in turn indicates a constant interdiffusion coefficient.

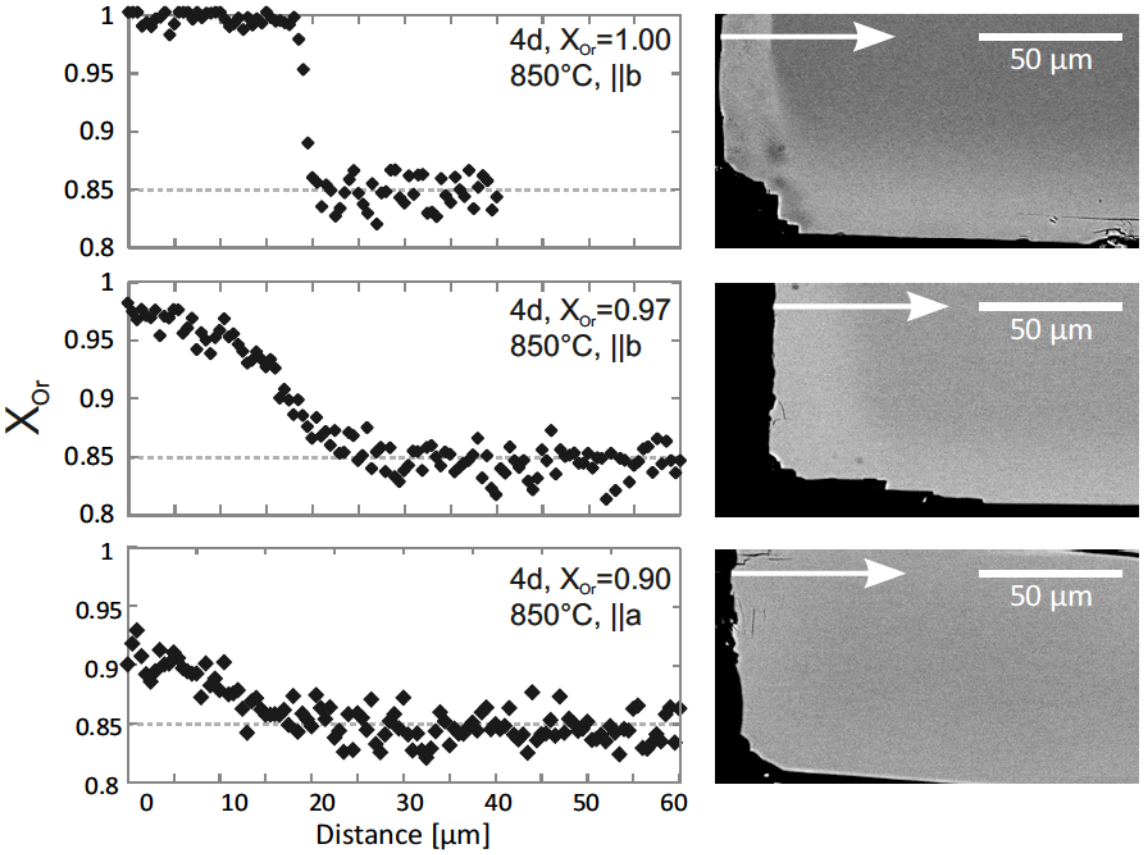

FIGURE 7.12: Chemical profiles measured with a FEG-SEM parallel b in Volkesfeld feldspar exchanged for 8 days at 850°C and shifted by 15 mole-% (top), 10 mole-% (middle) and 5 mole-% (bottom); the characteristic shape of the diffusion fronts only develops for shifts to compositions higher than X_{Or} 0.9

The sharp diffusion profiles parallel to the b-axis have a very narrow diffusion front with widths between 1 μm and 10μm, the width increasing only slightly with increasing temperature and run duration. The lower boundary of this width is only estimated because the resolution of the FEG-SEM is not sufficient to resolve the steep gradient further. Attempts to get a higher resolution and achieve a more accurate value with transmission electron microscopy (TEM) were unfortunately unsuccessful. The differences in the potassium concentration are within error of the measurements; sodium cannot be measured at all because its signal is masked by that of gallium ions embedded during preparation of the TEM-foils.

The wider diffusion profiles observed in the a-c-plane show diffusion fronts with widths between 10 μm and over 100 μm and thus are much shallower than the fronts parallel

to b (figure 7.13). Their width increases more significantly with increasing run duration, temperature, and time.

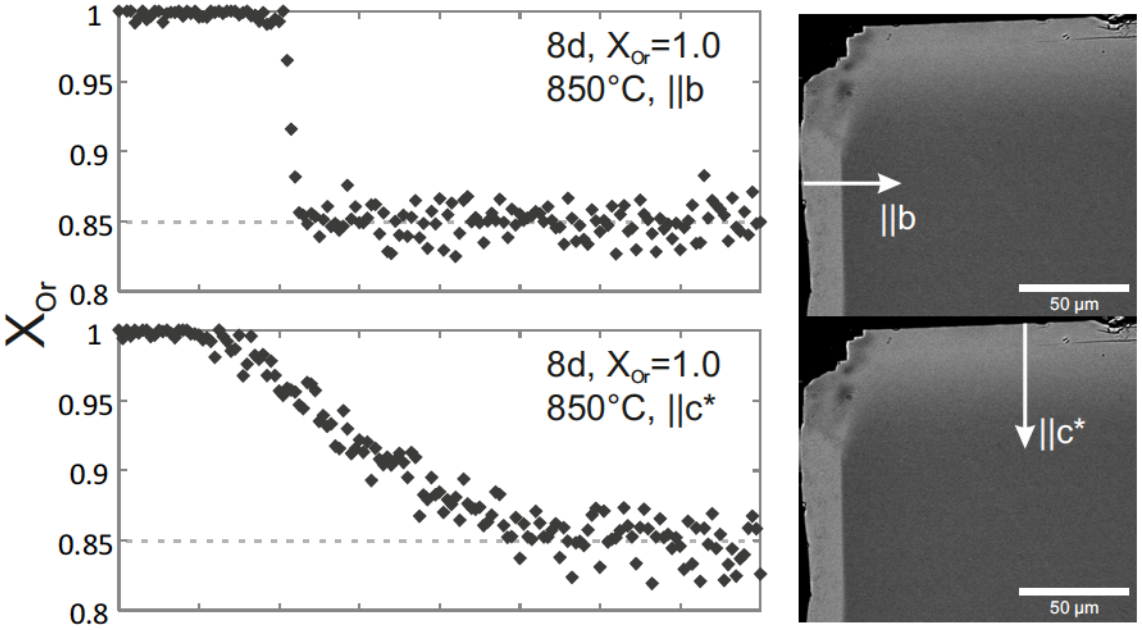

FIGURE 7.13: Chemical profiles measured with a FEG-SEM in a feldspar shifted towards more K-rich compositions parallel to b across a narrow diffusion front (top) and parallel to c^* across a wide diffusion front (bottom); in both cases the profiles show the characteristic shape with the two plateaus and an inflection point of the diffusion front, regardless of their width

Experiments using the specially prepared plates that allowed measurements of interdiffusion profiles in four additional directions showed that the shortest diffusion profiles are observed at 90° to [101] around b, i.e. $\approx [10\bar{2}]$. However, despite the overall diffusion profile being shorter the diffusion fronts themselves are relatively wide and comparable to the shallow profiles described before. Only the diffusion fronts in b-direction show extremely narrow, sharp diffusion fronts. Figure 7.14 shows a schematic block diagram summarizing the characteristics of the diffusion fronts in all crystallographic directions analysed in this study.

The distance of the inflection point from the edge of the crystal in the chemical profiles was taken as a measure of how far the diffusion front propagated into the feldspar. The linear relationship yielded when plotting these values against the square root of time indicates that development of the fronts is controlled by diffusion processes only (figure 7.15). It can be observed that for a given run duration the values for interdiffusion normal to (010) always plot somewhat lower than those for profiles measured in the (001) plane of the feldspar.

The interdiffusion coefficient for a certain composition can be extracted directly from

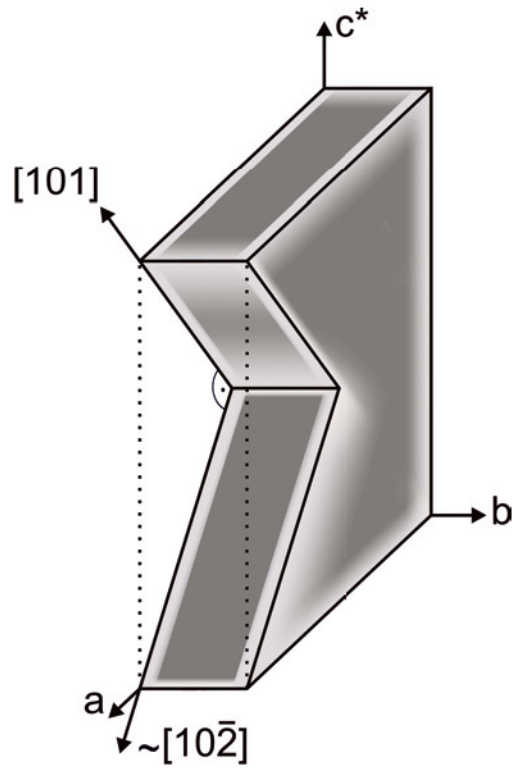

FIGURE 7.14: Schematic diagram showing the relative width and sharpness of all diffusion fronts observed in this study

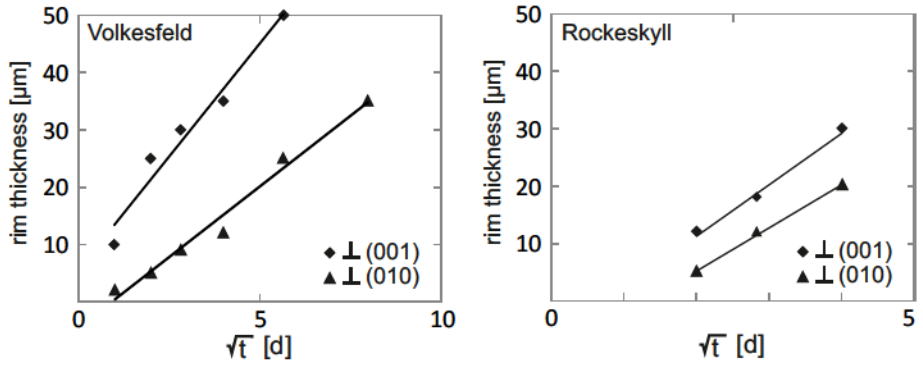

FIGURE 7.15: Plot of the rim thickness (defined by the position of the inflection point of the interdiffusion front propagating into the crystal) versus $t^{1/2}$ for Volkesfeld sanidine (left) exchanged to X_{Or} 1.0 at 850°C and Rockeskyll Sanidine (right) exchanged to X_{Or} 0.85 at 850°C

chemical profiles measured with the FEG-SEM. This requires solving the non-linear diffusion equation (equation 3.31) by applying Boltzmann's transformation and integrating the transformed diffusion equation as described in chapter 3.6. Treatment of the data is described in more detail in chapter 6.2.

The composition dependence of the interdiffusion coefficient was extracted from more than 130 diffusion profiles comprising experiments for both starting materials, directions normal to (001) and normal to (010), temperatures between 800 and 1000°C as well as run times between 1 and 64 days. Unfortunately, not all profiles yielded usable results. Chipped edges or cracks caused by preparation lead to profiles being incomplete, and in some cases the scatter in the data was too severe to allow for meaningful interpolation between data points. Some data sets had to be discarded because the experimental conditions could not be reconstructed with certainty, after samples had been mixed up during preparation. Sanidines from Rockeskyller Kopf were observed to be more susceptible to damage during cation exchange and preparation. Most samples had severely chipped edges which made measuring full profiles difficult. Thus the number of profiles measured in sanidine from Rockeskyll chosen for further analysis is small compared to the data set available for Volkesfeld sanidine.

A full list of the profiles chosen for further data treatment, which are the basis for the results shown in the following, can be found in table B.2 in appendix B.

Figure 7.16 shows the results of the extraction of the composition dependence of the interdiffusion coefficient from profiles measured normal to (001) and normal to (010) for experiments carried out at 850°C, which was the temperature most experiments were conducted at.

The sodium-potassium interdiffusion coefficient has little or no composition dependence over most of the composition ($0.65 \leq X_{Or} \leq 0.95$). At very potassium-rich compositions of $X_{Or} \geq 0.95$ it shows a substantial increase with increasing X_{Or}. The increase in D towards the potassium end-member composition of the alkali feldspar is observed in both the directions perpendicular to (010) and perpendicular to (001). The increase is, however, more abrupt and more localized in composition in the direction perpendicular to (010) than perpendicular to (001). It is also seen that for the entire composition range sodium-potassium interdiffusion is faster normal to (001) than normal to (010).

Experiments with smaller shifts generally show faster interdiffusion coefficients (see figures 7.16 and 7.17). For shifts towards more sodium-rich compositions this can partially be caused by the aforementioned influence of additional diffusion normal to developing cracks. However, the same effect can also be observed in crack-free samples which may indicate an influence of coherency strain on the diffusion pathways, meaning that with

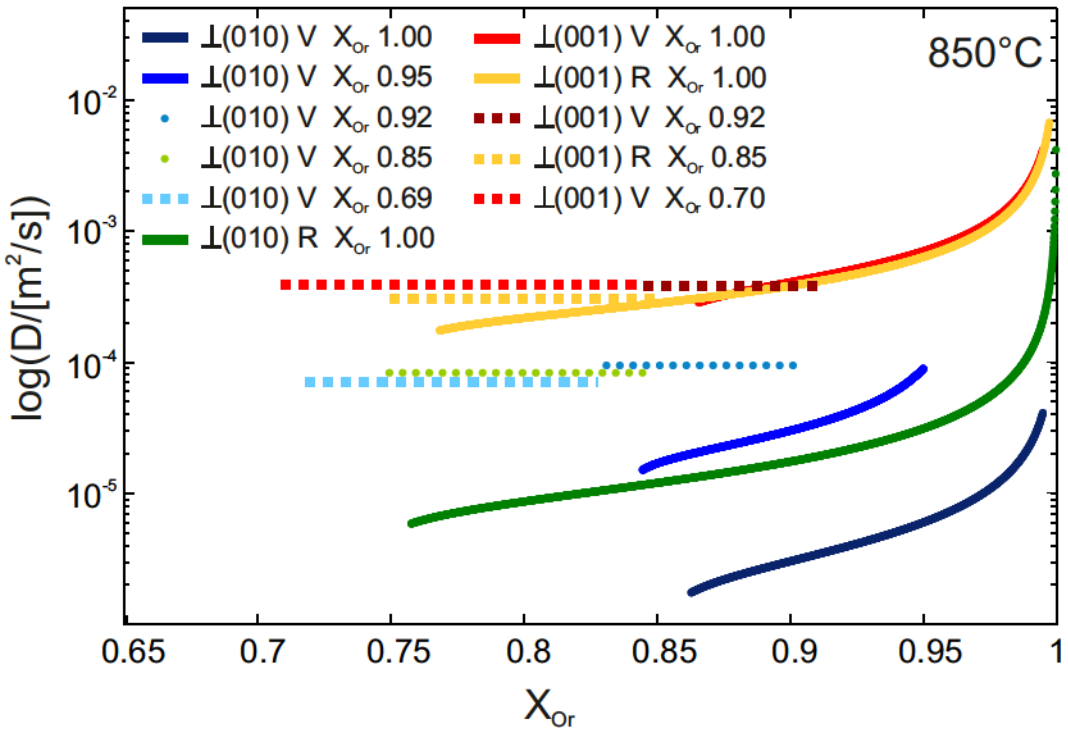

FIGURE 7.16: Results of the extraction of the interdiffusion coefficient for all experiments conducted at 850°C, including data for both starting materials (V- Volkesfeld, R- Rockeskyller Kopf) and profiles measured parallel to b and c^*; profiles corresponding to experiments with small shifts generally plot at higher values than those for larger shifts which may be an effect of coherency strain

increasing composition shift the distortion of the lattice leads to a decrease of the interdiffusion coefficient. For further considerations of the effect of coherency strain on interdiffusion see chapter 7.4. Because of this observation, experiments with smaller and larger shifts were treated separately for all further calculations.

Similar trends are observed at all temperatures considered in this study. In figure 7.17 the data is plotted separately by temperature and a comparison by crystallographic direction is given in figure 7.18. The former allows for an easier comparison of the effect of starting material and crystallographic direction, while the latter shows the effect of temperature more distinctly. In figure 7.17 all short profiles have been plotted, although it becomes obvious that in some cases the interdiffusion coefficient seems highly overestimated, which indicates that the chemical profiles were probably influenced by secondary interdiffusion normal to cracks, beyond any effect which may be caused by coherency stress. Some of these profiles were thus excluded for further considerations and have not been re-plotted in the comparison of all results in figure 7.18. No significant differences in interdiffusion rates between the two starting materials can be observed. The factor by which interdiffusion is faster normal to (001) relative to interdiffusion normal to (010) decreases with increasing temperature. Figure 7.18 shows that, as expected, the interdiffusion coefficient increases with temperature for a given composition. Also,

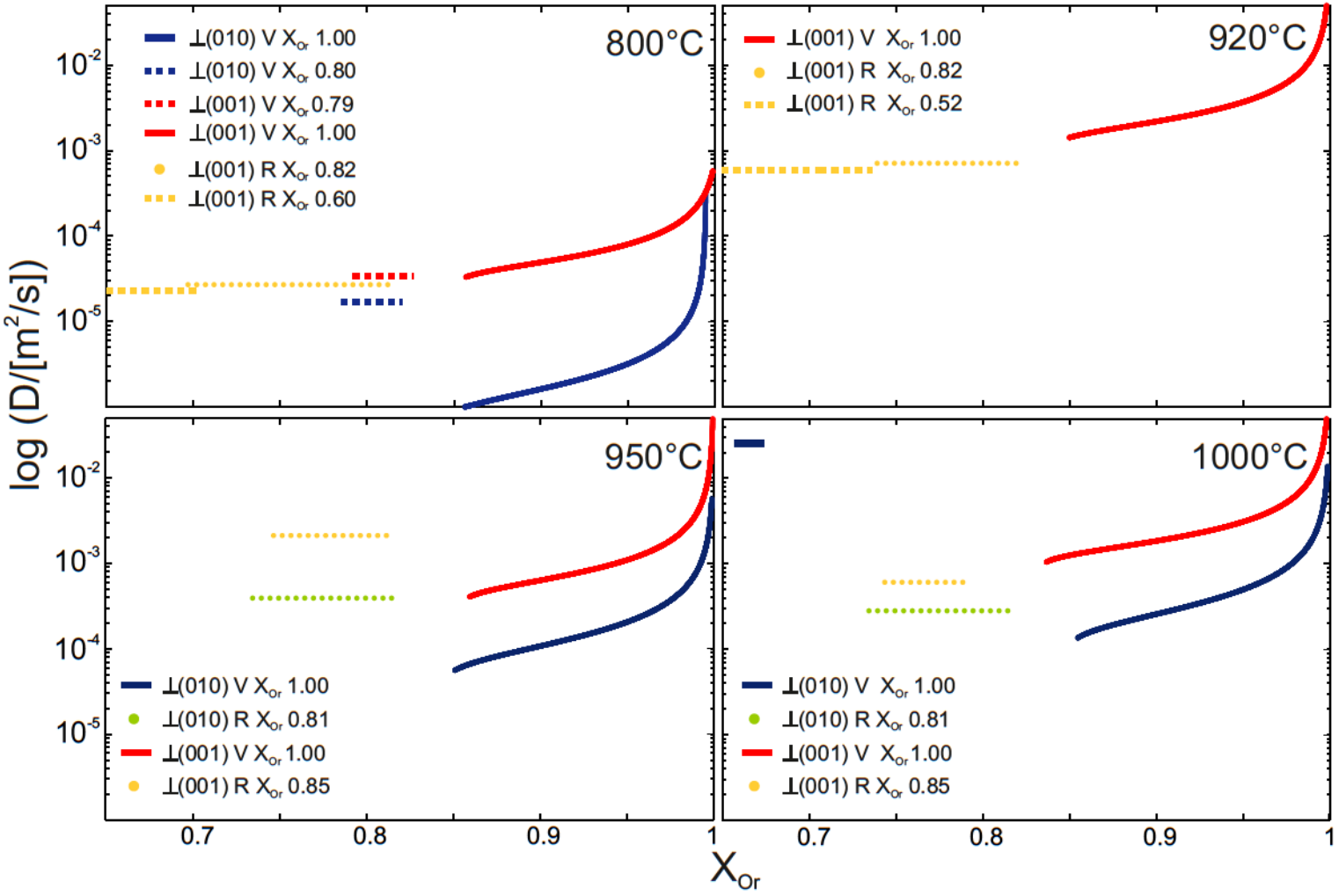

FIGURE 7.17: Results of the extraction of the interdiffusion coefficient for all experiments conducted at 800°C, 920°C, 950°C and 1000°C, including data for both starting materials (V- Volkesfeld sanidine, R- Rockeskyller Kopf sanidine) and profiles measured normal to (010) and (001); the data at 920°C are higher than would be expected, which may be an effect of the rapid changes of elastic properties often observed in Eifel feldspar in this temperature range (Bertelmann et al., 1985; Demtröder, 2011)

with increasing temperature the steep rise in interdiffusion rates observed at high X_{Or} becomes somewhat less localised, as can be seen in figure 7.17.

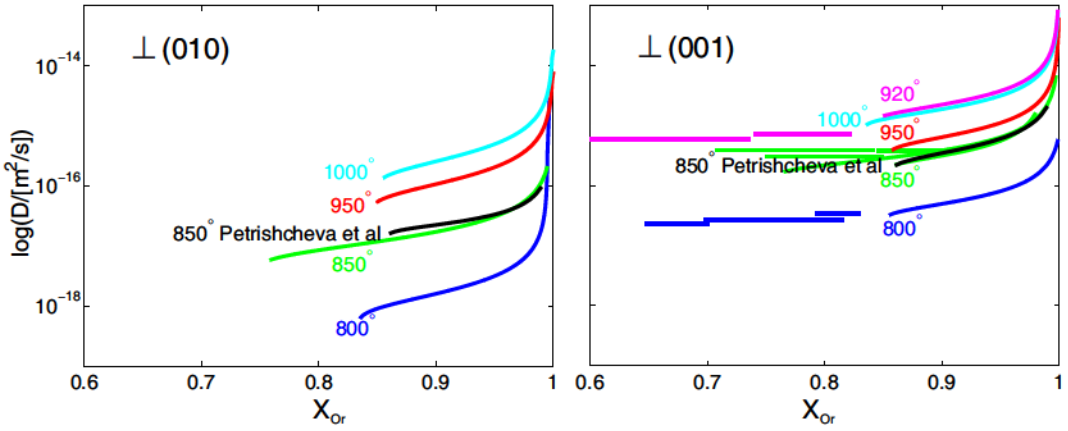

FIGURE 7.18: Comparison of composition dependence of the sodium-potassium interdiffusion coefficient at 800°C, 850°C, 920°C, 950°C, and 1000°C normal to (010) and (001)

The interdiffusion coefficient extracted from experiments at 920°C is much higher than would be expected, exceeding the values for 950°C and even 1000°C. Similar results being obtained from several, separately conducted experiments, indicates that this is not the effect of faulty measurements or preparation. The higher than expected values may be an effect of the changes of physical properties documented for Eifel sanidine in this temperature range (Bertelmann et al., 1985; Demtröder, 2011); the implications of these changes for sodium-potassium interdiffusion are not known to date. As it is stated in literature that the changes are irreversible, two plates of Volkesfeld sanidine with polished (010) surfaces were tempered at 1050°C for four days and cooled down very slowly. Subsequently they were exchanged at 850°C for 8 days and shifted to X_{Or} 1.0 and 0.73, respectively, to test if the anomalous behaviour has an influence on the overall processes of diffusion. The resulting diffusion profiles were identical to those observed in un-tempered samples. Thus, if the anomaly known for Eifel sanidines has an influence, it seems to be limited to the temperature range of the actual changes to the optical properties. Further experiments beyond the scope of this study would be needed to investigate this further. The values for D at 920°C were not considered in deriving the activation energy and pre-exponential factor.

7.4 Strain Analysis

In cases where the shifts towards more potassium-rich compositions do not induce fracturing the lattice misfit across the diffusion fronts is accommodated by elastic strain. The associated lattice distortion was investigated by EBSD combined with the cross

correlation method. Lattice strain across shallow and sharp diffusion fronts is treated separately. The sample chosen for analysis had a polished (010) surface and was exchanged with pure KCl melt for four days at 920°C. A sharp diffusion front developed inwards from the (010) surface, i.e., in *b*-direction. EBSD patterns were collected along several profiles which run from a starting point in the internal portions of the grain across the sharp diffusion front up to the polished surface. The patterns in the exchanged rim and across the diffusion front are clearly distorted relative to the reference pattern which was taken at the inner end of the profile where the original composition of the feldspar was preserved. The distortion of patterns recorded in the rim has the largest component in the *a*-direction of the crystal. Localized at the diffusion front itself a major shift parallel to the *b*-direction of the crystal is documented (figure 7.19).

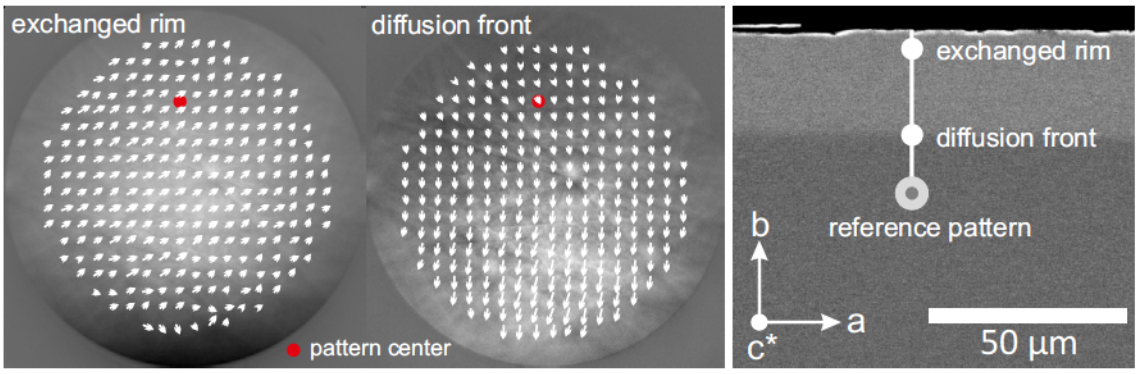

FIGURE 7.19: Exemplary EBSP with shifts relative to the reference pattern indicated by the white arrows (arrows scaled to ten); in the exchanged rim the shifts have a major component parallel to the *a*-direction of the crystal while in the diffusion itself a predominant shift parallel to the *b*-axis is observed

Using the cross correlation method the full strain tensor was determined for all points along the profile. As the tensor is symmetric only the upper half is shown in figure 7.20. The profiles show the distortion of the lattice relative to the reference pattern at the inner end of the profile. The diffusion front is located at a distance of about 20 μm from the polished (010) surface of the crystal and is about 5 μm wide. Four different profiles were measured to test for reproducibility. Except for some minor variation of ϵ_{11} the different measurements were generally in good accordance. The variations of the normal strains are most significant. The longitudinal strains along the *a*- and *b*-axes of the crystal, that is ϵ_{22} and ϵ_{11}, respectively, show the most pronounced variations. The variation of ϵ_{22} along the profile indicates a dilation of the lattice in *a*-direction within the exchanged rim relative to the reference pattern. This dilation decreases inwards from the sample surface and vanishes at the diffusion front. In contrast, ϵ_{11}, i.e. the strain in *b*-direction, is close to zero in both the rim and unexchanged core but indicates a localized dilation in *b*-direction at the diffusion front. Within error the values stay constant for ϵ_{33} all along the measured profile, indicating that no significant longitudinal strain occurred

in c^*-direction. ϵ_{12} shows the same trend as ϵ_{22} with a slight rise in the exchanged rim which then declines within the diffusion front. ϵ_{23} shows the opposite trend with values being slightly lower in the rim relative to the reference pattern before rising in the diffusion front. Neither profile shows any specific trend within the diffusion front itself. Within error the values stay constant for ϵ_{13} all across the profile.

Two profiles were measured normal to the (001) surface of the same sample (figure 7.21). Again only the upper half of the tensor is shown because of its symmetry. The diffusion fronts in the direction perpendicular to (001) are much wider than those evolving in the direction perpendicular to the (010) surface. The exchanged rim is approximately 20 μm wide and the diffusion front has a width of about 50 μm. In this case, the longitudinal strain in a-direction (ϵ_{11}) is characterized by a gradually increasing dilation from the internal regions of the grain across the diffusion front and towards the exchanged rim. For the b-direction we see the opposite trend with a gradual, slight compression across the diffusion front. ϵ_{33} again stays roughly constant across the entire profile indicating that no significant longitudinal strain occurred in c^*-direction.

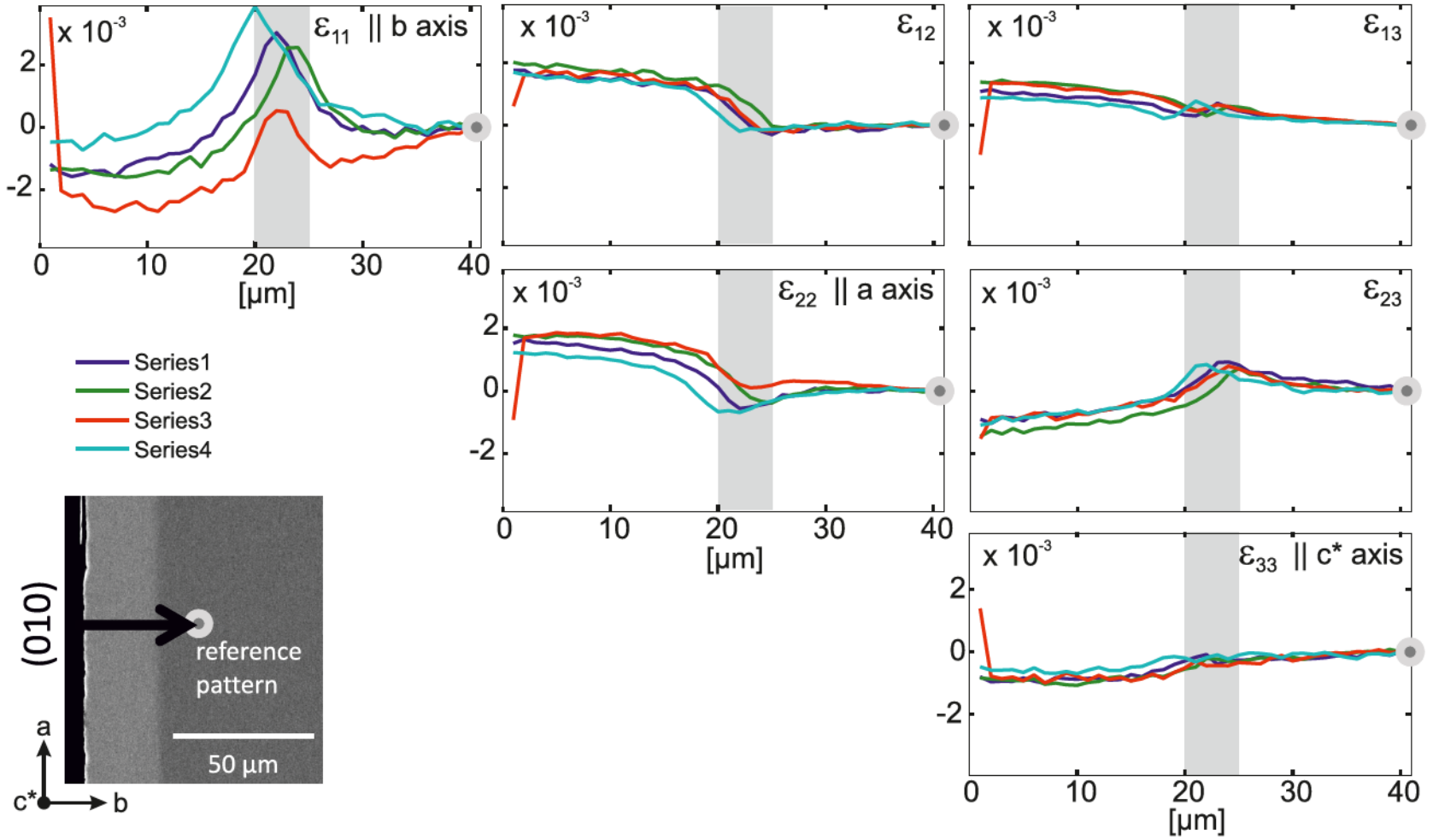

FIGURE 7.20: Upper half of the symmetric strain tensor for profiles measured across a sharp diffusion front; the differently coloured profiles represent different measurements executed to test reproducibility, the reference pattern is located at the right hand side as represented by the grey dot, the edge of the crystal is on the left hand side; the most notable features are the strain concentration parallel to b within the diffusion front and the extension parallel to a within the exchanged rim

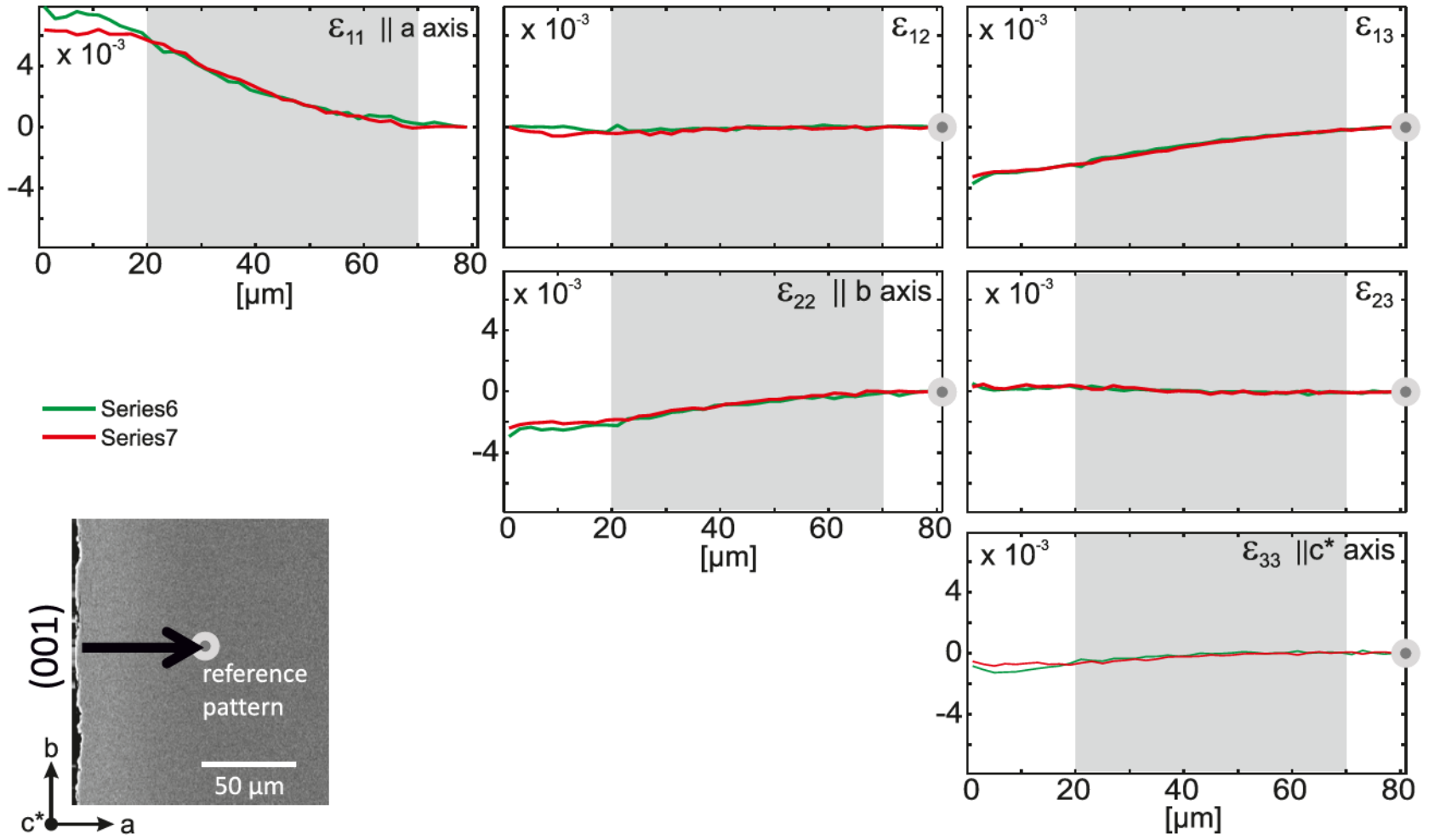

FIGURE 7.21: Upper half of the symmetric strain tensor for profiles measured across a wide diffusion front; the differently coloured profiles represent different measurements executed to test reproducibility, the reference pattern is located at the right hand side as represented by the grey dot, the edge of the crystal is on the left hand side; in contrast to what was observed for narrow diffusion profiles there is no strain concentration within the diffusion front, a gradually increasing dilation in a-direction is the most significant change observed

Chapter 8

Discussion

8.1 Chemically Induced Fracturing

Cation exchange between sanidine and Na^+ and K^+ bearing melts leads to the formation of surface layers chemically altered by diffusion. The transition between the exchanged surface layer and unexchanged core of the crystal can be interpreted as a diffusion front, which propagates inwards by Na-K-interdiffusion on the alkali sublattice. The exchanged rim differs chemically from the unexchanged core area in its K/Na-ratio while the Al,Si-network remains unaffected. The lattice parameters in feldspar show strong composition dependence. With increasing X_{Or} all lattice parameters undergo an extension. The a-parameter changes most significantly in the composition range $0.65 \leq X_{Or} \leq 1$ relevant for the experiments in this study; this equals a change by about 5% while b changes by only 0.5% and c by 0.2%. Thus the strain resulting from the changes in composition during cation exchange is extremely anisotropic. In consequence, fracturing can be observed for shifts towards more Na-rich as well as K-rich compositions.

Experiments using crushed feldspar shifted systematically to determine the critical shift for fracturing showed, that the first cracks appear when the shift exceeds 9 mole-%. From BSE images of the samples it is apparent that the first cracks nucleate at irregularities of the surface. The very regular crack spacing that develops for experiments with more severe shifts indicates however, that coherency stress and fracture mechanics rather than irregularly distributed defects in the crystal structure control the formation and propagation of the cracks. Propagation of cracks under stress is described by the field of fracture mechanics.

Generally three different types of crack opening are distinguished, depending on the movement of the crack planes (Blumenauer and Pusch, 1993):

- mode I: crack opening perpendicular to the crack surface, reflecting tensile stress in the sample
- mode II: crack surfaces move parallel against each other and normal to the direction of crack propagation, reflecting shear stress in the sample
- mode III: crack surfaces move parallel against each other and transversely to the direction of crack propagation, reflecting torsion stress in the sample.

Cracks emanating from the (001) surface are exactly perpendicular to the direction of the maximum tensile stress on this surface and as such can be treated as pure mode I cracks. For cracks emanating from the (010) surface the crack normal and the direction of maximum tensile stress enclose an angle of about 18° which results in a shear stress component parallel to the line of the crack tip. This corresponds to mode I cracks with a minor component of mode III. This deviation seems to conflict with the most natural assumption that the cracks should open normal to the direction of the maximum tensile stress. However, only the thin misfitting surface layer was taken into account for the analysis of fracture mechanics so far. As the cracks provide a faster diffusion pathway for the cations, additional interdiffusion takes place normal to the cracks, adding to the complexity of the strain field in the crystal and making the analysis a lot more complex. Further the geometry of the sample might have an influence on the cracks as well, especially at the edges of the plates where cracks emanating from different surfaces meet up. Experiments trying to eliminate this effect by shielding the edges of the plate with a coating have not been conducted successfully, as the high temperatures and salt melt destroyed the coating too fast.

From consideration of the geometry and the relation between the characteristic crack spacing and the induced stress it was possible to determine the critical stress intensity factor of the feldspar. The extracted stress intensity factor was 2.3 MPa $m^{1/2}$/ 73 MPa $mm^{1/2}$ to 2.72 MPa $m^{1/2}$/ 85 MPa $mm^{1/2}$. For the full treatment of the stress analysis the reader is referred to Scheidl et al. (2013) (appendix C).

According to fracture mechanics a zone of elastic strain should develop at the tip of a mode I crack (Griffith, 1921). This stored elastic energy is released when the crack propagates. If such a concentration of elastic energy was present at the crack tips in the samples shifted towards more sodium-rich compositions, it should be visible as a slight misorientation in an EBSD map. Neither of the two EBSD maps over crack tips in a sample exchanged for 2 days at 920°C and shifted to a composition of X_{Or} 0.6 shows this expected effect (figure 7.9). A possible explanation is that the step width necessitated by the low stability of feldspar under the electron beam is too large to record the zone, or that the elastic strain is so minor that it cannot be picked up with the method used.

However, the maps do show a zone of slight misorientation of up to 1° around the crack which widens towards its base. The shape of this zone is reminiscent of the bell-shaped alteration halo documented in the element maps (figure 7.1) and might thus be related to the lattice distortion caused by the substitution of the larger potassium cation with the smaller sodium cation. The more sharply bounded zone to one side of the crystal is probably a preparation effect caused by the crack emanating from a (010) surface and thus most likely not being entirely vertical.

The geometry of the cracks developing for shifts towards more potassium-rich compositions cannot be interpreted analogously to those developing for shifts towards more sodium-rich compositions. The crack patterns are not regular, although they show the influence of the anisotropy in the composition dependence of the lattice parameters of feldspar. The more severe dilatation of the a-parameter leads to shear stresses being much larger parallel to the a-axis compared to the other directions. Cracks accordingly tend to be longer parallel to the a-axis and shorter normal to it. Further the shear stress varies along the length of the crystal, being smallest in the centre and becoming more pronounced towards the edges, contributing to the curved shape of the cracks (figure 8.1).

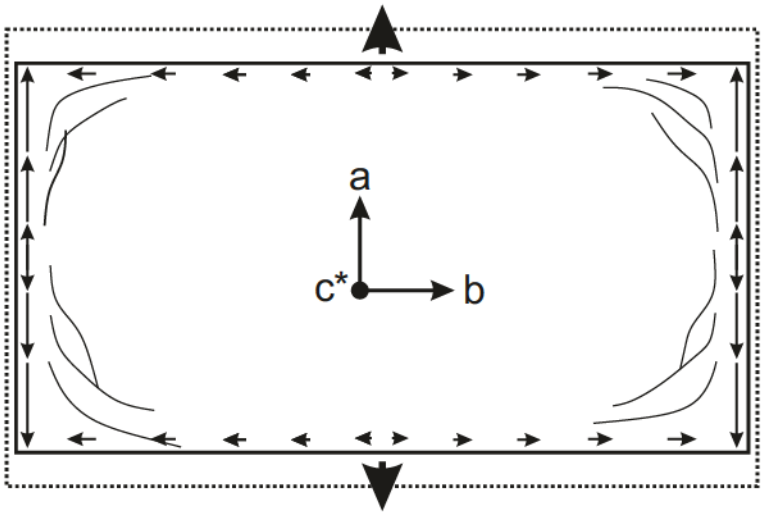

FIGURE 8.1: Due to the anisotropy of the composition dependence of the lattice parameters the crystal lattice only stretches significantly along the a-axis during cation exchange, leading to coherency stress; the stress is largest at the edges of the crystal. Nearly no extension takes place in the other directions, as a consequence cracks open normal to (001). The dashed lines exaggeratedly represent the way the crystal lattice deforms with a composition shift towards more K-rich compositions

8.2 Coherency Strain Across Diffusion Fronts

EBSD combined with the cross correlation method is a powerful tool for quantifying coherency strain in the range of 10^{-4} (Maurice et al., 2012; Britton and Wilkinson, 2012), provided the misorientation between test and reference pattern is limited to about 1°. A systematic error analysis of the cross correlation method has shown no significant difference in accuracy between normal and shear components (Tom Jäpel, personal communication).

For the measurements in this study the strain components in y-direction (ϵ_{11}, and ϵ_{12}, ϵ_{31}) will most probably show a reduced accuracy, because the patterns have been acquired by integration of an area extending 50 μm in y-direction (see section 6.1.4). This corresponds to a horizontal blur of about 1 pixel in the patterns. However, as the patterns are changing only in x-direction of the sample this horizontal blur stays constant for all measurements and should therefore not strongly reduce accuracy.

In the investigated feldspars lattice strain is localized across a sharp diffusion front forming in [010]-direction (figure 7.20). While the composition of the feldspar changes in a strictly monotonic manner with an outwards increase of X_{Or} from 0.85 to 1.00 across the diffusion front, the observed lattice strain across the sharp composition front is characterized by a substantial dilation of the b-parameter that is localized within the about 5 μm wide domain of the diffusion front. At the same time the a-parameter shows a slight and monotonic contraction and the c-parameter remains unchanged. This systematic change of lattice strain does not confer to the change of lattice strain which would occur in a stress free crystal of alkali feldspar subject to a similar composition change. When alkali feldspar with an initial composition of X_{Or} 0.85 is shifted to the pure potassium end-member composition, X_{Or} 1.00, this implies an expansion in all crystallographic directions; $a_0 = 8.545$ Å$\rightarrow$ $a_1 = 8.6$ Å, $b_0 = 13.025$ Å$\rightarrow$ $b_1 = 13.03$ Å, $c_0 = 7.175$ Å$\rightarrow$ $c_1 = 7.18$ Å, and a minute change in the angle β, $\beta_0 = 116.0° \rightarrow \beta_1 = 116.05°$ (Kroll et al., 1986). Within the plane of the diffusion front, that is within the contact plane between the compositionally distinct domains of the crystal, the lattice parameters are confined to those of the volumetrically by far dominant internal portion of the crystal in which the original composition is retained. As a consequence the volume change across the diffusion front is accommodated by change of the only unconstrained lattice direction, i.e. the b-direction in the case at hand, perpendicular to the constrained interface. Only a few micrometres towards the edge of the feldspar, outside the diffusion front, the mechanical coupling to the rigid substratum becomes less strong, and the crystal can expand in a-direction. As soon as the composition strain is accommodated by dilation in a-direction, the b-parameter shrinks again, leading to a strain similar to what is expected in a stress free crystal of alkali feldspar (figure 8.2, left).

The systematics of the strain along the profile taken across a shallow diffusion front formed perpendicular to (001) confers to what is expected for the composition induced eigenstrain in stress free feldspar. The a-parameter increases successively towards the outer portions of the crystal as here the free surface is perpendicular to [100] and thus the a-direction of the crystal lattice is not confined by the stronger substratum (figure 8.2, right).

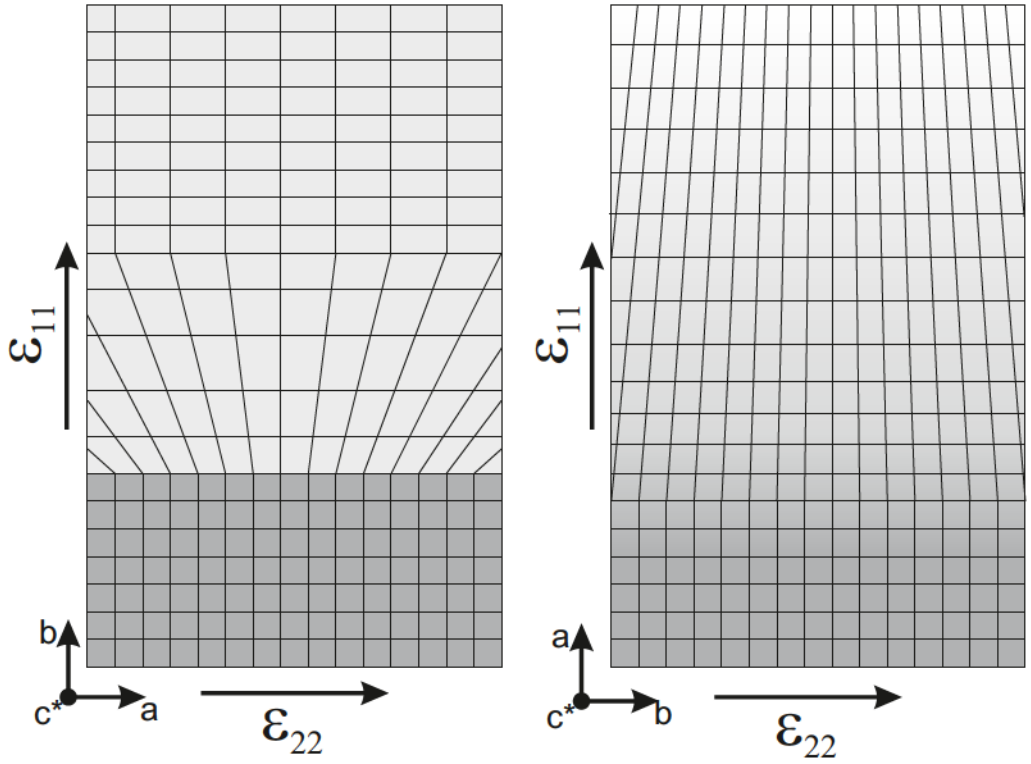

FIGURE 8.2: Schematic diagrams of the lattice distortion across the sharp (left) and shallow (right) diffusion fronts normal to (010) and (001), respectively; dark grey represents part of the unexchanged core, light grey represents part of the exchanged rim. For the sharp diffusion front the lattice dilates in b-direction as (010) is the only free surface while the a- and c-parameters are dominated by the unexchanged substratum; in the rim the dilatation in a, which would be expected in a stress free feldspar, takes over. The gradual dilation in a-direction observed for the shallow diffusion front in turn is in accordance with composition strain in an unstressed feldspar

The distortion of the lattice across the sharp diffusion front in [010]-direction may have an influence on the diffusion pathways in the feldspar structure. The main diffusion pathways are in the a-c-plane. The alkali cations occupy large cavities within the Al,Si-tetrahedral framework. The most likely interstitial sites for the large cations are $(0, 0, \frac{1}{2})$ and equivalent sites (Petrović, 1972). For unit jumps parallel to the a-direction the space between the atoms constituting the framework is large enough to allow alkali cations to jump to interstitial sites without the need for severe distortion of the lattice (Christoffersen, 1982). Parallel to the b-axis the cation sites are separated by the crankshaft-like chains formed by the Al,Si-tetrahedra (Ribbe, 1983) and atomic jumps in this direction

are much more difficult. The dilation in *b*-direction that is localized at the diffusion front corresponds to an increase in the length of the atomic jumps that the alkali cations contributing to diffusion in [010]-direction have to execute. It is conceivable that an increase in the jump distance between two neighbouring sites that are aligned in [010]-direction in the alkali sublattice goes along with an increase of the energy barrier between them. This would correspond to an increase in the activation energy for diffusion and would thus entail a reduction of the corresponding diffusion coefficient. Similar to the lattice distortion this effect would be localized at the diffusion front and contribute to further sharpening of an emerging diffusion front. This feedback of diffusion and induced lattice strain on the diffusion process itself maybe one of the reasons for the formation of the exceptionally sharp diffusion fronts normal to (010) for shifts towards more potassium-rich compositions. In the case at hand, the self-sharpening diffusion front acts as a diffusion barrier.

8.3 Interdiffusion as a Function of Composition

Cation exchange in the single crystal necessitates Na-K interdiffusion. The linear relation between the rim thickness and the square root of time further indicates that the exchange of K^+ and Na^+-cations between the salt melt and the feldspar occurs by a diffusion process only. Other studies, e.g. Norberg et al. (2011), explain the replacement of the more potassium-rich feldspar with a more sodium-rich phase as being caused by dissolution-reprecipitation. However, several differences between the products of this mechanism in comparison to the run products of the experiments in this study can be observed. Dissolution-reprecipitation leads to the formation of zones differing in their chemical composition in regard to minor and trace elements. The diffusion fronts in this study, however, are continuous and extend over ranges of tens of μm. The distribution of Ba is uninfluenced by the propagation of the diffusion fronts which has been tested both with microprobe analyses and element mappings (see figure 7.1). Further, the Al-Si-order remains constant and the lattice coherent over the diffusion front (Neusser et al., 2012) which further indicates that no reprecipitation took place.Thus the data obtained from the experiments in this study can be used to extract the interdiffusion coefficient.

The interdiffusion coefficient at 850°C was obtained for six different directions. The bulk of the experiments was carried out using plates with polished (010) and (001) plates, allowing measurements of chemical profiles parallel to a, b and c^*. Additional experiments with specially prepared plates gave data in ($\sqrt{2}/2$, $\sqrt{2}/2$, 0), ($\sqrt{2}/2$, 0, $\sqrt{2}/2$) and (0, $\sqrt{2}/2$, $\sqrt{2}/2$). While Christoffersen et al. (1983) provided data in several

crystallographic directions, the data set presented here was the first allowing the full determination of the diffusivity tensor in the composition interval $0.85 \leq X_{Or} \leq 0.97$. This full diffusivity tensor makes it possible to calculate an interdiffusion coefficient in any direction for Volkesfeld sanidine at 850°C. Future experiments are planned to also determine the diffusivity tensor at other temperatures.

Interdiffusion normal to (010), i.e. parallel to the *b*-axis, was found to be slower by a factor of 5 to 10 in both starting materials than interdiffusion parallel to c^*, the ratio by trend becoming smaller for higher temperatures. This fits the observations by Christoffersen et al. (1983) who reported interdiffusion normal to (010) to be slower than normal to (001) by a factor of ten at 1000°C. Petrović (1972) also documented the rates normal to (010) to be slower by up to two orders of magnitude than in the *a*-*c*-plane in the temperature interval between 850°C and 1000°C.

The fastest interdiffusion coefficients are found parallel to the [101]-direction of the feldspar while interdiffusion is slowest in the direction rotated 90° to this around the *b*-axis, which roughly equals the $[10\bar{2}]$-direction. This can be explained by looking at the feldspar structure. The long axis of the widest channel-like structures within the framework coincides with the fastest direction of interdiffusion, while the structure shows almost no channels perpendicular to it (see figures 2.9 and 2.10). This is a very interesting result because interdiffusion has mostly been assumed isotropic within the *a*-*c*-plane in older studies (Foland, 1974; Kasper, 1975). Details on the determination of the full diffusivity tensor can be found in Petrishcheva et al. (2014) (found in appendix E).

Further it is interesting to observe that although the slowest interdiffusion rates are found roughly parallel to $[10\bar{2}]$, and thus the shortest diffusion profiles are observed in this direction, only the diffusion fronts in *b*-direction show extremely narrow, sharp diffusion fronts. This is probably due to the fact that they develop in the direction normal to the *a*-*c*-plane, which is the only direction subject to the full effect of the severe changes in *a*-parameter with changes in feldspar composition. This further indicates that coherency strain plays a role in the development of these sharp diffusion fronts and has a noticeable influence on interdiffusion (compare chapter 8.2).

8.4 Comparison to Literature and a Theoretical Interdiffusion Model

Diffusion in alkali feldspar has been the subject of numerous studies. Most of these, however, focussed on tracer-diffusion of cations and only very few authors dealt with interdiffusion. These are diffusion couple, exchange and homogenisation experiments.

The latter, while providing valuable insights to overall rates and the influence of defects on diffusion rates, are limited by their experimental setup and starting materials in respect to observations of a composition dependence of the interdiffusion coefficient or a possible anisotropy, which were the main points of interest for this study. This leaves two studies by Petrović (1972) and Christoffersen et al. (1983), which yielded results comparable to the data at hand.

Both these authors observed a composition dependence of the interdiffusion coefficient D. Using albite with X_{Or} 0.00 and orthoclase with X_{Or} 0.86 in cation exchange experiments Petrović (1972) observed that D is independent of composition in the composition range $0.00 \leq X_{Or} \leq 0.1$ whereas a pronounced composition dependence was observed for potassium-rich compositions with $X_{Or} \geq 0.86$.

Christoffersen et al. (1983) conducted a study using a classical diffusion couple, where albite and adularia single crystals were brought into contact at a polished surface. The sigmoidal mole-fraction profiles developing during annealing were analysed using the Boltzmann-Matano analysis. The choice of starting materials allowed them to determine the composition dependent interdiffusion coefficient in the composition range $0.10 \leq X_{Or} \leq 0.80$. They found a minimum of the interdiffusion coefficient at approximately X_{Or} 0.4 and an increase by a factor of about 2.5 towards more sodium-rich compositions and an increase by a factor of about 10 towards X_{Or} 0.8 (figure 8.3).

In this study the interdiffusion coefficient was determined in the composition range $0.65 \leq X_{Or} \leq 0.99$ which is of particular interest as the composition dependence of the interdiffusion coefficient changes most severely in this composition interval. The analysis of the 1000°C experiments extends the earlier determinations by Christoffersen et al. (1983) to higher X_{Or} without any apparent jump for both the direction perpendicular to (010) and the direction perpendicular to (001) (figure 8.3). As the 850°C experiments extend over a wider composition range, this data was re-calculated to 1000°C using the activation energies determined from our experiments (dashed curves in figure 8.3). The recalculated values plot somewhat higher than the data measured at 1000°C, however, the deviation is within error. In the overlapping composition range $0.7 \leq X_{Or} \leq 0.8$, where the data of this study indicate only minor composition dependence of the interdiffusion coefficient, they deviate from those of Christoffersen et al. (1983), who observed a more pronounced composition dependence.

The strong composition dependence in the composition range $0.8 \leq X_{Or} \leq 0.99$ not covered by the data of Christoffersen et al. (1983) is predicted by theoretical calculations of the interdiffusion coefficient from self-diffusion coefficients. There are two models for the relation of the self- and interdiffusion coefficients. For neutral atomic interdiffusion, as often found in metals, the Darken equation (Darken, 1948) (equation 3.11) is used,

while in ionic crystals the Nernst-Planck relation (equation 3.22) is to be preferred (see chapter 3).

Numerous studies on tracer-diffusion in alkali feldspar were conducted which give a wide range of values for tracer-diffusion coefficients, pre-exponential factors and activation energies (see chapter 4 and table B.1). They were mostly determined for feldspar with either almost pure albite- or pure orthoclase-composition, as well as at X_{Or} 0.86 as these are the naturally available compositions suited for experimental treatment. To calculate the interdiffusion coefficient however, it is necessary to know the composition dependence of the tracer-diffusion coefficients. To this end, pairs of tracer-diffusion coefficients determined in starting materials of opposing ends of the composition spectrum have to be combined, and the composition dependence determined as a linear extrapolation between the given experimentally determined data. Apart from the fact that the linear extrapolation might induce a certain error, the available literature values were determined with a range of different techniques. Kasper (1975) modelled the experiments conducted in the scope of his PhD thesis after those by Foland (1974). Thus the combination of the results of these two studies constitutes the most consistent data set for tracer-diffusion coefficients available in literature to date, and was chosen for the calculation of the theoretical interdiffusion rates.

Figure 8.3 shows the theoretical calculations based on the Nernst-Planck relation (equation 3.22) in comparison with the directly determined values of the sodium-potassium interdiffusion coefficient from this study and from Christoffersen et al. (1983). There is reasonable qualitative agreement between our direct determinations of $D(c)$ for diffusion in the directions perpendicular to (001) and perpendicular to (010), and the theoretical calculations. The direct determinations, however, indicate slower sodium-potassium interdiffusion by a factor of about five to ten than calculated theoretically for diffusion perpendicular to (001) and slower by almost two orders of magnitude for diffusion in the direction perpendicular to (010).

This discrepancy in absolute numbers can probably be explained by tracer-diffusion data found in the literature having mostly been determined by bulk exchange methods. Crushed material was exchanged with hydrothermal solutions containing tracer isotopes and tracer-diffusion coefficients were determined assuming either spherical or cylindrical geometry of the single grains, systematically overestimating the actual diffusion coefficients. Further the fastest diffusion, which is in [101]-direction, would dominate this kind of experiment so that slower interdiffusion rates in other crystallographic directions would not be comparable to the theoretical values calculated based on these tracer-diffusion coefficients. Wilangowski (2013) recently conducted a study on the anisotropy

of sodium tracer-diffusion in Volkesfeld sanidine. They found a pronounced direction-dependence of tracer-diffusion at $T < 800°C$; at higher temperatures the anisotropy is only subtle. Experiments to determine the composition dependence of sodium tracer-diffusion in the composition range $0.85 \leq X_{Or} \leq 1$ are planned. Further studies to determine the anisotropy of the tracer-diffusion of potassium would be of interest.

As already noted in the comparison to the results by Christoffersen et al. (1983) there is a deviation of the directly determined data of this study from the trends obtained from the direct determinations of Christoffersen et al. (1983) and also from what is predicted by the theoretical interdiffusion model using the tracer-diffusion coefficients from Kasper (1975) and Foland (1974). In the composition range $0.65 \leq X_{Or} \leq 0.80$, both the older study and the theoretical calculation predict a significant increase in interdiffusion rates whereas the new data shows minute to no composition dependence of D. An interdiffusion coefficient independent of composition would be predicted from equation 3.22, if $D^*_{Na} \approx D^*_K \approx$ const. Such a situation, would, however, not predict the pronounced increase of D in the composition range of $0.95 \leq X_{Or} \leq 1.00$.

These differences between the theoretical calculations and the direct determinations can most likely be explained by two different sodium species contributing to sodium-potassium interdiffusion in alkali feldspar. Its small size allows Na^+ ions to occupy interstitial positions (Petrović, 1972; Christoffersen et al., 1983; Giletti and Shanahan, 1997). On one hand, the interstitial Na^+ could make a fast-diffusing Na-species by an interstitialcy mechanism (Petrović, 1972; Christoffersen et al., 1983; Giletti and Shanahan, 1997). On the other hand, such interstitial Na^+ could charge-balance vacancies on the regular alkali lattice sites, and by this mechanism lead to formation of vacancies on the alkali sublattice which would enhance sodium-potassium interdiffusion by the vacancy mechanism. The total concentrations of such interstitial Na^+ is probably very low, irrespective of the composition of the alkali feldspar. Towards high X_{Or}, however, when the total sodium-concentration in the feldspar becomes low, the interstitial Na^+ may form a substantial fraction of the total sodium contained in the feldspar. By this mechanism the self-diffusion of sodium would increase considerably towards high potassium mole fractions in the alkali feldspar, resulting in the observed considerable rise of the sodium-potassium interdiffusion coefficient. This would also explain the stronger compositional localisation of the steep increase as compared to the theoretical calculations, as these fast moving sodium species would only constitute a volumetrically significant fraction of the total sodium when the overall concentration of sodium is very low.

The stronger localisation may also partially be due to coherency strain across the diffusion front. As a consequence of the strong composition dependence and anisotropy of the lattice parameters in alkali feldspars every shift in composition causes a distortion

of the lattice and thus coherency stress. This coherency stress is localised within the diffusion front to varying degrees, which, especially in the case of the very narrow fronts normal to (010), may have an effect on the diffusion pathways (compare chapter 8.2).

Coherency stress may also explain the discrepancies between the results gained from experiments with larger and smaller shifts (compare chapter 7.3.2). For experiments with smaller shifts the lattice parameters do not change as significantly, leading to a less significant distortion of the lattice. For experiments with considerable change in composition the lattice distortion appears to influence the pathways and hinder the movement of the cations, leading to lower interdiffusion coefficients.

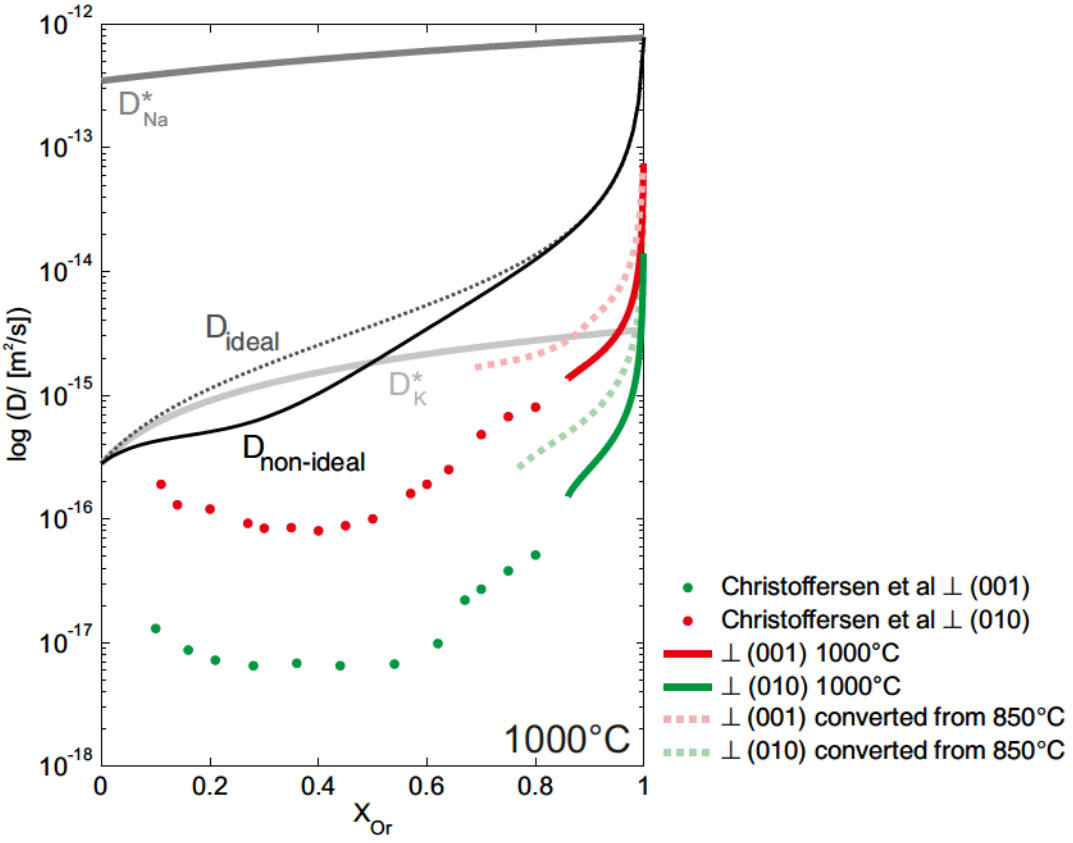

FIGURE 8.3: Comparison of the experimental results with a theoretical interdiffusion model based on the Nernst-Planck equation, and with literature data by Christoffersen et al. (1983); the theoretical values were calculated using tracer-diffusion coefficients for sodium and potassium determined by Foland (1974) and Kasper (1975)

8.5 Arrhenius Relation

The temperature dependence of the sodium-potassium interdiffusion coefficient is described by the Arrhenius relation (equation 3.49). Due to the composition dependence of the interdiffusion coefficient, the pre-exponential factor D_0 is not constant but a function of composition as well. Based on data for experiments at 800°C, 850°C, 950°C and

1000°C, the activation energy and pre-exponential factor were determined at different compositions as

$$D_0^{\perp(001)}(0.92) = 4.63 \cdot 10^{-8}\mathrm{m}^2/\mathrm{s}, \quad \mathrm{E}_\mathrm{A}^{\perp(001)}(0.92) = 179\ \mathrm{kJ/mole}$$
$$D_0^{\perp(001)}(0.98) = 1.66 \cdot 10^{-7}\mathrm{m}^2/\mathrm{s}, \quad \mathrm{E}_\mathrm{A}^{\perp(001)}(0.98) = 181\ \mathrm{kJ/mole}$$
$$D_0^{\perp(010)}(0.92) = 1.97 \cdot 10^{-4}\mathrm{m}^2/\mathrm{s}, \quad \mathrm{E}_\mathrm{A}^{\perp(010)}(0.92) = 286\ \mathrm{kJ/mole}$$
$$D_0^{\perp(010)}(0.98) = 3.27 \cdot 10^{-4}\mathrm{m}^2/\mathrm{s}, \quad \mathrm{E}_\mathrm{A}^{\perp(010)}(0.98) = 277\ \mathrm{kJ/mole}$$

.

The corresponding Arrhenius diagram is shown in figure 8.4.

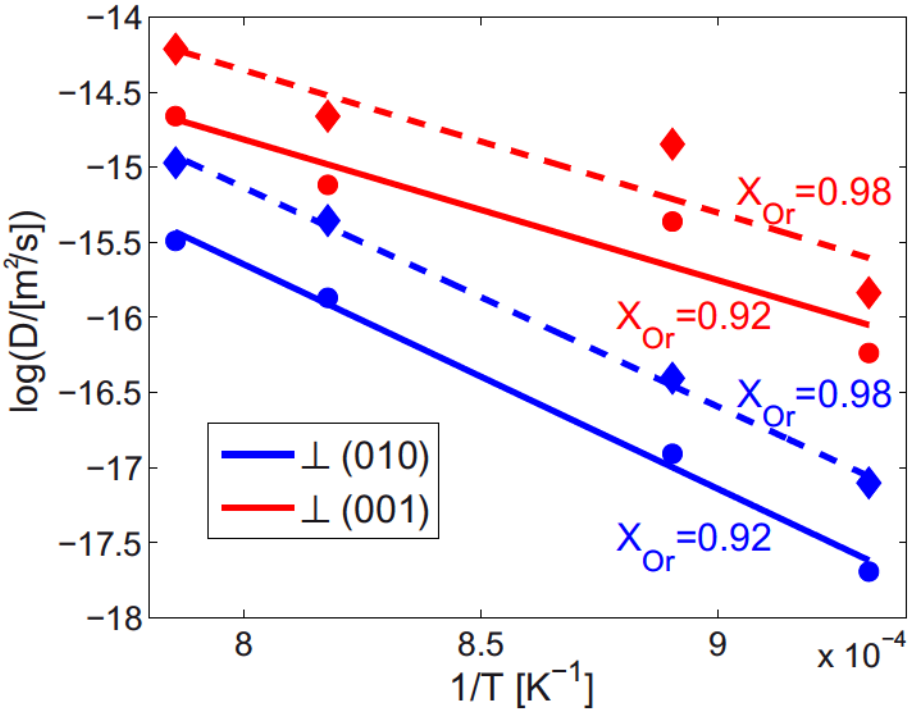

FIGURE 8.4: Temperature dependence of the interdiffusion coefficient for directions perpendicular to (001) and perpendicular to (010) and for two compositions; the data for D at 920° are not taken into account for the calculations

In figure 8.5 the direct determinations of the interdiffusion coefficient from this study and those by Christoffersen et al. (1983) are compared with experimental determinations of the sodium and potassium tracer-diffusion coefficients taken from literature. Although the various determinations of the tracer-diffusion coefficients show considerable scatter, it is nonetheless obvious that potassium tracer-diffusion is slower than sodium tracer-diffusion. Activation energies determined from experimental data for Na-K interdiffusion are in the range of those determined for sodium and potassium tracer-diffusion. In terms of absolute value the data from this study agree with those by Christoffersen et al. (1983) reasonably well.

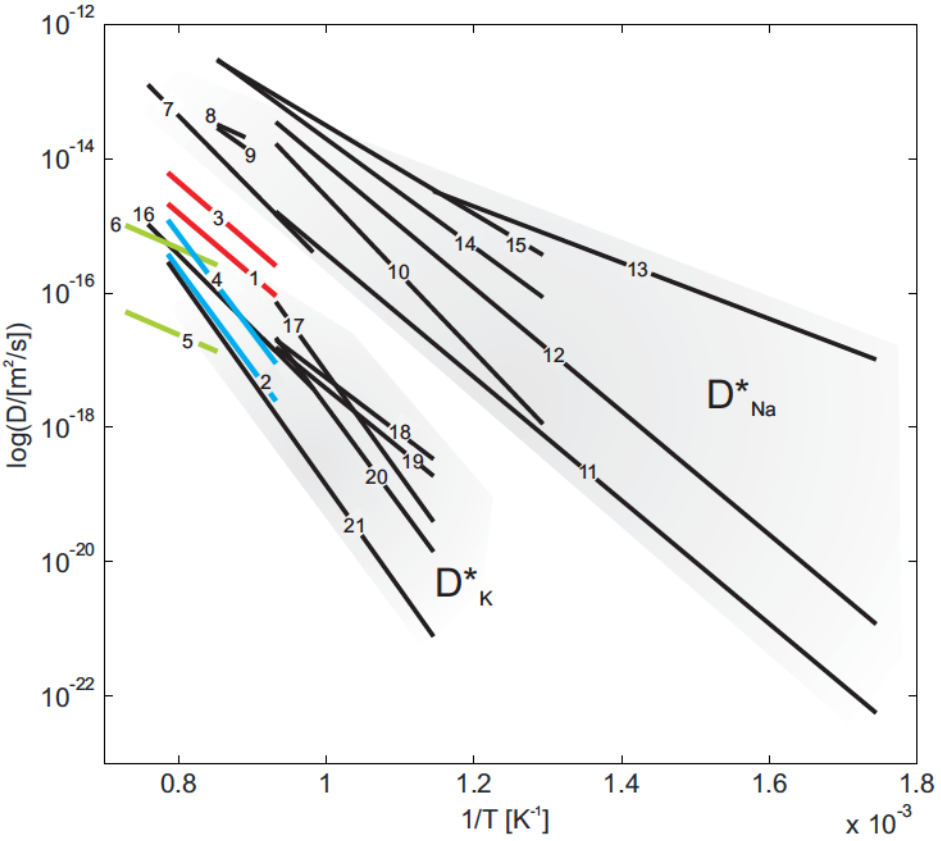

FIGURE 8.5: Arrhenius plot of available literature data for tracer-and interdiffusion coefficients as well as the interdiffusion data from this study determined at X_{Or} 0.92 and 0.98; 1 - $D_{Na/K}\perp$ (001)(X_{Or} = 0.92) - this study; 2 - $D_{Na/K}\perp$ (010)(X_{Or} = 0.92) - this study; 3 - $D_{Na/K}\perp$ (001)(X_{Or} = 0.98) - this study; 4 - $D_{Na/K}\perp$ (010)(X_{Or} = 0.98) - this study; 5 - $D_{Na/K}\perp$ (001) - Christoffersen et al. (1983); 6 - $D_{Na/K}\perp$ (010) - Christoffersen et al. (1983); 7 - D^*_{Na} - Petrović (1972); 8 - D^*_{Na} - Maury (1968); 9 - D^*_{Na} - Sippel (1963); 10 - D^*_{Na} - Foland (1974); 11 - D^*_{Na} - Kasper (1975); 12 - D^*_{Na} - Bailey (1971); 13 - D^*_{Na} - Lin and Yund (1972); 14 - D^*_{Na} $\perp$ (001) - Wilangowski (2013); 15 - D^*_{Na} $\perp$ (010) - Wilangowski (2013); 16 - D^*_K - Petrović (1972); 17 - D^*_K - Lin and Yund (1972); 18 - D^*_K - Giletti et al. (1974); 19 - D^*_K - Kasper (1975); 20 - D^*_K - Foland (1974); 21 - D^*_K - Giletti and Shanahan (1997)

8.6 Diffusion Mechanisms

The mechanisms of diffusion in feldspars are not yet fully understood, although a number of authors made considerations in this regard. Detailed discussions can be found in Petrović (1972), Foland (1974), Christoffersen (1982) and Behrens et al. (1990).

The large cations are mainly located in large cavities in the feldspar structure between the interlinked crankshaft-like chains and are thus separated by the bulky framework of the structure. The most likely interstitial sites that large cations can occupy are (0,0, $\frac{1}{2}$) and its equivalents, as in these positions the cations are still well shielded from each other (Petrović, 1972). Two of these positions exist per unit cell of sanidine. In *b*-direction jumps of large cations from one of these sites to the other are hindered by

the structure. As the interstitial mechanism is thus unlikely to be of significance in this direction, it has to be assumed that cations diffuse by a vacancy mechanism. On the other hand, movement between these interstitial sites is well possible in the *a*-*c*-plane due to the channel-like structures, the largest of which run parallel to [101]. This could explain the observation of interdiffusion being significantly faster in this direction.

Generally studies agree in assuming that the self-diffusion of potassium is mostly controlled by a vacancy mechanism, while sodium self-diffusion is usually assumed to occur mainly by an interstitial mechanism. The basis of these assumptions are the relatively low activation energies, the significant difference in the rates of tracer-diffusion of potassium and sodium, and observations of changes in diffusivity rates with changes in the defect concentration of the starting material (Petrović, 1972; Christoffersen, 1982).

The activation energies are too low for diffusion to involve breaking of Si,Al-O bonds. Thus the cations are assumed to diffuse through an intact, coherent Al-Si-framework (Christoffersen, 1982). This is further supported by water having no apparent effect on the diffusivities (Christoffersen et al., 1983; Giletti and Shanahan, 1997). Very similar results for tracer-diffusion coefficients of both potassium and sodium have been observed in a variety of starting materials. As it is unlikely that all feldspars used had the same concentration of impurities, defects and vacancies it is interpreted that diffusion rates are not extrinsically controlled (Petrović, 1972). The fact that sodium tracer-diffusion is considerably faster than potassium tracer-diffusion gives rise to the assumption that they have to be controlled by different mechanisms. The smaller size of the Na^+ cation should allow it to occupy interstitial positions, while potassium is unlikely to fit on these positions and would be limited to diffusion by a vacancy mechanism; theoretically diffusion by vacancy in combination with an interstitial mechanism should be possible for sodium. Another option for sodium self-diffusion would be an interstitialcy mechanism; for a complex structure like that of the feldspar it is very difficult to distinguish between these two mechanisms. The seeming incommensurateness of the almost constant interdiffusion rates for intermediate composition and pronounced rise at high X_{Or} indicates that a single diffusion mechanism is not sufficient to explain the diffusion behaviour of the cations and that a combination of several mechanisms has to be considered, especially for the smaller Na^+.

Behrens et al. (1990) observed a decrease of Na-diffusivity with increasing oxidation of iron. As increasing oxidation increases the number of vacancies they conclude that these are not the rate limiting factor for sodium-diffusion. Instead, the number of interstitial positions available seems to be relevant, which is in accordance with the theories found in other studies.

8.7 Influence of the Starting Material

The two sanidines used as starting material for the experiments differ, aside from their initial X_{Or}, in their barium content. With up to 1.5 wt-% the Rockeskyll material contains up to twice the amount of barium found in the Volkesfeld sanidine (max 1 wt-%). In literature it is mostly assumed that diffusion of potassium in feldspars is controlled by a vacancy mechanism, while sodium mainly diffuses by an interstitial mechanism (Petrović, 1972; Hokason and Yund, 1986; Zhang, 2010). Due to the requirement of charge neutrality the presence of divalent cations like Ba^{2+} should lead to a higher concentration of vacancies. This in turn should raise the probability for Na^{+} and especially K^{+} to jump into a neighbouring vacancy and thus raise the interdiffusion coefficient. Resulting from these considerations it would be expected that Na-K-interdiffusion is slightly faster in the sanidine from the Rockeskyller Kopf. Ba diffusion itself is about three orders of magnitude slower than diffusion of potassium although both have similar ionic radii, which is likely to be explained by its higher charge, which requires coupled movement of the cations with Si/Al or vacancies to ensure charge balance (Cherniak, 2001).

Within error of the available data no increase in the interdiffusion coefficient for the Rockeskyll sanidine could be observed. However, the starting material from the Rockeskyller Kopf was observed to be much more susceptible for damage during the experiments and especially preparation than the Volkesfeld sanidine used for the bulk of the experiments. Most samples showed severely chipped edges, making measuring full profiles hard and leading to a diminishment in the quality of the measured data. Thus the number of profiles that was chosen for further analysis is very small compared to the data set available for Volkesfeld sanidine. This makes a comparison between the interdiffusion coefficients of the two starting materials, and thus an estimation of the influence of the higher Ba-contents of the Rockeskyller Kopf material on interdiffusion, rather difficult.

Chapter 9

Conclusions

Exchange experiments between gem-quality sanidine from two localities in the Eifel (Volkesfeld, $X_{Or}^{initial}$ 0.85 and Rockeskyller Kopf, $X_{Or}^{initial}$ 0.72) and salt melts allowed the determination of new data on Na-K-interdiffusion in the composition range $0.65 \leq X_{Or} \leq 1.00$. The experiments were carried out in the temperature range between 800 and 1000°C and chemical profiles were measured in the b and c^*-directions of the feldspar. At 850°C additional measurements in directions contained in the a-b-, a-c- and b-c-planes supplied data to determine the full diffusivity tensor for Volkesfeld sanidine in the composition range $0.85 \leq X_{Or} \leq 0.97$. During cation exchange the formation of a core-rim structure can be observed. The outer rim of the feldspar is in equilibrium with the surrounding melt while the core area still retains the original composition. The transition between rim and core can be interpreted as diffusion fronts because in a single crystal cation exchange necessitates interdiffusion. Different shapes of diffusion fronts, and characteristic features develop depending on direction and extent of the composition shift. If cation exchange shifts the feldspar composition to $X_{Or} > 0.95$, the diffusion profile exhibits two plateaus corresponding to the exchanged rim in equilibrium with the melt and the completely unexchanged core, respectively. Between these plateaus an exchange front develops with an inflection point that progresses into the crystal with $t^{1/2}$. The width of this diffusion front varies greatly with the extent of chemical shift and crystallographic direction. Very wide and shallow diffusion profiles were observed parallel to the a- and c^*-axes of the crystal. The sharpest profiles are always found in b-direction.

The sharpest profiles, however, do not mark the direction of slowest interdiffusion. The fastest and slowest direction of interdiffusion are both contained within the a-c-plane, parallel to the [101]-direction and perpendicular to it ($\approx [10\bar{2}]$), respectively. The most likely explanation for this are channel-like structures formed by cavities between the

interconnected crankshaft-chains forming the building blocks of the feldspar structure. The largest of these channels are found parallel to [101], facilitating the movement of cations in this direction; no suitable channels exist within the *a*-*c*-plane at 90° to the [101]-direction.

The sharpness of the diffusion fronts normal to (010) is most likely a product of the effects of self-stress produced by the composition strain associated with cation exchange. The stress pattern and lattice distortion across the very sharp fronts developing in *b*-direction and the shallower profiles for directions within the *a*-*c*-plane were documented using EBSD combined with the cross correlation method. The strain changes gradually across the shallow front normal to (001) with a successive dilation primarily in the *a*-direction, which is in accordance with composition strain in an unstressed alkali feldspar. For the sharp diffusion fronts however, a pronounced dilation in the *b*-direction is localised at the diffusion front and is followed by a slight expansion in the *a*-direction in the exchanged potassium-rich rim. This strain distribution does not confer with what would be expected from the anisotropy of the composition dependence of the lattice parameters. It can be explained by the mechanical coupling of the thin misfitting surface layer and the mechanically much stronger substratum. It is hypothesized that the localisation of the lattice distortion at the diffusion front may have an influence on diffusion pathways, and possibly reduces component mobility across the diffusion front, leading to a self-sharpening feedback.

During shifts towards more sodium-rich composition the associated coherency strain leads to the development of a regular crack system with sub-parallel cracks following the general crystallographic direction (h0l). The cracks open roughly normal to the direction of maximum tensile stress. A slight deviation from this can be explained by the anisotropy of the elastic properties of the feldspar. The exchange front developing in this case lacks the inflection point observed for shifts towards more potassium-rich compositions. It was determined that the critical shift to induce fracturing is 9 mole-%, corresponding to a critical stress of about 350 MPa.

The interdiffusion coefficient was extracted using Boltzmann's method. A pronounced composition dependence of the interdiffusion coefficient D was documented. D is almost independent of composition in the composition range $0.65 \leq X_{Or} \leq 0.95$. For $X_{Or} > 0.95$ the interdiffusion coefficient shows a sharp increase towards the pure potassium end-member composition. Na-K-interdiffusion is markedly anisotropic with interdiffusion in c^*-direction being 5 to 10 times larger than in *b*-direction, the difference decreasing with increasing temperature. In the temperature range of 800 to 1000°C Na-K-interdiffusion in Volkesfeld sanidine follows an Arrhenius law with

$$D_0^{\perp(001)}(0.92) = 4.63 \cdot 10^{-8}\mathrm{m}^2/\mathrm{s}, \quad \mathrm{E}_\mathrm{A}^{\perp(001)}(0.92) = 179\ \mathrm{kJ/mole}$$

$D_0^{\perp(001)}(0.98) = 1.66 \cdot 10^{-7}\mathrm{m}^2/\mathrm{s}, \quad \mathrm{E}_\mathrm{A}^{\perp(001)}(0.98) = 181\ \mathrm{kJ/mole}$
$D_0^{\perp(010)}(0.92) = 1.97 \cdot 10^{-4}\mathrm{m}^2/\mathrm{s}, \quad \mathrm{E}_\mathrm{A}^{\perp(010)}(0.92) = 286\ \mathrm{kJ/mole}$
$D_0^{\perp(010)}(0.98) = 3.27 \cdot 10^{-4}\mathrm{m}^2/\mathrm{s}, \quad \mathrm{E}_\mathrm{A}^{\perp(010)}(0.98) = 277\ \mathrm{kJ/mole}.$

The composition dependence of the interdiffusion coefficient fits literature data by Christoffersen et al. (1983) quite well so that now the composition dependence of the sodium-potassium interdiffusion coefficient is known from direct determinations for the composition range $0.1 \leq X_{Or} \leq 1.00$.

No differences between Volkesfeld sanidine and Rockeskyll sanidine could be documented, although the Rockeskyll sanidine has a higher Ba-content, which is associated with a higher concentration of vacancies due to the requirement of charge balance, and might thus have been expected to lead to faster interdiffusion rates.

The results for interdiffusion rates deviate markedly from theoretical calculations with the Nernst-Planck-relation using sodium and potassium tracer-diffusion coefficients determined by Foland (1974) and Kasper (1975). Especially parallel to the *b*-direction interdiffusion rates are significantly slower than indicated by the model. This may be caused by the theoretical calculations relying on tracer-diffusion data from the literature which were mainly determined with bulk exchanged methods or in analyses with limited depth resolution and no discrimination between crystallographic directions. New values for tracer-diffusion would be required to look into this. First efforts in this regard were made by Wilangowski (2013).

The strong compositional localisation of the steep rise in interdiffusion rates for $X_{Or} > 0.95$, even more pronounced than predicted by the model, and the almost constant interdiffusion rates in the composition range $0.65 \leq X_{Or} \leq 0.95$ cannot be reproduced within the constraints of the model used. The Nernst-Planck relation only accounts for one type of diffusing species, thus it seems likely that several species of sodium are relevant at high X_{Or}.

Acknowledgements

I would like to thank the colleagues, friends and helpers that made this work possible.

First and foremost I would like to thank my supervisors Rainer Abart and Wilhelm Heinrich for giving me the opportunity to work on this interesting topic. They were always open for discussions and made it possible for me to visit numerous conferences to present my results and get into contact with fellow researchers. Further, special thanks go to Elena Petrishcheva for her invaluable help in the evaluation and interpretation of the data.

I am obliged to the Austrian Science Foundation for funding this project in the framework of the DFG-FWF research group FOR 741 and the University of Vienna for further funding within the doctoral school *Deformation Of Geological Materials (DOGMA): Mechanical-chemical feedback and the coupling across scales.*

Many thanks go to Katharina Scheidl for helpful discussions, great collaboration during her work on her Master's thesis in the scope of this project, and for allowing me the use of some of her data.

I would also like to thank Gerlinde Habler who helped with BSE imaging and EBSD measurements, and always made time in her busy schedule for discussions, questions and to help with various problems presenting themselves.

For providing the samples that present the very basis for this study I would like to thank Susan Schorr, Vera Hammer and Jürgen Schreuer, while thanks for sample preparation go to Andreas Wagner, Sigrid Hrabe, Claudia Beybel and Willy Tschudin. Further thanks go to Gerald Giester for orienting the feldspar crystals on a three circle goniometer.

For conducting the FEG-SEM measurements I owe thanks to Dieter Rhede at the GFZ Potsdam, who often made it possible to get data on rather short notice. Stefan Zaefferer and Tom Jäpel deserve my gratitude for making the strain analysis possible by allowing me the use of the EBSD facilities at the MPI for iron research in Düsseldorf and contributing their expertise and experience with the cross correlation technique.

Many other individuals deserve my gratitude, these include Heinz-Jürgen Bernhardt at the Ruhruniversität Bochum for providing his Mincalc software and helping with the evaluation of the EMP data, Hugh Rice and David Grebenstein for help with the Inspect S, and Flora Brocza for providing the fractionation curve for the bromides.

Others who deserve my thanks include Bastian Joachim, Benjamin Huet, Vanessa Helpa, and all members of the DOGMA doctoral school. Further, many thanks to all who made life in Vienna an interesting, memorable and happy experience.

Last but not least I would like to thank Heidy, Michael and Dorian for always being there when I need them most.

List of Figures

List of Tables

Appendix A

Abstract/Kurzfassung und Lebenslauf

Abstract

Cation exchange experiments between gem-quality sanidine from two localities in the Eifel with different initial compositions of $X_{Or}^{initial}$ 0.85 (Volkesfeld) and $X_{Or}^{initial}$ 0.72 (Rockeskyller Kopf), and Na-K-bearing salt melts were conducted. Except for some initial experiments using crushed material the material was prepared as crystallographically oriented plates with polished surfaces corresponding to the (010) and (001) planes of the feldspar. For some additional experiments further crystallographic orientations were prepared, allowing the determination of the full diffusivity tensor for Volkesfeld sanidine at 850°C in the composition interval $0.85 \leq X_{Or} \leq 0.97$.

Cation exchange leads to the formation of a core-rim structure; an exchanged rim in equilibrium with the melt is separated from an unexchanged core by a diffusion front. The geometry and sharpness of these diffusion fronts depends on crystallographic direction and the extent of the composition shift, i.e. the chemical difference between the exchanged and unexchanged portions of the crystal.

For shifts towards very potassium-rich compositions ($X_{Or} > 0.95$), the diffusion profile is characterised by two plateaus corresponding to the rim and core, respectively. Between these plateaus a diffusion front with an inflection point propagating into the crystal with $t^{1/2}$ can be observed. Diffusion fronts parallel to b are very sharp, while fronts parallel to c^* are comparatively shallow. The sharpness of the interdiffusion profiles normal to (010) indicates that interdiffusion might be influenced by coherency stress developing across the diffusion fronts. EBSD in combination with the cross correlation method

allows the determination of the full strain tensor from shifts in EBSD Kikuchi patterns. It was used to document strain patterns and lattice distortion across both sharp and shallow diffusion fronts.

A shift towards more sodium-rich compositions leads to the formation of a system of sub-parallel cracks in (h0l) due to coherency stress caused by the composition dependence of the lattice parameters of feldspar. In this case the diffusion fronts do not have an inflection point.

The geometry of the observed diffusion fronts can be explained with a composition dependent interdiffusion coefficient $D(X_{Or})$. The composition dependence of D parallel to b and c^* was extracted from measured data in the composition interval $0.65 \leq X_{Or} \leq 0.99$ using Boltzmann's transformation. At 850°C interdiffusion rates are roughly constant in the composition range $0.65 \leq X_{Or} \leq 0.95$ and then rise steeply. Interdiffusion normal to (001) is significantly faster than normal to (010), the difference decreasing with increasing temperature.

Using the Nernst-Planck equation for ionic crystals, a theoretical composition dependence of the interdiffusion coefficient was calculated from tracer-diffusion data found in literature (Foland, 1974; Kasper, 1975). Comparison of the extracted data with these theoretical values showed that interdiffusion has roughly the same trend in composition dependence, but turns out to be slower than predicted. While D is only slightly lower at a given composition for interdiffusion normal to (001), values for D normal to (010) are lower by more than a factor of ten. Further, for intermediate compositions the data of this study does not show a composition dependence, although a significant dependence is predicted by both the theoretical calculations and older direct determinations of D by Christoffersen et al. (1983).

The seeming inconssumerateness of the almost constant interdiffusion rates at intermediate compositions and the steep rise for $X_{Or} > 0.95$ indicates that several species of sodium may be present which move by different diffusion mechanisms.

Kurzfassung

Es wurden Kationenaustauschexperimente zwischen Sanidin von zwei verschiedenen Lokalitäten in der Eifel mit Ausgangszusammensetzungen von $X_{Or}^{initial}$ 0.85 (Volkesfeld) und $X_{Or}^{initial}$ 0.72 (Rockeskyller Kopf) und Na-K-haltigen Salzschmelzen durchgeführt. Der Sanidin wurde, nach anfänglichen Versuchen mit Streupräparaten, in Form von kristallographisch orientierten Plättchen präpariert, deren polierte Flächen den (010) oder (001) Flächen des Feldspates entsprechen. Für einige Versuche wurden weitere kristallographische Richtungen präpariert, wodurch der vollständige Diffusivitätstensor für den Volkesfelder Sanidin im Kompositionsbereich $0.85 \leq X_{Or} \leq 0.97$ bei 850°C bestimmt werden konnte. Die Zusammensetzung der Schmelze, die Temperatur (800 bis 1000°C) und die Laufzeit (1 bis 64 Tage) wurden systematisch variiert, um ihren Einfluss auf die Interdiffusion dokumentieren zu können.

Durch den Kationenaustausch entstand eine Kern-Rand-Struktur; ein ausgetauschter Randbereich im Gleichgewicht mit der Schmelze, getrennt von einem unausgetauschten Kern durch eine Diffusionsfront. Die Geometrie und Schärfe dieser Diffusionsfront sind abhängig von der kristallographischen Richtung und dem Unterschied in der absoluten Zusammensetzung zwischen den ausgetauschten und unausgetauschten Bereichen des Kristalles.

Für Verschiebungen zu sehr K-reichen Zusammensetzungen ($X_{Or} > 0.95$) zeigen die Diffusionsprofile zwei Plateaus, die mit dem ausgetauschten Rand und einem unausgetauschten Kernbereich der Probe korrelieren. Zwischen diesen Plateaus befindet sich eine Diffusionsfront mit einem Wendepunkt, die mit $t^{1/2}$ propagiert. Diffusionsfronten parallel zur b-Richtung sind deutlich schärfer als Fronten parallel zu c^*. Die Schärfe der Interdiffusionsprofile senkrecht auf (010) deutet darauf hin, dass Interdiffusion von Kohärenzstress beeinflusst wird, der sich über die Fronten hinweg durch den Kationenaustausch ergibt. EBSD in Kombination mit der Cross Correlation Methode erlaubt die Bestimmung des vollen Strain-Tensors auf Basis von relativen Verzerrungen in EBSD Kikuchi Patterns. Sie wurde genutzt, um die Stressverteilung und Gitterverzerrung über sowohl eine scharfe als auch eine weiche Front hinweg zu dokumentieren.

Eine Verschiebung Richtung Na-reicherer Kompositionen führt auf Grund von auftretenden Kohärenzspannungen zur Ausbildung eines Systems subparalleler, regelmäßiger Risse in (h0l). In diesem Fall zeigt die sich entwickelnde Diffusionsfront keinen Wendepunkt.

Die Geometrie der beobachteten Diffusionsfronten kann mit einem kompositionsabhängingen Interdiffusionskoeffizienten $D(X_{Or})$ erklärt werden. Mit Hilfe der Boltzmann Transformation wurde die Zusammensetzungsabhängigkeit von D aus den gemessenen Daten im

Zusammensetzungsbereich $0.65 \leq X_{Or} \leq 0.99$ parallel zu b und c^* extrahiert. Bei 850°C ist die Interdiffusion im Zusammensetzungsbereich $0.65 \leq X_{Or} \leq 0.95$ nahezu konstant, bevor sie für höhere X_{Or} stark ansteigt. Die Interdiffusion senkrecht auf (001) ist dabei deutlich schneller als senkrecht auf (010), wobei der Unterschied mit zunehmender Temperatur kleiner wird.

Mit Hilfe der Nernst-Planck Gleichung für ionische Kristalle wurde der Interdiffusionskoeffizient aus in der Literatur vorhandenen Tracerdiffusionskoeffizienten (Foland, 1974; Kasper, 1975) berechnet. Ein Vergleich der extrahierten Daten mit diesen theoretisch berechneten zeigte, dass zwar ein ähnlicher Trend zu beobachten ist, die Werte für Interdiffusion senkrecht auf (001) jedoch bei einer gegebenen Zusammensetzung etwas unter den theoretischen liegen und Werte für Interdiffusion senkrecht auf (010) mehr als eine Größenordnung langsamer sind. Weiterhin zeigen die Daten dieser Studie beinahe keine Kompositionsabhängigkeit des Interdiffusionskoeffizienten für intermediäre X_{Or}, obwohl diese nach den theoretischen Berechnungen und auch durch ältere Bestimmungen von Christoffersen et al. (1983) zu erwarten wäre.

Die scheinbare Unvereinbarkeit eines beinahe konstanten Interdiffusionskoeffizienten bei mittleren Zusammensetzungen und dem starken Anstieg der Interdiffusionrate bei $X_{Or} > 0.95$, deutet darauf hin, dass mehrere Natriumspezies an der Diffusion beteiligt sind, die sich mit unterschiedlichen Diffusionsmechanismen bewegen.

Lebenslauf

Persönliche Daten

Name:	Anne-Kathrin Schäffer
Geburtsdatum:	05.06.1986
Geburtsort:	Herdecke
Adresse:	Am Hermannsbrunnen 1, D-58239 Schwerte

Schulbildung

1992 - 1996	Grundschule Ergste, Schwerte
1993 - 1999	Friedrich-Bährens Gymnasium, Schwerte
Abschluss:	Abitur

Akademische Laufbahn

2005 - 2008	Ruhruniversität, Bochum
Abschluss:	B.Sc. Geowissenschaften am Institut für Geologie, Mineralogie und Geophysik Thema Bachelorarbeit: Untersuchung zu Aufbau und Eruption der Vulkane Rockeskyller Kopf und Baarley in der Westeifel (Lokalität 4)
2008 - 2010	Ruhruniversität, Bochum
Abschluss:	M.Sc. Geowissenschaften am Institut für Geologie, Mineralogie und Geophysik Thema Masterarbeit: Microfabrics and fossiliferous high pressure-low temperature marbles at Livadia, western Crete
seit 2011	Promotion im Rahmen der Forschergruppe 741 an der Universität Wien mit dem Titel: Alkali Interdiffusion in Alkali feldspars

Berufserfahrung und Praktika

02/2007 - 04/2010	studentische Hilfskraft am Institut für Sedimentologie, Ruhruniversität Bochum
07/2007 - 09/2007	Praktikum beim Institut für Bodensanierung, Wasser- und Luftanalytik GmbH, Iserlohn
02/2008 - 03/2008	Praktikum beim Institut für Wasserforschung GmbH, Dortmund

Appendix B

Data

TABLE B.1: Digest of all data for tracer- and interdiffusion in alkali feldspars found in literature

Starting Material	Initial Composition	Tracer Isotope	T [$\circ C$]	P [MPa]	E_a [$kJ/mole$]	$D_0[m^2/s]$	D^* [cm^2/s] at $850^\circ C$	Experimental Procedure	Reference
Self-Diffusion									
low albite	Ab_{100}	^{22}Na	200-600	200	79.4	2.31E-10	4.7108E-10	Liquid-solid exchange	Lin and Yund (1972)
pure microcline	Or_{100}	^{40}K	600-800	50 - 200	293 $\pm$8	1.340E-2	3.2244E-12	liquid-solid exchange	Lin and Yund (1972)
adularia	Or_{86}	Na	745-1051		213.2	3.00E-05	3.6947E-11	crystal-molten salt, EPMA	Petrović (1972)
adularia	Or_{86}	K	745-1051		209			crystal-molten salt, EPMA	Petrović (1972)
adularia	Ab_{88}, Ab_{96}	K	856-1011		242 $\pm$ 21	3.00E-07	1.6942E-14	Crystal-Molten Salt,$\parallel$ [010, 110, 001] EPMA	Petrović (1972)
orthoclase	$Or_{94}Ab_6$	^{22}Na	500-800	200	220.6444	8.92E-4	4.9523E-10	exchange with brine, bulk analysis, cylindrical model	Foland (1974)
orthoclase	$Or_{94}Ab_6$	^{22}Na	500-800	200	220.3	8.90E-4	5.1267E-10	Liquid-solid exchange, MS	Foland (1974)
orthoclase	$Or_{94}Ab_6$	K	600-800	200	285.5398	1.610E-3	8.6085E-13	exchange with brine, bulk analysis, cylindrical model	Foland (1974)
orthoclase	$Or_{94}Ab_6$	^{41}K	600-800	200	285.1	1.61E-3	9.0233E-13	Liquid-solid exchange	Foland (1974)
low albite	$Ab_{98}Or_{1.4}An_{0.6}$	K	750-1060	100	242.8344	3.0E-7	1.5494E-14		Petrović (1972)
low albite	$Ab_{98}Or_{1.4}An_{0.6}$	K	500-800	200	159.0984	1.1E-09	4.4309E-13	hydrothermal	Giletti et al. (1974)
low albite	Ab_{98}	^{41}K	500-800	200	158.8	1.1E-09	4.5747E-13	Liquid-solid exchange, $\parallel$ [001]SIMS	Giletti et al. (1974)
low albite	$Ab_{98}Or_{1.4}An_{0.6}$	Na	300-800	200	175.8456	1.25E-5	8.3869E-10	sectioning method	Bailey (1971)
low albite	$Ab_{98}Or_{1.4}An_{0.6}$	^{22}Na	300-800	200	176 ($\pm$8)	1.2503E-05	8.2511E-10	Exchange with $^{22}NaCl$ solution, cylindrical model	Kasper (1975)
low albite	$Ab_{98}Or_{1.4}An_{0.6}$	^{40}K	600-800	200	172 ($\pm$25)	7.4989E-09	7.5934E-13	exchange with ^{40}KCl solution, cylindrical model	Kasper (1975)
low albite	Ab_{98}	K	600-800	200	171.4	3.4E-09	3.6711E-13	Liquid-solid exchange	Kasper (1975)
low albite	Ab_{98}	Na	300-800		175.6	5.70E-7	3.9263E-11		Kasper (1975)
		^{24}Na	850-940		149	1.22E-07	1.4482E-10		Sippel (1963)
		Na	850-940		96	6E-10	2.0705E-10	electrical conductivity	Maury (1968)
albite	Ab_{98}	^{41}K	600-1000	0.1	296 30	3.98	6.94879E-14	SIMS depth profiling	Giletti and Shanahan (1997)
sanidine (010)	Or_{86}	^{22}Na	700-900	0.1	146.66	0.0243	3.70548E-09	sectioning method	Wilangowski (2013)
sanidine (001)	Or_{86}	^{22}Na	500-900	0.1	122.54	0.0013	2.61987E-09	sectioning method	Wilangowski (2013)
Inter-Diffusion									
adularia - albite	$Or_{89.6}$ to $Ab_{98.6}$	K-Na	900-1000	1500				diffusion couple, EMP profiles	Christoffersen et al. (1983)
microcline	Or_{100}	K-Na	420-570		91	0.0000001		liquid-solid-exchange	Wyart & Sabatier (1956)

TABLE B.2: Overview over the profiles with different run times that were reduced to one data set by introduction of the similarity variable

	T [°C]	X_K^{salt}	X_{Or}^{eq}	b	c*
Volkesfeld	800	0.48	0.80	2x 32d	2x 32d
		1.00	1.00	4x 32d	2x 32d
	850	0.30	0.70	2x 4d, 1x 8d	2x 4d, 2x 8d, 2x 16d
		0.35	0.92	2x 8d	-
		0.60	0.97	1x 1d, 1x 4d	2x 1d, 3x 4d
		0.85	0.73	1x 4d, 1x 8d, 1x 16d	
		1.00	1.00	1x 4d, 3x 8d, 2x 16d, 1x 64d	3x 1d, 2x 4d, x 8d
	920	1.00	1.00	1x 1d, 1x 2d, 1x 4d, 1x 8d	1x 1d, 1x 2d
	950	1.00	1.00	2x 2d	2x 2d
	1000	1.00	1.00	2x 2d	1x 2d
Rockeskyll	800	0.37	0.65	-	2x 32d
		0.55	0.80	-	3x 32d
	850	0.22	0.45	1x 8d	2x 4d, 2x 8d, 2x 16d
		0.50	0.85	2x 4d, 3x 8d, 2x 16d	2x 4d, 2x 8d, 2x 16d
		1.00	1.00	3x 8d	3x 8d
	920	0.28	0.52	1x 2d	1x 2d
		0.50	0.82	2x 2d	2x 2d
	950	0.50	0.81	1x 1d	2x 1d
	1000	0.50	0.81	1x 1d	1x 1d

TABLE B.3: List of all conducted experiments, V - Volkesfeld, R - Rockeskyll, N° - Number on thin section

Name	N°	Thin Section	Sample Type	Run Duration [d]	Salt Composition	T [°C]	Sample Geometry	X_{Or}^{eq}
					X_{KCl}			
S1-7-100-850	1	Sa1	V	7	1	850	crushed (200 to 400 μm)	1
S1-7-90-850	2	Sa1	V	7	0.9	850	crushed (200 to 400 μm)	0.98
S1-7-60-850	3	Sa1	V	7	0.6	850	crushed (100 to 200 μm)	0.91
S1-7-30-850	4	Sa1	V	7	0.3	850	crushed (200 to 400 μm)	0.71
S1-7-25-850	5	Sa1	V	7	0.25	850	crushed (200 to 400 μm)	-
S1-7-20-850	6	Sa1	V	7	0.2	850	crushed (200 to 400 μm)	-
S1-22-100-850	7	Sa2	V	22	1	850	crushed (200 to 400 μm)	1
S1-22-90-850	8	Sa2	V	22	0.9	850	crushed (200 to 400 μm)	0.98
S1-22-60-850	9	Sa2	V	22	0.6	850	crushed (200 to 400 μm)	0.91
S1-22-30-850	10	Sa2	V	22	0.3	850	crushed (200 to 400 μm)	0.71
S1-22-25-850	11	Sa2	V	22	0.25	850	crushed (200 to 400 μm)	-
S1-22-20-850	12	Sa2	V	22	0.2	850	crushed (200 to 400 μm)	-
					X_{KBr}			
SM4B10	1	P1	V	28	1	850	crushed (100 to 200 μm)	1
SM4B09	2	P1	V	28	0.9	850	crushed (100 to 200 μm)	0.98
SM4B08	3	P1	V	28	0.8	850	crushed (100 to 200 μm)	0.95
SM4B07	4	P1	V	28	0.7	850	crushed (100 to 200 μm)	0.92
SM4B06	5	P1	V	28	0.6	850	crushed (100 to 200 μm)	0.86
SM4B05	6	P1	V	28	0.5	850	crushed (100 to 200 μm)	0.81
SM4B04	7	P2	V	28	0.4	850	crushed (100 to 200 μm)	0.66
SM4B03	8	P2	V	28	0.3	850	crushed (100 to 200 μm)	0.41
SM4B02	9	P2	V	28	0.2	850	crushed (100 to 200 μm)	0.15
SM4B01	10	P2	V	28	0.1	850	crushed (100 - 200μm)	0.09
SM4B00	11	P2	V	28	0	850	crushed (100 to 200 μm)	0
					X_{KBr}			
SM0B00	A	P3	V	4	0	850	crushed (100 to 200 μm)	-
SM0B10	B	P3	V	4	100	850	crushed (100 to 200 μm)	-
					X_{KCl}			
SP1-100-850	1	SP001A	V	1	1	850	$\perp$ (001)	1
SP1-85-850	2	SP001A	V	1	0.85	850	$\perp$ (001)	0.98
SP1-60-850	3	SP001A	V	1	0.6	850	$\perp$ (001)	0.91
SP1 -30 -850	4	SP001A	V	1	0.3	850	$\perp$ (001)	-
SP1-30-850 b	4n	SP001A	V	1	0.3	850	$\perp$ (001)	0.76
SP4-100-850	5	SP001A	V	4	1	850	$\perp$ (001)	1
SP4-85-850	6	SP001A	V	4	0.85	850	$\perp$ (001)	0.97
SP4-60-850	7	SP001A	V	4	0.6	850	$\perp$ (001)	0.91

Continued on the next page

Name	N°	Thin Section	Sample Type	Run Duration [d]	Salt Composition	T [°C]	Sample Geometry	X_{Or}^{eq}
SP4 -30 -850	8	SP001A	V	4	0.3	850	⊥ (001)	0.7
SP8-100-850	9	SP001B	V	8	1	850	⊥ (001)	1
SP8-85-850	10	SP001B	V	8	0.85	850	⊥ (001)	0.98
SP8-60-850	11	SP001B	V	8	0.6	850	⊥ (001)	-
SP8-60-850 b	11n	SP001B	V	8	0.6	850	⊥ (001)	-
SP8 -30 -850	12	SP001B	V	8	0.3	850	⊥ (001)	0.7
SP16-100-850	13	SP001B	V	16	1	850	⊥ (001)	1
SP16-85-850	14	SP001B	V	16	0.85	850	⊥ (001)	0.98
SP16-60-850	15	SP001B	V	16	0.6	850	⊥ (001)	0.92
SP16 -30 -850	16	SP001B	V	16	0.3	850	⊥ (001)	0.7
SP32-100-850	17	SP010B	V	32	1	850	⊥ (001)	1
SP32-85-850	18	SP010B	V	32	0.85	850	⊥ (001)	-
SP32-60-850	19	SP010B	V	32	0.6	850	⊥ (001)	-
SP32 -30 -850	20	SP001C	V	32	0.3	850	⊥ (001)	0.71
SP64-100-850	21	SP001C	V	64	1	850	⊥ (001)	1
SP64-85-850	22	SP001C	V	64	0.85	850	⊥ (001)	-
SP64-60-850	23	SP001C	V	64	0.6	850	⊥ (001)	-
SP64 -30 -850	24	SP001C	V	64	0.3	850	⊥ (001)	-
SP3-100-920	25	SP001C	V	3	1	920	⊥ (001)	1
SP3-85-920	26	SP001C	V	3	0.85	920	⊥ (001)	
SP3-60-920	27	SP001D	V	3	0.6	920	⊥ (001)	
SP3 -30 -920	28	SP001D	V	3	0.3	920	⊥ (001)	0.6
SP8-100-920	29	SP001D	V	8	1	920	⊥ (001)	1
SP8-85-920	30	SP001D	V	8	0.85	920	⊥ (001)	
SP8-60-920	31	SP001D	V	8	0.6	920	⊥ (001)	
SP8 -30 -920	32	SP001D	V	8	0.3	920	⊥ (001)	
SP32-100-920	33	SP001E	V	32	1	920	⊥ (001)	1
SP32-85-920	34	SP001E	V	32	0.85	920	⊥ (001)	
SP32-60-920	35	SP001E	V	32	0.6	920	⊥ (001)	
SP32 -30 -920	36	SP001E	V	32	0.3	920	⊥ (001)	0.6
SPb1-100-850	1	SP010A	V	1	1	850	⊥ (010)	1
SPb1-85-850	2	SP010A	V	1	0.85	850	⊥ (010)	0.97
SPb1-60-850	3	SP010A	V	1	0.6	850	⊥ (010)	0.85
SPb1 -30 -850	4	SP010A	V	1	0.3	850	⊥ (010)	0.78
SPb4-100-850	5	SP010A	V	4	1	850	⊥ (010)	1
SPb4-85-850	6	SP010A	V	4	0.85	850	⊥ (010)	0.96
SPb4-60-850	7	SP010A	V	4	0.6	850	⊥ (010)	0.91
SPb4 -30 -850	8	SP010B	V	4	0.3	850	⊥ (010)	0.73
SPb8-100-850	9	SP010B	V	8	1	850	⊥ (010)	1
SPb8-85-850	10	SP010B	V	8	0.85	850	⊥ (010)	-
SPb8-60-850	11	SP010B	V	8	0.6	850	⊥ (010)	-

Continued on the next page

Name	N°	Thin Section	Sample Type	Run Duration [d]	Salt Composition	T [°C]	Sample Geometry	X_{Or}^{eq}
SPb8 -30 -850	12	SP010B	V	8	0.3	850	⊥ (010)	0.73
SPb16-100-850	13	SP010C	V	16	1	850	⊥ (010)	1
SPb16-85-850	14	SP010C	V	16	0.85	850	⊥ (010)	-
SPb16-60-850	15	SP010C	V	16	0.6	850	⊥ (010)	-
SPb16 -30 -850	16	SP010C	V	16	0.3	850	⊥ (010)	0.72
SPb32-100-850	17	SP010D	V	32	1	850	⊥ (010)	1
SPb32-85-850	18	SP010D	V	32	0.85	850	⊥ (010)	-
SPb32-60-850	19	SP010D	V	32	0.6	850	⊥ (010)	-
SPb32 -30 -850	20	SP010D	V	32	0.3	850	⊥ (010)	0.7
SPb64-100-850	21	SP010E	V	64	1	850	⊥ (010)	1
SPb64-85-850	22	SP010E	V	64	0.85	850	⊥ (010)	-
SPb64-60-850	23	SP010E	V	64	0.6	850	⊥ (010)	-
SPb64 -30 -850	24	SP010E	V	64	0.3	850	⊥ (010)	-
SPb4-100-920	25	SP010F	V	1	1	920	⊥ (010)	1
SPb4-85-920	26	SP010F	V	1	0.85	920	⊥ (010)	-
SPb4-60-920	27	SP010F	V	1	0.6	920	⊥ (010)	-
SPb4 -30 -920	28	SP010F	V	1	0.3	920	⊥ (010)	-
SPb8-100-920	29	SP010G	V	8	1	920	⊥ (010)	1
SPb8-85-920	30	SP010G	V	8	0.85	920	⊥ (010)	-
SPb8-60-920	31	SP010G	V	8	0.6	920	⊥ (010)	-
SPb8 -30 -920	32	SP010G	V	8	0.3	920	⊥ (010)	-
SPb16-100-920	33	SP010H	V	16	1	920	⊥ (010)	1
SPb16-85-920	34	SP010H	V	16	0.85	920	⊥ (010)	-
SPb16-60-920	35	SP010H	V	16	0.6	920	⊥ (010)	-
SPb16 -30 -920	36	SP010H	V	16	0.3	920	⊥ (010)	-
EP4-50-850	1	EP001A	R	4	0.5	850	⊥ (001)	0.87
EP4-22-850	2	EP001A	R	4	0.22	850	⊥ (001)	-
EP8-50-850	3	EP001A	R	8	0.5	850	⊥ (001)	0.86
EP8-22-850	4	EP001A	R	8	0.22	850	⊥ (001)	0.58
EP8-100-850	5	EP001A	R	8	1	850	⊥ (001)	1
EP16-50-850	6	EP001A	R	16	0.5	850	⊥ (001)	0.87
EP16-22-850	7	EP001A	R	16	0.22	850	⊥ (001)	-
EPb4-50-850	8	EP010A	R	4	0.5	850	⊥ (010)	0.86
EPb4-22-850	9	EP010A	R	4	0.22	850	⊥ (010)	-
EPb8-50-850	10	EP010A	R	8	0.5	850	⊥ (010)	0.86
EPb8-22-850	11	EP010A	R	8	0.22	850	⊥ (010)	-
EPb8-100-850	12	EP010A	R	8	1	850	⊥ (010)	1
EPb16-50-850	13	EP010A	R	16	0.5	850	⊥ (010)	0.87
EPb16-22-850	14	EP010A	R	16	0.22	850	⊥ (010)	-

Continued on the next page

Name	N°	Thin Section	Sample Type	Run Duration [d]	Salt Composition	T [°C]	Sample Geometry	X_{Or}^{eq}
SPb2-30-920	37	SP010i	V	2	0.3	920	⊥ (010)	-
SPb2-100-920	38	SP010i	V	2	1	920	⊥ (010)	1
SPb2-30-950	39	SP010i	V	2	0.3	950	⊥ (010)	-
SPb2-100-950	40	SP010i	V	2	1	950	⊥ (010)	1
SPb2-30-1000	41	SP010i	V	2	0.3	1000	⊥ (010)	-
SPb2-100-1000	42	SP010i	V	2	1	1000	⊥ (010)	1
SP1-100-920	A	Z1	V	1	1	920	⊥ (001)	1
EPb8-40-850	17	Z1	R	8	0.4	850	⊥ (010)	-
EP8-40-850	18	Z1	R	8	0.4	850	⊥ (001)	-
SPb32-100-800	43	SP001F	V	32	1	800	⊥ (010)	1
SPb32-48-800	44	SP001F	V	32	0.48	800	⊥ (010)	0.8
EP32-55-800	19	EP001C	R	32	0.55	800	⊥ (001)	0.8
EP32-37-800	20	EP001C	R	32	0.37	800	⊥ (001)	0.65
EPb32-55-800	21	EP001C	R	32	0.55	800	⊥ (010)	0.83
EPb32-37-800	22	EP001C	R	32	0.37	800	⊥ (010)	0.66
EP2-50-920	23	EP001B	R	2	0.5	920	⊥ (001)	0.81
EP2-28-920	24	EP001B	R	2	0.28	920	⊥ (001)	0.48
EP1-50-950	25	EP001B	R	1	0.5	950	⊥ (001)	0.8
EP1-28-950	26	EP001B	R	1	0.28	950	⊥ (001)	-
EP1-50-1000	27	EP001B	R	1	0.5	1000	⊥ (001)	0.8
EP1-28-1000	28	EP001B	R	1	0.28	1000	⊥ (001)	-
EPb2-50-920	29	EP010B	R	2	0.5	920	⊥ (010)	0.82
EPb2-28-920	30	EP010B	R	2	0.28	920	⊥ (010)	0.55
EPb1-50-950	31	EP010B	R	1	0.5	950	⊥ (010)	0.81
EPb1-28-950	32	EP010B	R	1	0.28	950	⊥ (010)	-
EPb1-50-1000	33	EP010B	R	1	0.5	1000	⊥ (010)	-
EPb1-28-1000	34	EP010B	R	1	0.28	1000	⊥ (010)	-
SPtb8-100-850	45	Z2	V	8	1	850	⊥ (010)	1
SPtb8-35-850	46	Z2	V	8	0.35	850	⊥ (010)	0.73
SP32-100-800	47	SP001F	V	32	1	800	⊥ (001)	1
SP32-48-800	48	SP001F	V	32	0.48	800	⊥ (001)	0.82
SP2-100-950	49	SP001F	V	2	1	950	⊥ (001)	1
SP2-100-1000	50	SP001F	V	2	1	1000	⊥ (001)	1
SPAu8-100-850	C	Z4	V	8	1	850	⊥ (001)	1

Continued on the next page

Name	N°	Thin Section	Sample Type	Run Duration [d]	Salt Composition	T [°C]	Sample Geometry	X_{Or}^{eq}
SPcb8-100-850	D	D	V	8	1	850	$(0, \sqrt{2}/2, \sqrt{2}/2)$	1
SPab8-100-850	E	E	V	8	1	850	$(\sqrt{2}/2, \sqrt{2}/2, 0)$,	1
SPca8-100-850	F	F	V	8	1	850	$(\sqrt{2}/2, 0, \sqrt{2}/2)$	1

TABLE B.4: Measurement of the spacing of the different hierarchies of the complex cracks for experiments with longer run durations and at higher temperatures shifting the feldspar to X_{or}^{eq}0.6; SPbx-y-z: SP - Volkesfeld Sanidine, b- plates with polished surfaces parallel (010), x- run duration in days, y- X_{KCl}, z- temperature [°C];the 1^{st} level comprises the longest cracks with the widest spacing, the 2^{nd} level is made up by cracks that are shorter and if the first level is present forms steeple-like structures as described in chapter 7.2, the 3^{rd} level can only be seen in few samples and consists of very short cracks forming between those of the second level; all values in μm

	SPb2-30-1000	SPb2-30-950	SPb2-30-950	SPb8-30-920	SPb2-30-920	SPb4-30-850
1^{st} level	125.4		147.6			
	129.8					
	54.4					
	63.2					
	56.1					
	72.8					
	66.7					
2^{nd} level	15.8	19.7	15.7	25.2	21.1	56.2
	15.8	21.9	13.0	27.9	24.6	48.2
	14.0	23.0	16.2	26.5	21.9	58.4
	20.2	17.5	19.5	25.2	15.8	42.3
	18.4	16.9	20.5	22.5	17.0	48.2
	11.4	13.7	18.4	26.5		51.1
	16.7	15.9	18.9	21.1		47.5
	21.9	19.7	19.5	24.5		56.2
	16.7	21.3	18.4	23.8		49.6
	19.3	15.9	11.9	22.5		57.7
	16.7	15.9	22.7	26.5		
	14.9	15.3	15.7	17.0		
	15.8	13.7	15.7	21.1		
	16.7	16.4	15.1	22.5		
	14.0	21.3	21.1	21.8		
		20.2				
		18.6				
3^{rd} level	10.5				12.6	
	9.7				13.7	
	9.7					
	7.9					
	7.0					
	9.7					
	8.8					
	6.1					
	8.8					
	7.9					
	7.9					
	6.1					
	9.7					
	10.5					

Appendix C

Scheidl et al. (2013)

Scheidl et al. (2013): Chemically induced fracturing in alkali feldspar

The execution of the experiments, BSE imaging and microprobe work were done by Katharina Scheidl and Anne-Kathrin Schäffer. The analysis of the fracture mechanics was mainly conducted by Katharina Scheidl and Elena Petrishcheva.

Phys Chem Minerals
DOI 10.1007/s00269-013-0617-1

ORIGINAL PAPER

Chemically induced fracturing in alkali feldspar

K. S. Scheidl · A. -K. Schaeffer · E. Petrishcheva · G. Habler · F. D. Fischer · J. Schreuer · R. Abart

Received: 11 February 2013 / Accepted: 10 July 2013

Abstract Fracturing in alkali feldspar during Na^+–K^+ cation exchange with a NaCl–KCl salt melt was studied experimentally. Due to a marked composition dependence of the lattice parameters of alkali feldspar, any composition gradient arising from cation exchange causes coherency stress. If this stress exceeds a critical level fracturing occurs. Experiments were performed on potassium-rich gem-quality alkali feldspars with polished (010) and (001) surfaces. When the feldspar was shifted toward more sodium-rich compositions over more than about 10 mole %, a system of parallel cracks with regular crack spacing formed. The cracks have a general (h0l) orientation and do not correspond to any of the feldspar cleavages. The cracks are rather oriented (sub)-perpendicular to the direction of maximum tensile stress. The critical stress needed to initiate fracturing is about 325 MPa. The critical stress intensity factor for the propagation of mode I cracks, K_{Ic}, is estimated as 2.30–2.72 MPa $m^{1/2}$ (73–86 MPa $mm^{1/2}$) from a systematic relation between characteristic crack spacing and coherency stress. An orientation mismatch of 18° between the crack normal and the direction of maximum tensile stress is ascribed to the anisotropy of the longitudinal elastic stiffness which has pronounced maxima in the crack plane and a minimum in the direction of the crack normal.

Keywords Alkali feldspar · Cation exchange · Coherency stress · Chemically induced fracturing · Stress intensity factor

K. S. Scheidl · A.-K. Schaeffer · E. Petrishcheva · G. Habler · R. Abart (✉)
Department of Lithospheric Research, University of Vienna, 1090 Vienna, Austria
e-mail: rainer.abart@univie.ac.at

F. D. Fischer
Institute of Mechanics, Montanuniversität Leoben, 8700 Leoben, Austria

J. Schreuer
Institute for Geology, Mineralogy and Geophysics, Ruhr-University Bochum, 44801 Bochum, Germany

Introduction

Feldspar is the most common mineral in the Earth's crust. It is an abundant rock-forming mineral in igneous and metamorphic rocks and is also found as clastic and authigenic component in sediments. Fracturing in feldspar is a quite common phenomenon. Fracturing is important in a variety of geological processes. It determines the brittle strength, which is crucial in the context of jointing or cataclasis. During rock deformation at conditions of low and medium grade metamorphism, feldspar usually yields by brittle failure (Paschier and Trouw 2005). Fracturing in feldspar is also common during fluid-mediated mineral replacement (Jamtveit et al. 2009). The resistance of a mineral against brittle failure is one of the most fundamental mechanical properties. There is a wealth of literature on fracturing of glass and ceramics. The data base for minerals is comparatively scarce. Broz et al. (2006) and Whitney et al. (2006) used an indentation technique for determining the so-called fracture toughness of a number of rock-forming minerals. This method yields consistent data for the fracture toughness of the rock-forming min-erals, but the kinematics and mechanics of the fracturing process associated with indentation are rather complex, and quantifying fracture toughness from indentation tests may be ambiguous (Quinn and Bradt 2007). Furthermore, the indentation tests are usually done at ambient conditions,

Published online: 24 July 2013

and the mechanical data must be extrapolated over large ranges in temperature when applied to the analysis of the fracturing associated with deformation or fluid mediated alteration at high temperature. In this study, we make use of the strongly anisotropic change in the lattice parameters that is associated with composition change in alkali feldspar to estimate the critical stress necessary for creating mode I cracks. To this end, we analyze the crack patterns forming during Na^+–K^+ exchange between alkali feldspar and a salt melt without application of externally imposed stress. Our approach entirely relies on the elastic stress associated with the eigenstrain due to composition change during cation exchange, and in this respect, it is complementary to mechanical testing by indentation.

Most feldspars pertain to the ternary solid-solution series among the end-member components $NaAlSi_3O_8$ (albite), $KAlSi_3O_8$ (orthoclase), and $CaAl_2Si_2O_8$ (anorthite). The feldspars belong to the group of framework silicates where an ($AlSi_3O_8$)-network is formed by corner-shared TO_4 tetrahedra with T = Al, Si. The Na^+, K^+, and Ca^{2+} cations, which ensure charge balance, are located in large, irregular cavities of the tetrahedral framework (Ribbe 1983).

The two end-member components of the alkali feldspar solid-solution series, albite and orthoclase, are related through Na^+–K^+ cation exchange. Miscibility in the alkali feldspars is complete at temperatures exceeding 550–800 °C, depending on pressure (Brown and Parsons 1988). At lower temperatures, a miscibility gap opens leading to separation of alkali feldspar with intermediate composition into a sodium- and a potassium-rich phase (perthite formation). During cooling, heating, or composition change, the alkali feldspars undergo a variety of phase transformations and structural changes including a ferroelastic monoclinic–triclinic transformation, Al–Si ordering on the tetrahedral sites, and exsolution. Due to the complex sub-solidus phase relations, the alkali feldspars show a wide variety of intra-crystalline microstructures and textures, which potentially bear petrogenetic information (Smith and Brown 1988). Experimental calibrations of the equilibrium phase relations in binary alkali feldspars (Thompson and Waldbaum 1968; Hovis et al. 1991) and in the ternary feldspar system (Fuhrman and Lindsley 1988; Benisek et al. 2010) have provided the basis for two-feldspar thermometry. The thermodynamics of alkali feldspar solid solutions was coupled with diffusion kinetics to derive quantitative models for the dynamics of phase separation during perthite formation (Yund 1984; Petrishcheva and Abart 2009, 2012; Abart et al. 2009a, b).

The lattice dimensions of the alkali feldspars are composition dependent (Kroll et al. 1986; Angel et al. 2012). As a consequence, any chemical heterogeneity in a feldspar single crystal leads to coherency stress. The associated strain energy contributes positively to the free energy and thus counteracts exsolution (Robin 1974). As a consequence, a coherent solvus and the corresponding strain-free solvus are discerned, where the miscibility gap extends to higher temperature in the strain-free case than in the coherent case (Brown and Parsons 1988). Coherency strain does not only affect the equilibrium phase relations, but it can also influence microstructure evolution. For instance, the exsolution lamellae in a perthite are oriented such that the interface energy between host and precipitate is minimized (Bollmann and Nissen 1968; Robin 1974).

Petrovic (1973) and Neusser et al. (2011) observed fracturing in alkali feldspar during Na^+–K^+ cation exchange with NaCl–KCl salt melt, which they interpreted as coherency stress effects. Neusser et al. (2011) presented a mechanical analysis of the stress state in a thin misfitting layer on a (010) surface of an alkali feldspar and concluded that cracks formed sub-perpendicular to the direction of maximum tensile stress.

In this communication, we address chemically induced fracturing in alkali feldspar. We focus on crack patterns that form during Na^+–K^+ cation exchange in samples with well-defined starting geometry. The treatment of Neusser et al. (2011) is extended to the stress analysis on a (001) surface, and use is made of the regularity of the system of parallel cracks emanating from polished (010) and (001) surfaces to attain insight into the fracture mechanics. We fully confirm the observations made earlier by Neusser et al. (2011) and provide more quantitative relations between coherency stress induced by cation exchange and fracturing.

Experimental

Starting material

Gem-quality sanidines from two different localities in the Eifel, Volkesfeld, and Rockeskyller Kopf, were used as starting materials. The composition of sanidine from Volkesfeld can be described as $Or_{84}Ab_{15}Cs_{01}$ whereas

Table 1 Representative chemical analyses of the starting materials

Phase	SiO_2	Al_2O_3	FeO	BaO	Na_2O	K_2O	MgO	Tot.	X_{Or}	X_{Ab}	X_{Cs}
PR	63.98	19.05	0.16	0.88	1.84	13.61	0.00	99.51	0.84	0.15	0.01
EPR	64.08	18.97	0.15	1.31	2.81	12.10	0.01	99.44	0.72	0.26	0.02

PR: Volkesfeld sanidine, EPR: Rockeskyller Kopf sanidine

the sanidine from the Rockeskyller Kopf is more sodium-rich with a composition of $Or_{72}Ab_{26}Cs_{02}$ (see Table 1). Both sanidines are characterized as monoclinic with space group C2/m, disordered (Al, Si) distribution ($\Sigma t_1 = 61$: Volkesfeld, $\Sigma t_1 = 0.58-0.62$: Rockeskyll) and are homogenous on the nanometer scale (Neusser et al. 2011; Demtroeder 2011). The crystals are optically clear and, apart from the (010) and (001) cleavages, devoid of cracks or any other flaws.

Two different sets of experiments were performed. On the one hand, crystal fragments obtained from crushing and sieving to a size of 100−200 μm were used to determine the critical composition shift needed to initiate fracturing on the (010) and (001) cleavage planes. On the other hand, crystals were machined to plates of 3 mm by 3 mm by 1 mm with polished (001) or (010) faces for later use in experiments, where well-defined starting geometry was important.

Cation exchange experiments

The Na^+–K^+ exchange experiments were done between alkali felspar and an NaCl–KCl salt melt at close to ambient pressure and without adding a fluid. About 0.1 g of crushed feldspar or one feldspar plate together with a NaCl–KCl salt mixture was sealed into quartz glass tubes with an outer diameter of 9 mm and an inner diameter of 7 mm under vacuum. The NaCl/KCl ratio of the salt mixture was chosen to produce the desired chemical shift of the alkali feldspar based on the Na/K fractionation data for feldspar—salt melt equilibria at 850 °C (Neusser et al. 2011). To ensure a constant composition of the salt melt during the exchange experiments, a 40-fold molar excess of Na^+ and K^+ cations in the salt relative to the feldspar was applied. The samples were then annealed under ambient pressure at 850 °C in a muffle furnace for 7–8 days (see Tables 2, 3). After annealing, the samples were quenched in cold water within seconds. Then, the tubes were opened, the salt was dissolved with deionized water, and the feld-spar was quantitatively retrieved. Grain mounts were pre-pared from the crystal fragments, and the feldspar plates were cut perpendicular to the polished surfaces and embedded in resin for preparation of polished sections.

Table 2 Results of the experiments conducted for determining the critical composition shift needed for initiation of fracturing

Label	X_{Or}^{init}	X_{KCl}	X_{Or}^{fin}	Shift	Cracks
SPR7-35-850	0.84	0.35	0.72	0.12	No
SPR7-34-850	0.84	0.34	0.71	0.13	Yes
SPR7-33-850	0.84	0.33	0.69	0.15	Yes
SPR7-32-850	0.84	0.32	0.68	0.16	Yes
SPR7-31-850	0.84	0.31	0.66	0.18	Yes

Analytical techniques

Scanning electron microscopy

For back-scatter electron (BSE) imaging, an FEI Inspect S scanning electron microscope with a tungsten filament was used. The images were taken at 10 and 15-kV beam acceleration voltage and 8-nA beam current.

Electron backscatter diffraction (EBSD) analyses were performed using a FEI Quanta 3D FEG instrument at the

Table 3 Relation between crack spacing and chemical shift

Label	Polished faces	X_{Or} init.	X_{KCl} melt	X_{Or} exch.	Shift	AS (μm)	AA (μm)	CS (μm)	CL (μm)
PR8-20-850	(001)	0.84	0.20	0.27	0.57	14	80	9	101
PR8-25-850	(001)	0.84	0.25	0.50	0.34	24	83	24	82
PR8-28-850	(001)	0.84	0.28	0.60	0.24	40	83	40	65
SP8-30-850	(001)	0.84	0.30	0.64	0.20	50	83	50	104
PRb8-20-850	(010)	0.84	0.20	0.27	0.57	10	7	10	151
PRb8-25-850	(010)	0.84	0.25	0.50	0.34	15	7	15	80
PRb8-28-850	(010)	0.84	0.28	0.60	0.24	30	7	30	62
SPb-30-850	(010)	0.84	0.30	0.64	0.20	45	7	45	46
EPR8-20-850	(001)	0.72	0.20	0.27	0.45	15	73	15	80
EP8-22-850	(001)	0.72	0.22	0.37	0.35	18	73	18	100
EPR8-25-850	(001)	0.72	0.25	0.50	0.22	23	73	23	32
EPR8-28-850	(001)	0.72	0.28	0.60	0.12	55	73	55	28
EPRb8-20-850	(010)	0.72	0.20	0.27	0.45	8	17	8	80
EPb8-22-850	(010)	0.72	0.22	0.37	0.35	23	17	12	32
EPRb8-25-850	(010)	0.72	0.25	0.50	0.22	35	17	37	21
EPRb8-28-850	(010)	0.72	0.28	0.60	0.12	145	17	152	18

AS apparent crack spacing, *AA* apparent crack angle, *CS* crack spacing, *CL* crack length

Department of Lithospheric Research (University of Vienna, Austria). The system is equipped with a field-emission electron source and an EDAX Digiview IV EBSD camera. The software packages OIM Data Collection and Analysis have been applied for EBSD data acquisition and processing. Prior to analysis, single crystals were embedded in epoxy resin, then first polished mechanically and subsequently chemo-mechanically using a colloidal silica suspension with pH 9.2–10 as polishing agent on a rotary polisher. Conductivity of the sample surface was established by thin carbon coating using a single carbon thread at a distance of about 8 cm between thread and sample at vacuum conditions of $<10^{-5}$ mbar during evaporation. For EBSD analyses, a working distance of 12 or 14 mm and a sample tilt of 70° were applied. The edges of the crystals were aligned parallel to the *x*- and *y*-directions of the scan reference system by stage rotation. The electron-beam settings were 15-kV accelerating voltage and 4-nA beam current in analytical mode (SEM aperture 1 mm). A 2 by 2 or 4 by 4 binning of the EBSD camera resolution was applied, and the camera exposure time and pattern contrast enhancement settings were adjusted for each grain according to the pattern quality. Hough settings of 1° 2θ step size, a binned pattern size of 160 pixels, and a minimum peak distance of 10° were applied for indexing 6–14 Hough peaks. A medium (9 by 9) or large (13 by 13) convolution mask was applied to the Hough space in order to eliminate artifacts and enhance weak bands. Only the interior portion of the EBSD pattern (ρ-fraction = 70–85 % of the Hough space) was used for indexing. EBSD mapping was performed by beam scanning across a 100 µm by 100 µm or 150 µm by 150 µm sized sample area of each crystal using a step size of 15 µm. Thus, 45–100 data points were collected for each crystal. In case of inconsistent indexing results for single maps, the data statistics as well as the different solutions for single point analyses were checked in order to detect the misindexed data points. All pole figures displayed in this work refer to the upper hemisphere.

Mineral chemical analysis and element mapping

Mineral chemical analyses and element mapping were done on a Cameca SX 100 electron microprobe at the Department of Lithospheric Research (University of Vienna, Austria). The elements Na, K, Fe, Ba, Mg, Al, and Si were considered in mineral chemical analysis. The standards and spectrometer settings are listed in Table 4. An acceleration voltage of 15 kV and a beam current of 20 nA were applied. A 6-µm defocussed beam was used to minimize loss of Na by evaporation. For element mapping of Na, K, Al, Ba, and Si, an accelerating voltage of 10 kV, a beam current of 50 nA, a dwell time of 60 ms per pixel, and stage scanning mode with 0.6 µm step size were used.

Table 4 Instrument setting and standard materials used for reference in electron microprobe analysis

Element	Spectrometer crystal	Standard	Counting time peak (s)	Counting time peak (s)
Na	TAP	Albite	8	4
K	PET	Orthoclase	8	4
Fe	LIF	Almandine	20	10
Ba	PET	BaSO4	25	15
Mg	TAP	Olivine	20	10
Al	TAP	Almandine	8	4
Si	TAP	Quartz	15	7.5

Results

Characteristics of the cracks

When a grain of alkali feldspar is exposed to NaCl–KCl salt melt, Na^+–K^+ cation exchange produces a chemically altered zone on the surface of the grain, and the alteration front progresses into the grain interior with time. Associated with the chemical change is the formation of cracks. As already described by Neusser et al. (2011), two fundamentally different crack patterns form depending on the direction of composition shift (see Fig. 1).

When the feldspar is shifted toward more sodium-rich compositions, a regular hierarchical pattern of cracks forms (Fig. 1a). The first hierarchical level is represented by a system of sub-parallel cracks, which extend approximately parallel to a (h0l) plane. These cracks are not perfectly planar but are somewhat uneven. They enclose an angle of 8°–18° with the positive *c*-axis, measured toward the positive *a*-axis. This corresponds to an angle of 73°–83° with the negative *a*-axis measured toward the positive *c*-axis, given that $\beta = 116°$ (see Figs. 2, 3). It is important to note that the cracks follow a general plane in the feldspar lattice, which is not related to any of the cleavages. Chemical alteration extends into the grain interior along the cracks (see Fig. 4) indicating that the cracks formed during cation exchange and cannot be interpreted as quench phenomena. The observed chemical patterns suggest that the salt melt penetrated into the grain interior along the cracks and chemical alteration further spread into the crystal from the crack surfaces. The cracks of the second hierarchical level are perfectly straight and run parallel to the (010) and (001) cleavages (see Fig. 1a). These cracks are devoid of any alteration haloes indicating that they formed very late during the experiment and may be interpreted as quenching effects. The orientation of the cracks of the first hierarchical level slightly differs between the Volkesfeld sanidine and the sanidine from the Rockeskyller Kopf. For the sanidine from Volkesfeld with its original $X_{Or} = 0.84$, the angle between the cracks and the negative *a*-axis is

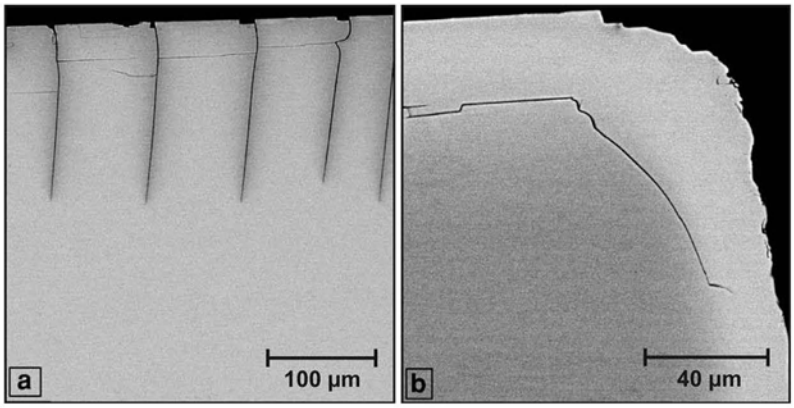

Fig. 1 Cracks formed from Na^+–K^+ cation exchange between gem-quality sanidine from Volkesfeld and a NaCl–KCl salt melt; run duration was 16 days: **a** BSE image of a system of parallel cracks emanating from a polished (001) surface of sanidine shifted from $X_{Or} = 0.84 \rightarrow 0.64$; the *dark shades of gray* along the cracks reflect low potassium contents in the exchanged portions; **b** BSE image of cracks along the transition zone between the altered rim and the unexchanged core of a sanidine shifted from $X_{Or} = 0.84 \rightarrow 1.00$; the *light gray shade* in the outermost zone reflects the increased potassium content in the chemically altered domain

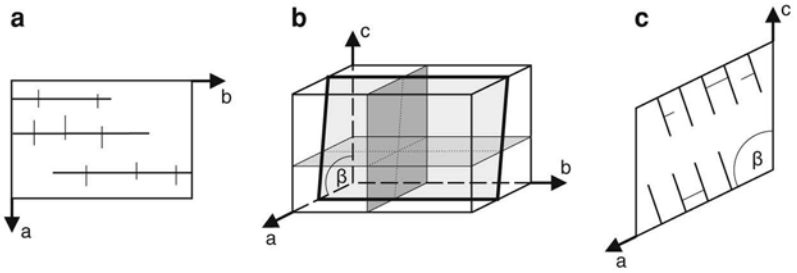

Fig. 2 Schematic sketch of a plate with parallel cracks of the first hierarchical level and subordinate cracks of the second hierarchical level; **a** view onto the (001) surface, view direction parallel c^*; **b** oblique view, *planes with light gray* and *dark gray shades* represent cracks of the first and second hierarchical level, respectively, **c** view onto the (010) surface, view direction parallel *b*

measured as 83° ($\sigma = 2.0°$; 48 measurements in 3 samples), and for the sanidine from the Rockeskyller Kopf with its original X_{Or} = 0.72 the angle is 73° ($\sigma = 2.8°$; 33 measurements in 2 samples). During the incipient stages of cation exchange, a few short cracks emanate perpendicular to the surface of the grains. With increasing run duration, the number of cracks increases, the cracks become longer, and they are deflected into the common (h0l) plane. Eventually no more cracks develop; at this stage, a characteristic crack spacing between 10 and 50 µm has been established, depending on the extent of composition shift (see below).

In contrast, when the sanidine is shifted toward more potassium-rich compositions, a potassium-enriched rim develops, which is separated from the unaltered grain interior by a more or less diffuse transition zone. The lattice parameters in the potassium-enriched rim are larger than in the unaltered substratum. The lattice mismatch leads to coherency stress and eventually cracks form along the transition zone between core and rim, a phenomenon that is particularly pronounced at the grain edges (Fig. 1b).

Critical shift for fracturing

To identify the critical composition shift needed to initiate fracturing fragments of crushed sanidine with initial $X_{Or} = 0.84$ were exchanged with NaCl–KCl salt melt at 850 °C for 7 days. The X_{KCl} of the salt mixture was varied from 0.35 to 0.31 in 1 mole % steps to achieve successively increasing composition shifts toward more sodium-rich compositions in the feldspar (see Table 2). The first cracks formed on the (010) and (001) (cleavage) surfaces, when X_{KCl} was 0.34 corresponding to an exchanged feldspar with X_{Or} = 0.71. The first cracks were thus observed when

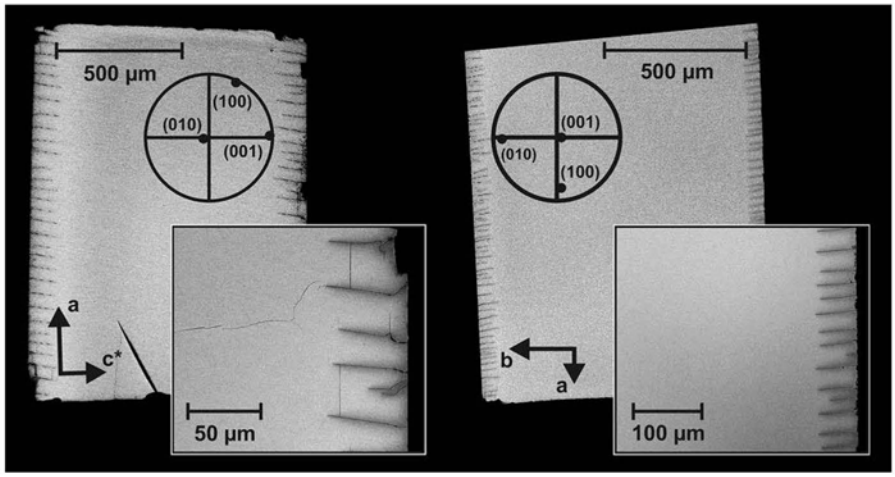

Fig. 3 System of parallel cracks in a sanidine from Volkesfeld; run duration 8 days; (*a*) sanidine with polished (001) faces shifted from $X_{Or} = 0.84 \rightarrow 0.64$; view onto the (010) plane; (*b*) sanidine with polished (010) faces shifted from $X_{Or} = 0.84 \rightarrow 0.60$; view onto the (001) plane

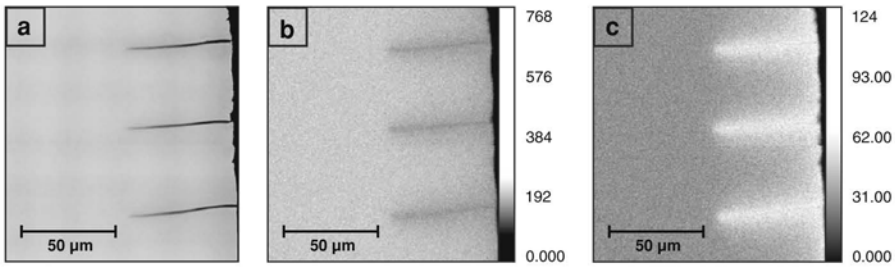

Fig. 4 **a** BSE image; **b** K-distribution map, **c** Na-distribution map showing cracks with halos enriched in sodium and depleted in potassium indicating that the cracks indeed formed during cation exchange; *numbers* on the color lookup tables indicate counts per second

the original feldspar was shifted over 13 mole % from its original composition.

Dependence of crack spacing on chemical shift

It was already noted qualitatively by Neusser et al. (2011) that the characteristic crack spacing decreases with increasing extent of chemical shift, i.e., with increasing coherency stress between the unaltered and the exchanged portions of the crystal. This relation could, however, not be verified quantitatively by the latter authors, because only crystal fragments were investigated where the fracture patterns were substantially influenced by irregularities on the grain surface. In our investigation, crystal plates with polished (001) or (010) faces were used to avoid the influence of surface topography on the nucleation of cracks. The initial compositions of the crystals were $X_{Or} = 0.84$ and $X_{Or} = 0.72$, and the NaCl/KCl ratio of the salt melt was varied systematically to attain composition shifts between 20 and 55 mole %. The run durations were varied between 8 and 32 days. The long time runs produced rather complex crack patterns, and only the results from 8 day experiments were used for establishing the relation between crack spacing and chemical shift (see Table 3, Fig. 5).

Figures 6 and 7 show the system of parallel cracks emanating from the polished (010) and (001) surfaces of sanidine from Volkesfeld and from the Rockeskyller Kopf, respec-tively. The crystals were mounted in resin in such a way that the polished surfaces of the crystals, either (010) or (001), were oriented perpendicular to the surface of the mount. The crystal orientations were determined using EBSD, and the corresponding pole figures are shown as inserts. As the cracks

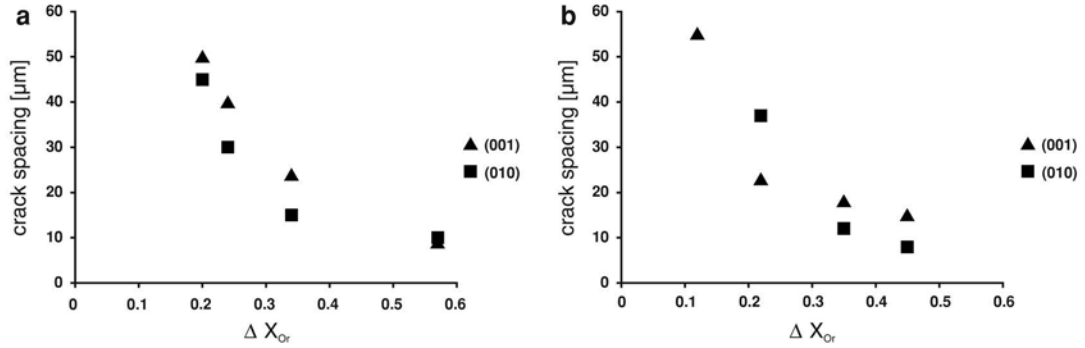

Fig. 5 Crack spacing as a function of the chemical shift $\Delta X = X_{Or}^{init} - X_{Or}^{fin}$; **a** sanidine from Voklesfeld, $X_{Or}^{init} = 0.84$; **b** sanidine from the Rockeskyller Kopf, $X_{Or}^{init} = 0.72$

run parallel to an (h0l) plane, they are always perpendicular to the polished (010) surfaces of the crystals, and the traces of the cracks that are visible on the surface of a particular sample are perpendicular to the trace of the polished (010) surface of the crystal. In general, the cracks are, however, not perpendicular to the surface of the polished mount, and the spacing between the traces of the cracks does not correspond to the actual spacing between the cracks. We denote the observed spacing between the crack traces as h'. Given that the crystallographic orientation has been determined from EBSD analyses and the true angle φ of intersection between the cracks and the (001) surface is known ($\varphi = 83°$ for the sanidine from Volkesfeld, and $\varphi = 73°$ for the sanidine from the Rockeskyller Kopf) the true angle ϵ between the sample surface and the cracks can be determined. The crack spacing h is then obtained from ϵ and h' according to

$$h = \sin\epsilon \cdot h'.$$

In samples where crystals with polished (001) faces have been mounted, the traces of the cracks are generally not perpendicular to the traces of the polished (001) planes, and the observed spacing between the traces of the cracks differs from the actual crack spacing. Again, we denote the spacing between the crack traces as h', and we denote the angle between the crack traces and the trace of the (001) surface as φ'. Given that φ the true angle of intersection between the cracks and the (001) surface is known, the actual crack spacing h is determined from the observed h' and φ' according to

$$h = \frac{\cos\varphi}{\cos\varphi'} \cdot h'.$$

The cracks emanating from the polished surfaces show a very regular spacing. In Fig. 5, the crack spacing is plotted as a function of composition shift. The crack spacing systematically decreases with increasing composition shift for both sanidines and for cracks emanating from both the (010) and (001) faces.

Discussion

Stress in a thin misfitting layer on a planar surface

It is inferred from the experimental evidence that formation of the cracks is related to the shift in composition caused by Na^+–K^+ exchange. Although chemically induced fracturing is observed with both directions of chemical shift, we restrict our analysis to the case with the chemical shift toward more sodium-rich compositions. This is due to the fact that regular crack patterns with simple geometry only occur in this case, and based on a straightforward mechanical analysis material properties can be extracted from the observed crack patterns. The cracks produced by shifts toward more potassium-rich compositions have irregular shape and extracting material parameters from an inverse approach does not appear to be feasible. Numerical forward modeling could potentially reproduce the observed crack patterns. For such modeling, the material properties would have to be known as input parameters though.

The lattice parameters of alkali feldspar depend on composition. A shift of a potassium-rich alkali feldspar toward more sodium-rich compositions leads to an anisotropic contraction of the lattice and a change in the angle β. We only consider composition shifts small enough to ensure that the monoclinic symmetry is preserved. The lattice contraction is most pronounced in the *a*-direction and by a factor of about five smaller along the *b*- and *c*-directions (Kroll and Ribbe 1983; Kroll et al. 1986). During Na^+–K^+ exchange, a zone in equilibrium with the salt melt develops at the grain surface and successively spreads into the grain interior by interdiffusion of Na^+ and

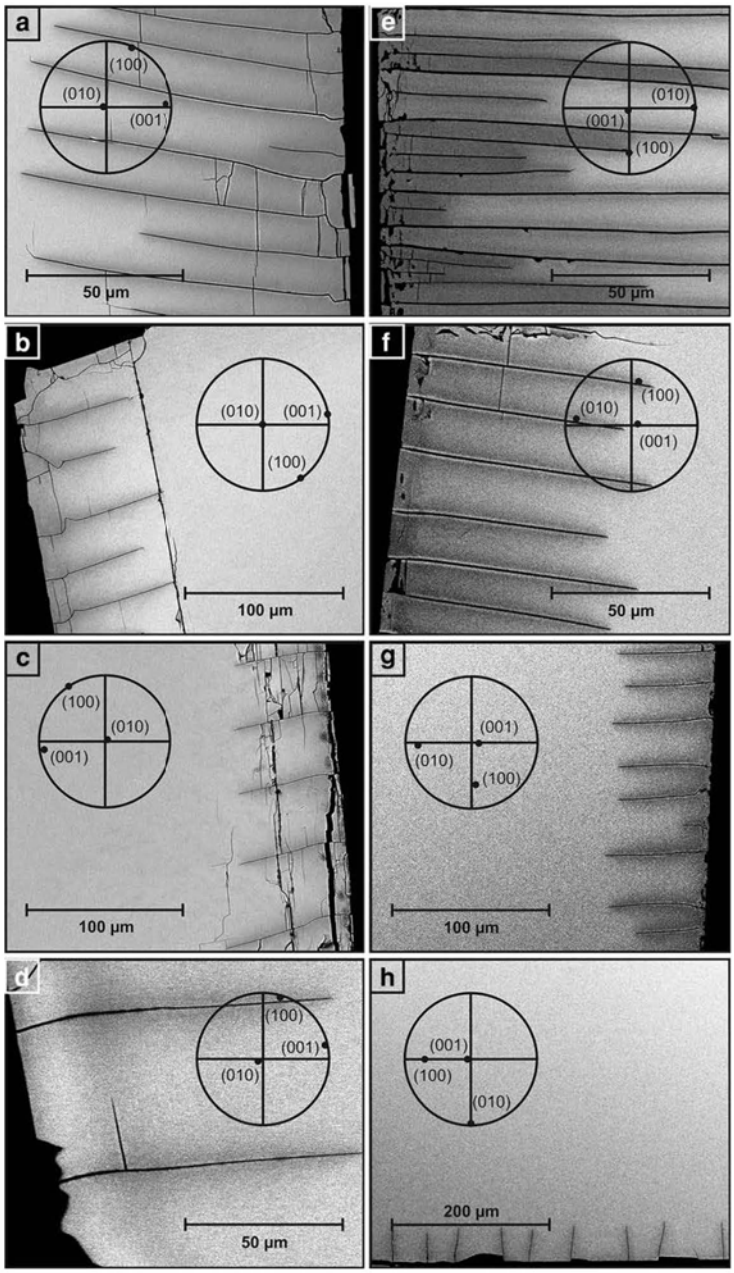

Fig. 6 BSE images showing the relations between crack spacing and chemical shift in sanidine from Volkesfeld with initial $X_{Or} = 0.84$; run duration: 7 days; the X_{KCl} of the salt melt was changed systematically; plate with (001) (**a**–**d**) and (010) (**e**–**f**) polished faces were used; **a** X_{Or} (exchanged) = 0.27; **b** X_{Or} (exchanged) = 0.50; **c** X_{Or} (exchanged) = 0.60; **d** X_{Or} (exchanged) = 0.64; **e** X_{Or} (exchanged) = 0.27; **f** X_{Or} (exchanged) = 0.50; **g** X_{Or} (exchanged) = 0.60 **h** X_{Or} (exchanged) = 0.64

K^+ on the alkali sub-lattice. Along the transition zone between the exchanged rim and the grain's interior, the concentration of the cations varies while the tetrahedral framework remains coherent. This produces elastic strain and therefore coherency stress that compensates for the lattice misfit. If this coherency stress exceeds a critical value, fracturing is initiated. Cracks start to form at an early stage of cation exchange when only a thin layer of

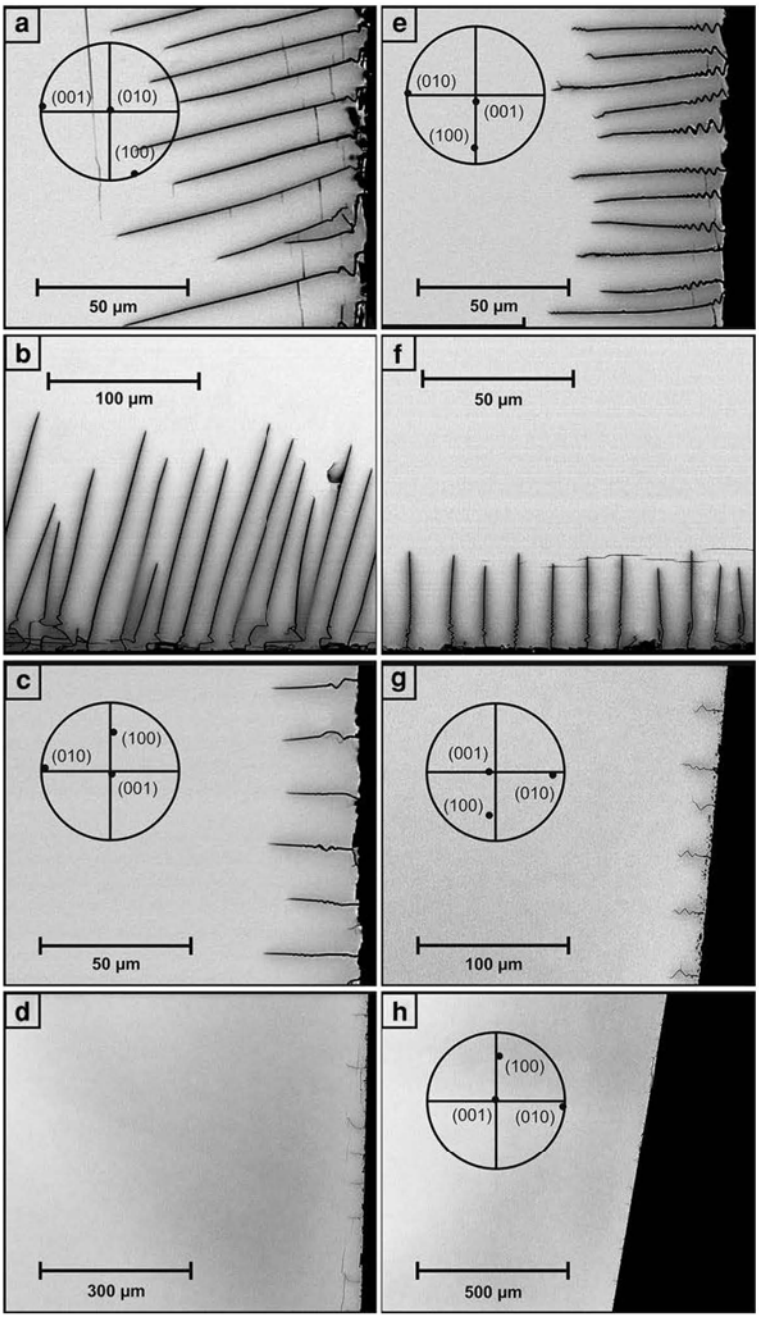

Fig. 7 BSE images showing the relations between crack spacing and chemical shift in sanidine from Rockeskyller Kopf with initial $X_{Or} = 0.72$; run duration: 7 days; the X_{KCl} of the salt melt was changed systematically; plates with (001) (**a**–**d**) and (010) (**e**–**f**) polished faces were used; **a** X_{Or} (exchanged) = 0.27; **b** X_{Or} (exchanged) = 0.50; **c** X_{Or} (exchanged) = 0.60; **d** X_{Or} (exchanged) = 0.64; **e** X_{Or} (exchanged) = 0.27; **f** X_{Or} (exchanged) = 0.50; **g** X_{Or} (exchanged) = 0.60 **h** X_{Or} (exchanged) = 0.64

chemically altered feldspar has been produced at the grain surface. At this stage, the unaltered domain in the grain interior is volumetrically by far dominant and, as a consequence, mechanically much stiffer than the thin misfitting surface layer. In this situation, the elastic strain and the associated coherency stress are localized in the thin misfitting surface layer. The unaltered substrate may be approximated as rigid.

The mechanical analysis of the stress state associated with the development of a thin misfitting layer due to composition change at the surface of a rigid substrate involves two basic tasks: Firstly, the eigenstrain due to composition change is calculated from the composition-dependent change in lattice parameters. Secondly, the elastic stress induced by the eigenstrain due to composition change is calculated for specific boundary conditions that reflect the orientation of the surface. We will restrict our analysis to planar surfaces of a monoclinic crystal.

Eigenstrain by composition change

As usual, we describe the crystal lattice with three vectors **a**, **b**, and **c**, where for the monoclinic system under consideration **b** is the diad axis and $\alpha = \gamma = 90°$ and $\beta > 90°$. We employ the orthogonal coordinate system *Oxyz* generated by **a**, **b**, and $\mathbf{c}^\star$, where $\mathbf{c}^\star \parallel \mathbf{a} \times \mathbf{b}$. Let the composition-induced change in lattice parameters in a monoclinic alkali feldspar be (see Fig. 8)

$$a_0, b_0, c_0, \beta_0 \rightarrow a_1, b_1, c_1, \beta_1.$$

According to the monoclinic symmetry, we have for the corresponding eigenstrain tensor, ε_{ij}

$$\varepsilon_{ij} = \begin{pmatrix} \varepsilon_{11} & 0 & \varepsilon_{13} \\ 0 & \varepsilon_{22} & 0 \\ \varepsilon_{13} & 0 & \varepsilon_{33} \end{pmatrix},$$

with (for a detailed derivation see the ''Appendix'' section)

$$\varepsilon_{11} = \frac{a_1}{a_0} - 1,$$

$$\varepsilon_{22} = \frac{b_1}{b_0} - 1,$$

$$\varepsilon_{33} = \frac{c_1 \sin\beta_1}{c_0 \sin\beta_0} - 1,$$

$$\varepsilon_{13} = \frac{c_1 \cos\beta_1}{2c_0 \sin\beta_0} - \frac{a_1 \cos\beta_0}{2a_0 \sin\beta_0}.$$

The composition dependence of the lattice parameters for disordered alkali feldspar was documented by Kroll et al. (1986). We use the lattice parameters that are given by the latter authors for the compositions $X_{Or} = 0.84$ and $X_{Or} = 0.69$ (see Table 5), because they most closely represent the com-position range of interest in the context of our experiments. Based on these data, we obtain $\varepsilon_{11} = -7.6 \times 10^{-3}$, $\varepsilon_{22} = -5.1 \times 10^{-4}$, $\varepsilon_{33} = -5.9 \times 10^{-4}$, $\varepsilon_{13} = -1.9 \times 10^{-3}$ for a composition shift of $X_{Or} = 0.84 \rightarrow 0.69$.

Stress and strain in a thin misfitting layer on a (010) surface

We now consider formation of a thin misfitting layer on a (010) surface of monoclinic alkali feldspar. The geometry of the system to be analyzed is shown schematically in Fig. 9. We follow the analysis of Neusser et al. (2011), and only a brief summary of the approach is given here. The total strain ε_{ij}^{tot} results from a combination of the eigenstrain due to composition change ε_{ij} and elastic strain ε_{ij}^{el}

$$\varepsilon_{ij}^{tot} = \varepsilon_{ij} + \varepsilon_{ij}^{el}. \quad (1)$$

When a thin misfitting layer forms on a (010) surface of a stiff, i.e., formally rigid alkali feldspar substratum, coherency of the tetrahedral framework across the transition zone requires that the in-plane components of the total strain vanish, i.e., $\varepsilon_{11}^{tot} = \varepsilon_{33}^{tot} = \varepsilon_{13}^{tot} = 0$ (see Fig. 9). The components ε_{12}^{tot} and ε_{23}^{tot} vanish because of the monoclinic symmetry. Applying Eq. (1) we obtain for the elastic strain tensor $\varepsilon_{ij}^{el} = \varepsilon_{ij}^{tot} - \varepsilon_{ij}$

$$\varepsilon_{ij}^{el} = \begin{pmatrix} -\varepsilon_{11} & 0 & -\varepsilon_{13} \\ 0 & \varepsilon_{22}^{el} & 0 \\ -\varepsilon_{13} & 0 & -\varepsilon_{33} \end{pmatrix}.$$

The strain component ε_{22}^{el} remains unspecified and must be calculated from additional constraints. We introduce Voigt notation

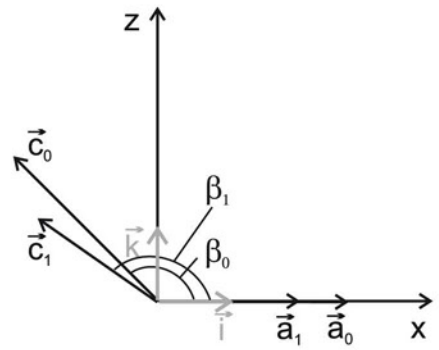

Fig. 8 Monoclinic coordinate system with unit vectors $\mathbf{a}_0$, $\mathbf{b}_0$, $\mathbf{c}_0$ and angle β_0 before and $\mathbf{a}_1$, $\mathbf{b}_1$, $\mathbf{c}_1$ and angle β_1 after transformation; view direction is along the positive crystallographic *b*-axes; also shown is the orthogonal coordinate system *Oxyz* with $Ox \parallel \mathbf{a}$, $Oy \parallel \mathbf{b}$, $Oz \parallel \mathbf{c}^\star$

Table 5 Composition dependence of lattice parameters of alkali feldspar after Kroll et al. (1986)

	$X_{Or} = 0.85$	$X_{Or} = 0.69$
a (Å)	8.54	8.47
b (Å)	13.026	13.02
c (Å)	7.171	7.168
β	115.99°	116.01°

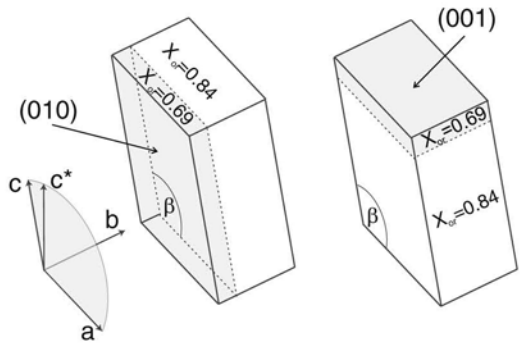

Fig. 9 Schematic sketch of the geometric setting of a misfitting surface layer on a (010) (*left*) and (001) (*right*) surface of alkali feldspar

$$\varepsilon_{ij}^{\mathrm{el}} \rightarrow \varepsilon_{i}^{\mathrm{el}},$$

where the indices transform as: $11 \rightarrow 1$, $22 \rightarrow 2$, $33 \rightarrow 3$, $23, 32 \rightarrow 4$, $13, 31 \rightarrow 5$, $12, 21 \rightarrow 6$ (see Fig. 9). According to Hooke's law we have

$$\sigma_i = c_{ij}\varepsilon_j^{\mathrm{el}}, \tag{2}$$

where

$$\sigma_i = \begin{pmatrix} \sigma_1 \\ \sigma_2 \\ \sigma_3 \\ \sigma_4 \\ \sigma_5 \\ \sigma_6 \end{pmatrix} \quad \text{and} \quad \varepsilon_j^{\mathrm{el}} = \begin{pmatrix} \varepsilon_1^{\mathrm{el}} \\ \varepsilon_2^{\mathrm{el}} \\ \varepsilon_3^{\mathrm{el}} \\ \frac{1}{2}\varepsilon_4^{\mathrm{el}} \\ \frac{1}{2}\varepsilon_5^{\mathrm{el}} \\ \frac{1}{2}\varepsilon_6^{\mathrm{el}} \end{pmatrix}$$

are the components of stress and elastic strain, and c_{ij} is the matrix of elastic constants, respectively, in Voigt notation, and Einstein summation is implied.

As cation exchange took place in a liquid environment, i.e., no shear stresses were transferred, and at close to ambient pressure, the out of plane stress components on the crystal surface vanish, and we have $\sigma_2 = \sigma_4 = \sigma_6 = 0$. Applying Eqs. (1) and (2), we obtain a system of linear equations

$$\begin{pmatrix} \sigma_1 \\ 0 \\ \sigma_3 \\ 0 \\ \sigma_5 \\ 0 \end{pmatrix} = \begin{pmatrix} c_{11} & c_{12} & c_{13} & 0 & c_{15} & 0 \\ c_{21} & c_{22} & c_{23} & 0 & c_{25} & 0 \\ c_{31} & c_{32} & c_{33} & 0 & c_{35} & 0 \\ 0 & 0 & 0 & c_{44} & 0 & c_{46} \\ c_{51} & c_{52} & c_{53} & 0 & c_{55} & 0 \\ 0 & 0 & 0 & c_{64} & 0 & c_{66} \end{pmatrix} \begin{pmatrix} -\varepsilon_1 \\ \varepsilon_2^{\mathrm{el}} \\ -\varepsilon_3 \\ 0 \\ -\frac{1}{2}\varepsilon_5 \\ 0 \end{pmatrix}.$$

Four of the six equations are independent, they can be solved to provide the unknown stresses σ_1, σ_3, σ_5, and the unknown elastic strain $\varepsilon_2^{\mathrm{el}}$. We interpolate the elastic constants for monoclinic alkali feldspar given by Schreuer et al. (in prep.) for $T = 850°$ C (see Table 6). For the composition change of $X_{Or} = 0.84 \rightarrow 0.69$, we obtain the stress

Table 6 Elastic constants (GPa) from J. Schreuer et al. (in prep.) referring to the standard orientation $Ox \parallel a$, $Oy \parallel b$ (diad axis), $Oz \mid c^{\star}$ and calculated for $T = 850$ °C

	$c_{i,1}$	$c_{i,2}$	$c_{i,3}$	$c_{i,4}$	$c_{i,5}$	$c_{i,6}$
$c_{1,j}$	61.8	43.8	34.0	0	−4.4	0
$c_{2,j}$	43.8	159.5	14.6	0	1.5	0
$c_{3,j}$	34.0	14.6	129.2	0	−28.9	0
$c_{4,j}$	0	0	0	14.5	0	0.3
$c_{5,j}$	−4.4	1.5	−28.9	0	29.4	0
$c_{6,j}$	0	0	0	0.3	0	36.4

$$\sigma_{ij}/\mathrm{GPa} = \begin{pmatrix} 0.39 & 0 & -0.025 \\ 0 & 0 & 0 \\ -0.025 & 0 & 0.27 \end{pmatrix}$$

and the elastic strain

$$\varepsilon_{ij}^{\mathrm{el}} = \begin{pmatrix} 0.076 & 0 & 9.6 \times 10^{-4} \\ 0 & -0.0021 & 0 \\ 9.6 \times 10^{-4} & 0 & 5.9 \times 10^{-4} \end{pmatrix},$$

again adopting tensor notation. According to the monoclinic symmetry of the feldspar, only the σ_2 principle axis of the stress tensor is parallel to the $\varepsilon_2^{\mathrm{el}}$ principle axis of the elastic strain tensor, and they are both parallel to the crystallographic b-axis (diad axis). The σ_1 and σ_3 principle axes of the stress tensor and the $\varepsilon_1^{\mathrm{el}}$ and $\varepsilon_3^{\mathrm{el}}$ principle axes of the strain tensor lie in the a−c plane. They are, however, in general not parallel to the crystallographic a- o r c-axes, neither are the principle axes of the stress and the strain tensors parallel to each other. The principle components of the stress tensor and the direction of principle axes are given by the well-known relations (Nye 1985)

$$\sigma_1 = \frac{\sigma_{11} + \sigma_{33}}{2} + \sqrt{\left(\frac{\sigma_{11} + \sigma_{33}}{2}\right)^2 + \sigma_{13}^2} = 0.40\,\mathrm{GPa},$$

$$\sigma_3 = \frac{\sigma_{11} + \sigma_{33}}{2} - \sqrt{\left(\frac{\sigma_{11} + \sigma_{33}}{2}\right)^2 + \sigma_{13}^2} = 0.27\,\mathrm{GPa},$$

$$\phi = \frac{1}{2}\arctan\frac{2\sigma_{13}}{\sigma_{11} - \sigma_{33}} = 11.72°.$$

The representation quadric of the derived stress tensor is shown in Fig. 10. The crack direction is roughly perpendicular to the σ_1 principle axis of the stress. The latter corresponds to the largest principle component σ_1, i.e., to the maximum tensile stress. Noting that fracturing is first initiated after a composition shift of 0.13 X_{Or}, the critical tensile stress that is needed to initiate fracturing on a (010) surface of alkali feldspar is derived from the above example, which was calculated for a composition shift of 0.16 X_{Or}, a s $\sigma_{1c} = 0.13/0.16\,\sigma_1 = 0.325$ GPa.

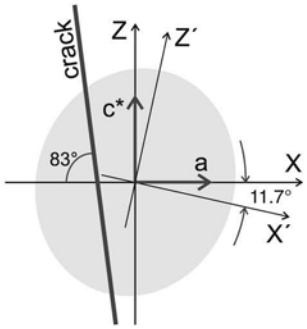

Fig. 10 Crack direction and representation quadric of the stress tensor in the $x - z$ plane; X' and Z' correspond to the directions of σ_1 and σ_3, i.e., to the directions of maximum and minimum tensile stress, respectively, in the (010) plane

Stress and strain in a thin misfitting layer on a (001) surface

We now investigate the strain and associated stress induced by chemical change in a thin layer on a (001) surface of monoclinic alkali feldspar. The conditions for the total stress imposed on a thin misfitting layer on a (001) surface through a coherent contact with a mechanically stiff, i.e., formally rigid substratum are $\varepsilon_{11}^{\mathrm{tot}} = \varepsilon_{22}^{\mathrm{tot}} = \varepsilon_{12}^{\mathrm{tot}} = 0$ (see Fig. 9). Applying again Eq. (1) and noting that $\varepsilon_{12}^{\mathrm{tot}} = \varepsilon_{23}^{\mathrm{tot}} = 0$ because of the monoclinic symmetry we have for the elastic strain tensor

$$\varepsilon_{ij}^{\mathrm{el}} = \begin{pmatrix} -\varepsilon_{11} & 0 & \varepsilon_{13}^{\mathrm{el}} \\ 0 & -\varepsilon_{22} & 0 \\ \varepsilon_{13}^{\mathrm{el}} & 0 & \varepsilon_{33}^{\mathrm{el}} \end{pmatrix}.$$

In this case, two strain components $\varepsilon_{13}^{\mathrm{el}}$ and $\varepsilon_{33}^{\mathrm{el}}$ must be calculated from additional constraints. Again, due to the fact that the chemical alteration took place in a liquid under a pressure of less than one atmosphere, the out of plane stress components vanish and $\sigma_{13} = \sigma_{23} = \sigma_{33} = 0$. Applying Hooke's law (in Voigt notation), we obtain a system of linear equations

$$\begin{pmatrix} \sigma_1 \\ \sigma_2 \\ 0 \\ 0 \\ 0 \\ \sigma_6 \end{pmatrix} = \begin{pmatrix} c_{11} & c_{12} & c_{13} & 0 & c_{15} & 0 \\ c_{21} & c_{22} & c_{23} & 0 & c_{25} & 0 \\ c_{31} & c_{32} & c_{33} & 0 & c_{35} & 0 \\ 0 & 0 & 0 & c_{44} & 0 & c_{46} \\ c_{51} & c_{52} & c_{53} & 0 & c_{55} & 0 \\ 0 & 0 & 0 & c_{64} & 0 & c_{66} \end{pmatrix} \begin{pmatrix} -\varepsilon_1 \\ -\varepsilon_2 \\ \varepsilon_3^{\mathrm{el}} \\ 0 \\ \frac{1}{2}\varepsilon_5^{\mathrm{el}} \\ 0 \end{pmatrix},$$

which can be solved for the unknowns σ_1, σ_2, σ_6, $\varepsilon_3^{\mathrm{el}}$ and $\varepsilon_5^{\mathrm{el}}$. For the composition change of $X_{\mathrm{Or}} = 0.84 \rightarrow 0.69$, we obtain again adopting tensor notation

$$\sigma_{ij}/\mathrm{GPa} = \begin{pmatrix} 0.42 & 0 & 0 \\ 0 & 0.38 & 0 \\ 0 & 0 & 0 \end{pmatrix},$$

and

$$\varepsilon_{ij}^{\mathrm{el}} = \begin{pmatrix} 7.58 \times 10^{-3} & 0 & -2.34 \times 10^{-3} \\ 0 & 5.07 \times 10^{-4} & 0 \\ -2.34 \times 10^{-3} & 0 & -2.31 \times 10^{-3} \end{pmatrix}.$$

The diagonal form of σ implies that the principal axes of the stress tensor coincide with the axes of the orthogonal coordinate system. The maximum tension stress is represented by σ_{11}, i.e., it is parallel to the x-direction. The cracks in the (001) surface are indeed perpendicular to the x-direction.

Fracture mechanics

One can assume that several crack nuclei (e.g., defects) are distributed on the surfaces of the specimen, especially along the edges, providing sites from where cracks can propagate through the chemically altered surface layer. Cracks form only when the chemical shift toward more sodium-rich compositions is 13 mole % or more. Referring to our stress analysis, this corresponds to a critical tensile stress of about 325 MPa that is necessary to induce frac-turing. Cracks emanating from the (001) surface are exactly perpendicular to the direction of the maximum tensile stress on this surface, and they may thus be regarded as pure mode I cracks. With cracks emanating from the (010) surface, the crack normal and the direction of maximum tensile stress enclose an angle of about 18°. If the stress is resolved on the crack plane, a shear stress component parallel to the line of the crack tip results, and the cracks only approximately correspond to mode I with a minor component of mode III (out of plane shear component). The experimental observation shows a system of parallel cracks that emanate from the surfaces and propagate through the entire specimen with time. It is intuitive to assume that fracturing is due to the tensile stress that is localized in the misfitting surface layer and the following analysis builds on the simplifying assumption that a homogeneous tensile stress in the surface layer provides the only driving force for fracturing. The analysis does, however, not account for the fact that chemical exchange also takes place at the crack surfaces (see Fig. 4). The envelopes of altered feldspar accompanying the cracks have an influence on the stress field at the crack tip and provide additional driving force for crack propagation. Considering this effect is beyond the scope of this com-munication. Our analysis thus can only deliver a rough

estimate for the parameter characterizing the fracture mechanics.

A number of fracturing criteria have been considered for brittle solids including concepts based on crystal structure, bond density and bond strength, elastic moduli, and surface energy (Schultz et al. 1994). Each of these concepts provides reasonable fracture criteria for specific materials, but none is universally applicable. The latter authors suggested the stress intensity factor, which is a measure for the stress field around a crack tip, as the most suitable parameter for describing fracturing. With regard to our samples, it is important to note that the spacing of the cracks emanating from the polished surfaces is quite constant for a given composition shift and that the characteristic spacing varies systematically with the extent of composition shift. We also note that the stress induced in the thin, misfitting layer is directly proportional to the eigenstrain due to composi-tion shift. Our observation thus documents a relation between the crack spacing and the induced stress. From this line of evidence, we infer that the crack spacing is pri-marily controlled by the induced stress rather than by the occurrence of pre-existing randomly distributed defects, which would produce a more irregular crack pattern. We make use of the observed relation between the extent of composition shift and characteristic crack spacing to estimate the critical value of the stress intensity factor K_{Ic}, -which may also be referred to as the ''fracture toughness,'' for mode I cracks. In all crack patterns that we produced the relation between crack length a and crack spacing $2h$ is so that the crack spacing factor $s = a/(a + h) > 0.25$. According to Tada et al. (2000) (p. 264, Part III), the corresponding stress intensity factor for mode I cracks in this regime is

$$K_I \approx \sigma\sqrt{h}, \tag{3}$$

with the stress σ acting along the edge, i.e., orthogonal to the cracks. The observed relation between crack spacing and chemical shift, i.e., between crack spacing and coher-ency stress nicely reflects this proportionality (see Fig. 5). For the cracks emanating from the (001) surface of sani-dine from Volkesfeld, a fit of Eq. (3) to the data given in Table 3 yields an estimate of $K_{Ic} = 2.72$ MPa $m^{1/2}$/ 86 MPa $mm^{1/2}$. The corresponding estimate for cracks emanating from the (010) surface is $K_{Ic} = 2.30$ MPa $m^{1/2}$/ 73 MPa $mm^{1/2}$. These estimates are different from what was found by Broz et al. (2006) and by Whitney et al.(2006) using an indentation technique for measuring the fracture toughness of rock-forming minerals. Thereby, the fracture toughness is determined from the length of radial cracks emanating from the corners of a load mark produced with a Vickers indenter. For orthoclase single crystals, an indentation fracture toughness of 0.88 ± 0.13 MPa $m^{1/2}$ (Broz et al. 2006) and of 1.1 ± 0.4 MPa $m^{1/2}$ (Whitney et al. 2006) was found, which is considerably lower than the values obtained in our study. Bernardo et al. (2007) give an indentation fracture toughness of 1.5–2.0 for sin-tered $KAlSi_3O_8$ glass ceramics, the indentation fracture toughness for aluminum-oxide ceramics is 3–5 MPa $m^{1/2}$. There are several possible reasons for the discrepancy between the toughness estimates from this study and those from Broz et al. (2006) and Whitney et al. (2006). The cracks associated with the load mark of a Vickers indenter have a complex 3D geometry. No analytical solution exists for the associated stress field, and the ''fracture toughness'' obtained from indentation experiments merely rests on an empirical relation among the length of radial cracks from indentation, the applied load, the indentation hardness, and the elastic modulus, but it does not directly confer to the continuum mechanical definition of the stress intensity factor (Quinn and Bradt 2007). The nature (mode I, II, or III) of the cracks produced from indentation is not well defined, but the continuum mechanical definition of the stress intensity factor clearly discerns a K_I, K_{II}, and K_{III} for mode I, mode II, and mode III cracks, respectively (Quinn and Bradt 2007). The ''indentation fracture tough-ness'' is thus not directly comparable to the critical value of the stress intensity factor that we obtained form our anal-ysis, and the comparison of numerical values must be made with caution. Furthermore the sample used by Broz et al.(2006) had a perthitic microstructure and may differ in its mechanical properties from our gem-quality sanidines, which are chemically and structurally homogeneous down to the nm scale. Finally, due to the potential contribution of the lattice strain associated with chemical alteration next to the crack walls, there is also some uncertainty with our experiments, which has not yet been evaluated. Nevertheless, we think that our experiments do present an interesting alternative to conventional mechanical testing which rests on a well-defined geometry of the crack pattern for which analytical solutions or approximations are available (Tada et al. 2000).

Since K_I is nearly independent of crack length at $s \geq 0.3$, which is characteristic for the observed crack patterns, the crack length cannot be predicted using Eq. (3). The growth of an initial crack (say a crack with $s \geq 0.3$) is controlled by the stability behavior of the growth process itself as it has been treated in the literature. We refer to, e.g., Muhlaus (1996) and do not concentrate on this aspect.

Finally, the question arises up to the reason for the approximately 18° orientation mismatch between the plane normal of the cracks and the direction of maximum tensile stress. There is no obvious relation to the anisotropy of the crystal's bonding system as represented in terms of peri-odic bond chains. However, the crack plane almost coincides with the plane defined by the directions of the two pronounced maxima of the longitudinal elastic stiffness

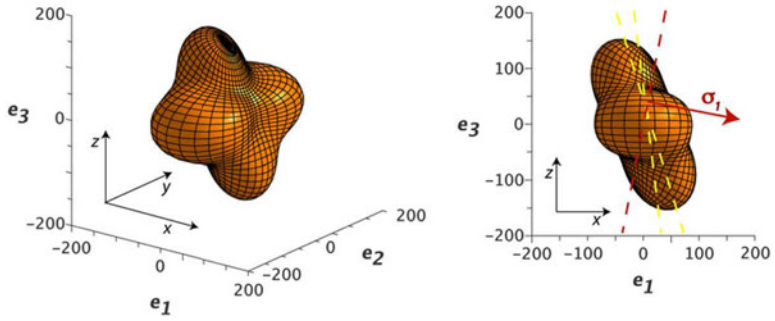

Fig. 11 Representation surface of longitudinal elastic stiffness [GPa] (Schreuer et al., in prep.), *yellow dashed lines* indicate range of observed crack orientations, *red arrow* indicates direction of maximum tensile stress σ_1, *dashed red line* trace of normal plane to the direction of maximum tensile stress

(see Fig. 11). One maximum points into the *b*-direction, the other lies in the *a*–*c* plane pointing into a direction that encloses an angle of approximately 78° with the negative *a*-axis measured toward the positive *c*-axis. Thus, the longitudinal elastic stiffness is generally high in a plane that is sub-parallel to the cracks (Fig. 11) and has its lowest values in the direction sub-perpendicular to the cracks. Although the atomistic mechanisms underlying this relation are not known, it appears likely that the anisotropy of the longitudinal elastic stiffness at least partially controls the orientation of the cracks and is responsible for the mismatch between the crack normal and the direction of maximum tensile stress.

Conclusions

It has been confirmed experimentally that fracturing in alkali feldspar may occur due to coherency stress associated with composition change in the course of Na^+–K^+ cation exchange. This phenomenon is due to a substantial composition dependence of the lattice parameters of alkali feldspar and its marked anisotropy. The mechanical analysis of a thin misfitting surface layer under tensile stress, that is the situation corresponding to a composition shift toward more sodium-rich compositions, delivers an estimate of ≈ 325 MPa for the critical tensile stress needed to initiate mode I cracks. The regularity of systems of parallel cracks that emanate from polished (010) and (001) surfaces indicates that the characteristic spacing between cracks is controlled by the induced coherency stress rather than by irregularly distributed defects or flaws in the crystal structure. This allows extraction of the stress intensity factor, $K_I = 2.3$ MPa $m^{1/2}$/73 MPa $mm^{1/2}$ to 2.72 MPa $m^{1/2}$/86 MPa $mm^{1/2}$ from the relation between characteristic crack spacing and induced stress. A slight orientation mismatch between the crack normal and the direction of maximum tensile stress is tentatively ascribed to the anisotropy of the longitudinal elastic stiffness. With our experiments on the chemically induced fracturing in alkali feldspar, an alternative means of investigating fracturing behavior in brittle materials is documented.

Acknowledgments This work was funded by the Deutsche Forschungsgemeinschaft project AB 314/2-1 and by the Austrian Science foundation, FWF project I 474-N19, both in the framework of the research unit FOR 741-DACH. We are grateful to G. Giester and A. Wagner for their help in preparing oriented single crystal plates.

Appendix

Eigenstrain due to composition change

Let **r** and **R** indicate the position of a specific point in the crystal lattice before and after composition change, respectively,

$$\mathbf{r} = (x_1, x_2, x_3), \quad \mathbf{R} = (X_1, X_2, X_3)$$

The two vectors are related through the displacement vector **u**(**r**)

$$\mathbf{R} = \mathbf{r} + \mathbf{u}(\mathbf{r}).$$

The associated strain tensor ε_{ij} is defined as a symmetric sum

$$\varepsilon_{ij} = \frac{1}{2}(I_{ij} + I_{ji}) \quad \text{with} \quad I_{ij} = \frac{\partial u_i}{\partial x_j},$$

where I_{ij} denotes the displacement gradient. If the strain is homogeneous, $I_{ij} = \text{const}$, one can explicitly find the components of **u**(**r**)

$$u_i = I_{ij} x_j, \quad X_i - x_i = I_{ij} x_j.$$

The linear transformation from **r** to **R** can now be written in a compact matrix notation

$$\mathbf{R} = M\mathbf{r}, \quad M = I + \text{id} \tag{4}$$

where id denotes the 3 × 3 identity matrix.

We now consider a monoclinic coordinate system with axes **a**, **b**, **c** and corresponding angles $\alpha = \gamma = 90°$, $\beta \neq$

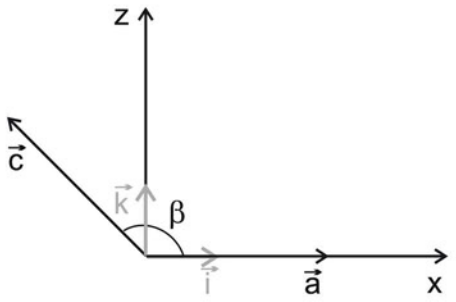

Fig. 12 Monoclinic and orthogonal coordinate systems with **a** ∥ *Ox*, **b** ∥ *Oy*, **c*** ∥ *Oz* viewed down the crystallographic *b*-axes, **i**, **j**, **k** are the unit vectors along the *Ox*-, *Oy*-, and *Oz*-axes

90°. Let **i**, **j**, **k** be the unit vectors along the *Ox*-, *Oy*- , and *Oz*-axes of the orthogonal coordinate system, and let the monoclinic coordinate system be oriented such that **a** ∥ *Ox*, **b** ∥ *Oy*, **c*** ∥ *Oz* (see Fig. 12). The vectors **a**, **b**, and **c** can be related to **i**, **j**, **k** by the matrix equation

$$\begin{pmatrix}\mathbf{a}\\ \mathbf{b}\\ \mathbf{c}\end{pmatrix} = \begin{pmatrix} a & 0 & 0\\ 0 & b & 0\\ c\cos\beta & 0 & c\sin\beta\end{pmatrix}\begin{pmatrix}\mathbf{i}\\ \mathbf{j}\\ \mathbf{k}\end{pmatrix} = S\begin{pmatrix}\mathbf{i}\\ \mathbf{j}\\ \mathbf{k}\end{pmatrix},$$

where $S = S(a, b, c, \beta)$ is the transformation matrix. In what follows we denote $S(a_0, b_0, c_0, \beta_0)$ by S_0 and $S(a_1, b_1, c_1, \beta_1)$ by S_1.

For the vector **r** we have

$$\begin{aligned}\mathbf{r} &= (x_1 \quad x_2 \quad x_3)\begin{pmatrix}\mathbf{i}\\ \mathbf{j}\\ \mathbf{k}\end{pmatrix} = (m \quad n \quad p)\begin{pmatrix}\mathbf{a}_0\\ \mathbf{b}_0\\ \mathbf{c}_0\end{pmatrix}\\ &= (m \quad n \quad p)S_0\begin{pmatrix}\mathbf{i}\\ \mathbf{j}\\ \mathbf{k}\end{pmatrix},\end{aligned}$$

such that

$$\begin{pmatrix}x_1\\ x_2\\ x_3\end{pmatrix} = S_0^T\begin{pmatrix}m\\ n\\ p\end{pmatrix}.$$

Similarly, the components of **R** with respect to *Oxyz* are related to the components referring to the monoclinic system through

$$\begin{aligned}\begin{pmatrix}X_1\\ X_2\\ X_3\end{pmatrix} &= S_1^T\begin{pmatrix}m\\ n\\ p\end{pmatrix} = S_1^T(S_0^{-1})^T\begin{pmatrix}x_1\\ x_2\\ x_3\end{pmatrix}\\ &= (S_0^{-1}S_1)^T\begin{pmatrix}x_1\\ x_2\\ x_3\end{pmatrix},\end{aligned}$$

such that

$\mathbf{R} = (S_0^{-1}S_1)^T\mathbf{r}$. (5) Comparing Eqs. 4 and 5, we obtain an explicit expression for M

$M = (S_0^{-1}S_1)^T$.

For the displacement gradient, we thus have

$I = (S_0^{-1}S_1)^T - \mathrm{id},$

and the strain tensor reads

$$\varepsilon = \frac{S_0^{-1}S_1 + (S_0^{-1}S_1)^T}{2} - \mathrm{id}.$$

For the case at hand, the components of the strain tensor are calculated as

$$\begin{pmatrix} \frac{a_1}{a_0} - 1 & 0 & \frac{c_1\cos\beta_1}{2c_0\sin\beta_0} - \frac{a_1\cos\beta_0}{2a_0\sin\beta_0}\\ 0 & \frac{b_1}{b_0} - 1 & 0\\ \frac{c_1\cos\beta_1}{2c_0\sin\beta_0} - \frac{a_1\cos\beta_0}{2a_0\sin\beta_0} & 0 & \frac{c_1\sin\beta_1}{c_0\sin\beta_0} - 1\end{pmatrix}.$$

References

Abart R, Petrishcheva E, Rhede D, Wirth R (2009a) Exsolution by spinodal decomposition II: perthite formation during slow cooling of anatexites from Ngoronghoro, Tanzania. Am J Sci 309: 450–475. doi:10.2475/06.2009.02

Abart R, Petrishcheva E, Kässner S, Milke R (2009b) Perthite microstructure in magmatic alkali feldspar with oscillatory zoning; Weinsberg Granite, Upper Austria. Mineral Petrol 97: 251–263. doi:10.1007/s00710-009-0090-1

Angel R, Sochalski-Kolbus LM, Tribaudino M (2012) Tilts and tetrahedra: the origin of the anisotropy of feldspars. Am Mineral 97:765–778

Benisek A, Dachs E, Kroll H (2010) A ternary feldspar-mixing model based on calorimetric data: development and application. Contrib Mineral Petrol 160:327–337

Bernardo E, Doyle J, Hampshire S (2007) Sintered feldspar glass ceramics and glass—ceramic matrix composites. Ceram Int 34:2037–2042

Bollmann W, Nissen H-U (1968) Study of optimal phase boundaries: the case of exsolved alkali feldspars. Acta Cryst A24:546–557

Brown WL, Parsons I (1988) Zoned ternary feldspars in the Klokken intrusion: exsolution microtextures and mechanisms. Contrib Miner Petrol 98:444–454

Broz ME, Cook RF, Whitney DL (2006) Microhardness, toughness, and modulus of Mohs scale minerals. Am Mineral 91:135–142

Demtroeder (2011) Untersuchung zur Al/Si-Ordnung an Sanidin-Megakristallen aus der Eifel. unpublished MSc Thesis Ruhr-Universität Bochum

Fuhrman ML, Lindsley DH (1988) Ternary-feldspar modeling and thermometry. Am Mineral 73:3–4

Hovis GL, Delbove F, Bose MR (1991) Gibbs energies and entropies of K–Na mixing for alkali feldspar from phase equilibrium data: implications for feldspar solvi and short range order. Am Mineral 76:913–927

Jamtveit B, Putnis C, Malthe-Sorenssen A (2009) Reaction induced fracturing during replacement processes. Contrib Mineral Petrol 157:127–133. doi:10.1007/s00410-008-0324-y

Kroll H, Ribbe PH (1983) Lattice parameters, composition and Al, Si order in alkali feldspars. In: Ribbe PH (ed) Feldspar mineralogy. Reviews in mineralogy 2:57–100

Kroll H, Schmiemann I, von Coelln G (1986) Alklai feldspar solid-solutions. Am Mineral 71:1–16

Muhlaus HB, Chou KT, Ord A (1996) Bifurcation crack pattern in arrays of two-dimensional cracks. Int J Fract 77:1–14

Neusser G, Abart R, Fischer FD, Harlov D, Norberg N (2011) Experimental Na/K exchange between alkali feldspar and an NaCl–KCl salt melt: chemically induced fracturing and element partitioning. Contrib Mineral Petrol 164:341–358

Nye JP (1985) Physical properties of crystals. Oxford University Press, New York

Passchier CW, Trouw RJ (2005). Microtectonics. Springer, Heidelberg

Petrishcheva E, Abart R. (2009) Exsolution by spinodal decomposition I: evolution equation for binary mineral solutions with anisotropic interfacial energy. Am J Sci 309:431–449

Petrishcheva E, Abart R (2012) Exsolution by spinodal decomposition for multicomponent mineral solutions. Acta Mater 60: 5481–5493

Petrovic R (1973) Effect of coherency stress on mechanism of reaction albite+K^+ reversible K-feldspar+Na^+ and on mechanical state of resulting feldspar. Contrib Mineral Petrol 41:151–170

Quinn GD, Bradt R (2007) On the Vickers indentation fracture toughness test. J Am Ceram Soc 90:673–680

Ribbe PH (1983) Chemistry, structure and nomenclature of Feldspars. In: Ribbe PH (ed) Feldspar mineralogy. Reviews in mineralogy, vol 2, 2nd edn. Mineralogical Society of America, Washington, DC, pp 1–19

Robin P (1974) Stress and strain in cryptoperthite lamellae and the coherent solvus of alkali feldspar. Am Mineral 59:1299–1318

Schreuer J, Sondergeld P, Demtröder K (in prep.) Elastic properties of monoclinic alkali feldspars up to 1370 K. Phys Chem Min, in preparation

Schultz RA, Jensen MC, Bradt RC. (1994) Single crystal cleavage of brittle materials. Int J Fract 65:291–312

Smith JV, Brown W (1988) Feldspar minerals, volume 1: crystal structures, physical, chemical, and microtextural properties. Springer, Berlin, p 828

Tada H, Paris PC, Irwin GR (2000) The stress analysis of cracks handbook, 3rd edn. ASME Press/Professional Engineering Publishing/ASM, New York

Thompson JB Jr, Waldbaum DR (1968) Mixing properties of sanidine crystalline solutions. I. Calculations based on ion-exchange data. Am Mineral 53:1965–1999

Whitney DL, Broz ME, Cook RF (2006) Hardness, toughness, and modulus of some common metamorphic minerals. Am Mineral 92:281–288

Yund R (1984) Alkali Feldspar exsolution: Kinetics and dependence on alkali interdiffusion. In: Brown WL (ed) Feldspars and feldspathoids: structure, properties, and occurrences. Dordrecht, D. Reidel Publishing Company, NATO Advanced Science Institute Series C, v. 137:. 281–315

Appendix D

Schäffer et al. (submitted)

Schäffer et al. (submitted): Lattice strain across Na-K interdiffusion fronts in alkali feldspar: an electron back-scatter diffraction study

The execution of the experiments, BSE imaging and microprobe work were done by Anne-Kathrin Schäffer. EBSD measurements were done at the Max-Planck Institute for Iron Research in Düsseldorf in cooperation with Stefan Zaefferer. Analysis of the EBSP patterns with help of the Cross Court 3 software was done by Tom Jäpel and Anne-Kathrin Schäffer.

Noname manuscript No.
(will be inserted by the editor)

Lattice strain across Na-K interdiffusion fronts in alkali feldspar: an electron back-scatter diffraction study

Anne-Kathrin Schaeffer · Tom Jaepel · Stefan Zaefferer · Rainer Abart · Dieter Rhede

Received: date / Accepted: date

Abstract **Keywords** alkali feldspar · interdiffusion · coherency strain · EBSD

Cation exchange experiments between gem quality sanidine ($X_{Or} = 0.85$) and KCl melt produced chemical alteration of alkali feldspar starting at the grain surface and propagating inwards by highly anisotropic Na-K interdiffusion on the alkali sublattice. Diffusion fronts developing normal to (010) are very sharp while diffusion fronts normal to (001) are comparatively shallow. Due to the composition dependence of the lattice parameters of alkali feldspar the diffusion induced compositional heterogeneity induces coherency stress and elastic strain. Electron back-scatter diffraction combined with the cross correlation technique was employed to determine the lattice strain distribution across the Na-K interdiffusion fronts in partially exchanged single crystals of alkali feldspar. The strain changes gradually across the shallow fronts normal to (001) with a successive dilation primarily in a-direction conferring to the composition strain in unstressed alkali feldspar. In contrast, lattice strain characterized by pronounced dilation in b-direction is localized at the sharp diffusion fronts normal to (010) followed by a slight expansion in a-direction in the orthoclase-rich rim. This strain pattern does not confer with the composition induced lattice strain in a stress free alkali feldspar. It may rather be explained by the mechanical coupling of the exchanged surface layer and the mechanically strong substratum. The lattice distortion localized at the sharp

Anne-Kathrin Schaeffer · Rainer Abart
University of Vienna, Department of Lithospheric Research, Althanstrasse 14, 1090 Vienna
Tel.: +49-0251-83-36323
Fax: +43-1-4277-9534
E-mail: anne-kathrin.schaeffer@univie.ac.at

Tom Jaepel · Stefan Zaefferer
Max-Planck Institute for Iron Research, Max-Planck-Strae 1, 40237 Duesseldorf

Dieter Rhede
GFZ German Research Centre for Geosciences, Telegrafenberg, 14473 Potsdam, Germany

diffusion front may have an influence on the diffusion process and appears to produce a self-sharpening feedback leading to a local reduction of component mobilities.

1 Introduction

Alkali feldspars are among the most abundant rock-forming minerals in the Earth's crust. They pertain to the binary solid-solution series comprising the end-member components orthoclase ($KAlSi_3O_8$) and albite ($NaAlSi_3O_8$). Alkali feldspars occur in magmatic, metamorphic and sedimentary environments. Mineral parageneses involving alkali feldspar, and in particular its chemical composition and zoning patterns, may bear important petrogenetic information (Spear, 1993). In this context the robustness of chemical compositions during prolonged thermal annealing or metamorphic overprint are of crucial interest.

Chemical alteration of alkali feldspar in the solid state requires the interdiffusion of $Na^+$and K^+ and potentially substituting minor components on the respective sublattice. Na-K interdiffusion is relatively rapid (Cherniak, 2010) and Na-K cation exchange reactions involving alkali feldspar such as the two feldspar thermometer, and the compositions of the albite- and orthoclase-rich phases in a perthite (Yund, 1984; Abart et al, 2009) are prone to re-equilibration during slow cooling. Quantification of these potential effects requires knowledge of the Na-K interdiffusion coefficient in alkali feldspar. Among others, this motivated cation exchange experiments (Petrović, 1972, Neusser et al 2012; Petrishcheva et al, submitted; Schaeffer et al, submitted) and diffusion couple experiments (Christoffersen et al, 1983), which delivered composition-distance data from which the interdiffusion coefficient can be extracted. Complications may arise during interdiffusion experiments due to the composition dependence of the lattice parameters of alkali feldspar. The crystal structure of alkali feldspar is comprised of an aluminosilicate framework where corner-sharing AlO_4- and SiO_4-tetrahedra are linked in a three-dimensional network forming crankshaft-like chains parallel to the a-axis. Cavities in the tetrahedral framework are occupied by the Na^+ and K^+ cations with minor substitution by Rb^+, Ca^{2+}, and Ba^{2+} (Ribbe, 1983). Incorporation of differently sized cations is mainly accommodated by the stretch of the crankshaft-like chains parallel to the a-axis (Petrović, 1972; Angel et al, 2012). This leads to a pronounced anisotropy of the composition dependence of the lattice parameters which is about five times higher in the a-direction than in the b- and c-directions (Kroll et al, 1986; Angel et al, 2012). Thus any compositional heterogeneity in alkali feldspar, such as a chemically altered surface layer produced by cation exchange, causes coherency stress. The lattice contraction associated with a composition shift towards more sodium-rich composition may produce tensile (mode I) cracks (Petrović, 1972; Neusser et al, 2012; Scheidl et al, 2013).

If alkali feldspar of intermediate composition is shifted towards more potassium-rich compositions, this typically produces a potassium-rich surface layer, which is separated from the internal portions of the feldspar grain by a more or less sharp composition front, which propagates into the feldspar with time. If the composition shift exceeds about 15 mole %, this produces mixed mode cracks, which tend to follow the cation exchange fronts. The fronts are exceptionally sharp in the [010]-direction and more shallow in directions lying within the (010) plane. Petrishcheva et al (submitted) and Schaeffer et al (submitted) produced surface layers with $X_{Or} = 1.00$ on sanidine with an original composition of $X_{Or} = 0.85$ by cation exchange with a KCl salt melt at 850°C and $\approx$ 1 bar. The composition fronts in the [010]-direction are less than about 2 μm wide. In a stress-free alkali feldspar this composition shift corresponds to a change in lattice parameters of about 1% in the a-direction and 0.2% in the b- and c-directions. If the lattice is coherent across the composition front, this induces substantial stress and elastic strain. In this communication we focus on the quantification of the coherency strain across a sharp composition front in alkali feldspar by direct measurement. To this end we employ electron back scatter diffraction (EBSD) measurements combined with the cross correlation method to obtain the lattice strain along profiles taken across such a sharp composition front. The full strain tensor is obtained and the corresponding elastic stress is calculated. The systematics of the lattice strain are analysed in the light of the mechanical boundary conditions and implications of a potential feedback between Na-K interdiffusion, diffusion induced coherency strain and associated distortion of the crystal lattice are discussed.

2 Methods

2.1 Cation exchange experiments

Cation exchange experiments were done using alkali feldspar and NaCl-KCl salt mixtures. Gem quality sanidine from Volkesfeld (Eifel) with an initial composition of $X_{Or} = 0.85$ and minor Ba contents of up to 1 wt %, (0.01 apfu) and Fe contents of up to 0.2 wt. %, 0.01 apfu) was used as a starting material. The sanidine is chemically homogeneous and devoid of cracks, twins, exsolutions, second phase precipitates or other structural or chemical heterogeneities (Riley and Bailey, 2003; Parsons and Lee, 2005; Weitz, 1972; Neusser et al, 2012; Demtröder, 2011). It has a monoclinic symmetry and crystallizes in the space group C2/m. Aluminium and silicon on the tetrahedral site are highly disordered (t1 = 61) (Neusser et al, 2012). Plates of 3x3 mm size and 1 mm thickness were prepared. They were pre-oriented on the basis of their optical extinction under polarized light. Plates with polished (010) surfaces were produced (figure 1).

The crystallographically oriented plates were sealed in quartz glass tubes under vacuum together with a mixture of KCl and NaCl salts. The K over Na ratio of the salt mixture was chosen according to the experimentally de-

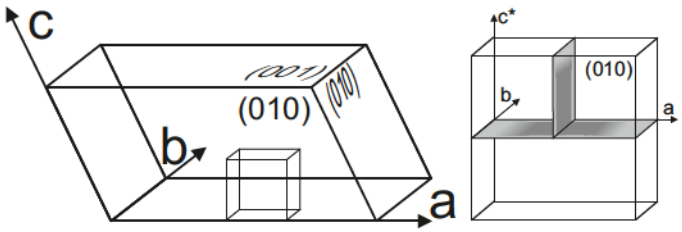

Fig. 1 Sample geometry of the prapared plates; left: orientation of the plate within the unit cell of feldspar, right: after the experiment the plate was cut in two mutually perpendicular directions to allow documentation of interdiffusion fronts in three different crystallographic directions

termined Na-K partitioning between crystal and alkali chloride melt (Neusser et al, 2012) so that specific composition shifts were obtained. To ensure constant concentration boundary conditions during the exchange experiment the amounts of salt and feldspar were chosen so that a 40:1 molar proportion of the alkali cations contained in the salt relative to those contained in the feldspar was obtained. The quartz glass tubes were then placed in a pre-heated muffle furnace and kept at constant temperature for 1 to 64 days at temperatures ranging from 800°C to 1000°C. Temperatures were accurate within ± 1°C. At the end of the experiment the melt was quenched within seconds by dropping the quartz glass tubes into cold water. The feldspar was retrieved by dissolving the salt with deionised water at room temperature. The crystals were subsequently cut in two mutually perpendicular directions normal to the polished surface (figure 1) to allow for the measurement of chemical profiles along three crystallographic directions. They were mounted in epoxy resin, first polished mechanically and then chemically using a colloidal silica suspension with a pH of 9.2 to 10.

2.2 Mineral chemical analysis

Mineral chemical analysis was carried out at the Helmholtz Zentrum Potsdam, GFZ German Research Centre for Geosciences in Potsdam using a JEOL Hyperprobe JXA-8500F with a thermal field-emission cathode. The instrument was operated at an accelerating voltage of 8 kV and a beam current of 10 nA. For calibration the beam was defocused to 10 μm, for measurements the beam was fully focussed. Peak measurements were set to 10 seconds and background measurements to 5 seconds. The relatively short counting time was necessary to minimize loss of alkali cations by evaporation during the measurement. The small excitation volume makes the measurements sensitive to imperfections and contamination of the sample surface and leads to some scattering in the data. The relative error is within 3.5 to 4% for potassium and 7 to 8% for sodium.

2.3 Electron microscopy

Back scattered electron (BSE) imaging was done using an FEI InspectS scanning electron microscope equipped with a tungsten filament. The instrument was operated at acceleration voltages of 10 and 15 kV and a beam current of 8 nA. The surface of the sample was coated with carbon using carbon evaporation of a double-thread of carbon fibre at a distance of about 8 cm from the sample under vacuum of 10^{-5} mbar during evaporation to establish electrical conductivity.

Electron backscatter diffraction (EBSD) measurements were performed at the Max-Planck Institute for Iron Research in Düsseldorf using a Zeiss XB 1540 cross beam instrument with thermal field emission gun operated at 15 kV and about 5 nA beam current. Conductivity of the sample was established by a carbon sputter coating of 2 to 3 nm thickness applied with a Gatan PECS precision etching and coating instrument. The sample was mounted at 70°C sample tilt and the measurements were done at a working distance of 13 mm.

Profiles were measured normal to the polished (010) and (001) surfaces of the crystal; the sample was oriented so that the trace of the respective surface was parallel to the tilt axis. To minimize beam damage on the beam sensitive feldspar, patterns were collected by scanning the beam over a rectangular area of 1 x 50 μm with its long axis perpendicular to the trace of the chemical gradient. This window was moved in 1 μm steps for profiles normal to (010) and in 2 μm steps for profiles normal to (001).

The OIM Data Collection software 5.3 was used for data acquisition. A TSL Hikari EBSD detector with a 640 x 640 pixel resolution was used for pattern recording. Patterns were recorded at 1x1 binning and subsequently corrected by subtracting the measured background, histogram normalisation and applying a dynamic background subtraction. The background pattern was taken on a carbon-coated glass sample mounted on the same sample holder. For each pattern the camera exposition time was 200 ms and 40 patterns were averaged, resulting in a total exposure time of about 8 seconds. For orientation determination the patterns were binned to a pattern size of 240 pixels and a Hough transform with an angular resolution of 0.25 2θ step size was applied. The Hough transform was convoluted with a 13 x 13 pixel large convolution mask and 20 peaks were identified with a minimum peak distance of 16 pixels. Only the inner part of the pattern was considered with the ρ fraction of the Hough space being set to 84 %.

2.4 EBSD cross correlation technique

The acquired EBSD patterns (EBSP) were used to determine the full elastic strain tensor employing a pattern cross correlation technique implemented in the commercial software Cross court 3 by BLG Productions. This technique is based on the measurement of pattern distortion by comparing the current pattern with a reference pattern obtained at a region which serves as

a starting point for lattice strain determination. It is important that all acquisition parameters are kept constant during measurement of the reference and current pattern and that the relative positions of the reference area and the measurement area are well known. In the present case the diffusion zone rim is thin compared to the bulk of the sample. The internal region of the crystal is therefore mechanically much stronger than the thin chemically altered surface layer. As in the interior portions the original composition is preserved the crystal lattice can be assumed to be practically undeformed in the grain interior. Accordingly, the pattern obtained at the inner end of the profile in the chemically unaltered portion of the crystal was chosen as reference pattern representing the original, unstrained lattice. Shifts of the EBSPs' features in the regions of interest of each pattern obtained along the measured profile further outwards and across the sharp composition front were then compared to their equivalent in the reference pattern. Variations in these shifts across the pattern give insight into the nature of the strain within the diffracting volume (Wilkinson et al, 2009).

The analysis of pattern distortion was performed on the basis of 253 square regions of interest (ROI) each with 64 x 64 pixel size placed on the recorded EBSP in a regular grid within the circular area of the pattern with an overlap area of 7.5 px^2 between neighbouring regions of interest. The sensitivity of the cross correlation method strongly depends on pattern quality. For very good patterns shifts as small as a few hundredths of pixels can be determined (Wilkinson and Britton, 2012); such a high quality can unfortunately not be achieved for feldspars due to the necessity for a carbon coating of the surface, the low symmetry and density of the crystal as well as its low stability under the electron beam. Furthermore, as the patterns were taken by integration over an approximately 50 μm large area they contain an inherent horizontal blurring of about 0.5 pixels (pixel size is 80 μm). Nevertheless, the pattern quality obtained in our measurements was sufficient to reach a sensitivity of about 0.5 pixels (compare Wilkinson et al, 2006). The strain sensitivity for high resolution Kikuchi patterns is 1.3 x 10^{-4} (Wilkinson et al, 2006).

Fast fourier filters were employed on the ROIs in order to reduce high frequency intensity noise and low frequency intensity background influences. With this the translational shifts in the tested pattern ROIs can be tracked more accurately by the cross correlation in the fourier domain (Wilkinson et al, 2009). The low frequency cut off was set to 2 px^{-1} with a cut off width of 0 while the high frequency cut off was set to 15 px^{-1}, also with a cut off width of 0.

3 Results

3.1 Chemical patterns from cation exchange

Figure 2 shows a BSE image of alkali feldspar with an original X_{Or} of 0.85, which was reacted with pure KCl salt melt at 850°C for 32 days. The bright

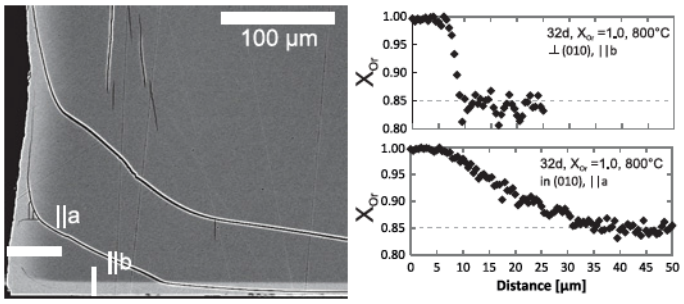

Fig. 2 Feldspar plate prepared with polished (010) surfaces exchanged with pure KCl at 850°C for 32 days; the BSE image shows bright areas along the grain surfaces which were in equilibrium with the melt, separated from darker areas of unexchanged feldspar in the core (left) by clearly anisotropic diffusion fronts; FEG-EMP measurements along the profiles indicated in the BSE image (right) show that even though the diffusion profiles vary in sharpness and width they both exhibit the same shape, characterized by two plateaus and an inflection point of the diffusion front

areas along the grain surfaces represent the K-rich surface layer, which is separated from the dark grey internal regions of the grain by more or less sharp composition fronts. Cation exchange in the single crystal necessitates Na-K interdiffusion, and the composition fronts may be interpreted as diffusion fronts, which propagate into the crystal with time. The shape of the diffusion fronts, and in particular their sharpness, exhibits clear direction dependence. The widest diffusion fronts are observed in directions lying in the (001) plane while the narrowest fronts develop in the direction normal to (010). The chemical profiles measured with a field emission gun-electron microprobe (FEG-EMP) across the diffusion fronts confirm this observation. It is important to note that the profiles exhibit two plateaus corresponding to the exchanged rim and the core in which the original composition is preserved, respectively, and the diffusion front between the two plateaus exhibits an inflection point (figure 2).

Apart from crystallographic direction, the sharpness of the diffusion front also depends on the extent of the chemical shift, i.e. the composition difference between the exchanged rim and unexchanged core. For a composition shift of only 5 mole-% to X_{Or} 0.90 the front is very indistinct and its geometry confers to what is expected for interdiffusion with constant concentration boundary conditions and constant interdiffusion coefficient. For a shift of 10 mole-% to a composition of X_{Or} 0.95 the plateaus begin to form and the front with the inflection point becomes apparent (Petrishcheva et al, submitted, Schaeffer et al, submitted). Only if the composition is shifted to values of X_{Or} larger than 0.95 the described characteristic shape with its two sharply defined plateaus separated by a very narrow front develops. A composition shift from an initial X_{Or} 0.85 to pure orthoclase composition often leads to the formation of complex crack patterns (figure 3), especially in experiments with long run durations and/or at high temperatures. These cracks run roughly parallel to the diffusion fronts, and they curve close to the edges of the sample where the cracks which are parallel to two different surfaces of the sample link up.

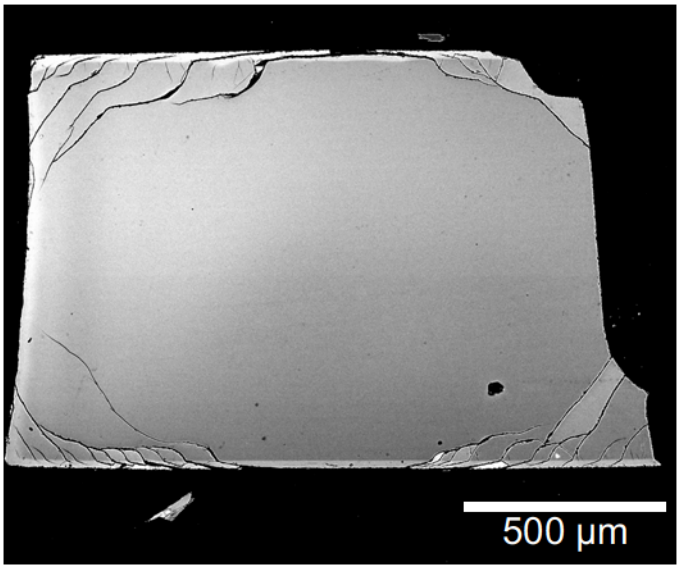

Fig. 3 Feldspar plate with polished (010) surfaces exchanged with pure KCl at 920°C for 2 days; feldspars shifted to pure orthoclase composition often show complex crack patterns with cracks running rouhly parallel to the interdiffusion fronts, caused by the anisotropy of the composition dependence of the lattice parameters

Often the cracks form within yet unexchanged portions of the crystal slightly beneath the diffusion front.

3.2 Lattice strain across diffusion fronts

In cases where the shifts towards more potassium-rich compositions do not induce fracturing the lattice misfit across the diffusion fronts is accommodated by elastic strain. The associated lattice distortion was investigated by EBSD combined with the cross correlation method. Lattice strain across wide and sharp diffusion fronts is treated separately. The sample chosen for analysis was polished on the (010) surface and then exchanged with pure KCl melt for four days at 920°C. A sharp diffusion front developed inwards from the polished (010) surface, i.e., in *b*-direction. EBSD patterns were collected along several profiles, which start in the unexchanged grain interior, run across the sharp diffusion front, and end at the polished surface. The patterns in the exchanged rim and across the diffusion front are clearly distorted relative to the reference pattern which was taken at the inner end of the profile where the original composition of the feldspar is preserved. The shifts of the patterns recorded in the rim relative to the reference pattern have the largest component in the *a*-direction, indicating that the largest distortion of the crystal occurs in this direction. Localised at the diffusion front itself a major component parallel to the *b*-direction of the crystal is documented (figure 4).

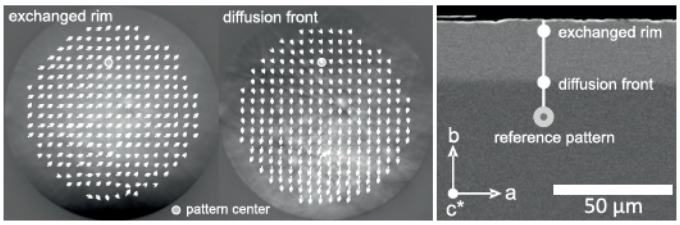

Fig. 4 EBSP with shifts relative to the reference pattern indicated by the white arrows (arrows scaled to ten); in the exchanged rim the shifts have a major component parallel to the *a*-direction of the crystal while in the diffusion itself a predominant shift parallel to the *b*-axis is observed

Using the cross correlation method the full strain tensor was determined for all measurement points along the profile. As the tensor is symmetric only the upper half is shown in figure 5. The profiles show the distortion of the lattice relative to the reference pattern. The diffusion front is located at a distance of about 20 μm from the polished (010) surface of the crystal and is about 5 μm wide. Four different profiles were measured to test for reproducibility. Except for some minor variation for ϵ_{11} the different measurements were generally in good accordance.

The variations of the normal strains are most significant. The longitudinal strains along the *a*- and *b*-axes of the crystal, that is ϵ_{22} and ϵ_{11}, respectively, show the most pronounced variations. The variation of ϵ_{22} along the profile indicates a continuous dilation of the lattice in *a*-direction within the exchanged rim relative to the reference pattern. This dilation decreases inwards from the sample surface and vanishes at the diffusion front. In contrast, ϵ_{11}, i.e. the strain in *b*-direction is close to zero in both the rim and unexchanged core but indicates a localized dilation in *b*-direction at the diffusion front. Within error the values stay constant for ϵ_{33} all along the measured profile indicating that no significant longitudinal strain occurred in c^*-direction.

ϵ_{12} shows the same trend as ϵ_{22} with a slight rise in the exchanged rim which then declines within the diffusion front. ϵ_{23} shows the opposite trend with values being slightly lower in the rim relative to the reference pattern before rising in the diffusion front. None of the profiles shows any specific trend within the diffusion front itself. Within error the values stay constant for ϵ_{13} all across the profile.

Two profiles were measured normal to the (001) surface of the same sample (figure 6). The diffusion fronts in the direction perpendicular to (001) are much broader than those evolving in the direction perpendicular to the (010) surface. The exchanged rim is about 20 μm wide and the diffusion front has a width of about 50 μm. In this case, the longitudinal strain in *a*-direction (ϵ_{11}) is characterized by a gradually increasing dilation from the internal regions of the grain across the diffusion front and towards the exchanged rim. For the *b*-direction we see the opposite trend with a gradual, slight contraction across the diffusion front. ϵ_{33} again stays roughly constant across the entire profile indicating that no significant longitudinal strain occurred in the c^*-direction.

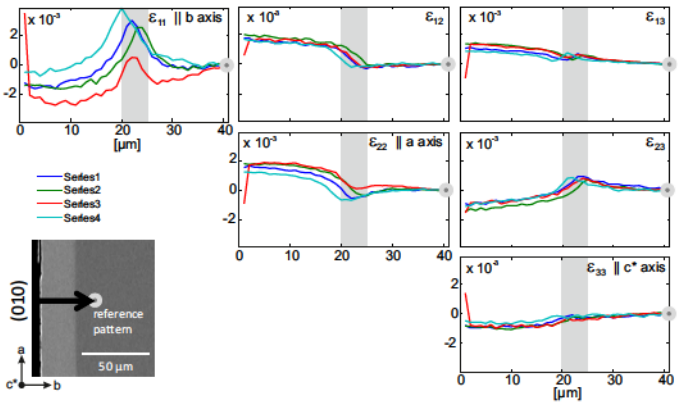

Fig. 5 Upper half of the symmetric strain tensor for profiles measured across a sharp diffusion front; the differently coloured profiles represent different measurements executed to test reproducibility, the reference pattern is located at the righthand side as represented by the grey dot, the edge of the crystal is on the left hand side; the most notable features are the strain concentration parallel to b within the diffusion front and the extension parallel to a within the exchanged rim

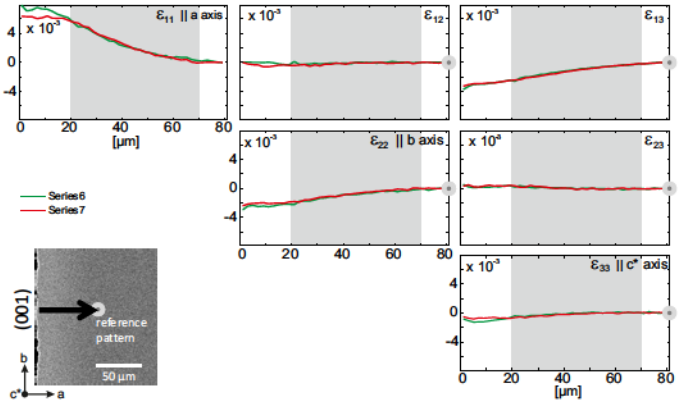

Fig. 6 Upper half of the symmetric strain tensor for profiles measured across a sharp diffusion front; the differently coloured profiles represent different measurements executed to test reproducibility, the reference pattern is located at the righthand side as represented by the grey dot, the edge of the crystal is on the left hand side; in contrast to what was observed for narrow diffusion profiles there is no strain concentration within the diffusion front, a gradually increasing dilation in a-direction is the most significant change observed

4 Discussion

EBSD combined with cross correlation method is a powerful tool for quantifying coherency strain in the range of 10-4 (Maurice et al, 2012; Britton and Wilkinson, 2012) provided the misorientation between test and reference pattern is limited to about 1°. A systematic error analysis of the cross correlation method has shown no significant difference in accuracy between normal and shear components (Tom Jaepel, personal communication).

For the present measurements the strain components in y-direction (ϵ_{22}, and ϵ_{12}, ϵ_{32}) will most probably show a reduced accuracy, because the patterns have been acquired by integration of an area extending 50 μm in y-direction. This corresponds to a horizontal blur of about 1 pixel in the patterns. However, as the patterns are changing only in x-direction of the sample this horizontal blur stays constant for all measurements and should therefore not strongly reduce accuracy.

In the investigated feldspars we find lattice strain localized across a sharp diffusion front forming in [010]-direction (figure 5). While the composition of the feldspar changes in a strictly monotonic manner with an outwards increase of X_{Or} from 0.85 to 1.00 across the diffusion front the observed lattice strain across the sharp composition front is characterized by a substantial dilation of the b-parameter that is localized to within an about 5 μm wide domain around the diffusion front. At the same time the a-parameter shows a slight and monotonic contraction and the c-parameter remains unchanged. This systematic change of lattice strain does not confer to the change of lattice strain which would occur in a stress free crystal of alkali feldspar subject to a similar composition change. When alkali feldspar with an initial composition of $X_{Or} = 0.85$ is shifted to the pure potassium end-member composition, $X_{Or} = 1.00$, this implies an expansion in all crystallographic directions; $a_0 = 8.545\mathring{A} \rightarrow a_1 = 8.6\mathring{A}$, $b_0 = 13.025\mathring{A} \rightarrow b_1 = 13.03\mathring{A}$, $c_0 = 7.175\mathring{A} \rightarrow c_1 = 7.18\mathring{A}$, and a minute change in the angle β, $beta_0 = 116.0° \rightarrow beta_1 = 116.05°$ (Kroll et al, 1986). Within the plane of the diffusion front, that is within the contact plane between the compositionally distinct domains of the crystal, the lattice parameters are confined to those of the volumetrically by far dominant internal portion of the crystal, in which the original composition is retained. As a consequence the volume change across the diffusion front occurs via change of the only unconstrained lattice direction (here the b-direction), perpendicular to the constrained interface. Only a few micrometers outside from the diffusion front the mechanical coupling to the rigid substratum becomes less strong, and the crystal can expand in a-direction (figure 7, left). As soon as the composition strain is accommodated by dilation in a-direction, the b-parameter shrinks again leading to a strain similar to what is expected in a stress free crystal of alkali feldspar.

The systematics of the strain along the profile taken across a broad diffusion front formed perpendicular to (001) confers to what is expected for the composition induced eigenstrain in a stress-free feldspar. The a-parameter increases successively towards the outer portions of the crystal as here the free surface is perpendicular to [100] and thus the a-direction of the crystal lattice is not confined by the stronger substratum (figure 7, right).

The mechanical effects due to the eigenstrain associated with diffusion induced composition change may have an influence on diffusion. The eigenstrain may interact with diffusion in two ways. On the one hand, it may change the thermodynamic driving force for diffusion, and on the other hand, the energy barriers for atomic jumps may be modified by lattice distortion. In a theoretical study Larche and Cahn (1982) showed that the diffusion induced self-stress

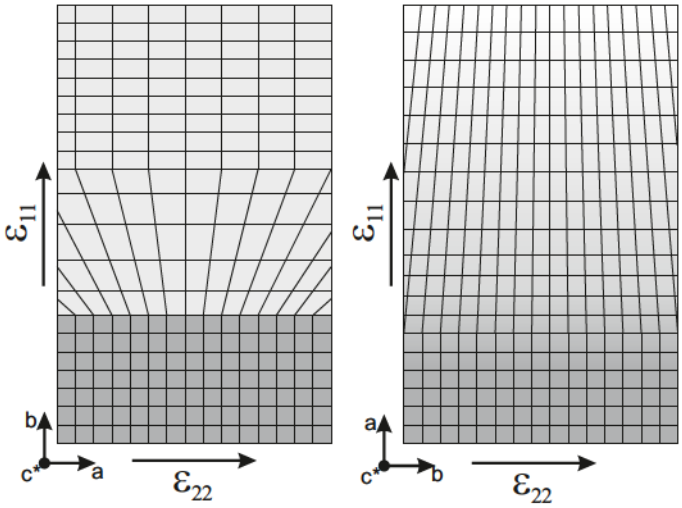

Fig. 7 Schematic diagrams of the lattice distortion across the sharp (left) and broad (right) diffusion fronts normal to (010) and (001), respectively; the dark grey colour represents part of the unexchanged core, the light grey represents part of the exchanged rim; for the sharp diffusion front the lattice dilates in *b*-direction as (010) is the only free surface while the *a*- and *c*-parameters are dominated by the unexchanged substratum, in the rim the dilatation in *a* which would be expected in a stress free feldspar takes over, the gradual dilation in *a*-direction observed for the broad diffusion front in turn is in accordance with composition strain in an unstressed feldspar

has an influence on the driving force for diffusion which they expressed as the gradient in a generalized diffusion potential. This theory was extended by the consideration of the interplay between vacancy generation and annihilation and stress by Stephenson (1988). A more general concept for the kinetics of diffusion in a stressed solid was introduced by Svoboda et al (2006). In this work, a distinction is made between interstitial and substitutional components and vacancies, and the role of non-ideal vacancy sources and sinks as well as the role of stress are addressed. The concept is based exclusively on the knowledge of the tracer diffusion coefficients and of the thermodynamic state functions of the bulk phase. As the shape of the diffusion fronts shows marked direction dependence, we do not think that the thermodynamic effect is the primary link between diffusion and self-stress. We rather think that the diffusion process is influenced via the effect of lattice distortion on atomic jumps.

The distortion of the lattice across the sharp diffusion front in [010] direction may have an influence on the diffusion pathways in the feldspar structure. The main diffusion pathways are in the *a*-*c*-plane. The alkali cations occupy large cavities within the Si- and Al-tetrahedral framework .The most likely interstitial sites for the large cations are $(0, 0, \frac{1}{2})$ and equivalent sites while no interstitial sites are available the *b*-direction (Petrović, 1972). For unit jumps parallel to the *a*-direction the space between the atoms constituting the framework is large enough to allow the alkali cations to jump to the interstitial sites

without the need for severe distortion of the lattice (Petrović, 1972). Parallel to the b-axis the cation sites are separated by the crankshaft-like chains formed by the Al- and O-tetrahedra (Ribbe, 1983) and the atomic jumps in this direction are more difficult. The dilation in b-direction that is localized at the diffusion front corresponds to an increase in the length of the atomic jumps that the alkali cations contributing to diffusion in [010] direction have to execute. It is conceivable that an increase in the jump distance between two neighboring sites that are aligned in [010]-direction in the alkali sublattice goes along with an increase of the energy barrier between them. This would correspond to an increase in the activation energy for diffusion and would thus entail a reduction of the corresponding diffusion coefficient. Similarly to the lattice distortion this effect would be localized at the diffusion front and contribute to further sharpening of an emerging diffusion front. This feedback of diffusion induced lattice strain into the diffusion process itself maybe one of the reasons for the formation of the exceptionally sharp diffusion fronts normal to (010) for shifts towards more potassium-rich compositions. In the case at hand, the self sharpening diffusion front acts as a diffusion barrier, a feature that might be of interest in domain single crystals.

5 Conclusions

We document the evolution of sharp concentration fronts during sodium-potassium interdiffusion in alkali feldspar in b-direction. In contrast, the concentration profiles are comparatively broad in directions contained in the a-c-plane. The extraordinarily sharp composition gradients in b-direction only occur at $X_{Or} > 0.95$ and do not confer with theoretical predictions from interdiffusion models. The sharp composition gradient is related to a sharp lattice distortion gradient as measured using EBSD combined with a pattern cross correlation method. The phenomenon of the extraordinarily sharp composition gradients is ascribed to the combined effects of the pronounced composition dependence of the interdiffusion coefficients and the distortion of the feldspar lattice in response to chemical eigenstrain. The lattice distortion due to chemically induced coherency stress may act as a self-induced diffusion barrier. This phenomenon has potential applications in designing domain single crystals with custom tailored transport properties.

Acknowledgements We thank Gerald Giester for orienting the feldspar crystals on a three circle goniometer and Andreas Wagner for preparing the single crystal plates with polished surfaces. This work was funded by the Austrian Science Foundation, FWF grant I 474-N19 in the framework of the DFG-FWF research group FOR 741.

6 References

Abart R, Petrishcheva E, Wirth R, Rhede D (2009) Exsolution by spinodal decomposition: Ii: perthite formation during slow cooling of anatexites from

ngornghoro, tanzania. American Journal of Science 309:450-475

Angel RJ, Sochalski-Kolbus LM, Tribaudino M (2012) Tilts and tetrahedra: The origin of the anisotropy of feldspars. American Mineralogist 97:765-778

Britton T, Wilkinson A (2012) Stress fields and geometrically necessary dislocation density distributions near the head of a blocked slip band. Acta Materialia 60:5773-5782

Cherniak D (2010) Cation diffusion in feldspars. Reviews in Mineralogy & Geochemistry 72:691-733

Christoffersen R (1982) I. Disordering Kinetics and Stability of Low-Andesine, II. Na-K Interdiffusion in the Alkali Feldspars. Ph.D. thesis, Brown University, Providence, Rhode Island

Christoffersen R, Yund R, Tullis J (1983) Interdiffusion of K and Na in alkali feldspars: homogenization experiments. American Mineralogist 68:1126-1133

Demtröder K (2011) Untersuchung zur Al/Si-Ordnung an Sanidin Megakristallen aus der Eifel. Master's thesis, Ruhr-Universität Bochum

Kroll H, Schmiemann I, von Cölln G (1986) Feldspar solid solutions. AmericanMineralogist 71:1-16

Larche F, Cahn J (1982) The effect of self-stress on diffusion in solids. Acta Metallurgica 30:1835-1845

Maurice C, Driver JH, Fortunier R (2012) On solving the orientation gradient dependency of high angular resolution EBSD. Ultramicroscopy 113:171-181

Neusser G, Abart R, Fischer F, Harlov D, Norberg N (2012) Experimental Na/K exchange between alkali feldspar and salt melt: coherency effects, microstructure evolution, and element partitioning. Contributions to Mineralogy and Petrology 164:341-358

Parsons I, Lee MR (2005) Minerals are not just chemical compounds. The Canadian Mineralogist 43:1959-1992

Petrović R (1972) Alkali Ion Diffusion in Alkali Feldspars. Ph.d. thesis, Yale University

Ribbe P (1983) Chemistry, Structure and Nomenclature of Feldspars, Mineralogical Society of America, pp 119

Riley TR, Bailey DK (2003) Barium-rich sanidine megacrysts from the West

Eifel (Germany). Neues Jahrbuch für Mineralogie - Monatshefte 41:18-30

Scheidl K, Schäffer AK, Petrishcheva E, Habler G, Fischer F, Schreuer J, Abart R (2013) Chemically induced fracturing in alkali feldspar. Physics and Chemistry of Minerals

Spear FS (1993) Metamorphic Phase Equilibria and Pressure-TemperatureTime Paths. Mineralogical Society of America, Washington, DC Stephenson G (1988) Deformation during interdiffusion. Acta Metallurgica 36:2663

Svoboda J, Fischer F, Fratzl P (2006) Diffusion and creep in multi-component alloys with non-ideal sources and sinks for vacancies. Acta Materialia 54:3043-3053

Weitz G (1972) Die Struktur des Sanidins bei verschiedenen Ordnungsgraden. Zeitschrift für Kristallographie 136:418-426

Wilkinson AJ, Britton BT (2012) Strains, planes, and EBSD in materials science. Materials Today 15(9):366-376

Wilkinson AJ, Meaden G, Dingley DJ (2006) High-resolution elastic strain measurement from electron backscatter diffraction patterns: New levels of sensitivity. Ultramicroscopy 106:307-313

Wilkinson AJ, Meaden G, Dingley DJ (2009) Mapping strains at the nanoscale using electron back scatter diffraction. Superlattices and Microstructures 45:285-294

Yund R (1984) Alkali Feldspar Exsolution: Kinetics and Dependence on Alkali Interdiffusion, Reidel Publishing Company, pp 281-315

Appendix E

Petrishcheva et al. (submitted)

Petrishcheva et al. (submitted): Na-K interdiffusion in alkali feldspar I experimental determination of the composition-dependent diffusivity tensor

The execution of the experiments, BSE imaging and microprobe work were done by Anne-Kathrin Schäffer. Analysis of the data and determination of the full diffusivity tensor were done by Elena Petrishcheva.

Noname manuscript No.
(will be inserted by the editor)

Na-K interdiffusion in alkali feldspar I: experimental determination of the composition-dependent diffusivity tensor

E. Petrishcheva · R. Abart · A.-K. Schaeffer · G. Habler · D. Rhede

Received: date / Accepted: date

Abstract Anisotropic diffusion is described by a tensor of diffusivities, $D_{\alpha\beta}$, which may be composition dependent leading to nonlinear anisotropic diffusion. In this work the practical problem of reconstructing such a tensor for Na-K interdiffusion in potassium-rich alkali feldspar with $0.85 \leq X_{\mathrm{Or}} \leq 1.00$ is addressed. Cation exchange experiments were performed using gem quality sanidine with an initial composition of $X_{\mathrm{Or}} = 0.85$ and KCl salt melt at 850°C and ≈1 bar. To this end, plates of sanidine with polished surfaces in six different crystallographic directions were used, and $D_{\alpha\beta}$ was reconstructed from the respective composition profiles produced from cation exchange. The dependencies $D_{\alpha\beta}(X_{\mathrm{Or}})$ were extracted using a suitable generalization of the Boltzmann approach, which adequately accounts for our experimental setup and for diffusion anisotropy. The results were tested by solving the anisotropic nonlinear diffusion equation using the previously determined diffusivities. Na-K interdiffusion in potassium-rich alkali feldspar is considerably composition dependent and anisotropic. All diffusivities $D_{\alpha\beta}(X_{\mathrm{Or}})$ increase as X_{Or} tends to 1. The principal axes of the diffusivity tensor representing the directions of highest and lowest diffusivity lie in the *a*-*c* plane and the direction with intermediate diffusivity is parallel to the crystallographic *b* axis. Our main result is given in the form of numerical values for all components of the $D_{\alpha\beta}(X_{\mathrm{Or}})$ tensor for $0.85 \leq X_{\mathrm{Or}} \leq 1$.

This work was funded by the Austrian Science Foundation, FWF grant I 474-N19 in the framework of the DFG-FWF research group FOR 741.

E. Petrishcheva, R. Abart, A.-K. Schaeffer, G. Habler
Department of Lithospheric Research, University of Vienna,
Althanstrasse 14, A-1090, Vienna, Austria
E-mail: elena.petrishcheva@univie.ac.at

D. Rhede
Helmholtzzentrum Potsdam, Deutsches GeoForschungsZentrum, Telegraphenberg,
D-14473, Potsdam, Germany

Keywords sodium-potassium interdiffusion · potassium-rich alkali feldspar · anisotropy · composition dependence

1 Introduction

Alkali feldspar is among the most abundant rock forming minerals in the Earth's crust. The alkali feldspars form a solid-solution series along the binary join between the sodium ($NaAlSi_3O_8$) and potassium ($KAlSi_3O_8$) end-members. The interdiffusion of Na^+ and K^+ on the alkali sublattice of alkali feldspar plays a pivotal role in the re-equilibration of Na-K partitioning between alkali feldspar and other Na- and K-bearing minerals in rocks undergoing pressure-temperature change (Voll et al (1994)). Understanding such re-equilibration phenomena is crucial for the application of geo-thermobarometers such as the two feldspar thermometer (Fuhrman and Lindsley (1988); Benisek et al (2010)). Furthermore, Na-K interdiffusion determines the kinetics of exsolution in alkali feldspar. In particular it governs the coarsening rate of exsolved precipitates and their composition evolution during cooling (Yund (1984); Petrishcheva and Abart (2009); Abart et al (2009b); Abart et al (2009a); Petrishcheva and Abart (2012)). Quantifying re-equilibration phenomena and exsolution kinetics in alkali feldspar requires knowledge of the Na-K interdiffusion coefficient.

For ionic crystals forming a binary solid-solution the interdiffusion coefficient can be calculated from the experimentally determined tracer diffusion coefficients of the atoms representing the end-member phase components (Manning (1968)). For the interdiffusion of sodium and potassium in alkali feldspar this reads

$$D_{\mathrm{NaK}} = \frac{D^*_{Na}(c) D^*_K(c)}{(1-c)\, D^*_{Na}(c) + c D^*_K(c)} \left[1 + \frac{\partial \ln \gamma_c}{\partial \ln c}\right], \tag{1}$$

where D_{NaK} is the Na-K interdiffusion coefficient, and c is a short hand notation for the orhtoclase mole fraction in alkali feldspar $c \equiv X_{\mathrm{Or}} = \frac{K}{K+Na}$ in atomic units; $D^*_{Na}(c)$ and $D^*_K(c)$ are the sodium and the potassium tracer-diffusion coefficients, respectively, which are considered as composition dependent; γ_c is the activity coefficient of the potassium end-member phase component, which can be calculated from thermodynamic mixing models for the alkali feldspar solid-solution such as given by Hovis et al (1991). A number of tracer diffusion experiments have been done in which radioactive tracers including ^{22}Na (Foland (1974); Lin and Yund (1972); Kasper (1975)), ^{40}K (Lin and Yund (1972)), and ^{41}K as a stable isotope tracer (Foland (1974); Giletti and Shanahan (1997)) were used to determine the tracer diffusion coefficients of sodium and potassium in alkali feldspar. It was generally found that sodium diffuses much faster than potassium. In terms of the absolute values the results from the different studies show, however, considerable scatter (see the review by Cherniak (2010)), and calculation of Na-K interdiffusion coefficients from the respective tracer diffusion coefficients is rather uncertain. Alternatively, the Na-K interdiffusion coefficient can be determined directly

from interdiffusion experiments. Thereby a diffusion couple consisting of two alkali feldspars of different compositions is annealed at elevated temperature to induce sodium-potassium exchange between the two feldspars. The interdiffusion coefficient is then obtained from the resulting composition profile across the interface between the two feldspars. The interdiffusion coefficient is generally expected to be composition dependent (Mehrer (2007)), which must be accounted for when determining the Na-K interdiffusion coefficient from composition-distance data. Christoffersen et al (1983) determined the Na-K interdiffusion coefficient in the composition range $0.1 \leq X_{Or} \leq 0.8$ at temperatures of 900^oC and 1000^oC and at pressures of 0.5 and 1.5 GPa. They found a pronounced composition dependence with a minimum in D_{NaK} at $X_{Or} \approx 0.4$. Moreover, a diffusion anisotropy was revealed, where diffusion perpendicular to (010) is about 12 times slower than perpendicular to (001). Comparison of the experimentally determined interdiffusion coefficients with those obtained from equation (1) using the experimentally determined Na- and K-tracer diffusion coefficients of Kasper (1975) for albite and of Foland (1974) for orthoclase with $X_{Or} = 0.94$ delivered a similar composition dependence of D_{NaK} as experimentally determined. In terms of the absolute values the experimentally determined interdiffusion coefficients were, however, by a factor of 10 ($\perp$ (001)) and 100 ($\perp$ (010)) lower than predicted from equation (1). The study of Christoffersen et al (1983) contributed substantially to the understanding of Na-K interdiffusion in alkali feldspar. Several questions remained unanswered though. In particular, the composition range of $0.8 \leq X_K \leq 1.0$ was not covered. This composition range is, however, of considerable interest, because most potassium-rich alkali feldspars in natural rocks fall into this composition range. Christoffersen et al (1983) give the interdiffusion coefficients for selected crystallographic directions, they do, however, not provide the full diffusivity tensor, which is necessary for a comprehensive description of the direction dependence of Na-K interdiffusion. Furthermore, it has been shown that localized, diffusion induced composition change in single crystal alkali feldspar produces coherency stress, which may eventually induce fracturing (Petrovic (1972); Neusser et al (2012); Scheidl et al (2013)). According to Scheidl et al (2013) fracturing may occur, when composition shifts exceed about 10 mole %. The feldspars in the diffusion couples of Christoffersen et al (1983) were shifted by about 50 mole % close to the contact plane of the two feldspars. It is therefore possible that in the experiments of Christoffersen et al (1983) the composition induced coherency strain was accommodated by creep or by the formation of microcracks. The associated increase in defect density may have an influence on Na-K interdiffusion, but such effects were neither documented nor evaluated by the latter authors.

In this study we present the results of dedicated Na-K interdiffusion experiments. In contrast to the study by Christoffersen et al (1983) we used a single crystal alkali feldspar and KCl salt melt as a diffusion couple, and composition shifts in the feldspar did not exceed 15 mole %. That way mechanical effects due to large composition shift in a single crystal feldspar and their potential feedback on interdiffusion could be minimized. The theory necessary for data

reduction in the specific setting of composition-dependent, anisotropic Na-K interdiffusion in monoclinic alkali feldspar is presented and the full diffusivity tensor and its composition dependence in the composition range $0.85 \leq X_{\mathrm{Or}} \leq 1.0$ is derived for 850^oC and $\approx$1 bar. The temperature dependence of D_{NaK} in the temperature range from 800^oC to 1000^oC and for compositions in the range $0.85 \leq X_{\mathrm{Or}} \leq 1.0$ for diffusion in the directions perpendicular to (001) and (010) are presented in the companion paper by Schaeffer et al (2014b).

2 Experiment

2.1 Cation exchange experiments

Interdiffusion of Na^+ and K^+ in alkali feldspar was studied by means of cation-exchange experiments, where Na^+ and K^+ ions were exchanged between alkali feldspar of intermediate composition ($X_{\mathrm{Or}} = 0.85$) and a KCl salt melt at 850^oC and $\approx$1 bar. Cation exchange produced a composition shift towards pure potassium end-member composition at the surface of the feldspar grain. The chemical alteration propagated into the grain interior with time requiring Na-K interdiffusion on the alkali sublattice. The composition variation from the grain surface into the grain interior was analyzed with a field-emission gun electron microprobe. The interdiffusion coefficient was then extracted from the composition profiles.

Gem quality sanidine from Volkesfeld (E-Eifel) with an original composition of $X_{\mathrm{Or}} = 0.85$ was used as starting material. The sanidine is practically free of calcium and has minor Ba contents of up to 1.3 wt. %, Fe up to 0.2 wt. %, and Sr up to 0.2 wt. % (Demtröder (2011); Neusser et al (2012)). The sanidine is chemically homogeneous down to the nanometer scale. It is devoid of cracks, twins, exsolutions, second phase precipitates or other structural or chemical heterogeneities (Riley and Bailey (2003), Weitz (1972), Neusser et al (2012), Demtröder (2011)). Aluminum and silicon are highly disordered on the tetrahedral site with t1 = 61 (Neusser et al (2012)) resulting in monoclinic symmetry, space group C2/m.

Selected sanidine grains were oriented on a single crystal diffractometer and then machined to plates of about 3 x 3 x 1 mm. The plates were cut in six different crystallographic orientations, and the 3 x 3 mm surfaces were polished. The feldspar plates were then put into quartz glass tubes with an inner diameter of 8 mm together with reagent grade KCl salt. The amount of KCl was chosen so as to achieve a molar ratio of 40:1 for the alkali cations contained in the salt and in the feldspar, respectively. That way an essentially constant composition of the salt melt was ensured during the exchange experiments. The quartz glass tubes were then sealed under vacuum and put into a pre-heated box furnace at 850^oC for 1 to 64 days (see table 1). The temperature was monitored with a type N thermocouple placed directly at the sample and was accurate to within $\pm\ 2^o$. It was shown by Neusser et al (2012) that the Al-Si ordering state does not change during cation exchange between sanidine

and NaCl-KCl salt melt at 850°C. After the exchange experiment the samples were quenched within a few seconds by dropping the quartz glass tubes into cold water. The tubes were opened and the feldspar was retrieved by dissolving the salt in deionized water. The feldspars retained their surface polish and no indications of surface reactions could be detected. The feldspar plates were then mounted in epoxy with the polished faces perpendicular to the surface of the mount. The sample was then cut, ground and polished mechanically using diamond paste down to 0.25 μm grain size. Finally a chemomechanical polish using a silica suspension with basic pH was applied to remove the defect rich surface layer for later electron back scatter diffraction (EBSD) analysis.

2.2 Scanning electron microscopy

Scanning electron microscopy was done on a Quanta 3D FEG instrument at the Center of Earth Sciences, University of Vienna. Back scattered electron images were taken to document chemical alteration of the feldspar which is readily discerned from the change in grey shade on BSE images (see Fig. 1). In general, cation exchange between the sanidine and the KCl melt lead to a composition shift from the original composition of $X_{\mathrm{Or}} = 0.85$ to pure potassium end-member composition with $X_{\mathrm{Or}} = 1.00$. On the BSE images light grey zones of constant width are observed along the rims of the grains showing that chemical alteration starts from the grain surfaces and progresses into the grain interior with time. The exchanged outer domains of the grains and the internal domains with the original composition preserved are separated by more or less sharp transition zones (see Fig. 1). Chemical alteration within the single crystal sanidine requires that Na^+ and K^+ interdiffuse on the alkali sublattice of the feldspar, and the transition zone may be referred to as a diffusion front. Interestingly, the diffusion front is relatively sharp in [010]-direction and comparatively broad in the direction perpendicular to the (001) plane indicating diffusion anisotropy. In some cases, the lattice strain associated with cation exchange induced fracturing and produced irregularities in sample geometry and in the chemical pattern. Only those portions of the crystal were chosen for further mineral chemical analysis, where the diffusion fronts were perfectly parallel to the polished sample surface and the fronts themselves were undisturbed.

The crystal lattice orientation of the feldspar samples embedded in epoxy resin was determined by Electron backscatter diffraction analysis (EBSD). The Quanta 3D FEG instrument equipped with an EDAX Digiview IV EBSD camera was operated at 15 keV accelerating voltage and 2-3 nA probe current in analytical mode. During analysis the sample surface was tilted to establish a beam incidence angle of 20 at a working distance of 10-14 millimeters. EBSD data collection and processing was performed using the EDAX OIM Data Collection and Analysis Software (versions 5.31 or 6.2). The background correction filter was generated on a natural polycrystalline alkali feldspar aggregate sample. To optimize the EBSD pattern contrast and intensity histogram nor-

malization filter, a dynamic background subtraction filter and for some grains also a mean smoothing filter were applied. Due to partly weak EBSD patterns, the camera and Hough settings were adjusted for each grain separately. EBSD camera settings were at 2x2 binning using an exposure time of 300 - 400 msec. Hough settings of a binned pattern size of 160x160 pixels, a Theta step size of 0.5° to 1° and a 9x9 or 11x11 convolution mask were applied to a Rho-fraction of 72 % to 85 % for indexing at minimum 3 - 6 and at maximum 9 - 19 bands at a minimum distance of 8 - 17 pixels in Hough space. The orientation data were derived from 100x100 micrometer sized areas taken in a central portion of each crystal. Using step sizes of 10 - 25 micrometers in hexagonal grid mode yielded 23 - 126 data points per grain. In case of ambiguous results due to similar first and second solutions, single EBSD patterns were collected using 5 - 8 frames and evaluated manually for the different solutions in order to determine the actual orientation.

2.3 Mineral chemical analysis

Mineral chemical analyses were done on a field emission gun electron microprobe JEOL Hyperprobe JXA-8500F at Helmholtzzentrum Potsdam. Point analyses were taken along profiles from the polished sample surface inwards across the diffusion front and into the internal domains of the crystal. The exact orientation of each analysis profile with respect to the crystal lattice was reconstructed based on the EBSD data that were collected for each grain. Composition profiles were measured in six crystallographic directions which are given by the direction cosines with respect to the $(\mathbf{a}, \mathbf{b}, \mathbf{c}^*)$ frame: profile 1 (1, 0, 0); profile 2 (0, 1, 0); profile 3 (0, 0, 1); profile 4 ($\sqrt{2}/2$, $\sqrt{2}/2$, 0); profile 5 ($\sqrt{2}/2$, 0, $\sqrt{2}/2$); profile 6 (0, $\sqrt{2}/2$, $\sqrt{2}/2$) (see table 1). Point analyses were taken at 0.5 to 1 μm steps. The acceleration voltage and the beam current were set to 8 kV and 10 nA, respectively. Counting times were 10 seconds on the peak and 5 seconds on the background on both sides of the peak. Short counting times were necessary to minimize loss of sodium by evaporation under the electron beam. Due to the small footprint of the beam and excitation volume, the analyses were very sensitive to imperfections of the sample surface such as scratches or beam induced carbon deposition. Despite of the resulting scatter in the data, the analyzed trends clearly reflect the shapes of well defined diffusion profiles. Two examples of measured composition profiles are shown in Fig. 2. The exchanged portions of the crystal attained pure potassium endmember composition of $X_{\mathrm{Or}} = 1.00$. Corresponding to the variation in grey shade in the BSE image, the profile that evolved perpendicular to the (010) surface shows a relatively sharp transition zone between the outer exchanged domain and the grain interior with its original composition preserved. The sharp change in composition perpendicular to the (010) surface may give the impression of a dissolution-precipitation feature. The perfect preservation of the surface polish after cation exchange and the lack of evidence for surface reaction argue against this interpretation. Furthermore, in cation exchange

Table 1 Directions of measurement profiles and number of experiments done for different run durations.

direction	direction cosines	1 day	4 days	8 days	16 days	32 days
1	1 0 0	2	1			
2	0 1 0		1	3	2	1
3	0 0 1	3	2	2		
4	$\frac{\sqrt{2}}{2}$ $\frac{\sqrt{2}}{2}$ 0			1	2	
5	$\frac{\sqrt{2}}{2}$ 0 $\frac{\sqrt{2}}{2}$			1		
6	0 $\frac{\sqrt{2}}{2}$ $\frac{\sqrt{2}}{2}$			1		

experiments using similar experimental setup and starting material the Ba distribution remained unaffected across Na-K exchange fronts (Neusser et al (2012)). In contrast, the Ba and also the Fe distribution in Eifel sanidine was completely changed across reaction fronts that developed during fluid induced albitization of Eifel sanidine by reaction with NaCl brine, which is clearly associated with dissolution-precipitation (Norberg et al (2012)) suggesting that dissolution-precipation occurs when feldspar is reacted with a fluid but does not occur when sanidine is reacted with a "dry" alkali halide melt. Moreover, in an EBSD study on the lattice strain across a sharp concentration front along the [010] direction produced in Eifel sanidine during cation exchange in a similar experimental setup Schaeffer et al (2014a) found localized elastic lattice strain but no indication for recrystallization across the sharp composition front, which further corroborates the interpretation of the observed composition contrasts as diffusion fronts. The transition between the exchanged external and the pristine internal portions of a grain is more gradual in the direction perpendicular to the (001) plane than in [010] direction. In the profiles in both crystallographic directions a plateau is visible in the outer portion, where the composition is at $X_{\mathrm{Or}} = 1.00$, and an inflection point is located in the transition zone. Given that the composition of the salt remained essentially unchanged during the cation exchange experiments, and Na-K interdiffusion occurred under a constant concentration boundary condition at the crystal surface, such a front geometry can only be explained by a composition dependence of the interdiffusion coefficient. In the following we present the theory used for data reduction in the specific case of composition dependent anisotropic interdiffusion of Na^+ and K^+ in an alkali feldspar with monoclinic symmetry.

3 Theory

A diffusive particle flux, further denoted by $\mathbf{j}(\mathrm{r}, t)$, results solely from the nonuniform distribution of the diffusant Crank (1975). In what follows, the distribution of the diffusant is denoted by $c(\mathrm{r}, t)$, the latter may refer to the, e.g., volume concentration or mole-fraction, depending on the problem at hand. For our case $c(\mathrm{r}, t)$ is identical to $X_{\mathrm{Or}}(\mathrm{r}, t)$. The non-uniformity is characterized

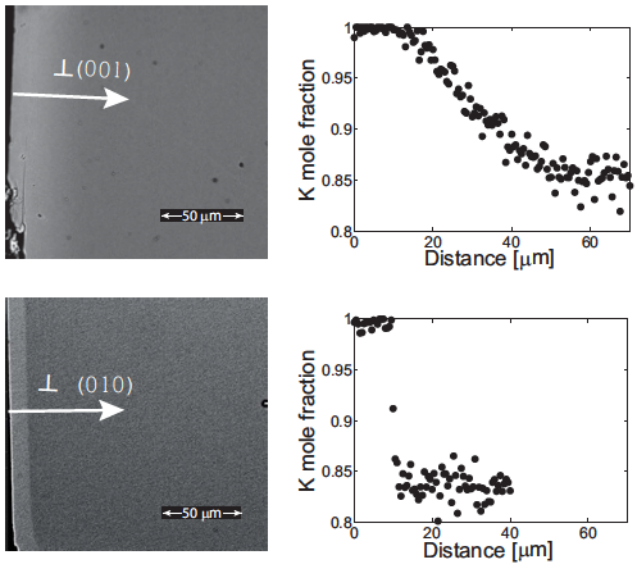

Fig. 1 Back-scatter electron images and composition - distance data for analysis profiles perpendicular to a polished (001) (top) and (010) (bottom) surface of sanidine after exchange with KCl melt at 850°C for 8 days.

by the gradient vector $\nabla c(\mathbf{r},t) = (\partial c/\partial x_1, \partial c/\partial x_2, \partial c/\partial x_3)$ pointing to where the concentration of the diffusant increases the most. The concept behind Fick's diffusion law is that in an isotropic medium the flux vector and the gradient vector are antiparallel and proportional to each other, $\mathbf{j} = -D\nabla c$. In the isotropic case the quantity D is just a scalar quantity and is referred to as the diffusivity.

If the diffusivity depends on diffusant concentration, $D = D(c)$, this is referred to as nonlinear diffusion. Combining Fick's law with the general conservation law for the particle number

$$\frac{\partial c}{\partial t} = -\nabla \mathbf{j}, \tag{2}$$

we obtain the diffusion equation

$$\frac{\partial c}{\partial t} = \sum_{\alpha} \frac{\partial}{\partial x_\alpha}\left[D(c)\frac{\partial c}{\partial x_\alpha}\right], \qquad \alpha = 1,2,3, \tag{3}$$

where α denotes axes of an orthogonal coordinate frame chosen within the material.

If one knows $D(c)$, Eq. (3) can be discretized and solved numerically to obtain $c(\mathbf{r},t)$ from $c(\mathbf{r},0)$ and boundary conditions. If $D(c)$ is unknown, one can address the inverse problem: obtain $D(c)$ from the experimentally measured $c(\mathbf{r},t)$. An example thereof is the Boltzmann-Matano analysis Matano (1933).

In this section we use the above reported experimental data and reconstruct diffusivities for the anisotropic case. It is important to note that our geometry

differs from that of the Boltzmann-Matano analysis. Therefore we first revisit the reconstruction scheme.

3.1 Reduction

In a crystal, where anisotropy is encountered, Fick's law remains valid, but becomes more complicated. The relation between the two vectors $\mathbf{j}$ and ∇c is described by a tensor (Crank (1975))

$$j_\alpha = -\sum_\beta D_{\alpha\beta}\frac{\partial c}{\partial x_\beta}, \qquad \alpha,\beta = 1,2,3,$$

where the elements of the second-rank diffusivity tensor may depend on the diffusant concentration, $D_{\alpha\beta} = D_{\alpha\beta}(c)$. Then the diffusion equation Eq. (3) is replaced by

$$\frac{\partial c}{\partial t} = \sum_{\alpha,\beta}\frac{\partial}{\partial x_\alpha}\left[D_{\alpha\beta}(c)\frac{\partial c}{\partial x_\beta}\right]. \tag{4}$$

At a first glance, all directions are mixed in Eq. (4). Still, it is possible to reduce Eq. (4) to an effectively one-dimensional equation. To explain this we consider diffusive flow into a semi-infinite block, $x_1 \geq 0$, consisting of an anisotropic solid with the boundary at $x_1 = 0$. Let us assume that $c = c(x_1, t)$. Even such a simple plane-parallel distribution leads to a three-component flux

$$\mathbf{j} = -\begin{pmatrix} D_{11} & D_{12} & D_{13} \\ D_{21} & D_{22} & D_{23} \\ D_{31} & D_{32} & D_{33} \end{pmatrix}\begin{pmatrix} \frac{\partial c}{\partial x_1} \\ 0 \\ 0 \end{pmatrix} = -\begin{pmatrix} D_{11}\frac{\partial c}{\partial x_1} \\ D_{21}\frac{\partial c}{\partial x_1} \\ D_{31}\frac{\partial c}{\partial x_1} \end{pmatrix}.$$

Still only $j_{x1} = -D_{11}(c)\partial c/\partial x_1$ contributes to $\nabla\mathbf{j}$ in Eq. (2). Therefore the plane-parallel distribution evolves in full analogy with the simplest diffusion equation in one spatial dimension

$$\frac{\partial c}{\partial t} = \frac{\partial}{\partial x_1}\left[D_{11}(c)\frac{\partial c}{\partial x_1}\right]. \tag{5}$$

Hence, if we prepared a large enough feldspar plate with one of the axes parallel to Ox and measured how the cations from the salt penetrate into the crystal along this axis, we would get $c(x_1, t)$. We then could retrieve $D_{11}(c)$.

This approach can be extended to recover the full tensor $D_{\alpha\beta}(c)$. Consider diffusion along some arbitrary direction given by a unit vector $\mathbf{n}$ with the components (direction cosines) n_1, n_2, and n_3. The plane-parallel diffusant distribution is given by $c = c(\xi, t)$, where the "propagation coordinate" ξ is defined as

$$\xi = n_1x_1 + n_2x_2 + n_3x_3,$$

and the origin of the (x_1, x_2, x_3) frame is taken at the salt-crystal interface, such that the boundary conditions are specified at $\xi = 0$. Using the chain rule

$$\frac{\partial}{\partial x_\alpha} = n_\alpha \frac{\partial}{\partial \xi},$$

it is easy to see that Eq. (5) is generalized to the form

$$c = c(\xi, t), \qquad \frac{\partial c}{\partial t} = \frac{\partial}{\partial \xi}\left[D_n(c)\frac{\partial c}{\partial \xi}\right], \tag{6}$$

where $D_n(c)$ denotes the scalar diffusivity along the direction $\mathbf{n}$

$$D_n(c) = \sum_{\alpha,\beta} D_{\alpha\beta}(c) n_\alpha n_\beta. \tag{7}$$

Equation (6) is naturally coupled with the following initial and boundary conditions

$$\xi \geq 0, \qquad c(\xi, t)\big|_{\xi=0} = c_1, \qquad c(\xi, t)\big|_{t=0} = c_2, \tag{8}$$

where c_1 and c_2 are the potassium mole fraction of the alkali feldspar in equilibrium with the salt melt, and the initial potassium mole fraction in the crystal, respectively. Now, if we recover $D_n(c)$ for a large enough number of directions, we can consider Eq. (7) as a system of linear equations that delivers the unknowns $D_{\alpha\beta}(c)$.

According to Onsager's principle $D_{\alpha\beta} = D_{\beta\alpha}$ so that only six diffusivities are left. Moreover, $D_{\alpha\beta}$ is affected by symmetries of the crystal. For the monoclinic symmetry at hand, we chose the $(\mathbf{a}, \mathbf{b}, \mathbf{c}^*)$ frame in which $\mathbf{b}$ is set parallel to the crystallographic dyad axis. The diffusivity tensor then takes the form

$$D_{\alpha\beta} = \begin{pmatrix} D_{11} & 0 & D_{13} \\ 0 & D_{22} & 0 \\ D_{31} & 0 & D_{33} \end{pmatrix},$$

so that only four unknown diffusivities are left. However, to improve the accuracy, we considered six directions and measured up to seven profiles $c(\xi, t)$ for each direction (see table 1). The components $D_{\alpha\beta}$ were then obtained from Eq. (7) using the least squares method.

3.2 Boltzmann's method

In this section we explain how $D_n(c)$ is recovered from the experimentally measured concetration distance data, i.e. solutions $c(\xi, t)$ of Eqs. (6)–(8). The latter system has an important feature first noticed by Boltzmann (1894). Namely, one can introduce a combined space-time variable

$$\eta = \frac{\xi}{2\sqrt{t}} \quad \text{defined for} \quad t > 0, \tag{9}$$

and look for a special class of solutions of the diffusion equation: functions $c(\xi, t)$ that are reduced to a composite function $c(\eta)$ of a single variable (9). It is easy to see that for such solutions the nonlinear diffusion equation (6) transforms to

$$-2\eta \frac{dc}{d\eta} = \frac{d}{d\eta}\left[D_n(c)\frac{dc}{d\eta}\right], \qquad 0 \le \eta < +\infty \tag{10}$$

which is an ordinary differential equation. The key question is: are the initial and boundary conditions compatible with the ansatz $c = c(\eta)$? For instance, this is the case for the Boltzmann-Matano analysis. Our geometry is different but still compatible with the Boltzmann variable. From Eq. (8) we obtain that

$$c(\eta)\big|_{\eta=0} = c_1 \qquad \text{and} \qquad c(\eta)\big|_{\eta=+\infty} = c_2. \tag{11}$$

Therefore, the initial value problem for the partial differential system (6)–(8) exactly reduces to a boundary value problem for an ordinary differential system (10)–(11).

We now turn to the inverse problem and express $D(c)$ in terms of $c(\eta)$. To this end we integrate Eq. (10) over $d\eta$ over the interval $[\eta, \infty]$. Note, that it is natural to assume that $c'(\eta) = dc/d\eta \to 0$ for $\eta \to \infty$. Therefore

$$2\int_{\eta}^{\infty} \eta c'(\eta) d\eta = c'(\eta) D_n(c)\big|_{c=c(\eta)}. \tag{12}$$

Finally we note that with the increase of η, $c(\eta)$ decreases monotonically from $c(0) = c_1$ to $c(\infty) = c_2$. Therefore one can introduce the inverse function $\eta = \eta(c)$ and transform Eq. (12) to the form

$$D_n(c) = -2\eta'(c)\int_{c_2}^{c} \eta(c) dc. \tag{13}$$

In what follows equation (13) is used for calculating $D(c)$.

3.3 Results for diffusivities

The results from all interdiffusion experiments which were done along six different crystallographic directions are shown in figure 2. Let (ξ_s, c_s), $1 \le s \le S$ denote experimental observations of the mole fraction profile $c = c(\xi, t)$ for some fixed direction $\mathbf{n}$ and time $t = t_0$. First, the space coordinate was rescaled to $\eta_s = \xi_s/(2\sqrt{t_0})$ and then the points (η_s, c_s) obtained from all experiments done along this specific direction were plotted together (see Fig. 2). Although the measurements had been done for several values of t_0, all rescaled points approximately belong to the same curve. The latter represents $c(\eta)$ for the fixed direction $\mathbf{n}$. In a second step, the data were smoothed assigning the same weight to each of the profiles measured along one direction. The smoothed data set (η_s, c_s) was then used to derive the inverse function $\eta(c)$. The latter

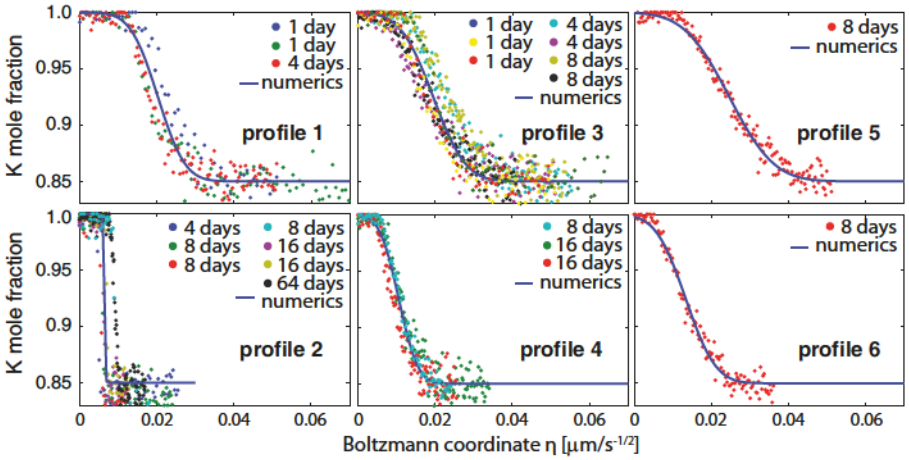

Fig. 2 Potassium mole fractions in alkali feldspar along different crystallographic directions versus rescaled Boltzmann coordinate η; direction cosines with respect to the $(\mathbf{a}, \mathbf{b}, \mathbf{c}^*)$ frame: profile 1 (1, 0, 0); profile 2 (0, 1, 0); profile 3 (0, 0, 1); profile 4 ($\sqrt{2}/2$, $\sqrt{2}/2$, 0); profile 5 ($\sqrt{2}/2$, 0, $\sqrt{2}/2$); profile 6 (0, $\sqrt{2}/2$, $\sqrt{2}/2$); different run-durations are indicated by different colors; after rescaling to η, all points from a certain direction approximately belong to the same curve; solid lines: mole fractions obtained from numerical solutions of Eq. (4) using the diffusivities determined from the experimental observations; the corresponding values of $D_{\alpha\beta}(c)$ are reported in Fig. 3.

was inserted into Eq. (13) to obtain $D_n(c)$. We calculated $D_n(c)$ for six directions, each one with up to seven values of t_0. Finally Eq. (7) was solved with respect to $D_{\alpha\beta}(c)$ to recover the unknown components of the diffusivity tensor. The results for the components of $D_{\alpha\beta}(c)$ are shown in Fig. 3, and the numerical values are given in table 2. Finally we tested our results by direct calculation of the numerical solutions of the nonlinear diffusion Eq. (4) with the previously extracted composition-dependent diffusivities. Both the boundary and the initial conditions reflect the experimental setup. The numerical results are shown by the solid lines in Fig. 2. A reasonable agreement with the actually observed composition-distance data (points in Fig. 2) was found. Based on our results the Na-K interdiffusion coefficient for 850°C can now be calculated for any direction in alkali feldspar using Eq. (7).

One immediately observes that Na-K interdiffusion is composition dependent, see Fig. 3. At close to potassium end-member composition $X_{\mathrm{Or}} \geq 0.95$ all diffusivities quickly decrease together with X_{Or}. In the composition range $0.85 \leq X_{\mathrm{Or}} \leq 0.95$ D_{NaK} still decreases with X_{Or}, the composition dependence is, however, less pronounced. Furthermore, Na-K interdiffusion is markedly anisotropic. The diffusion anisotropy is best visualized by plotting characteristic surfaces for the tensor $D_{\alpha\beta}(c)$. Four exemplary values of the potassium mole fraction were used, see Fig. 4. We recall (Nye (1957)) that the characteristic ellipsoid shows how diffusivity depends on direction: the larger the diffusivity in some direction, the more oblate-shaped is the ellipsoid in this direction. Na-K interdiffusion is represented by a three-axed ellipsoid with the

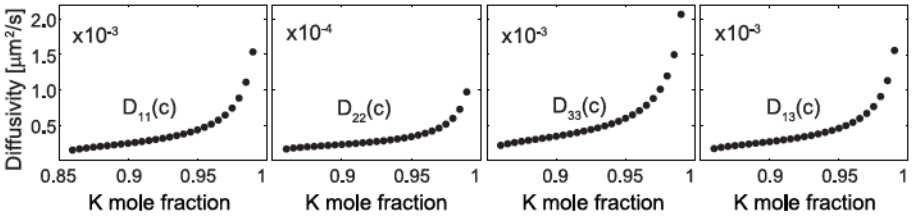

Fig. 3 Nonzero components of the diffusivity tensor $D_{\alpha\beta}(c)$ versus mole fraction of K cations in feldspar. The indices $1 \leq \alpha, \beta \leq 3$ refer to the $(\mathbf{a}, \mathbf{b}, \mathbf{c}^*)$ frame in which $\mathbf{b}$ is set parallel to the crystallographic dyad axis such that both D_{12} and D_{23} vanish.

Table 2 Nonzero components of the diffusivity tensor $D_{\alpha\beta}(c)$.

K mole fraction	0.86	0.875	0.89	0.905	0.92
D11 [$\mu m^2/s$]	1.5×10^{-4}	1.9×10^{-4}	2.2×10^{-4}	2.5×10^{-4}	3.0×10^{-4}
D22 [$\mu m^2/s$]	1.6×10^{-5}	1.9×10^{-5}	2.1×10^{-5}	2.3×10^{-5}	2.6×10^{-5}
D33 [$\mu m^2/s$]	2.1×10^{-4}	2.7×10^{-4}	3.1×10^{-4}	3.6×10^{-4}	4.2×10^{-4}
D13 [$\mu m^2/s$]	1.7×10^{-4}	2.1×10^{-4}	2.5×10^{-4}	2.8×10^{-4}	3.2×10^{-4}
K mole fraction	0.935	0.95	0.965	0.98	0.99
D11 [$\mu m^2/s$]	3.5×10^{-4}	4.3×10^{-4}	5.7×10^{-4}	8.8×10^{-4}	15.3×10^{-4}
D22 [$\mu m^2/s$]	2.9×10^{-5}	3.4×10^{-5}	4.2×10^{-5}	5.9×10^{-5}	9.7×10^{-5}
D33 [$\mu m^2/s$]	4.9×10^{-4}	6.0×10^{-4}	7.8×10^{-4}	12.0×10^{-4}	20.1×10^{-4}
D13 [$\mu m^2/s$]	3.8×10^{-4}	4.6×10^{-4}	6.0×10^{-4}	9.1×10^{-4}	15.6×10^{-4}

intermediate principal axis parallel to the [010] direction and the shortest and longest principal axes in the (010) plane. The shortest principle axis of the representative ellipsoid encloses an angle of 50^o with the positive a-axis measured towards the positive c-axis. This direction exactly coincides with the crystallographic [101] direction ndicating that the strongest diffusion anisotropy is in the (010) plane with fastest diffusion in the [101] direction and slowest diffusion in the direction within (010) that is perpendicular to [101]. The diffusion anisotropy is most pronounced for smaller values of the mole fraction ($X_{\mathrm{Or}} \approx 0.87$) and is less pronounced close to potassium end-member compositions ($X_{\mathrm{Or}} \approx 1.00$).

4 Discussion

The most remarkable results of our study are the composition dependence of Na-K interdiffusion at $X_{\mathrm{Or}} \geq 0.85$ and the marked diffusion anisotropy.

A composition dependence of the Na-K interdiffusion coefficient was already suggested by earlier workers. Using similar cation exchange experiments as described in this study Petrovic (1972) found a substantial increase of D_{NaK} with increasing X_{Or} at compositions with $X_{\mathrm{Or}} \geq 0.86$, which is in line with our observations. With regard to the direction dependence Petrovic (1972), however, found Na-K interdiffusion to be quasi isotropic within the (010) plane

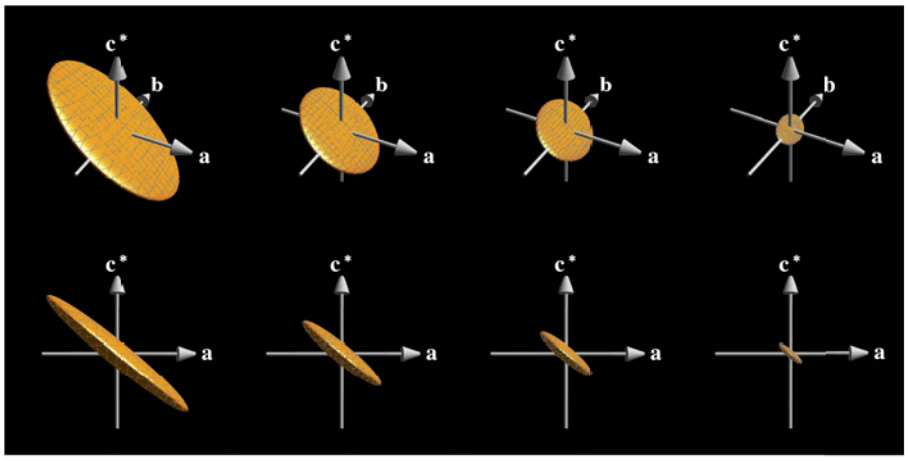

Fig. 4 Four examples of characteristic surfaces representing the composition dependent diffusivity tensor; note that D_{NaK} in a certain direction is inversely proportional to the length of the ellipses radius vector in this direction.

and two orders of magnitude slower in [010] direction than within the (010) plane. Neusser et al (2012) performed cation exchange experiments between alkali feldspar and a large reservoir of NaCl-KCl salt melt ensuring constant composition of the salt melt during cation exchange. From the geometry of the diffusion fronts they inferred that D_{NaK} increases with X_{Or}, but no quantification of the Na-K interdiffusion coefficient was done. In the context of homogenization experiments on synthetic and natural cryptoperthite Brady and Yund (1983) remarked that considerable composition dependence of the interdiffusion coefficient may be expected at physical conditions where a solid-solution deviates significantly from a thermodynamic ideal solution. Actually, this notion is inherent in exsolution by spinodal decomposition and can be predicted from theoretical considerations (Petrishcheva and Abart (2009, 2012)). It is also manifest in equation 1, in which the expression in parentheses corresponds to the "thermodynamic term" accounting for the non-ideality of the solution phase. Christoffersen et al (1983) compared their direct determinations of D_{NaK} from classical diffusion couple experiments at 1000^{o}C to predictions based on equation 1 and indeed found a minimum in D_{NaK} at $X_{\mathrm{Or}} \approx 0.4$ as is predicted from equation 1, if the non-ideality of the alkali feldspar solid-solution is taken into account. These latter authors inferred a diffusion anisotropy with Na-K interdiffusion being 12 times faster perpendicular to (001) than perpendicular to (010). They also found a diffusion anisotropy within the (010) plane with Na-K interdiffusion in [100] direction being six times slower than perpendicular to (001). Both these observations are in reasonable agreement with our findings.

A comparison of our experimentally determined Na-K interdiffusion coefficient and predictions based on equation (1) using experimentally determined tracer diffusion coefficients is shown in figure 5. The non-ideality of the al-

kali feldspar solid-solution is most pronounced at intermediate compositions, it can, however, not explain the strong composition dependence of the Na-K interdiffusion coefficient at close to potassium end-member composition. The steep raise of D_{NaK} with increasing X_{Or} at potassium-rich compositions is mainly due to the fact that the potassium tracer-diffusion coefficient is substantially lower than the sodium tracer diffusion coefficient. It must be noted that the tracer diffusion coefficients for sodium and potassium in albite by Kasper (1975) and in orthoclase by Foland (1974) were determined from bulk-exchange experiments, and only the potassium tracer-diffusion coefficient in albite from Giletti and Shanahan (1997) was measured parallel to the [010] direction. Irrespective of the choice of the tracer diffusion coefficients, our direct determinations of D_{NaK} are lower than the predictions from equation (1) by a factor of 3 to 5 for $D_{\mathrm{NaK}}^{\perp(001)}$ and by more than an order of magnitude for $D_{\mathrm{NaK}}^{\perp(010)}$. A reasonable agreement between theoretical prediction and experimental determination is obtained, if diffusion in the fastest direction, i.e., $D_{\mathrm{NaK}}^{\mathrm{max}}$ is used for comparison. For further comparison of the interdiffusion model expressed by equation (1) and our direct determinations the sodium and potassium tracer diffusion coefficients were back-calculated from $D_{\mathrm{NaK}}(c)$ assuming that they are independent of X_{Or} (see figure 5). There is reasonable agreement between our back-calculated and the experimentally determined tracer diffusion coefficients for the direction of fastest diffusion, but our back-calculated values are substantially slower for the [010] direction (see figure 6). This is probably due to the fact that the tracer diffusion coefficients obtained from bulk exchange experiments largely represent the fastest diffusion direction. There is reasonably good agreement between our back-calculated tracer diffusion coefficient for potassium in the [010] direction and the corresponding value given by Giletti and Shanahan (1997) (figure 6). Potassium tracer diffusion perpendicular to (010) has been estimated to be 0.1 to 0.6 times as slow as perpendicular to (001) by Bailey (1971) and Giletti et al (1974), which is in line with our back-calculated potassium tracer diffusion coefficients.

The observed diffusion anisotropy agrees well with what is expected from the crystal structure. Alkali feldspar contains wide channels parallel to the crystallographic [101] direction with the shortest diameter being about 4.5 Å, along which the alkali cations are aligned. By combining dielectric spectroscopy and atomistic computer simulation Jones et al (2004) identified these channels as the most likely pathways for the migration of Na^+ and K^+ cations by vacancy mediated conventional hopping giving raise to substitutional interdiffusion. These channels lie in the (010) plane and enclose an angle of 50^o with the crystallographic a-axis measured from the positive a-axis towards the positive c-axis. This is exactly parallel to the principle axis of the experimentally determined diffusivity tensor which represents the fastest diffusion direction (see figure 4. No comparatively wide channels that would be suitable for alkali diffusion exist along other directions within the (010)-plane nor along the [010] direction. The anisotropy of Na-K interdiffusion becomes less accentuated at close to potassium end-member compositions. This is also the

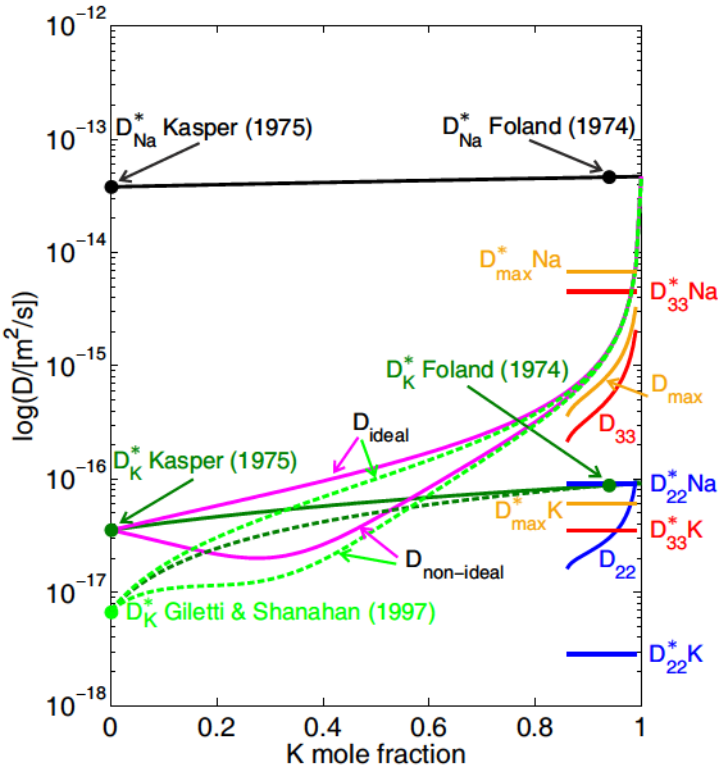

Fig. 5 Comparison of direct determinations of the Na-K intrdiffusion coefficient and predictions based on equation (1) and using experimentally determined Na- and K- tracer diffusion coefficients of Kasper (1975) and Giletti and Shanahan (1997) for albite and of Foland (1974) for orthoclase, and the thermodynamic mixing model for the disordered alkali feldspar solid-solution of Hovis et al (1991); orange, red and blue curves represent our experimental determinations of the Na-K interdiffusion coefficient in the fastest diffusion direction, perpendicular to (001) and perpendicular to (010), respectively; the horizontal lines in similar colors represent the back-calculated tracer diffusion coefficients.

composition region with the strongest increase of D_{NaK}. It may be hypothesized that at very potassium rich compositions another diffusion mechanism may become important. At close to potassium end-member composition Na-K interdiffusion is primarily controlled by the Na- tracer diffusion coefficient. It may be speculated that the small Na^+ may also migrate by an interstitial mechanism (Behrens et al (1991)) and the interstitial mechanism may not be restricted to the channels in [010] direction.

Finally, it must be noted that the concentration-distance data we used for determining the diffusivity tensor reflect the effective diffusivities in the sense that all effects potentially influencing the interdiffusion of Na and K, in particular its composition dependence and anisotropy, are integrated into the obtained diffusivities. The influence of deviations from thermodynamic ideal mixing behavior of the alkali feldspar solid-solution can safely be excluded, as

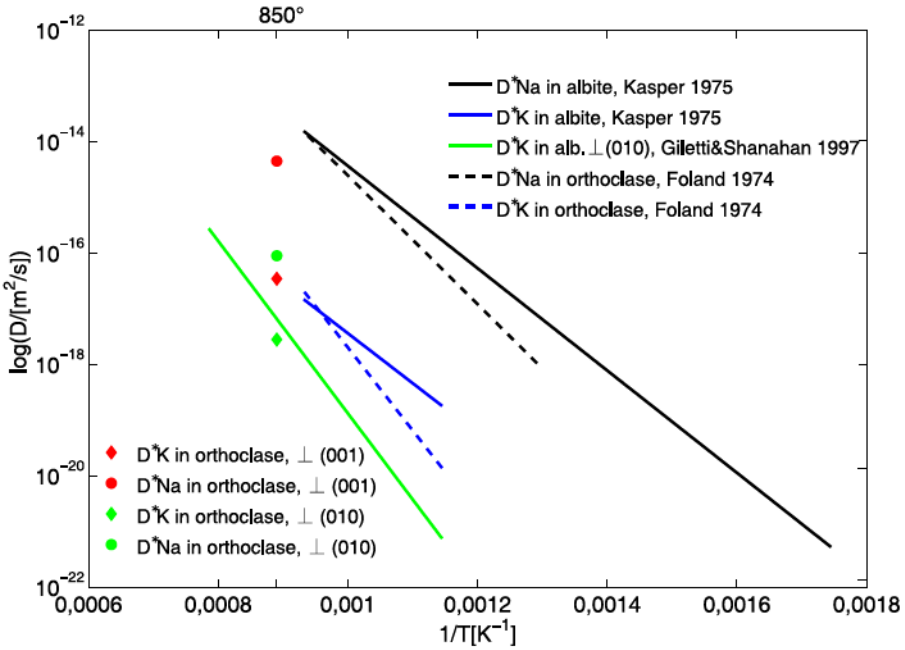

Fig. 6 Arrhenius diagram showing experimentally determined Na- and K- tracer diffusion coefficients from the literature (solid and dashed lines) and the Na- and K- tracer diffusion coefficients calculated from the composition dependence of D_{NaK} at 850°C using equation (1) for two crystallographic directions (circular and diamond symbols).

the non-ideality of disordered alkali felspar at 850°C, at ≈ 1 bar and in the composition range of $X_{\mathrm{Or}} \geq 0.85$ is minute (see figure 5). Another potential influence is the coherency strain associated with compositional heterogeneities in a single crystal of alkali feldspar (Petrovic (1972); Neusser et al (2012); Scheidl et al (2013)). On the one hand, the elastic stress associated with coherency influences cation interdiffusion via the stress dependence of the chemical potentials of the diffusing components (Larche and Cahn (1982); Svoboda et al (2002)). On the other hand, the crystal lattice may be appreciably distorted across sharp composition fronts such as those observed along the [010] direction (Schaeffer et al (2014a)), and this lattice distortion may influence the ease of atomic jumps and thus Na-K interdiffusion in these domains. Boltzmann's approach, which we used for extracting diffusivities from composition-distance data, does not make any assumptions regarding these potential effects. It is independent of the microscopic mechanisms underlying the diffusion process, or of charge balance and crystal chemical constraints such as implicit in equation 1(Manning (1968)). The reasonable agreement between the model predictions and our experimental determinations suggests that equation 1 is a useful model for Na-K interdiffusion in alkali feldspar. The above mentioned effects influencing Na-K interdiffusion are probably of second order within the accuracy of the available calibrations of Na and K tracer diffusion. Nevertheless, theo-

retical calculations of Na-K interdiffusion coefficients should be applied with care when dealing with Na-K interdiffusion. In particular, it remains to be seen, whether new, direction specific determinations of the respective tracer diffusion coefficients do show the according anisotropy needed to produce the observed direction dependence of the of Na-K interdiffusion if inserted into equation 1.

5 Conclusions

The interdiffusion of Na^+ and K^+ in disordered, monoclinic alkali feldspar was investigated by cation exchange experiments using gem quality alkali feldspar single crystals with well defined geometry and a KCl salt melt as a diffusion couple at 850^oC and $\approx$1 bar. The Na-K interdiffusion in alkali feldspar is anisotropic and composition dependent. The full diffusivity tensor was extracted in the composition range $0.85 \leq X_{Or} \leq 1.00$. The interdiffusion of Na^+ and K^+ in the direction parallel to the crystallographic b axis is by a factor of about 10 slower than in the a - and c^* directions. The strongest diffusion anisotropy is within the (010) plane with relatively fast diffusion parallel to the [101] direction and relatively slow diffusion in the direction in the (010) plane that is perpendicular to [101]. Based on our results the Na-K interdiffusion coefficient at 850^oC can now be calculated for any direction in alkali feldspar. The interdiffusion coefficient shows a weak increase with increasing X_{Or} in the composition range $0.85 \leq X_{Or} \leq 0.95$. At $X_{Or} \geq 0.95$ the composition dependence is much more pronounced, and D_{NaK} strongly increases with increasing X_{Or}. This renders alkali feldspar with close to potassium end-member composition ($X_{Or} > 0.95$) particularly sensitive to re-equilibration during slow cooling.

Acknowledgements We thank Gerald Giester for orienting the feldspar crystals on a three circle goniometer and Andreas Wagner for preparing the single crystal plates with polished surfaces. We are indebted to D.J. Cherniak and an anonymous reviewer for their constructive comments on an earlier version of the manuscript.

References

Abart R, Petrishcheva E, Kaessner S, Milke R (2009a) Perthite microstructure in magmatic alkali feldspar with oscillatory zoning; Weinsberg Granite, Upper Austria. Mineralogy and Petrology 97:251–263

Abart R, Petrishcheva E, Wirth R, Rhede D (2009b) Exsolution by spinodal decomposition II: perthite formation during slow cooling of anatexites from Ngoronghoro, Tanzania. American Journal of Science 309:450–475

Bailey A (1971) Comparison of low-temperature with high-temperature diffusion of sodium in albite. Geochimica et Cosmochimica Acta 35:1073–1081

Behrens H, Johannes W, Schmalzried H (1991) On the mechanics of cation diffusion processes in ternary feldspars. Phys Chem Min 17:62–78

Benisek A, Dachs E, Kroll H (2010) A ternary feldspar-mixing model based on calorimetric data: development and application. Mineralogy and Petrology 160:327–337

Boltzmann L (1894) Zur Integration der Diffusionsgleichung bei variablen Diffusionskoeffizienten. Annln Phys 53:959–964
Brady J, Yund R (1983) Interdiffusion of K and Na in alkali feldspars: homogenization experiments. American Mineralogist 68:106–111
Cherniak D (2010) Cation diffusion in feldspars. Reviews in Mineralogy and Geochemistry 72:691–733
Christoffersen R, Yund R, Tullis J (1983) Inter-difrusion of K and Na in alkali feldspars: diffusion couple experiments. Am Mineral 68:1126–1133
Crank J (1975) The Mathematics of Diffusion. Oxford University Press
Demtröder K (2011) Untersuchung zur Al/Si-Ordnung an Sanidin Megakristallen aus der Eifel. Master's thesis. Ruhr-Universität Bochum
Foland K (1974) Alkali diffusion in orthoclase. Geochemical transport and kinetics, Carnegie Institution of Washington 634:77–98
Fuhrman M, Lindsley D (1988) Ternary-feldspar modeling and thermometry. Am Mineral 73:3–4
Giletti B, Shanahan T (1997) Alkali diffusion in plagioclase feldspar. Chemical Geology 139:3–20
Giletti B, Semet M, Kasper R (1974) Self-diffusion of potassium in low albite using an ion microprobe. Geol Soc Am Abstracts with Programs 6:754
Hovis G, Delbove F, Bose M (1991) Gibbs energies and entropies of K-Na mixing for alkali feldspar from phase equilibrium data: implications for feldspar solvi and short range order. Am Mineral 76:913–927
Jones A, Islam M, Mortimer M, Palmer D (2004) Alkali ion migration in albite and K-feldspar. Phys Chem Minerals 31:313–320
Kasper R (1975) Cation and Oxygen diffusion in albite, Ph.D. Dissertation. Brown University
Larche F, Cahn J (1982) The effect of self-stress on diffusion in solids. Acta Metallica 30:1335–1345
Lin T, Yund R (1972) Potassium and sodium self-diffusion in alkali feldspar. Contrib Mineral Petr 34:177–184
Manning J (1968) Diffusion kinetics for atoms in crystals. Van Norstrand, Princeton
Matano C (1933) On the relation between the diffusion-coefficients and concentrations of solid metals (the nickel-copper system). Jap J Phys 8:109–113
Mehrer H (2007) Diffusion in Solids - Fundamentals, Methods, Materials, Diffusion-Controlled Processes. Springer
Neusser G, Abart R, Fischer F, Harlov D, Norberg N (2012) Experimental Na/K exchange between alkali feldspar and an NaCl-KCl salt melt: chemically induced fracturing and element partitioning. Contrib Mineral Petr 164:341–358
Norberg N, Neusser G, Wirth R, Harlov D (2012) Microstructural evolution during experimental albitization of k-rich alkali feldspar. Contrib Mineral Petr 162:531–546
Nye J (1957) Physical Properties of Crystals. Oxford at the Clarendon Press
Petrishcheva E, Abart R (2009) Exsolution by spinodal decomposition I: evolution equation for binary mineral solutions with anisotropic interfacial energy. American Journal of Science 309:431–449
Petrishcheva E, Abart R (2012) Exsolution by spinodal decomposition in multicomponent mineral solutions. Acta Mater 60:5481–5493
Petrovic R (1972) Alkali ion diffusion in alkali feldspars, Ph.D. Dissertation. Yale University
Riley T, Bailey D (2003) Barium-rich sanidine megacrysts from the West Eifel (Germany). Neues Jahrbuch für Mineralogie - Monatshefte 41:18–30
Schaeffer A, Jaepel T, Zaefferer S, Abart R, Rhede D (2014a) Lattice strain across na-k interdiffusion fronts in alkali feldspar: an electron backscatter diffraction study (submitted). Phys Chem Min
Schaeffer A, Petrishcheva E, Halber G, Abart R, Rhede D, Giester G (2014b) Sodium-potassium interdiffusion in potassium-rich alkali feldspar ii: composition- and temperature-dependence obtained from cation exchange experiments (submitted)
Scheidl K, Schaeffer A, Petrishcheva E, Habler G, Fischer F, Schreuer J, Abart R (2013) Chemically induced fracturing in alkali feldspar. Phys Chem Miner

Svoboda J, Fischer F, Fratzl P (2002) Diffusion in multi-component systems with no or dense sources and sinks for vacancies. Acta Mater 50:1369–1381

Voll G, Evangelakakis C, Kroll H (1994) Revised two-feldspar geothermometry applied to Sri Lankan feldspars. Precambrian Res 66:351–377

Weitz G (1972) Die Struktur des Sanidins bei verschiedenen Ordnungsgraden. Zeitschrift für Kristallographie 136:418–426

Yund R (1984) Feldspars and feldspathoids. Alkali Feldspar exsolution: Kinetics and dependence on alkali interdiffusion. D. Reidel Publishing Company

Appendix F

Schäffer et al. (submitted)

Schäffer et al. (submitted): Sodium-potassium interdiffusion in potassium-rich alkali feldspar II composition- and temperature-dependence obtained from cation exchange experiments

The execution of the experiments and BSE imaging were done by Anne-Kathrin Schäffer. Microprobe measurements were executed by Dieter Rhede. Analysis of the data was done by Elena Petrishcheva and Anne-Kathrin Schäffer.

Noname manuscript No.
(will be inserted by the editor)

Sodium-potassium interdiffusion in potassium-rich alkali feldspar II: composition- and temperature-dependence obtained from cation exchange experiments

Anne-Kathrin Schäffer · Elena Petrishcheva · Gerlinde Habler · Rainer Abart · Dieter Rhede · Gerald Giester

Received: date / Accepted: date

Keywords alkali feldspar · Na-K interdiffusion · composition- temperature-dependence

Abstract Na-K interdiffusion in disordered potassium-rich alkali feldspar was studied experimentally using cation exchange between gem quality sanidine from the Eifel and alkali-halide melt at temperatures of 800^oC to 1000^oC and at close to ambient pressure. The sodium-potassium interdiffusion coefficient D_{NaK} was determined for potassium mole fractions in the range $0.65 \leq \mathrm{X_{Or}} \leq 0.99$. At $0.65 \leq \mathrm{X_{Or}} \leq 0.95$ the sodium-potassium interdiffusion coefficient is largely independent of composition. At $X_{Or} \geq 0.95$ it rises sharply with increasing potassium mole fraction. Diffusion perpendicular to (001) is about one order of magnitude faster and less strongly temperature dependent than perpendicular to (010). The parameters of the Arrhenius equation describing the temperature dependence of the sodium-potassium interdiffusion coefficient $D_{\mathrm{NaK}} = D_0 \,\mathrm{Exp}\left(-\frac{E_A}{RT}\right)$ were estimated as

$$
\begin{aligned}
D_0^{\perp(001)}(0.92) &= 4.63 \cdot 10^{-8}\mathrm{m}^2/\mathrm{s}, \quad & \mathrm{E_A}^{\perp(001)}(0.92) &= 179\ \mathrm{kJ/mole} \\
D_0^{\perp(001)}(0.98) &= 1.66 \cdot 10^{-7}\mathrm{m}^2/\mathrm{s}, \quad & \mathrm{E_A}^{\perp(001)}(0.98) &= 181\ \mathrm{kJ/mole} \\
D_0^{\perp(010)}(0.92) &= 1.97 \cdot 10^{-4}\mathrm{m}^2/\mathrm{s}, \quad & \mathrm{E_A}^{\perp(010)}(0.92) &= 286\ \mathrm{kJ/mole} \\
D_0^{\perp(010)}(0.98) &= 3.27 \cdot 10^{-4}\mathrm{m}^2/\mathrm{s}, \quad & \mathrm{E_A}^{\perp(010)}(0.98) &= 277\ \mathrm{kJ/mole}
\end{aligned}
$$

The results of our direct determinations are compared with theoretical cal-

A-K Schäffer · E Petrishcheva · G Habler · R Abart · G Giester
University of Vienna, Department of Lithospheric Research, Althanstrasse 14, A-1090 Vienna
E-mail: anne-kathrin.schaeffer@univie.ac.at

D Rhede
Helmholtzzentrum Potsdam, Deutsches GeoForschungsZentrum, Telegraphenberg, D-14473 Potsdam

culations using the corresponding sodium- and potassium tracer-diffusion coefficients, and the processes underlying the observed composition- and temperatuee dependence of sodium-potassium interdiffusion are discussed.

1 Introduction

Alkali feldspar forms a solid-solution between the sodium ($NaAlSi_3O_8$) and potassium ($KAlSi_3O_8$) end-member components. The alkali feldspars are among the most abundant rock-forming minerals in the Earth's crust and are involved in a multitude of mineral reactions (Spear, 1993). Their occurrence in virtually every crustal environment makes it vital to have a sound knowledge of their properties and large variety of intracrystalline microstructures they exhibit and the processes underlying their formation. In particular, the chemical compositions, zoning patterns, as well as size and composition of exsolution lamellae may bear important petrogenetic information (Benisek et al, 2010; Yund, 1983; Abart et al, 2009; Petrishcheva et al, 2009). It is highly relevant for extracting quantitative information from such phenomena that the kinetics of diffusion, in particular the kinetics of sodium-potassium interdiffusion in alkali feldspar are known. Reviews of the state of knowledge on diffusion in alkali feldspar may be found in Freer (1981), Brady (2012) and Cherniak (2010).

Major efforts to understand diffusion of Na^+ and K^+ in alkali feldspars have been made in the 1970s and 80s. Most of these early studies focused on the quantification of Na- and K- tracer-diffusion using isotope tracer experiments. Both, the sectioning method (Sippel, 1963; Bailey, 1971, Giletti and Shanahan 1997), as well as bulk exchange experiments (Bailey, 1971; Lin and Yund, 1972; Foland, 1974; Giletti et al, 1974; Kasper, 1975) were employed. The determination of the Na- and K- tracer-diffusion coefficients was motivated in part by the notion that the sodium-potassium interdiffusion coefficient D_{NaK} can be calculated from the respective tracer diffusion coefficients (Manning, 1968). However, the results of the early studies on Na- and K- tracer-diffusion in alkali feldspar show considerable scatter, probably due to the insufficient homogeneity of the starting material used and the limited analytical possibilities available at the time. Calculation of D_{NaK} from the tracer-diffusion coefficients is therefore problematic, rendering direct determination of D_{NaK} by interdiffusion experiments necessary.

Relatively few studies dealing with the direct determination of the sodium-potassium interdiffusion coefficient have been conducted. Based on the notion that alkali feldspar can exchange Na^+ and K^+ with its surroundings without changing the state of Si-Al ordering on the tetrahedral site, Petrović (1972) performed cation exchange experiments between alkali feldspar and an alkali-chloride salt melt. Under dry conditions, cation exchange can only occur by the interdiffusion of Na^+ and K^+ on the alkali sub-lattice of the feldspar. The chemical alteration of alkali feldspar produced by cation exchange can thus be used for direct determination of the sodium-potassium interdiffusion coef-

ficient from concentration-distance data. One of the main problems with direct determinations of the sodium-potassium interdiffusion coefficient in alkali feldspar is related to the formation of micro-cracks. The lattice parameters of alkali feldspar show considerable compositional dependence (Kroll et al, 1986; Angel et al, 2012), and any composition heterogeneity introduced into an alkali feldspar crystal during cation exchange induces coherency stress. This may lead to fracturing, if the change in chemical composition exceeds about 10 mole % for chemical shifts towards more sodium-rich compositions, and about 15 mole % for chemical shifts towards more potassium-rich compositions (Petrović, 1972, 1973; Neusser et al, 2012; Scheidl et al, 2013). Special care must be taken during direct determination of the sodium-potassium interdiffusion coefficient in alkali feldspar to avoid fracturing.

Keeping the chemical shifts lower than 14 mole % Petrović (1972) derived D_{NaK} from a chemical shift of albite to a composition of $\mathrm{X_{Or}} = 0.1$, and from a chemical shift of adularia with initial $\mathrm{X_{Or}} = 0.86$ to $\mathrm{X_{Or}} = 1.00$, where $\mathrm{X_{Or}}$ is the potassium mole fraction in the alkali sublattice of the alkali feldspar. Whereas for the composition interval $0 \leq \mathrm{X_{Or}} \leq 0.1$ the sodium-potassium interdiffusion coefficient was found to be independent of composition, a substantial compositional dependence was found for the composition interval $0.86 \leq \mathrm{X_{Or}} \leq 1.00$. Irrespective of the composition domain the activation energy was determined at about 250 kJ/mole.

An alternative approach was pursued by Christoffersen et al (1983), who used diffusion couple experiments for direct determination of D_{NaK}. Single crystals of albite and adularia were put into contact at a polished face and annealed at 900^oC and 1000^oC and at pressures of 0.5 and 1.5 GPa. During annealing the initial composition jump across the contact plane evolved into a sigmoidal concentration profile by sodium-potassium interdiffusion. From a pronounced asymmetry of the concentration profile across the contact plane a compositional dependence of D_{NaK} was inferred, and the Boltzmann-Matano method (Matano, 1933) was used for extracting $D_{\mathrm{NaK}}(c)$. A clear compositional dependence of D_{NaK} with a minimum at $\mathrm{X_{Or}} \approx 0.4$ and a strong increase towards more potassium-rich compositions was found. Diffusion in the direction perpendicular to (010) was found to be about one order of magnitude slower than in the direction perpendicular to (001), indicating diffusion anisotropy. Reasonable qualitative agreement between Na- and K- tracer-diffusion coefficients calculated from self-diffusion coefficients by Kasper (1975) and Foland (1974), and the direct determination was found. The absolute values of the direct determinations were, however, substantially lower than predicted theoretically. Due to the limitations of the method, the analysis of Christoffersen et al (1983) was restricted to the composition range of $0.10 \leq \mathrm{X_{Or}} \leq 0.80$, and the composition range $0.80 \leq \mathrm{X_{Or}} \leq 1.00$ was not covered. Many alkali feldspars, however, fall into this composition range, and knowledge of the diffusion properties of potassium-rich alkali feldspars is of great interest. Furthermore, a pronounced compositional dependence of $D_{\mathrm{NaK}}(c)$ was documented in this composition range (Neusser et al, 2012; Petrishcheva et al, submitted). It must be noted at this point that the composition shifts

within the two crystals of the diffusion couple were about 50 mole % close to the contact plane, and mechanical effects related to the associated change in the lattice parameters of the two crystals may be expected. Such effects have, however, not been documented in the study of Christoffersen et al (1983), and the potential effects on sodium-potassium interdiffusion in these experiments are not known.

The sodium-potassium interdiffusion coefficient was also determined from homogenization experiments done on perthitic alkali feldspar (Brady and Yund, 1983; Hokason and Yund, 1986). These determinations are, however, restricted to the direction perpendicular to the exsolution lamellae and usually cover a rather limited composition range. Brady and Yund (1983) used a synthetic perthite prepared from natural adularia, and natural perthite as starting materials. The samples were annealed at 600°C in Pt containers open to the atmosphere. They were removed repeatedly to take precession photographs in order to document the progression of homogenization. The average interdiffusion coefficient was then calculated using the diffusion equation for the finite, one-dimensional geometry of a lamellar intergrowth by Crank (1975), the critical values being the time needed for homogenization and the lamellar spacing. They point out that the sodium-potassium interdiffusion coefficient cannot be constant for the conditions. Hokason and Yund (1986) conducted the same experiments using a number of natural feldspars, focussing on the influence of the degree of ordering on the homogenization. It was found that disordered crystals homogenized at 600°C, in contrast, ordered feldspars did not homogenize even when tempered at 1000°C.

More recently cation exchange experiments similar to those of Petrović (1972) were done using gem quality sanidine from the Eifel with an initial composition of $X_{Or} = 0.84$ and KCl melt, which are rpesented in teh companion paper by Petrishcheva et al, (submitted). Single crystals of sanidine were machined to plates 3x3x1 mm with polished bottom and top faces. Six types of differently oriented plates were used for the cation exchange experiments. From the chemical profiles obtained in six different crystallographic directions the full diffusivity tensor and its compositional dependence in the composition range $0.86 \leq X_{Or} \leq 0.99$ were determined for 850^{o}C and 1 bar. Sodium-potassium interdiffusion was found to be markedly anisotropic with slow diffusion in the direction perpendicular to (010). A substantial diffusion anisotropy was also found within the (010) plane with relatively fast diffusion in the direction perpendicular approximately to (101) and relatively slow diffusion in the direction perpendicular approximately to $(10\bar{1})$. In the composition range $0.86 \leq X_{Or} \leq 0.95$ only a weak compositional dependence of D_{NaK} was found, whereas at $X_{Or} \geq 0.95$ a substantial increase of D_{NaK} with increasing X_{Or} was detected.

In this study we present direct determinations of the Na-K interdiffusion coefficients in the range of 800^{o}C to 1000^{o}C and covering the composition range $0.65 \leq X_{Or} \leq 0.99$. We use two different sanidines from the Eifel with initial compositions $X_{Or} = 0.72$ and $X_{Or} = 0.84$ so that the entire composition range could be covered while keeping the composition shifts towards more

sodium-rich compositions lower than about 10 mole % and composition shifts towards more potassium-rich compositions lower than about 16 mole %, so that the mechanical effects associated with chemically induced lattice strain could be minimized. The chemical patterns produced by cation exchange were used for direct determination of the compositional dependence of the interdiffusion coefficient. The theoretical basis for analyzing composition dependent, anisotropic diffusion in a monoclinic crystal is presented in the companion paper by Petrishcheva et al., (submitted). The results are discussed in the light of earlier determinations and theoretical calculations based on an interdiffusion model for ionic crystals (Manning 1968).

2 Methods

Starting materials

Two gem quality sanidines from the localities Volkesfeld and Rockeskyll from the Eifel (Germany) were used as starting materials. The sanidines from the Eifel are known for their chemical homogeneity and have been well characterized in various studies (Riley and Bailey, 2003; Parsons and Lee, 2005; Weitz, 1972; Neusser et al, 2012; Demtröder, 2011). The chosen crystals are optically clear. The sanidine from Volkesfeld is either colorless or smoky brown in color. The sanidine from Rockeskyll is colorless. Pieces of each feldspar were analyzed using scanning electron microscopy and electron microprobe analysis. The selected feldspars turned out to be chemically homogenous within the resolution of the applied methods and are free of twins, exsolutions, second phase precipitates, microcracks or any other structural flaws or heterogeneities. Mineral chemical analyses of both feldspars are given in table 1. The initial compositions of the Volkesfeld- and the Rockeskyll sanidines are $Or_{85}Ab_{14}Cs_1$, and $Or_{72}Ab_{26}Cs_2$ (Demtröder, 2011), respectively, with minor iron contents of about 0.1 to 0.2 wt. % FeO. Both feldspars have monoclinic symmetry and crystallized in the space group C2/m. Aluminum and silicon on the tetrahedral site are highly disordered with $\Sigma t_1 = 61$ (Volkesfeld) (Neusser et al, 2012) and $\Sigma t_1 = 0.58$ - 0.62 (Rockeskyll) (Demtröder, 2011). Although there is no difference in chemical composition or Al-Si-order between the colorless and smoky brown variants of the sanidine from Volkesfeld all samples were prepared from the smoky brown variant to ensure that the starting material is as uniform as possible. The lattice orientations of milimetre-sized pieces of the feldspars were determined on a four-circle goniometer. They were then prepared as polished plates of 3x3 mm size and 1 mm thickness with the polished surfaces corresponding to either the (001) or (010) planes of the feldspar.

Exchange experiments

For each experiment a single polished plate of sanidine was sealed in a quartz glass tube under vacuum together with a mixture of NaCl-KCl (or NaBr-KBr

Table 1 Electron microprobe analyses of both starting materials; V5,V14,V16 and V22 are samples of the sanidine from Volkesfeld. Samples ERN3, ERS1 and ERS37 are sanidines from Rockeskyll, they were analzed by Demtöder (2011) at the Ruhr-University Bochum.

wt%	V5	V14	V16	V22	ERN3	ERS1	ERS37
SiO2	63.68	64.30	63.93	64.72	64.86	64.95	64.75
Al2O3	18.62	18.56	18.82	18.71	18.66	18.9	18.9
TiO2	0.00	0.00	0.04	0.00	0.03	0.03	0.04
FeO	0.18	0.14	0.18	0.10	0.15	0.16	0.21
MgO	0.00	0.00	0.00	0.00	0.01	0.01	0.02
CaO	0.01	0.01	0.01	0.02	0.01	0.01	0.02
Na2O	1.65	1.64	1.72	1.70	2.83	3.03	2.95
K2O	14.01	14.32	13.97	13.85	12.26	12.13	12.1
BaO	0.83	0.60	0.86	0.55	1.23	1.25	1.46
SrO	0.18	0.05	0.14	0.07	0.2	0.22	0.04
Rb2O	0.03	0.05	0.05	0.05	n/a	n/a	n/a
Σ	99.181	99.686	99.722	99.775	100.23	100.7	100.49

for 800°C experiments) salts. **The plates were pre-polished by hand on a diamond polishing disk, the final polishing was done on a silk polishing cloth with 1 μm diamond powder. The salt had a specific potassium mole fraction to produce the desired composition shift in the feldspar through cation exchange.** The amount of salt was chosen so that a 40:1 molar proportion of the alkali cations was contained in the salt relative to the feldspar to ensure quasi constant composition of the salt during cation exchange. The sealed tubes were then heated to temperatures between 800 and 1000°C in a box furnace at atmospheric pressure. **Temperatures were measured with a type N thermoelement and were accurate within ± 1 °C.**

Experiments with selected salt concentrations were done for run durations of 1 to 64 days and at temperatures between 850°C and 1000°C using NaCl and KCl salt. For experiments at 800°C NaBr (T_{melt} = 747°C) and KBr (T_{melt} = 734°C) salts were used. All experiments are listed in table 2.

The crystal plates retained their surface polish after cation exchange and no indication of surface reaction or recrystallization was found. After exchange the plates were cut in two mutually perpendicular directions and thick slides were prepared that allowed measurements of concentration profiles in three crystallographic directions (figure 1). The samples were polished mechanically using diamond paste with decreasing grain sizes down to 0.25 μm on polyamide pads. For orientation analysis by electron back-scatter diffraction the samples were additionally polished chemo-mechanically using a colloidal silica suspension (Köstrosol, pH 9.2 to 10), a polyurethane polishing pad and an active rotary head polishing apparatus to ensure a defect free crystal lattice at the immediate sample surface.

Table 2 Temperatures, salt mixtures and run durations for cation exchange experiments.

	T [°C]	X_K^{salt}	X_{Or}^{eq}	run duration [d]
Volkesfeld	800	0.48	0.80	32
		1.00	1.00	32
	850	0.30	0.70	1, 2, 4, 8, 16, 32, 64
		0.35	0.92	8
		0.60	0.97	1, 2, 4, 8, 16, 32, 64
		0.85	0.73	1, 2, 4, 8, 16, 32, 64
		1.00	1.00	1, 2, 4, 8, 16, 32, 64
	920	1.00	1.00	1, 2, 4, 8, 16
	950	1.00	1.00	1, 2
	1000	1.00	1.00	1
Rockeskyll	800	0.37	0.65	32
		0.55	0.80	32
	850	0.22	0.45	4, 8, 16
		0.50	0.85	4, 8, 16
		1.00	1.00	8
	920	0.50	0.82	2
	950	0.50	0.81	1
	1000	0.50	0.81	1

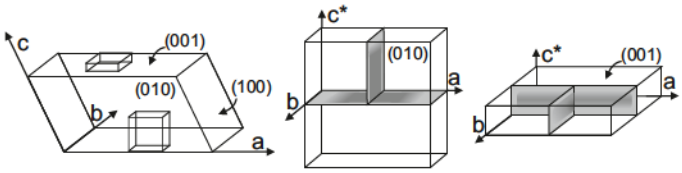

Fig. 1 left: sketch of feldspar crystal with (100), (010), and (001) faces developed; 3x3x1 mm sized plates with their large faces parallel to (010) or (001) were cut from the feldspar for use in cation exchange experiments; after cation exchange the (010) (middle) and (001) (right) plates were cut in two directions, mounted in resin, ground and polished so that the planes shown in grey are on the polished sample surface ready for EMPA analysis; grey shades schematically indicate chemical alteration of the crystal.

Scanning electron microscopy and crystal orientation analysis

The samples were carbon coated using a double carbon-thread at a distance of about 8 cm from the sample surface under vacuum conditions better than 10^{-5} mbar chamber pressure to establish electrical conductivity. BSE imaging was done using an FEI Inspect S scanning electron microscope with a tungsten filament electron source. BSE imaging was done at high contrast settings so that variations in X_{Or} of a few percent could readily be discerned from changes in the grey shade on BSE images.

For electron back-scatter diffraction analysis (EBSD) a thinner carbon coating than for imaging was applied, using only a single carbon thread at the same conditions to establish electrical conductivity. EBSD data were acquired using a FEI Quanta 3D FEG microscope equipped with a field-emission electron source and an EDAX Digiview IV EBSD camera. The sample was tilted to 70° in order to reach a beam incidence angle of 20° with respect to the sample

surface. The edges of the feldspar crystals were aligned parallel to the x- and y-directions of the scan reference system by stage rotation. The electron-beam was set to 15 kV accelerating voltage and 4 nA probe current in analytic mode using a SEM aperture of 1 mm. The working distance was between 12 and 14 mm. A 2x2 or 4x4 binning of the EBSD camera-resolution was applied. Hough settings were adjusted for each grain according to the EBSD pattern quality of the grain. Common settings were 1° theta step size and a minimum peak distance of 8 to 12 mm for indexing 3 to 20 Hough peaks. A medium (9x9) or large (13x13) convolution mask was applied to the Hough space in order to eliminate artificial peaks and enhance weak bands. Only the interior portion of the EBSD pattern was used for indexing, determined by the ρ-fraction of 60% to 85%. EBSD maps were obtained by beam-scanning across a 40x40 μm to 100x100 μm sized area using a hexagonal grid at a step size of 10 to 15 μm. The large step-width was chosen to avoid beam degradation due to the low electron-beam-stability of feldspar. The electron backscatter diffraction patterns were acquired and processed using the software packages OIM Data Collection and Analysis. 10 to 100 data points were collected for each crystal. In case of inconsistent automatic indexing, additional single point analyses were performed and indexing statistics were checked in order to identify the correct orientation of the crystal.

Electron microprobe analysis

For testing the homogeneity and determining the initial composition of the starting materials, fragments of several crystals were embedded in epoxy resin and polished. EPMA measurements were done using a CAMECA SX-100 at the Center for Earth Sciences, University of Vienna. The instrument was operated at a high voltage of 15 kV and a beam current of 15 to 20 nA. The beam was defocused to 3 μm in diameter to minimize the loss of Na and K by migration. Mineral chemical analysis of the samples after cation exchange was done using a thermal field emission electron gun JEOL JXA-8500F (Hyperprobe) at the Helmholtzzentrum Potsdam - German Research Centre for Geosciences. Mineral compositions were analyzed along profiles between 15 and 150 μm length with 0.5 μm or 1 μm step-size, depending on the width and sharpness of the diffusion fronts. The profiles were measured normal to the traces of the surfaces of the exchanged samples (figure 1). The instrument was operated at an accelerating voltage of 8 kV and at a beam current of 10 nA. The beam was defocused to 10 μm for calibration and fully focused during measurements. All elements were measured simultaneously. Peak counting times were set to 10 seconds and background counting time to 5 seconds to minimize loss of Na and K by migration during measurement. With these settings a lateral resolution of better than 500 nm could be achieved for mineral chemical analyses.

3 Results

Diffusion Fronts

In all experiments the cation exchange between feldspar and NaCl-KCl or NaBr-KBr salt melt produced a zone chemically altered by diffusion along the surfaces of the feldspar plates. The composition of the chemically altered surface layer was determined by the composition of the salt melt and by the alkali-feldspar-salt-melt equilibrium partition coefficient. Different chemical patterns and microstructures evolved during cation exchange depending on whether the composition of the feldspar was shifted towards more sodium-rich or towards more potassium-rich compositions.

For shifts towards more potassium-rich compositions regular, light grey rims are observed on BSE images along the outer edges of the crystal plates (figure 2). They correspond to the domains within the feldspar which have been enriched in potassium during cation exchange. The potassium-enriched domains propagate further into the interior of the crystal plates with time. Penetration of the potassium into the crystal and concomitant removal of sodium from the crystal interior can only occur by sodium-potassium interdiffusion on the alkali sublattice of the feldspar. The chemically altered rim and the interior domains with the original composition preserved are separated by more or less sharp transition zones, which will henceforth be referred to as diffusion fronts. From BSE images and chemical profiles measured across the diffusion fronts produced from exchange with pure KCl melt at 850^oC it is seen that diffusion fronts are sharp along profiles measured in the direction perpendicular to the (010) plane and comparatively broad in profiles measured along the direction perpendicular to the (001) plane (figure 2). It is interesting to note that sharp diffusion fronts in the direction perpendicular to (010) only occur if the feldspar composition is shifted to potassium mole fractions in excess of 0.95. If the composition shift is less, the fronts are comparatively broad (see figure 3)

Identifying the position of the diffusion fronts by the position of the inflection point in the composition profile and plotting the front-position relative to the grain surface versus the square root of time yields a linear trend (figure 4), as is expected for diffusion controlled cation exchange. It is interesting to note that the rate of front propagation is somewhat slower in the direction perpendicular to (010) than perpendicular to (001).

For shifts towards more sodium-rich compositions a gradual change in composition from the fully exchanged surface towards the grain interior is observed, irrespective of the crystallographic direction. The composition profiles do not show an inflection point. For composition shifts towards more sodium-rich compositions of more than about 10 mole-% the development of a system of parallel cracks is observed. This is due to the pronounced compositional dependence of the lattice parameters of alkali feldspar. The chemically induced changes in the lattice parameters are about five times larger in the crystallographic a-direction than in the b- and c-directions (Kroll et al, 1986; Angel et

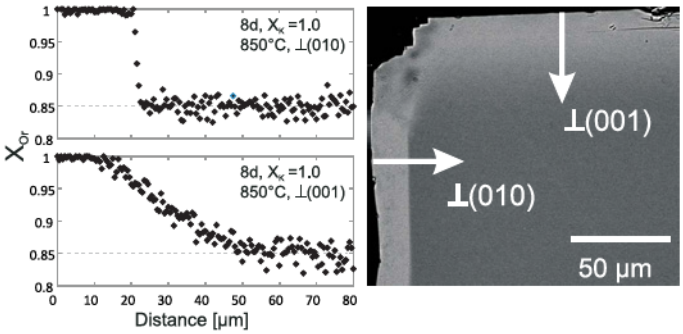

Fig. 2 Composition-distance data and corresponding BSE image obtained from Volkesfeld sanidine after a composition shift towards $X_{Or} = 1.0$ at 850°C: top: profile perpendicular to (010) typically shows a sharp composition front; bottom: profile perpendicular to (001) typically shows a broad composition front; dotted horizontal lines indicate the original composition of the sanidine $X_{Or} = 0.85$.

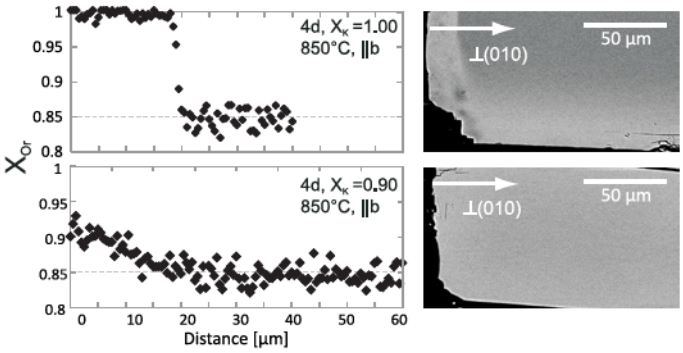

Fig. 3 Composition-distance data and corresponding BSE images obtained from Volkesfeld sanidine after cation exchange; both profiles were taken parallel to the crystallographic *b*-direction top: shift to $X_{Or} = 1.0$ produces a sharp composition front; bottom: shift to $X_{Or} = 0.90$ produces a comparatively broad front; white arrows on BSE images indicate position and orientation of the profiles; dotted horizontal lines indicate the original composition of the sanidine $X_{Or} = 0.85$.

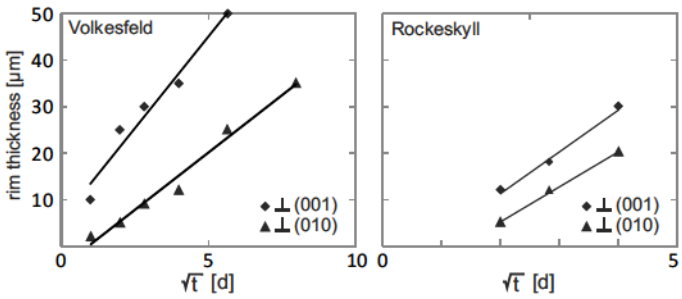

Fig. 4 Thickness of the chemically altered surface layer for shifts towards more potassium-rich compositions versus $\sqrt{t}$; data for 850°C.

al, 2012). Any compositional heterogeneity in a single crystal of alkali feldspar produces coherency strain and associated elastic stress. If the chemically induced stress becomes larger than some critical value, fracturing occurs. The fracturing produced by cation exchange and chemical shift of alkali feldspar towards more sodium-rich compositions was analyzed in detail by Neusser et al (2012) and Scheidl et al (2013). The latter authors showed that the salt melt penetrated into the interior of the crystal plates along the cracks, and chemical alteration also extended from the crack walls into the feldspar crystal producing complex chemical patterns. Actually, in some exchange experiments with pure KCl melt, i.e., for composition shifts towards more potassium-rich composition, cracks, albeit with a complex geometry, were also observed (Schaeffer et al, submitted). In the analysis of sodium-potassium interdiffusion that follows we avoided such cracks and their composition haloes in order to keep the diffusion problem one-dimensional. **The presence of unobserved cracks within the activation volume during analysis can of course not be completely ruled out but due to the small size of the activation volume and the geometry of the cracks we are reasonably certain that the majority of our analyses are uninfluenced by cracks.**

Extraction of the Na-K interdiffuson coefficient

Given the 40-fold molar excess of the alkali cations contained in the salt-melt as compared to the alkali cations contained in the feldspar the composition of the melt remains practically constant during cation exchange implying a constant Na/K ratio at the crystal surface. In the light of this boundary condition, the geometry of the mole fraction profiles, in particular the existence of inflection points in the mole fraction profiles obtained for shifts towards potassium-rich compositions with $X_{Or} \geq 0.95$, point to a compositional dependence of the sodium-potassium interdiffusion coefficient (Crank, 1975; Petrishcheva et al, submitted). When extracting the sodium-potassium interdiffusion coefficient from the concentration-distance data, the concentration dependent nature of the interdiffusion process must be accounted for. A technique for integrating the diffusion equation with a composition dependent diffusion coefficient was developed by Boltzmann (1894). It has been adapted for application to the specific initial and boundary conditions corresponding to the experimental setting of our cation exchange experiments in the companion paper by Petrishcheva et al (submitted). The calculation procedure is briefly summarized below, a derivation is given in Petrishcheva et al (submitted).

We consider diffusion only in the directions perpendicular to the (001) and the (010) surfaces of the crystal plates. The profiles were all taken at sufficiently large distances from the edges of the crystal plates and from cracks so that complexities of the chemical patterns were avoided. The diffusion process underlying the observed composition profiles can then be treated as strictly one-dimensional. The basic equation for obtaining the composition dependent

sodium-potassium interdiffusion coefficient then reads (Petrishcheva et al, submitted)

$$D(c) = -2\frac{d\eta}{dc}\int_{c_2}^{c}\eta(c)dc, \tag{1}$$

where c is a shorthand notation for X_{Or}, c_2 is the initial bulk mole fraction in the feldspar crystal and

$$\eta = \frac{x}{2\sqrt{t}} \quad \text{defined for} \quad t > 0, \tag{2}$$

is Boltzmann's similarity variable combining the space variable x and time t into a single variable.

The procedure of extracting $D_{NaK}(c)$ involved two steps. In a first step $\eta = x/(2\sqrt{t})$ was calculated for each mole fraction profile, which was then recast in the form $c(\eta)$ and smoothed. In a second step, the inverse function $\eta(c)$ was inserted into eq. (1) to obtain $D_{NaK}(c)$. The validity of the analysis was tested by back modeling of the diffusion using the extracted sodium-potassium interdiffusion coefficient, which generally gave perfect agreement between calculated and experimentally observed mole fraction profiles (see also Petrishcheva et al, submitted).

Smooth mole fraction profiles without sharp diffusion fronts yield a nearly constant sodium-potassium interdiffusion coefficient. In this case the interdiffusion coefficient can also be obtained by fitting to the well known error-function solution for diffusion into a semi-infinite half-space with a constant concentration on the boundary and a constant diffusion coefficient (Crank, 1975). Both approaches indicate that the compositional dependence of D_{NaK} is minute for $c < 0.95$, see figure 5. On the other hand, to explain the observed steep fronts developing for composition shifts to high-potassium mole fractions with $X_{Or} \geq 0.95$ it is crucial to account for the quick increase of $D_{NaK}(c)$ as c approaches 1. This increase is quantified by eq. (1). These results are discussed in more detail in the next section.

Composition and temperature dependence of the sodium-potassium interdiffusion coefficient

The compositional dependence of the interdiffusion coefficient was extracted for the composition interval $0.65 < X_{Or} < 0.99$, for the directions normal to (001) and normal to (010), for temperatures between 800 and 1000°C, and for run durations between 1 and 64 days (see figure 5).

The sodium-potassium interdiffusion coefficient has little or no compositional dependence over most of the composition range of $0.65 \leq X_{Or} \leq 0.95$. At very potassium-rich compositions of $X_{Or} \geq 0.95$ it shows a substantial increase with increasing X_{Or}. The increase in D_{NaK} towards the potassium end-member composition of the alkali feldspar is observed in both the directions perpendicular to (010) and perpendicular to (001). The increase is,

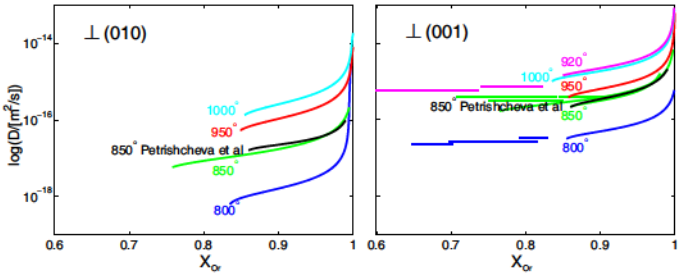

Fig. 5 Compositional dependence of D_{NaK} at 800°C, 850°C, 920°C, 950°C, and 1000°C.

however, more abrupt and more localized in composition in the direction perpendicular to (010) than perpendicular to (001). It is also seen that for the entire composition range sodium-potassium interdiffusion is faster normal to (001) than normal to (010).

Similar trends are observed at all temperatures considered in this study. For a given composition D_{NaK} increases with temperature with the only exception at 920°C. The interdiffusion coefficient extracted from experiments at 920°C is much higher than would be expected, exceeding the values for 950°C and even 1000°C. Similar results being obtained from several, separately conducted experiments, indicated that this is not the effect of faulty measurements or preparation. The higher than expected values may be an effect of the changes of physical properties documented for Eifel sanidine in this temperature range (Bertelmann et al, 1985; Demtröder, 2011), the implications of which for sodium-potassium interdiffusion are not known to date. As it is stated in literature that the changes are irreversible, two plates of Volkesfeld sanidine with polished (010) surfaces were tempered at 1050°C for four days and cooled down very slowly. Subsequently they were exchanged at 850°C for 8 days and shifted to X_{Or} 1.0 and 0.73, respectively, to test if the anomalous behaviour has an influence on the overall processes of diffusion. The resulting diffusion profiles were identical to those observed in untempered samples. Thus, if the anomaly known for Eifel sanidines has an influence, it seems to be limited to the temperature range of the actual changes to the optical properties. Further experiments beyond the scope of this study would be needed to investigate this further. The values for D at 920°C were not considered in deriving an activation energy.

$D_{\mathrm{NaK}} = D_0 \,\mathrm{Exp}\left(-\frac{E_A}{RT}\right)$, where

$$D_0^{\perp(001)}(0.92) = 4.63 \cdot 10^{-8}\mathrm{m}^2/\mathrm{s}, \quad \mathrm{E}_\mathrm{A}^{\perp(001)}(0.92) = 179\ \mathrm{kJ/mole}$$
$$D_0^{\perp(001)}(0.98) = 1.66 \cdot 10^{-7}\mathrm{m}^2/\mathrm{s}, \quad \mathrm{E}_\mathrm{A}^{\perp(001)}(0.98) = 181\ \mathrm{kJ/mole}$$
$$D_0^{\perp(010)}(0.92) = 1.97 \cdot 10^{-4}\mathrm{m}^2/\mathrm{s}, \quad \mathrm{E}_\mathrm{A}^{\perp(010)}(0.92) = 286\ \mathrm{kJ/mole}$$
$$D_0^{\perp(010)}(0.98) = 3.27 \cdot 10^{-4}\mathrm{m}^2/\mathrm{s}, \quad \mathrm{E}_\mathrm{A}^{\perp(010)}(0.98) = 277\ \mathrm{kJ/mole}$$

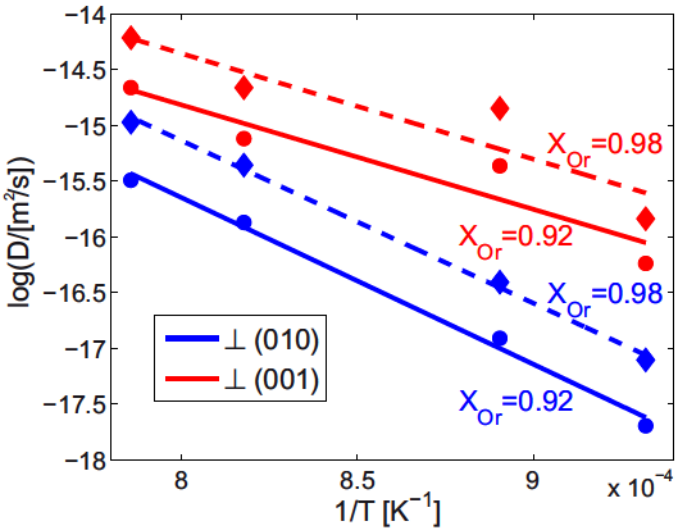

Fig. 6 Temperature dependence of D_{NaK} for directions perpendicular to (001) and perpendicular to (010) and for two compositions.

Table 3 Interdiffusion coefficients in [m^2/s] for Volkesfeld sanidine in the directions perpendicular to (001) and perpendicular to (010) and for two compositions

		⊥ (001)		⊥ (010)	
	X_{Or}	0.92	0.98	0.92	0.98
T [°C]	800	$5.80 * 10^{-17}$	$1.46 * 10^{-16}$	$2.03 * 10^{-18}$	$7.90 * 10^{-18}$
	850	$4.90 * 10^{-16}$	$1.40 * 10^{-15}$	$3.83 * 10^{-18}$	$1.29 * 10^{-17}$
	920	$2.62 * 10^{-15}$	$7.38 * 10^{-15}$		
	950	$7.62 * 10^{-16}$	$2.19 * 10^{-15}$	$1.35 * 10^{-16}$	$4.41 * 10^{-16}$
	1000	$2.19 * 10^{-15}$	$6.12 * 10^{-15}$	$3.24 * 10^{-16}$	$1.07 * 10^{-15}$

.

The corresponding Arrhenius diagram is shown in figure 6, the interdiffusion coefficients are found in table 3.

4 Discussion

Our findings from the cation exchange experiments can be summarized as follows: (1) sodium-potassium interdiffusion is markedly composition dependent at $X_{Or} \geq 0.95$. (2) In contrast, the compositional dependence of D_{NaK} is minute or entirely absent in the composition range $0.65 \leq X_{Or} \leq 0.95$. (3) For all compositions sodium-potassium interdiffusion is slower in the direction perpendicular to (010) then in the direction perpendicular to (001). (4) This behavior is found at all temperatures from 800^{o}C to 1000^{o}C.

A compositional dependence of D_{NaK} was already found in earlier studies (Petrović, 1972; Christoffersen et al, 1983; Petrishcheva et al, submitted).

Using albite with $X_{Or} = 0.00$ and orthoclase with $X_{Or} = 0.86$ in cation exchange experiments Petrović (1972) observed that D_{NaK} was independent of composition in the composition range $0.00 \leq X_{Or} \leq 0.1$ whereas a pronounced compositional dependence was observed for potassium-rich compositions with $X_{Or} \geq 0.86$.

In the study by Christoffersen et al (1983) classical diffusion couples were used, which were comprised of albite and adularia single crystals put into contact at a polished interface. During annealing at 900^oC and 1000^oC the initial compositional difference across the albite-adularia contact degraded by Na^+-K^+ cation exchange between the two crystals producing a sigmoidal mole-fraction profile. The classical Boltzmann-Matano analysis was used for extracting the composition dependent D_{NaK} in the composition range $0.10 \leq X_{Or} \leq 0.80$. A minimum was found in D_{NaK} at $X_{Or} \approx 0.4$ and an increase by a factor of 2.5 towards $X_{Or} = 0.1$ as well as an increase by a factor of about 10 towards $X_{Or} = 0.8$ (figure 7). The analysis of our 1000^oC experiments yields $D_{NaK}(c)$ which extends the earlier determinations by Christoffersen et al (1983) to higher X_{Or} without any apparent jump for both the direction perpendicular to (010) and the direction perpendicular to (001) (figure 7). As our 850^oC experiments extend over a wider composition range we re-calculated them for 1000^oC using the activation energies determined from our experiments (dashed curves in figure 7). The recalculated values plot somewhat higher than the data measured at 1000^oC. In the overlapping composition range $0.7 \leq X_{Or} \leq 0.8$, where we observe only minor compositional dependence of D_{NaK}, our data deviates from those of Christoffersen et al (1983), who observed a more pronounced compositional dependence.

Actually a strong increase in $D_{NaK}(c)$ similar to what we observe in our experiments is predicted from the model for substitutional interdiffusion in an ionic crystal as given by Manning (1968), when the self-diffusion of sodium is assumed to be significantly faster than that of potassium; based on existing literature data this assumption can be safely made. For the case of sodium-potassium interdiffusion in alkali feldspar this reads

$$D_{NaK} = \frac{D^*_{Na}(c) D^*_K(c)}{(1-c)\, D^*_{Na}(c) + c D^*_K(c)} \left[1 + \frac{\partial \ln \gamma_{Or}}{\partial \ln c}\right], \qquad (3)$$

where $D^*_{Na}(c)$ and $D^*_K(c)$ are the sodium and the potassium self-diffusion coefficients, respectively, which are considered as composition dependent, and γ_{Or} is the activity coefficient of the orthoclase phase component in the alkali feldspar solid-solution.

Figure 7 shows theoretical calculations based on equation 3 in comparison with the directly determined values of $D_{NaK}(c)$ from this study and from Christoffersen et al (1983). There is reasonable qualitative agreement between our direct determinations of $D_{NaK}(c)$ for diffusion in the directions perpendicular to (001) and perpendicular to (010) and the theoretical calculations. Our direct determinations indicate, however, slower sodium-potassium interdiffusion by a factor of about five to ten than calculated theoretically for diffusion

perpendicular to (001) and slower by almost two order of magnitude for diffusion in the direction perpendicular to (010). The same trend was observed by Christoffersen et al (1983), however, their values deviate even more significantly from those predicted for more sodium-rich compositions, which were not covered in our experiments. These discrepancies in absolute numbers are probably due to the fact that the Na- and K- tracer-diffusion coefficients that were inserted into equation 3 for constructing the diagram in figure 7 were determined using bulk exchange experiments. For the sodium-rich composition both D^*_{Na} and D^*_K were taken from Kasper (1975), and for the potassium-rich composition both D^*_{Na} and D^*_K were taken from Foland (1974). In these studies carefully sized fragments of natural orthoclase ($X_{Or} = 0.94$) and albite ($X_{Or} = 0.01$), were exchanged with a ^{41}KCl - ^{22}NaCl aqueous solution, the composition of which was chosen to ensure chemical equilibrium between the feldspar and the solution so that measured bulk isotope exchange could safely be ascribed to diffusion rather than dissolution re-precipitation. To account for potential diffusion anisotropy the diffusion coefficients were calculated assuming cylindrical geometry. By this method slow diffusion in one direction ($\perp$(010) - corresponding to the cylinder axis) and fast diffusion in the plane perpendicular to this direction (i.e., in the (010) plane) can be taken into consideration. It was argued by Petrović (1973) that sodium-potassium interdiffusion is isotropic within the (010) plane of alkali feldspar. Recent findings by Petrishcheva et al (submitted) revealed, however, a pronounced anisotropy of sodium-potassium interdiffusion within the (010) plane of alkali feldspar. It is thus well possible that the determinations of the tracer diffusion coefficients by bulk exchange (Foland, 1974; Kasper, 1975) were biased by the contribution of diffusion in the fastest direction. The theoretically calculated $D_{\mathrm{NaK}}(c)$ thus probably corresponds to diffusion in the fastest direction, which is parallel to the [101] direction (Petrishcheva et al, submitted). The $D^{\perp(001)}_{\mathrm{NaK}}(c)$ and $D^{\perp(010)}_{\mathrm{NaK}}(c)$ are thus expected to be slower than this theoretically calculated interdiffusion coefficient, which is in line with the relations shown in figure 7.

It must be noted that a reasonable qualitative agreement between the direct determinations of $D_{\mathrm{NaK}}(c)$, which were conducted by Christoffersen et al (1983) and in our study, with the predictions obtained from the interdiffusion model in equation (3) is only obtained, if the data for the tracer-diffusion coefficients D^*_{Na} and D^*_K are taken from Kasper (1975) for sodium-rich compositions and from Foland (1974) for potassium-rich compositions. There are several other determinations of D^*_{Na} and D^*_K available in literature (see figure 7). For constructing the diagram in figure 7 the choice of the self-diffusion coefficients was made such that $D^*_{Na}(c) \gg D^*_K(c)$. At potassium-rich compositions of the alkali feldspar D_{NaK} approaches $D^*_{Na}(c)$ (see eq. 3), and this choice of the tracer-diffusion coefficients produces the strong increase in the calculated $D_{\mathrm{NaK}}(c)$ towards potassium end-member composition.

This choice of the tracer-diffusion coefficients combined with the non ideality of the alkali-feldspar solid-solution also produces the pronounced compositional dependence of D_{NaK} at intermediate compositions with the minimum

of $D_{\mathrm{NaK}}(c)$ at a composition of $X_{\mathrm{Or}} \approx 0.4$ as observed by Christoffersen et al (1983). In the composition range $0.65 \leq X_{\mathrm{Or}} \leq 0.80$ the trends in $D_{\mathrm{NaK}}(c)$ derived from our direct determinations are, however, different from the trends obtained from the direct determinations of Christoffersen et al (1983) and also from what is predicted based on equation 3 using the tracer-diffusion coefficients from Kasper (1975) and Foland (1974). In particular, we find a minute or no compositional dependence of D_{NaK} in this composition range, whereas a substantial increase of D_{NaK} with increasing X_{Or} is documented in the study of Christoffersen et al (1983) and is also predicted theoretically. A D_{NaK} which is independent of composition would be predicted from equation 3, if $D^*_{Na} \approx D^*_K \approx$ const. Such a situation, would, however, not predict the pronounced increase of D_{NaK} in the composition range of $0.95 \leq X_{\mathrm{Or}} \leq 1.00$. In the light of this apparent incommensurateness between theoretical predictions and direct determinations we speculate about the presence of two different sodium species that may contribute to sodium-potassium interdiffusion in alkali feldspar. Due to its relatively small ionic radius, Na^+ may occupy interstitial positions (Behrens et al, 1990; Giletti and Shanahan, 1997). On the one hand, such interstitial Na^+ could charge-balance vacancies on the regular alkali lattice sites, and by this mechanism it could foster vacancy formation on the alkali sublattice and thus enhance sodium-potassium interdiffusion by the vacancy mechanism. On the other hand, the interstitial Na^+ could make a fast-diffusing Na-species by an interstitialcy mechanism (Petrović, 1972; Christoffersen et al, 1983; Giletti and Shanahan, 1997). The total concentrations of such interstitial Na^+ is probably very low, irrespective of the composition of the alkali feldspar. Towards high X_{Or}, when the total sodium-concentration in the feldspar becomes low, the interstitial Na^+ may form a substantial fraction of the total sodium contained in the feldspar. By this mechanism the self-diffusion of sodium would increase appreciably towards high potassium mole fraction in the alkali feldspar, and a concomitant rise of D_{NaK} would result. It may be argued based on the crystal structure (Petrović, 1972; Jones et al, 2004) that a vacancy mechanism is indispensable for diffusion in the direction perpendicular to (010). In contrast, within the (010) plane an interstitialcy mechanism may operate in addition to the vacancy mechanism. This may explain the different degrees of localization of the rise of D_{NaK} at potassium-rich compositions and the different sharpness of the diffusion fronts in the directions perpendicular to (001) and (010).

In the intermediate composition range substitutional interdiffusion on regular sites of the alkali sub-lattice is probably the main diffusion mechanism. Cation vacancies are an indispensable pre-requisite for substitutional interdiffusion to operate (Mehrer, 2007). Apart from the thermally induced point defects extrinsic defects such as heterovalent substitutions may provide additional vacancies (Mehrer, 2007). In this context the difference in the barium contents between the sanidine from Volkesfeld (0.01 Ba^{2+} a.p.f.u.) and from Rockeskyll (0.02 Ba^{2+} a.p.f.u.) may be worth considering. The Ba^{2+} may be charge-balanced by cation vacancies in the alkali sub-lattice, and sodium-potassium interdiffusion may be expected to be enhanced in the sanidine from

Rockeskyll as compared to the sanidine from Volkesfeld. Such an effect was, however, not observed systematically in our experiments.

It was found by earlier workers that diffusion in the direction perpendicular to (010) is slower than within the (010) plane (Petrović, 1972; Christoffersen et al, 1983). In the companion paper by Petrishcheva et al (submitted) the full diffusivity tensor and its compositional dependence in the range $0.85 \leq X_{\mathrm{Or}} \leq 1.00$ was determined.. These latter authors found similar differences between the rates of sodium-potassium interdiffusion in the directions perpendicular to (001) and (010) as Christoffersen et al (1983), and in addition they documented a diffusion anisotropy also within the (010) plane with the fastes diffusion in the [101] direction and slowest diffusion in the direction within the (010) plane and perpendicular to the [101] direction. Our experimental observatsion are perfectly in line with these earlier studies. We generally find for both starting materials that sodium-potassium interdiffusion in the direction perpendicular to (010), i.e. parallel to the crystallographic b-axis, is slower by a factor of 5 to 10 than in the direction perpendicular to (001), i.e. parallel to c^*. The diffusion anisotropy tends to become smaller towards higher temperatures. This diffusion anisotropy reflects the different ease of atomic jumps within the (010) plane and in the direction perpendicular to (010), which can be argued on crystal-chemical grounds (Petrović, 1972; Jones et al, 2004; Petrishcheva et al., submitted). In addition the diffusion anisotropy may, in part, also be due to the mechanical effects of composition changes associated with sodium-potassium interdiffusion. Due to the compositional dependence of the lattice parameters any composition heterogeneity that exists in a single crystal of alkali feldspar causes a distortion of the lattice and thus coherency stress. This coherency stress is localized within the diffusion front, which may lead to a feedback producing self-sharpening diffusion fronts and an overall retardation of diffusion in the direction perpendicular to (010) (Schaeffer et al, submitted). In particular, this is the case for the very narrow fronts perpendicular to (010) whereas no such effect is expected in the direction perpendicular to (001), where the diffusion fronts are comparatively broad.

In figure 8 our direct determinations of D_{NaK} and those of Christoffersen et al., (1983) are compared with experimental determinations of the sodium- and potassium tracer-diffusion coefficients taken from the literature. Although the determinations of the tracer diffusion coefficients show considerable scatter, it is generally observed that potassium tracer diffusion is slower than sodium tracer diffusion. Our determinations of D_{NaK} are shown as blue (perpendicular to (010)) and red (perpendicular to (001)) lines for $X_{\mathrm{Or}} = 0.92$ (solid) and X_{Or} 0 0.98 (dashed). The pair of black lines shows the corresponding interdiffusion coefficients given by Christoffersen et al., (1983). The activation energies that we determined for Na-K interdiffusion are in the range of the activation energies determined for sodium- and potassium tracer diffusion. In terms of absolute values the determinations of D_{NaK} by Christoffersen et al., (1983) are in good agreement with our findings, the temperature dependence of D_{NaK} as reconstructed from the data of the latter authors is however substantially lower than in our experiments.

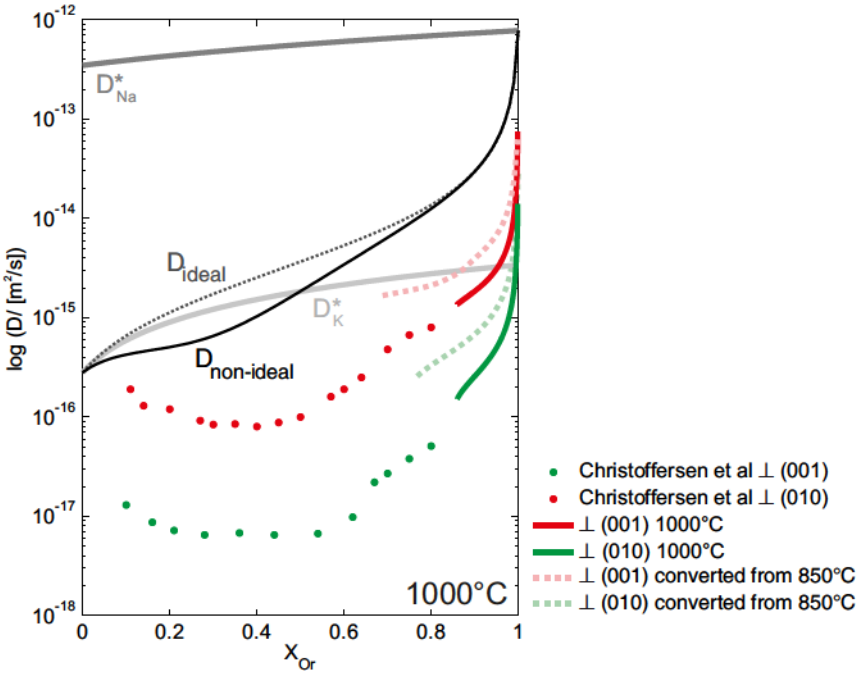

Fig. 7 Comparison of our experimental results with a theoretical interdiffusion model based on the Nernst-Planck equation, and with literature data by Christoffersen et al (1983); the theoretical values were calculated using self-diffusion coefficients for Na and K determined by Foland (1974) and Kasper (1975).

5 Conclusions

Sodium-potassium interdiffusion in disordered alkali feldspar was quantified by means of cation exchange experiments between gem quality sanidine from the Eifel and NaCl-KCl (or NaBr-KBr) salt melt at temperatures from 800^{o}C to 1000^{o}C and close to ambient pressure. Due to mechanical effects associated with large composition shifts and the limited composition range of homogeneous alkali feldspars ($X_{Or} \geq 0.72$) the sodium-potassium interdiffusion coefficient could only be determined for $X_{Or} \geq 0.65$. D_{NaK} is markedly composition dependent at $X_{Or} \geq 0.95$. In the composition range $0.95 \leq X_{Or} \leq 1.00$ D_{NaK} increases substantially with increasing X_{Or}. The compositional dependence of D_{NaK} is, however, minute or entirely absent in the composition range $0.65 \leq X_{Or} \leq 0.95$.

A pronounced diffusion anisotropy was found at all temperatures from 800^{o}C to 1000^{o}C; for all compositions sodium-potassium interdiffusion is slower in the direction perpendicular to (010) than in the direction perpendicular to (001). Also, the rise in D_{NaK} towards potassium end-member compositions is more localized for diffusion in the direction perpendicular to (010) than perpendicular to (001). We suspect that the sharp rise in D_{NaK} towards potassium

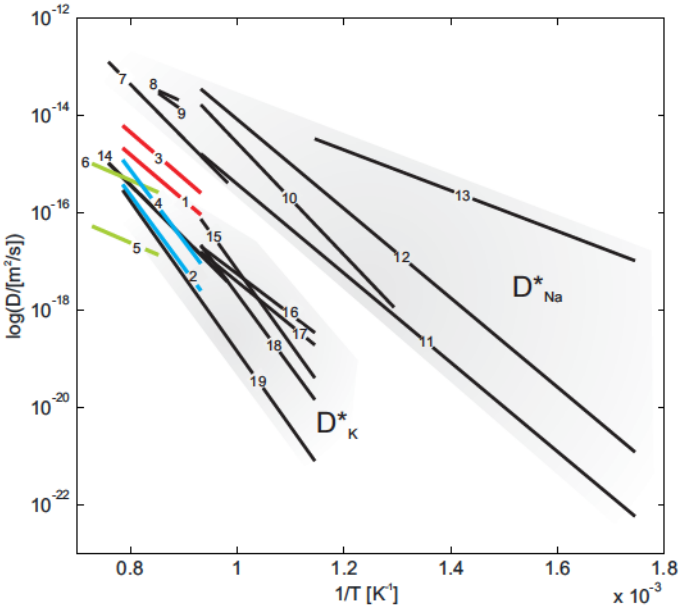

Fig. 8 Arrhenius diagram: 1 - $D^{\perp(001)}_{Na/K}(X_{Or} = 0.92)$ - this study; 2 - $D^{\perp(010)}_{Na/K}(X_{Or} = 0.92)$ - this study; 3 - $D^{\perp(001)}_{Na/K}(X_{Or} = 0.98)$ - this study; 4 - $D^{\perp(010)}_{Na/K}(X_{Or} = 0.98)$ - this study; 5 - $D^{\perp(001)}_{Na/K}$ - Christoffersen et al. (1983); 6 - $D^{\perp(010)}_{Na/K}$ - Christoffersen et al. (1983); 7 - D^{*}_{Na} $(X_{Or} = 0.86)$ - Petrovic (1972) 8 - D^{*}_{Na} - Maury (1986); 9 - D^{*}_{Na} - Sippel (1963); 10 - D^{*}_{Na} $(X_{Or} = 0.94)$ - Foland (1974); 11 - D^{*}_{Na} $(X_{Or} = 0.02)$ - Kasper (1975); 12 - D^{*}_{Na} $(X_{Or} = 0.014)$ - Bailey (1971); 13 - D^{*}_{Na} $(X_{Or} = 0.00)$ - Lin and Yund (1972); 14 - D^{*}_{K} $(X_{Or} = 0.86)$ - Petrovic (1972) 15 - D^{*}_{K} $(X_{Or} = 1.00)$ - Lin and Yund (1972); 16 - D^{*}_{K} $(X_{Or} = 0.014)$ - Giletti et al. (1974); 17 - D^{*}_{K} $(X_{Or} = 0.02)$ - Kasper (1975); 18 - D^{*}_{K} $(X_{Or} = 0.94)$ - Foland (1974); 19 - D^{*}_{K} $(X_{Or} = 0.02)$ - Giletti & Shanahan (1997) .

end-member compositions is due to the contribution of a Na^+ species occupying interstitial sites, which can contribute to the formation of vacancies on the alkali sublattice and by this enhance substitutional interdiffusion by the vacancy mechanism. In addition, interstitial Na^+ may constitute a fast diffusing Na-species by itself, where the latter mechanism may operate only within the (010) plane and is unlikely to occur in the direction perpendicular to (010). In addition the interplay between lattice distortion that is localized at the sharp diffusion fronts in the direction perpendicular to (010) and diffusion may cause a feedback leading to a self-sharpening diffusion fronts.

Acknowledgements We thank Andreas Wagner for preparing the single crystal plates with polished surfaces. This work was funded by the Austrian Science Foundation, FWF grant I 474-N19 in the framework of the DFG-FWF research group FOR 741.

6 References

Abart R, Petrishcheva E, Wirth R, Rhede D (2009) Exsolution by spinodal decomposition: Ii: perthite formation during slow cooling of anatexites from ngornghoro, tanzania. American Journal of Science 309:450-475

Angel RJ, Sochalski-Kolbus LM, Tribaudino M (2012) Tilts and tetrahedra: The origin of the anisotropy of feldspars. American Mineralogist 97:765-778

Bailey A (1971) Comparison of low-temperature with high-temperature diffusion of sodium in albite. Geochimica et Cosmochimica Acta 35:1073-1081

Behrens H, Johannes W, Schmalzried H (1990) On the Mechanics of Cation Diffusion Processes in Ternary Feldspars. Physics and Chemistry of Minerals 17:62-78

Benisek A, Dachs E, Kroll H (2010) Excess heat capacity and entropy of mixing in ternary series of high-structural-state feldspars. European Journal of Mineralogy 22:403-410

Bertelmann D, Förtsch E, Wondratschek H (1985) Zum Temperverhalten von Sanidinen: Die Ausnahmerolle der Eifelsanidin-Megakristalle. Neues Jahrbuch Mineralogische Abhandlungen 152:123-141

Boltzmann L (1894) Zur Integration der Diffusionsgleichung bei variablen Diffusionskoeffizienten. Annalen der Physik 53:959-964

Brady J (2012) Stressfields and geometrically necessary dislocation density distributions near the head of a blocked slip band. Acta Materialia 275:954-983

Brady J, Yund R (1983) Interdiffusion of K and Na in alkali feldspars: homogenization experiments. American Mineralogist 68:106-111

Cherniak D (2010) Cation diffusion in feldspars. Reviews in Mineralogy & Geochemistry 72:691-733

Christoffersen R, Yund R, Tullis J (1983) Interdiffusion of K and Na in alkali feldspars: homogenization experiments. American Mineralogist 68:1126-1133

Crank J (1975) Mathematics of Diffusion, 2nd edn. Oxford University Press, New York

Demtröder K (2011) Untersuchung zur Al/Si-Ordnung an Sanidin Megakristallen aus der Eifel. Master's thesis, Ruhr-Universität Bochum

Foland K (1974) Alkali Diffusion in Orthoclase, de Gruyter, Carnegie Institution, Washington, pp 77-98

Freer R (1981) Diffusion in Silicate Minerals and Glasses: A Data Digest and Guide to the Literature. Contributions to Mineralogy and Petrology 768:440-454

Giletti B, Shanahan T (1997) Alkali diffusion in plagioclase feldspar. Chemical Geology 139:3-20

Giletti B, Semet M, Kasper R (1974) Self-diffusion of potassium in low albite using an ion microprobe. Geol Soc Am Abstracts with Programs 6:754

Hokason S, Yund R (1986) Comparison of alkali interdiffusion rates for cryptoperthites. American Mineralogist 71:1409-1414

Jones A, Islam M, Mortimer M, Palmer D (2004) Alkali ion migration in albite and K-feldspar. Physics and Chemistry of Minerals 31:313-320

Kasper R (1975) Cation and Oxygen diffusion in albite. Ph.d. thesis, Brown University, Providence, Rhode Island

Kroll H, Schmiemann I, von Cölln G (1986) Feldspar solid solutions. American Mineralogist 71:1-16

Lin TH, Yund R (1972) Potassium and Sodium Self-Diffusion in Alkali Feldspar. Contributions to Mineralogy and Petrology 34:177-184

Manning J (1968) Diffusion Kinetics for Atoms in Crystals. Van Nostrand, New York

Matano C (1933) On the Relation between the Diffusion-Coefficients and Concentrations of Solid Metals (The Nickel-Copper System). Japanese Journal of Physics 8:109-113

Mehrer H (2007) Diffusion in Solids - Fundamentals, Methods, Materials, Diffusion-Controlled Processes. Springer, Heidelberg

Neusser G, Abart R, Fischer F, Harlov D, Norberg N (2012) Experimental Na/K exchange between alkali feldspar and salt melt: coherency effects, microstructure evolution, and element partitioning. Contributions to Mineralogy and Petrology 164:341-358

Parsons I, Lee MR (2005) Minerals are not just chemical compounds. The Canadian Mineralogist 43:1959-1992

Petrishcheva E, Abart R (2009) Exsolution by spinodal decomposition:I: evolution equation for binary mineral solutions with anisotropic interface energy . American Journal of Science 309:431-449

Petrishcheva E, Abart R, Schäffer AK, Habler G, Rhede D, (submitted) Sodium-potassium interdiffusion in potassium-rich alkali feldspar I: experimental determination of the composition dependent diffusivity tensor

Petrović R (1972) Alkali Ion Diffusion in Alkali Feldspars. Ph.d. thesis, Yale University

Petrović R (1973) The Effect of Coherency Stress on the Mechanism of the Reaction Albite + $K^+ \rightleftharpoons$ K-Feldspar + Na^+ and on the Mechanical State of the Resulting Feldspar. Contributions to Mineralogy and Petrology 41:151-170

Riley TR, Bailey DK (2003) Barium-rich sanidine megacrysts from the West Eifel (Germany) . Neues Jahrbuch für Mineralogie - Monatshefte 41:18-30

Scheidl K, Schäffer AK, Petrishcheva E, Habler G, Fischer F, Schreuer J, Abart R (2013) Chemically induced fracturing in alkali feldspar. Physics and Chemistry of Minerals

Sippel R (1963) Sodium self diffusion in natural minerals. Geochimica et Cosmochimica Acta 27:107-120

Spear FS (1993) Metamorphic Phase Equilibria and Pressure-Temperature-Time Paths. Mineralogical Society of America, Washington DC

Weitz G (1972) Die Struktur des Sanidins bei verschiedenen Ordnungsgraden. Zeitschrift für Kristallographie 136:418-426

Yund R (1983) Diffusion in Feldspars, Mineralogical Society of America, pp 203-222

Bibliography

Angel, R. J., Sochalski-Kolbus, L. M., and Tribaudino, M. (2012). Tilts and tetrahedra: The origin of the anisotropy of feldspars. *American Mineralogist*, 97:765–778.

Bailey, A. (1971). Comparison of low-temperature with high-temperature diffusion of sodium in albite. *Geochimica et Cosmochimica Acta*, 35:1073–1081.

Behrens, H., Johannes, W., and Schmalzried, H. (1990). On the Mechanics of Cation Diffusion Processes in Ternary Feldspars. *Physics and Chemistry of Minerals*, 17:62–78.

Bertelmann, D., Förtsch, E., and Wondratschek, H. (1985). Zum Temperverhalten von Sanidinen: Die Ausnahmerolle der Eifelsanidin-Megakristalle. *Neues Jahrbuch Mineralogische Abhandlungen*, 152:123–141.

Blumenauer, H. and Pusch, G. (1993). *Technische Bruchmechanik*. Deutscher Verlag für Grundstoffindustrie, Leipzig, 3rd edition.

Boltzmann, L. (1894). Zur Integration der Diffusionsgleichung bei variablen Diffusionskoeffizienten. *Annalen der Physik*, 53:959–964.

Brady, J. (1995). *Diffusion Data for Silicate Minerals, Glasses, and Liquids*, pages 269–290. American Geophysical Union.

Brady, J. and Yund, R. (1983). Interdiffusion of K and Na in alkali feldspars: homogenization experiments. *American Mineralogist*, 68:106–111.

Britton, T. and Wilkinson, A. (2012). Stress fields and geometrically necessary dislocation density distributions near the head of a blocked slip band. *Acta Materialia*, 60:5773–5782.

Cherniak, D. (2001). Ba diffusion in feldspar. *Geochimica et Cosmochimica Acta*, 9:1641–1650.

Cherniak, D. (2010). Cation diffusion in feldspars. *Reviews in Mineralogy & Geochemistry*, 72:691–733.

Christoffersen, R. (1982). *I. Disordering Kinetics and Stability of Low-Andesine, II. Na-K Interdiffusion in the Alkali Feldspars.* Ph.D. thesis, Brown University, Providence, Rhode Island.

Christoffersen, R., Yund, R., and Tullis, J. (1983). Interdiffusion of K and Na in alkali feldspars: homogenization experiments. *American Mineralogist*, 68:1126–1133.

Crank, J. (1956). *Mathematics of Diffusion.* Clarendon Press, Oxford.

Crank, J. (1975). *Mathematics of Diffusion.* Oxford University Press, New York, 2nd edition.

Darken, L. (1948). Diffusion, Mobility and Their Interrelation through Free Energy in Binary Metallic Systems. *Transactions of the American Institute of Mining, Metallurgical, and Petroleum Engineers*, 175:184–194.

Deer, W. A., Howie, R. A., and Zussman, J. (2001). *Framework silicates: Feldspars*, volume 4A. The Geological Society, London, 2nd edition.

Demtröder, K. (2011). Untersuchung zur Al/Si-Ordnung an Sanidin Megakristallen aus der Eifel. Master's thesis, Ruhruniversität Bochum.

Erdman, N., Kikuchi, N., Laudate, A., and Robertson, V. (2009). Multispectral imaging in an FEG-SEM. *Advanced Materials & Processes*, 167:28–31.

Everett, D. H. (1972). Manual of Symbols and Terminology for Physicochemical Quantities and Units, Appendix II: Definitions, Terminology and Symbols in Colloid and Surface Chemistry. *Pure and Applied Chemistry*, 31:577–638.

Fick, A. (1855). Ueber Diffusion. *Annalen der Physik*, 170:59–86.

Foland, K. (1974). *Alkali Diffusion in Orthoclase*, pages 77–98. de Gruyter, Carnegie Institution, Washington.

Freer, R. (1981). Diffusion in Silicate Minerals and Glasses: A Data Digest and Guide to the Literature. *Contributions to Mineralogy and Petrology*, 768:440–454.

Giletti, B., Semet, M., and Kasper, R. (1974). Self-diffusion of potassium in low albite using an ion microprobe. *Geol. Soc. Am. Abstracts with Programs*, 6:754.

Giletti, B. and Shanahan, T. (1997). Alkali diffusion in plagioclase feldspar. *Chemical Geology*, 139:3–20.

Griffith, A. A. (1921). The Phenomena of Rupture and Flow in Solids. *Philosophical Transactions of the Royal Society of London*, 221:163–198.

Hokason, S. and Yund, R. (1986). Comparison of alkali interdiffusion rates for cryptoperthites. *American Mineralogist*, 71:1409–1414.

Kasper, R. (1975). *Cation and Oxygen diffusion in albite*. Ph.d. thesis, Brown University, Providence, Rhode Island.

Kroll, H., Schmiemann, I., and von Cölln, G. (1986). Feldspar solid solutions. *American Mineralogist*, 71:1–16.

Lin, T.-H. and Yund, R. (1972). Potassium and Sodium Self-Diffusion in Alkali Feldspar. *Contributions to Mineralogy and Petrology*, 34:177–184.

Manning, J. (1968). *Diffusion Kinetics for Atoms in Crystals*. Van Nostrand, New York.

Maurice, C., Driver, J. H., and Fortunier, R. (2012). On solving the orientation gradient dependency of high angular resolution EBSD. *Ultramicroscopy* , 113:171–181.

Maury, R. (1968). Conductibilite electrique des tectosilicates. I. Methode et resultats experimentaux. *Bulletin de la Société Francaise Minéralogie et de Cristallographie*, 91:267–278.

Mehrer, H. (2007). *Diffusion in Solids - Fundamentals, Methods, Materials, Diffusion-Controlled Processes*. Springer, Heidelberg.

Neusser, G., Abart, R., Fischer, F., Harlov, D., and Norberg, N. (2012). Experimental Na/K exchange between alkali feldspar and salt melt: coherency effects, microstructure evolution, and element partitioning. *Contributions to Mineralogy and Petrology*, 164:341–358.

Norberg, N., Neusser, G., Wirth, R., and Harlov, D. (2011). Microstructural evolution during experimental albitization of K-rich alkali feldspar. *Contributions to Mineralogy and Petrology*, 162:531–546.

Okrusch, M. and Matthes, S. (2009). *Mineralogie: Eine Einführung in die spezielle Mineralogie, Petrologie und Lagerstättenkunde*. Springer, Berlin Heidelberg New York, 8 edition.

Onsager, L. (1931). Reciprocal Relations In Irreversible Processes I. *Physical Review*, 37:405–426.

Parsons, I., editor (1994). *Feldspars and Their Reactions*. Proceedings of the NATO Advanced Study Institute, Edinburgh, United Kingdom.

Parsons, I. and Lee, M. R. (2005). Minerals are not just chemical compounds. *The Canadian Mineralogist*, 43:1959–1992.

Petrishcheva, E., Abart, R., Schäffer, A.-K., Habler, G., and Rhede, D. (2014). Sodium-potassium interdiffusion in potassium-rich alkali feldspar I: experimental determination of the composition dependent diffusivity tensor.

Petrović, R. (1972). *Alkali Ion Diffusion in Alkali Feldspars*. Ph.d. thesis, Yale University.

Petrović, R. (1973). The Effect of Coherency Stress on the Mechanism of the Reaction Albite + $K^+ \rightleftharpoons$ K-Feldspar + Na^+ and on the Mechanical State of the Resulting Feldspar. *Contributions to Mineralogy and Petrology*, 41:151–170.

Phillips, M. and Ribbe, P. (1973). The structures of monoclinic potassium-rich feldspars. *American Mineralogist*, 58:263–270.

Reed, S. (2005). *Electron Microprobe Analysis and Scanning Electron Microscropy in Geology*. Cambridge University Press, Cambridge, New York, Melbourne, 2nd xiii edition.

Ribbe, P. (1983). *Chemistry, Structure and Nomenclature of Feldspars*, pages 1–19. Mineralogical Society of America.

Riley, T. R. and Bailey, D. K. (2003). Barium-rich sanidine megacrysts from the West Eifel (Germany) . *Neues Jahrbuch für Mineralogie - Monatshefte*, 41:18–30.

Scheidl, K., Schäffer, A.-K., Petrishcheva, E., Habler, G., Fischer, F., Schreuer, J., and Abart, R. (2013). Chemically induced fracturing in alkali feldspar. *Physics and Chemistry of Minerals*.

Schmidt, N.-H. and Olesen, N. (1989). Computer-aided determination of crystal-lattice orientation from electron-channeling patterns in the SEM. *Canadian Mineralogist*, 27:15–22.

Schreuer, J., Sondergeld, P., and Demtröder, K. (2013). Elastic properties of monoclinic alkali feldspars up to 1370 K. *Physics and Chemistry of Minerals*.

Sippel, R. (1963). Sodium self diffusion in natural minerals. *Geochimica et Cosmochimica Acta*, 27:107–120.

Snow, E. and Kidman, S. (1991). Effect of fluorine on solid-state alkali interdiffusion rates in feldspar. *Nature*, 349:231–233.

Spear, F. S. (1993). *Metamorphic Phase Equilibria and Pressure-Temperature-Time Paths*. Mineralogical Society of America, Washington, DC.

Taylor, W. (1933). The structure of sanidine and other feldspars. *Zeitschrift für Kristallographie*, 85:435–442.

Wagner, C. (1969). The evaluation of data obtained with ditrusion couples of binary single-phase and multiphase systems. *Acta Metallurgica*, 17:99–107.

Weitz, G. (1972). Die Struktur des Sanidins bei verschiedenen Ordnungsgraden. *Zeitschrift für Kristallographie*, 136:418–426.

Wilangowski, F. (2013). Tracerdiffusion von Natrium in einem kaliumreichen Feldspat. Master's thesis, Institut für Materialphysik Münster.

Wilkinson, A. J. and Britton, B. T. (2012). Strains, planes, and EBSD in materials science. *Materials Today*, 15(9):366–376.

Wilkinson, A. J., Meaden, G., and Dingley, D. J. (2006). High-resolution elastic strain measurement from electron backscatter diffraction patterns: New levels of sensitivity. *Ultramicroscopy*, 106:307–313.

Wilkinson, A. J., Meaden, G., and Dingley, D. J. (2009). Mapping strains at the nanoscale using electron back scatter diffraction. *Superlattices and Microstructures*, 45:285–294.

Yund, R. (1984). *Alkali Feldspar Exsolution: Kinetics and Dependence on Alkali Interdiffusion*, pages 281–315. Reidel Publishing Company.

Zhang, Y. (2010). *DIffusion in Minerals and Melts: Theoretical Background*, pages 5–59. Mineralogical Society of America, Geochemical Society.